The Industrial Application of Methane Pyrolysis

Tomas Kreuger

The industrial application of methane pyrolysis

Tomas Kreuger

THE INDUSTRIAL APPLICATION OF METHANE PYROLYSIS

PROEFSCHRIFT

ter verkrijging van
de graad van doctor aan de Universiteit Twente,
op gezag van de rector magnificus,
prof. dr. ir. A. Veldkamp,
volgens besluit van het College van Promoties
in het openbaar te verdedigen
op vrijdag 25 november 2022 om 12:45 uur

door

Tomas Kreuger
geboren op 4 april 1993
in Hoorn, Nederland

Dit proefschrift is goedgekeurd door:
de promotor
prof.dr. S.R.A. Kersten

This work was conducted in the Sustainable Process Technology (SPT) group of the Faculty of Science and Technology at the University of Twente, The Netherlands. This work was financially supported by Shell Global Solutions, Amsterdam, The Netherlands.

Printed by Gildeprint
ISBN: 978-90-365-5461-9
DOI: 10.3990/1.9789036554619

De promotiecommissie:

Voorzitter	prof.dr. J.L. Herek	Universiteit Twente
Promotor	prof. dr. S.R.A Kersten	Universiteit Twente
Leden	prof. dr. G. Mul	Universiteit Twente
	prof. dr. ir. L. Lefferts	Universiteit Twente
	prof. dr. ir. W.P.M. van Swaaij	Universiteit Twente
	prof. dr. ir. A.N.R. Bos	Ghent University, Shell Global Solutions
	prof. dr. ir. E.L.V. Goetheer	TU Delft, TNO

Contents

1 Introduction

With increasing world population, and increasing living standards across the globe, humanity's resource consumption is set to increase in the coming decades[7, 28]. Mainly due to this, the anthropogenic carbon emissions have increased since the start of the industrial revolution[15]. As a result, atmospheric concentration of CO_2 has increased over the last centuries. In the 2015 Paris accords worldwide governments agreed to mitigate the effects of climate change, among others by developing more sustainable methods of resource development[65].

A renewable-resource based economy is therefore seen as a goal. However, it is foreseen that in the coming decades, fossil fuels will still play a significant role in the worldwide energy and chemicals mix. Most notably, natural gas, consisting of mostly methane (CH_4), is seen as a transition fuel that will be used for the decades to come[1].

Several pathways to utilize natural gas as fuel or source for the chemical industry have been developed[29]. In some of these pathways, CH_4 is first converted into synthesis gas, being a mixture of CO and H_2. Synthesis gas is a feedstock for various processes, making it an important platform chemical. The total world market of synthesis gas is approximately 280 Mtpa[11]. With the requirement for cleaner fuels, this figure is expected to rise in the coming decades[66].

From synthesis gas, numerous products can be synthesized[66, 69]. Some examples include ammonia, methanol, synthetic fuels and waxes. Furthermore, most of the worlds hydrogen is produced via synthesis gas reforming[29].

This work regards the noncatalytic thermal conversion of methane to synthesis gas and hydrogen. The industrial potential of this pyrolysis process is evaluated.

1.1 The production of synthesis gas

Numerous industrial processes for the production of synthesis gas have been developed[13, 70]. In principle, syngas can be produced from any hydrocarbon source, but natural gas and coal are nowadays the major feedstock used for syngas generation[11, 70]. Three technologies account for the vast majority of produced syngas. Most notable methane steam reforming[70], partial oxidation of methane and authothermal reforming. These technologies will be discussed briefly.

The desired composition (being the H_2:C ratio, or syngas ratio) of the obtained synthesis gas is dependent on the intended use of this syngas. In most cases this ranges between two and three. Depending on used feedstock and production process, the produced ratio will vary. The syngas ratio is not a variable that can be controlled to a large extent, it is more or less fixed. It is therefore a challenge to match the produced and desired syngas ratio. A used solution for this is the utilization of two techniques in parallel, and mixing the obtained streams to the desired ratio[29, 53].

1.1.1 Partial oxidation

Partial oxidation (POX) is a process used in industry to convert hydrocarbons to CO and H_2[29]. It involves oxidizing the hydrocarbon with an amount of pure oxygen insufficient for complete combustion. Due to the low ratio of oxygen to carbon, combined with the high temperature (1300-1600 °C) , CO and H_2 are formed instead of CO_2 and water. Typically C and O_2 are fed in a 2:1 molar ratio. The syngas ratio obtained with PO approximately two, evident from reaction 1.1.

$$CH_4 + \frac{1}{2}O_2 \longrightarrow CO + 2H_2 \tag{1.1}$$

A large advantage of partial oxidation is that a large variety of hydrocarbons can be used as feed stock. The extreme conditions ensure that any carbon-carbon bond can be broken. The partial oxidation of hydrocarbons is exothermic, meaning that the system does not need external fuel. To prevent excessive temperature rise, steam is often added. The endothermic reaction between steam and a hydrocarbon yields additional hydrogen and simultaneously cools the system. Hence, one can effectively control the temperature in the reactor. Some processes use a catalyst in the partial oxidation reactor. This is usually a metal such as Ni, Ru or Rh (among others) supported on alumina. It is also possible not to use a catalyst, such as Shell in its gas to liquid (GTL) process[53]. POX is approximately 70-80% energy efficient[45] and emits 3 to 5.5 $kgCO_2 \cdot kgH_2{}^{-1}$ produced [40].

Disadvantages of this route arise in the process temperature and subsequent heat recovery[70]. Additionally, for the combustion pure oxygen is required, meaning an air separation installation is required[53]. The relatively low syngas ratio makes this unfavourable for applications where hydrogen rich syngas is required.

1.1.2 Methane steam reforming

The steam reforming process converts hydrocarbons towards CO and H_2 via a catalytic reaction with steam. Methane steam reforming (SMR) is the most important technology in terms of produced hydrogen volume[29, 60]. The process consists of two main reaction steps. First, methane is contacted with steam (reaction 1.2) over a Ni catalyst, typically in a multitubular fixed bed at 800-900 °C.

The resulting CO/H_2 mixture is then taken to one or more shift reactors, where, according to reaction 1.3 the CO further converted to yield more H_2 . The equilibrium of this reaction leans towards the side of H_2 at lower temperatures. Hence, this conversion is often split over a high- and a low-temperature shift reactor. The high temperature step takes advantage of kinetics, whilst the second low temperature step favours equilibirium.

$$CH_4 + H_2O \longrightarrow CO + 3H_2 \tag{1.2}$$

$$CO + H_2O \longrightarrow CO_2 + H_2 \tag{1.3}$$

All the reactions used in methane stream reforming are endothermic. Energy is supplied by a furnace. Process conditions are mild, when compared to POX or methane pyrolysis processes. Methane steam reforming is approximately 65-75% efficient[1] [10] . A disadvantage of SMR is the CO_2 emission, amounting to approximately 7 kg $CO_2 \cdot kgH_2{}^{-1}$[60]. SMR is responsible for approximately 3% of the worldwide CO_2 emissions[60].

A third production technique that is briefly named can be seen as a combination of SMR and POX. Autothermal reforming of methane (ATR) feeds methane, steam and oxygen into a single unit.

[1] Energy efficiency defined as energy in products over the total energy into the process. Some variation exists depending on how this is defined exactly.

The energy for the endothermic steam reforming reactions 1.2 and 1.3 is supplied by the partial combustion of some of the feedstock (reaction 1.4), making the reaction enthalpy near 0. Note that the reactor still requires a significant amount of energy to operate.

$$4\,CH_4 + 2\,H_2O + O_2 \longrightarrow 4\,CO + 10\,H_2 \tag{1.4}$$

1.2 Methane pyrolysis and carbon gasification

The syngas or hydrogen production process investigated in this work is the thermal decomposition, or pyrolysis, of methane. Throughout this work, these terms are used interchangeably. The process is based on the decomposition of methane at high temperature, in absence of oxygen:

$$CH_4 \longrightarrow C + 2\,H_2 \qquad \Delta H_r = 70\text{kJ}\cdot\text{mol}_c{}^{-1}, 1073\text{K} \tag{1.5}$$

The pyrolysis of methane is endothermic, with an energy consumption of approximately 70 $\text{kJ}\cdot\text{mol}_c{}^{-1}$ (1073 K). The equilibrium conversion is presented in figure 1.2. It can be seen that high temperatures are required to achieve full conversion. Increasing pressure pushes back the equilibrium conversion due to the net production of moles.

The pyrolysis reaction has the advantage that pure hydrogen is obtained, this is already separated from the deposited carbon. The deposited carbon contains approximately 40% of the energy in the system. It may be sold as is, or it can be gasified to yield extra products. In figure 1.1 a possible CH_4 pyrolysis schematic is presented. Here, carbon is first deposited. Afterwards, a steam gasification step is present. The remaining carbon is then oxidized using O_2 to yield energy and a clean carrier.

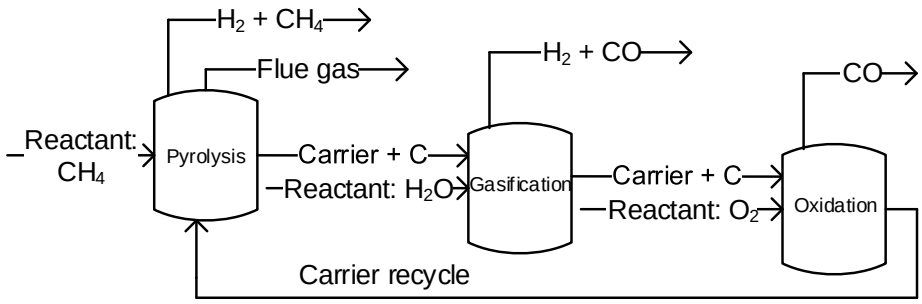

Figure 1.1: A possible CH_4 pyrolysis process schematic

In this work, three gasification options are presented:

$$C + H_2O \longrightarrow CO + H_2 \qquad \Delta H_r = 133\text{kJ} \cdot \text{mol}_c{}^{-1}, 1073\text{K} \tag{1.6}$$

$$C + CO_2 \rightleftharpoons 2\,CO \qquad \Delta H_r = 165\text{kJ} \cdot \text{mol}_c{}^{-1}, 1073\text{K} \tag{1.7}$$

$$C + \frac{1}{2}O_2 \longrightarrow CO \qquad \Delta H_r = -116\text{kJ} \cdot \text{mol}_c{}^{-1}, 1073\text{K} \tag{1.8}$$

The oxidation of carbon at high temperature yields CO instead of CO_2 due to the Boudouard reaction (Eq. 1.7). Therefore, depending on the heating method used for this process, hydrogen or synthesis gas may be produced with a small CO_2 footprint. Furthermore, by employing a mix of the gasification reactions, a syngas ratio between 1 and 3 can be obtained. This level of flexibility is not present in the conventional techniques.

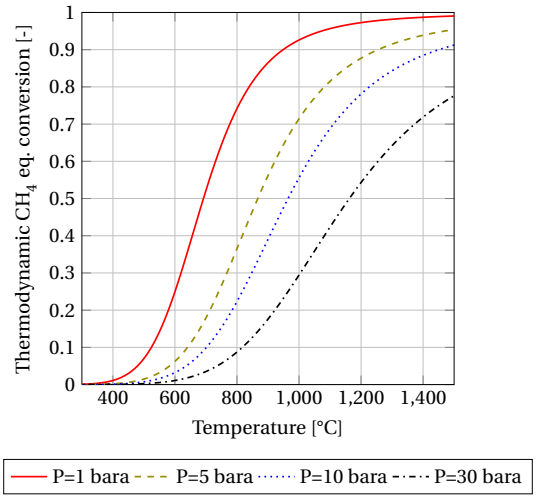

Figure 1.2: Thermodynamic equilibrium conversion of methane via reaction 1.5 for various overall pressures

1.2.1 The deposition of carbon

The decomposition reaction mechanism has been studied extensively[5, 16, 19, 27, 30, 39, 43, 44, 55, 56]. It is generally accepted that the formation of solid carbon from methane is achieved via the formation of acetylene and benzene[30, 31, 57]. The simplified reaction network is a stepwise dehydrogenation: $CH_4 \rightarrow C_2H_6 \rightarrow C_2H_4 \rightarrow C_2H_2 \rightarrow C_6H_6 \rightarrow C$. Several authors have proposed more expanded reaction networks consisting of hundreds of reactions[46, 57, 67]. Methane is an exceptionally stable molecule. Therefore, the initial activation of this molecule is slow. A high activation energy is present for this initial activation. The reactions of all the intermediates are significantly faster[34, 71]. Some debate exists on the exact initiating step[34], but it is agreed

upon this is a free radical mechanism. Furthermore, it is known that the conversion of methane is accelerated by the presence of a surface [37, 54].

The formation mechanism of carbon as a solid is a topic still debated in literature[23, 27, 37, 44, 55, 64, 72]. Some authors suggest a condensation mechanism, where an intermediate condenses before solid carbon may be formed [24, 34, 71]. Some authors observe an autoacceleration in carbon deposition[37]. This is attributed to a nucleation formation mechanism[22, 64]. After this initial nucleus has been formed, carbon growth is accelerated[54]. What is clear is that the presence of a surface greatly accelerates the formation of carbon[37, 54].

The form of the carbon deposited is dependent on the pyrolysis conditions under which it has been produced[25, 38]. At relatively low temperature (800-900 °C) a soot-like, soft, sticky and black material is obtained[8, 25]. This type contains many polyaromatic hydrocarbons (PAH)[18], and could be seen as an intermediate between methane and graphite. At higher temperature (1100 °C and higher) a gray, hard and almost metallic like material is obtained. This is pyrolytic graphite[6, 25]. It has a much lower H/C ratio and contains a negligible to zero amount of PAH intermediates[8, 25].

1.2.2 Substrate materials and catalysts

Various materials have been tested for the deposition of carbon. It is known that metal catalysts are able to reduce the required temperatures for the methane decomposition to occur[51]. Among others, the usage of Cu, Fe and Ni catalysts to decompose methane are widely reported in literature[3, 21, 61]. Temperatures above 350°C are required for a measurable conversion. This is a significant decrease when compared to the approximately 850°C for purely ceramic surfaces[37, 42].

The major trade-off for this temperature decrease is the stability of the metal catalyst. Due to the decomposition of carbon, the active surface of the catalyst does not remain available over time[42]. Deactivation time of metal catalysts ranges from complete deactivation in hours to a stable production lasting several days, albeit at low concentrations and flows[36, 61]. In some cases, the deposited carbon to catalyst weight ratio may exceed 100 $g \cdot g^{-1}$[12]. The work in this thesis focuses on various unfunctionalized carriers, due to the vastly enhanced stability of these, compared to metal functionalized carriers.

To further complicate this, it is reported that, other than gasification of the carbon, no mechanical or chemical method is able to remove the carbon from the catalyst surface[51]. Therefore, it is paramount that the catalyst is able to withstand these gasification conditions without deactivation. The harsh conditions required for gasification accelerate the permanent deactivation of the catalyst due to the loss of active sites.

A carbon surface can also be used to facilitate the decomposition reaction. The major advantage of this is that the final material is composed of only carbon, and no separation is required. The overall catalytic activity is lower than that of a metal based catalyst[2]. Several surfaces have been characterized, more disordered forms are found to be more catalytically active than ordered carbons[48, 49]. This is attributed to the higher concentration of active sites (e.g. edges, corners, faults) present in the disordered carbons.

Work regarding carbon deposition in or on various porous media has been published[4, 5, 18, 26, 48–51, 62, 68]. It is reported that the initial decomposition rate is related to surface area, and the

concentration of high energy groups[4, 48–50, 62]. The amount of carbon that can be deposited before deactivation is dependent on pore volume, pore size, pore area and surface groups, but also dependent on process conditions. It is found that the amount of carbon that can be deposited scales with the initial pore volume.

1.2.3 Gasification of carbon

Gasification of numerous types of carbonaceous materials ranging from activated carbon to graphite is extensively reported in literature[9, 17, 20, 41, 58, 68], and is generally well understood. It is found that the gasification rate of various types of coal is inversely proportional to the mass percentage of carbon[32, 47] in this coal, most notably for the high rank[1] coals (wt.% C> 80). This is supported as follows. Generally, the lower rank coals contain more contaminants, such as ash, defects, or oxygenated groups. It is known that these groups act as active sites for the gasification step[52, 63, 73].

Note that the highest rank coal contains significantly more contaminants and/or defects than (pyrolytic) graphite[8]. Hence, if the trend discussed is extended to graphite, it is to be expected that the gasifiation rate of graphite is slower than these coals. This is also found in literature[14, 33, 52, 58, 59, 68]. The more perfect the graphite, the slower the gasification occurs.

Highly ordered graphite requires extreme temperatures (2000 °C and higher) to be gasified with steam or CO_2 [35]. Depending on the pyrolysis conditions, the gasification characteristics of the produced carbon change[8]. A lower pyrolysis temperature results in a more reactive gasification. This can be related directly to the degree of graphitization of the material[37].

1.3 Thesis scope and outline

In this work, first steps towards an industrial application of methane pyrolysis are made. The overall goal of this work is two fold. First, it is aimed to demonstrate a continuous lab scale pyrolysis process. Second, it is aimed to identify the most important parameters affecting the viability of an industrial methane pyrolysis process.

Initially it was found that limited to no data is present on the deposition and gasification of carbon on unfunctionalized surfaces. Hence, the initial part of this study aims to gather information. In **chapter 2** an experimental method is developed in which the inherent methane pyrolysis and carbon deposition kinetics are measured on a single, nonporous, unfunctionalized α-Al_2O_3 particle. A fixed bed setup (gram C per day scale) was also used to characterize various aspects of methane conversion and side product formation.

The gasification reactions are investigated using the same method as in **chapter 3**, again on nonporous, unfunctionalized α-Al_2O_3 particles. Steam, CO_2 and air are used as oxidants. The deposited carbon is also characterized, using various analysis techniques. A method is presented to predict gasification rates as function of the pyrolysis conditions.

In **chapter 4**, the deposition kinetics are expanded to various types of porous particles. The internal area enhances the vollumetric reaction rates [$mol_c \cdot m_r^{-3} \cdot s^{-1}$] obtainable in a reactor, and are therefore of great interest for industrial application. The influence of particle characteristics on

[1] The rank of coal is a measure for the coals purity or energy content of the material. A higher rank coal has a higher mass fraction of carbon and fewer impurities.

the carbon deposition within the particle were characterized. Additionally, mass transfer within the particle was investigated. Using this knowledge, a simple particle model was then presented.

Using the information obtained in chapters 2-4, a continuous kg C per day lab scale setup was designed. This is documented in **chapter 5** and appendix B. First, various designs were evaluated using numerical models. The most suitable design was constructed. The extension towards the continuous domain allowed to gather information relevant for the further development of this process.

Finally, in **chapter 6** various industrial process configurations are evaluated. Using the knowledge obtained in all the earlier chapters, numerous reactor and process models models were constructed. By evaluating the energy and carbon efficiencies of these processes, the most promising were selected and evaluated further. The important parameters driving the viability of these processes were presented. Lastly, a comparison to the industrial standard was presented. **Chapter 7** presents the conclusions and reflections of this thesis.

Bibliography

[1] 2021-2025: Rebound and beyond, 2020. URL https://iea.blob.core.windows.net/assets/555b268e-5dff-4471-ac1d-9d6bfc71a9dd/Gas_2020.pdf.

[2] A. Abánades, E. Ruiz, E. M. Ferruelo, F. Hernández, A. Cabanillas, J. M. Martínez-Val, J. A. Rubio, C. López, R. Gavela, G. Barrera, C. Rubbia, D. Salmieri, E. Rodilla, and D. Gutiérrez. Experimental analysis of direct thermal methane cracking. *International Journal of Hydrogen Energy*, 36(20):12877–12886, 2011. ISSN 03603199. doi: 10.1016/j.ijhydene.2011.07.081.

[3] Rita Aiello, Jeffrey E. Fiscus, Hans Conrad Zur Loye, and Michael D. Amiridis. Hydrogen production via the direct cracking of methane over Ni/SiO2: Catalyst deactivation and regeneration. *Applied Catalysis A: General*, 192(2):227–234, 2000. ISSN 0926860X. doi: 10.1016/S0926-860X(99)00345-2.

[4] J. Ashok, S. Naveen Kumar, A. Venugopal, V. Durga Kumari, S. Tripathi, and M. Subrahmanyam. CO free hydrogen by methane decomposition over activated carbons. *Catalysis Communications*, 9(1):164–169, 1 2008. ISSN 15667367. doi: 10.1016/j.catcom.2007.05.046. URL https://linkinghub.elsevier.com/retrieve/pii/S1566736707002452.

[5] Zongqing Bai, Haokan Chen, Baoqing Li, and Wen Li. Catalytic decomposition of methane over activated carbon. *Journal of Analytical and Applied Pyrolysis*, 73(2):335–341, 2005. ISSN 01652370. doi: 10.1016/j.jaap.2005.03.004.

[6] A. Becker and K. J. Hüttinger. Chemistry and kinetics of chemical vapor deposition of pyrocarbon - IV pyrocarbon deposition from methane in the low temperature regime. *Carbon*, 36 (3):213–224, 1998. ISSN 00086223. doi: 10.1016/S0008-6223(97)00177-2.

[7] Fatih Birol. World Energy Outlook. *International Energy Agency*, 2009.

[8] L C Blackman, G Saunders, and A R Ubbelohde. Defect structure and properties of pyrolytic carbons. *Proceedings of the Royal Society of London. Series A. Mathematical and Physical Sciences*, 264(1316):19–40, 1961. ISSN 0080-4630. doi: 10.1098/rspa.1961.0183.

[9] T.H. BLAKELEY. the Gasification of Carbon in Carbon Dioxide and Other Gases At Temperatures Above 900°C. *Carbon*, 4th Editio:95–105, 1960. doi: 10.1016/b978-1-4831-9835-4.50017-3.

[10] A. Carrara, A. Perdichizzi, and G. Barigozzi. Simulation of an hydrogen production steam reforming industrial plant for energetic performance prediction. *International Journal of Hydrogen Energy*, 35(8):3499–3508, 2010. ISSN 03603199. doi: 10.1016/j.ijhydene.2009.12.156. URL http://dx.doi.org/10.1016/j.ijhydene.2009.12.156.

[11] Gabriele Centi and Siglinda Perathoner. Chemistry and energy beyond fossil fuels. A perspective view on the role of syngas from waste sources. *Catalysis Today*, 342(March 2018):4–12, 2020. ISSN 09205861. doi: 10.1016/j.cattod.2019.04.003. URL https://doi.org/10.1016/j.cattod.2019.04.003.

[12] Vladimir V Chesnokov and Alexandra S Chichkan. 1-s2.0-S036031990900144X-main.pdf. *international journal of hydrogen energy*, 34(7):2979–2985, 2009.

[13] T. H. Christensen, R. Cossu, and R. Stegmann. Gas Production. In *Landfilling of Waste: Biogas*, pages 235–315. 2020. doi: 10.1201/9781003062097-4.

[14] X. Chu and L. D. Schmidt. Reactions of NO, O2, H2O, and CO2 with the basal plane of graphite. *Surface Science*, 268(1-3):325–332, 1992. ISSN 00396028. doi: 10.1016/0039-6028(92)90972-9.

[15] Monica Crippa, Diego Guizzardi, Enrico Pisoni, Efisio Solazzo, and Antoine Guion. Global anthropogenic emissions in urban areas : patterns , trends , and challenges. 2009.

[16] Gilles H. Denis and Thomas E. Daubert. Application of quasilinearization to methane pyrolysis. *AIChE Journal*, 20(4):720–727, 1974. ISSN 15475905. doi: 10.1002/aic.690200413.

[17] Initial Distribution, I S Limited, F O R Additional, Copies See, and Back Cover. Reactions between Gases and Solids. *Agard*, (32), 1970.

[18] Alan M. Dunker, Sudarshan Kumar, and Patricia A. Mulawa. Production of hydrogen by thermal decomposition of methane in a fluidized-bed reactor - Effects of catalyst, temperature, and residence time. *International Journal of Hydrogen Energy*, 31(4):473–484, 2006. ISSN 03603199. doi: 10.1016/j.ijhydene.2005.04.023.

[19] B Eisenberg and H Bliss. Kinetics of methane pyrolysis. In *Chem. Eng. Prog. Symp. Ser.*, volume 63, pages 3–17. Yale Univ., New Haven, CT, 1967. URL `http://www.osti.gov/energycitations/product.biblio.jsp?osti_id=5142124`.

[20] Sabri Ergun. Kinetics of the reaction of carbon dioxide with carbon. *Journal of Physical Chemistry*, 60(4):480–485, 1956. ISSN 00223654. doi: 10.1021/j150538a022.

[21] M. A. Ermakova, D. Yu Ermakov, and G. G. Kuvshinov. Effective catalysts for direct cracking of methane to produce hydrogen and filamentous carbon. Part I. Nickel catalysts. *Applied Catalysis A: General*, 201(1):61–70, 2000. ISSN 0926860X. doi: 10.1016/S0926-860X(00)00433-6.

[22] D. V. Fedoseev, S. P. Vnukov, and B. V. Derjaguin. Physico-chemical theory of graphite growth from hydrocarbons. *Carbon*, 17(6):453–458, 1979. ISSN 00086223. doi: 10.1016/0008-6223(79)90033-2.

[23] D. V. Fedoseev, S. P. Vnukov, and B. V. Derjaguin. Physico-chemical theory of graphite growth from hydrocarbons. *Carbon*, 17(6):453–458, 1979. ISSN 00086223. doi: 10.1016/0008-6223(79)90033-2.

[24] Radiation Gas. The emission spectrum of hydrocarbon flames. *Proceedings of the Royal Society of London. Series A. Mathematical and Physical Sciences*, 174(956):110–125, 1940. ISSN 0080-4630. doi: 10.1098/rspa.1940.0009.

[25] C. Guéret, F. Billaud, B. Fixari, and P. Le Perchec. Thermal coupling of methane, experimental investigations on coke deposits. *Carbon*, 33(2):159–170, 1995. ISSN 00086223. doi: 10.1016/0008-6223(94)00120-O.

[26] Ling Han, Tae Ki Lim, Young Jun Kim, Hyun Sik Hahm, and Myung Soo Kim. Hydrogen production by catalytic decomposition of methane over carbon nanofibers. *Materials Science Forum*, 510-511(2):30–33, 2006. ISSN 16629752. doi: 10.4028/0-87849-995-4.30.

[27] Peter Harris. 'Chemistry and physics of carbon'. *Materials Science and Technology*, 13(12): 1066–1066, 1997. ISSN 0267-0836. doi: 10.1179/mst.1997.13.12.1066.

[28] Howard Herzog. Carbon Dioxide Capture and Storage. In *The Economics and Politics of Climate Change*. 2015. ISBN 9780191808616. doi: 10.1093/acprof:osobl/9780199573288.003.0013.

[29] Heinz Hiller, Rainer Reimert, Friedemann Marschner, Hans-Joachim Renner, Walter Boll, Emil Supp, Miron Brejc, Waldemar Liebner, Georg Schaub, Gerhard Hochgesand, Christopher Higman, Peter Kalteier, Wolf-Dieter Müller, Manfred Kriebel, Holger Schlichting, Heiner Tanz, Hans-Martin Stönner, Helmut Klein, Wolfgang Hilsebein, Veronika Gronemann, Uwe Zwiefelhofer, Johannes Albrecht, Christopher J. Cowper, and Hans Erhard Driesen. Gas Production. *Ullmann's Encyclopedia of Industrial Chemistry*, 2006. doi: 10.1002/14356007.a12{_}169.pub2.

[30] A. Holmen, O. A. Rokstad, and A. Solbakken. High-Temperature Pyrolysis of Hydrocarbons. 2. Naphtha to Acetylene. *Industrial and Engineering Chemistry Process Design and Development*, 18(4):653–657, 1979. ISSN 01964305. doi: 10.1021/i260072a014.

[31] Anders Holmen. Direct conversion of methane to fuels and chemicals. *Catalysis Today*, 142 (1-2):2–8, 2009. ISSN 09205861. doi: 10.1016/j.cattod.2009.01.004.

[32] Muhammad F. Irfan, Muhammad R. Usman, and K. Kusakabe. Coal gasification in CO2 atmosphere and its kinetics since 1948: A brief review. *Energy*, 36(1):12–40, 2011. ISSN 03605442. doi: 10.1016/j.energy.2010.10.034. URL `http://dx.doi.org/10.1016/j.energy.2010.10.034`.

[33] Yoshiaki Kashiwaya, Maki Iwasa, and Kuniyoshi Ishii. Kinetic analysis of the gasification of diamond. *Materials Transactions*, 49(7):1563–1571, 2008. ISSN 13459678. doi: 10.2320/matertrans.MRA2008069.

[34] M S Khan and Billy L Crynes. Survey of recent methane pyrolysis literature. *Industrial & Engineering Chemistry*, 62(10):54–59, 1970. ISSN 00197866. doi: 10.1021/ie50730a005.

[35] Merrill K. King. Kinetics of high-temperature reactions of graphite with carbon dioxide and water. *Journal of Spacecraft and Rockets*, 8(5):470–476, 1971. ISSN 00224650. doi: 10.2514/3.59680. URL `https://arc.aiaa.org/doi/abs/10.2514/3.59680?journalCode=jsr`.

[36] A. Konieczny, K. Mondal, T. Wiltowski, and P. Dydo. Catalyst development for thermocatalytic decomposition of methane to hydrogen. *International Journal of Hydrogen Energy*, 33(1): 264–272, 2008. ISSN 03603199. doi: 10.1016/j.ijhydene.2007.07.054.

[37] T. Kreuger, W. P.M. van Swaaij, A. N.R. Bos, and S. R.A. Kersten. Methane decomposition kinetics on unfunctionalized alumina surfaces. *Chemical Engineering Journal*, 427(June 2021):130412, 2022. ISSN 13858947. doi: 10.1016/j.cej.2021.130412. URL `https://doi.org/10.1016/j.cej.2021.130412`.

[38] Tomas Kreuger, Kersten, S.R.A, and A.N.R. Bos. Predicting gasification rates of pyrolytic graphite deposited from methane. *Chemical Engineering Journal*, 2022.

[39] J. Lahaye, G. Prado, and J. B. Donnet. Nucleation and growth of carbon black particles during thermal decomposition of benzene. *Carbon*, 12(1):27–35, 1974. ISSN 00086223. doi: 10.1016/0008-6223(74)90037-2.

[40] Janice M Lane and Pamela L Spath. Technoeconomic Analysis of the Thermocatalytic Decomposition of Natural Gas. *Nrel*, (December), 2001.

[41] Milton Levy. Oxidation of pyrolytic graphite in air between 1250° and 1850°F. *Industrial and Engineering Chemistry Product Research and Development*, 1(1):19–23, 1962. ISSN 01964321. doi: 10.1021/i360001a005.

[42] Aik Chong Lua and Hong Yan Wang. Hydrogen production by catalytic decomposition of methane over Ni-Cu-Co alloy particles. *Applied Catalysis B: Environmental*, 156-157(6):84–93, 2014. ISSN 09263373. doi: 10.1016/j.apcatb.2014.02.046.

[43] K. I. Makarov and V. K. Pechik. Kinetics of methane thermal decomposition on the carbon surface in transient regime. *Carbon*, 7(2):279–285, 1969. ISSN 00086223. doi: 10.1016/0008-6223(69)90110-9.

[44] K. I. Makarov and V. K. Pechik. Kinetics of methane pyrolysis under conditions of pyrolytic carbon formation. *Carbon*, 12(4):391–403, 1974. ISSN 00086223. doi: 10.1016/0008-6223(74)90004-9.

[45] Angel Martínez-Rodríguez and Alberto Abánades. Comparative analysis of energy and exergy performance of hydrogen production methods. *Entropy*, 22(11):1–17, 2020. ISSN 10994300. doi: 10.3390/e22111286.

[46] David M. Matheu, Anthony M. Dean, Jeffrey M. Grenda, and William H. Green. Mechanism generation with integrated pressure dependence: A new model for methane pyrolysis. *Journal of Physical Chemistry A*, 107(41):8552–8565, 2003. ISSN 10895639. doi: 10.1021/jp0345957.

[47] Kouichi Miura, Kenji Hashimoto, and Peter L. Silveston. Factors affecting the reactivity of coal chars during gasification, and indices representing reactivity. *Fuel*, 68(11):1461–1475, 1989. ISSN 00162361. doi: 10.1016/0016-2361(89)90046-X.

[48] R Moliner, I Suelves, M J Lázaro, and O Moreno. Thermocatalytic decomposition of methane over activated carbons: influence of textural properties and surface chemistry. *International Journal of Hydrogen Energy*, 30(3):293–300, 2005.

[49] N. Muradov. Catalysis of methane decomposition over elemental carbon. *Catalysis Communications*, 2(3-4):89–94, 2001. ISSN 15667367. doi: 10.1016/S1566-7367(01)00013-9.

[50] Nazim Muradov, Franklyn Smith, and Ali T-Raissi. Catalytic activity of carbons for methane decomposition reaction. *Catalysis Today*, 102-103:225–233, 2005. ISSN 09205861. doi: 10.1016/j.cattod.2005.02.018.

[51] Nazim Z. Muradov. CO2-free production of hydrogen by catalytic pyrolysis of hydrocarbon fuel. *Energy and Fuels*, 12(1):41–48, 1998. ISSN 08870624. doi: 10.1021/ef9701145.

[52] K. Otto, L. Bartosiewicz, and M. Shelef. Catalytic steam gasification of graphite: Effects of calcium, strontium, and barium with and without sulfur. *Carbon*, 17(4):351–357, 1979. ISSN 00086223. doi: 10.1016/0008-6223(79)90008-3.

[53] Rob Overtoom, Niels Fabricius, and Wim Leenhouts. *Shell GTL, from Bench scale to World scale.* Elsevier Ltd., 1 edition, 2009. doi: 10.1016/b978-0-444-53292-3.50046-8. URL https://doi.org/10.1016/B978-0-444-53292-3.50046-8.

[54] H. B. Palmer, J. Lahaye, and K. C. Hou. On the kinetics and mechanism of the thermal decomposition of methane in a flow system. *Journal of Physical Chemistry*, 72(1):348–353, 1968. ISSN 00223654. doi: 10.1021/j100847a068.

[55] H. B. Palmer, J. Lahaye, and K. C. Hou. On the kinetics and mechanism of the thermal decomposition of methane in a flow system. *Journal of Physical Chemistry*, 72(1):348–353, 1968. ISSN 00223654. doi: 10.1021/j100847a068.

[56] J. L. Pinilla, I. Suelves, M. J. Lázaro, and R. Moliner. Kinetic study of the thermal decomposition of methane using carbonaceous catalysts. *Chemical Engineering Journal*, 138(1-3):301–306, 2008. ISSN 13858947. doi: 10.1016/j.cej.2007.05.056.

[57] Sylvain Rodat, Stéphane Abanades, Julien Coulié, and Gilles Flamant. Kinetic modelling of methane decomposition in a tubular solar reactor. *Chemical Engineering Journal*, 146(1): 120–127, 2009. ISSN 13858947. doi: 10.1016/j.cej.2008.09.008.

[58] Daniel E. Rosner and Joseph P. Strakey. High-temperature kinetics of pyrolytic graphite gasification by fluorine atoms and molecules. *Journal of Physical Chemistry*, 77(5):690–699, 1973. ISSN 00223654. doi: 10.1021/j100624a027.

[59] M. Shelef and P. L. Walker. Transient phenomena in the gasification of graphite by high-purity carbon dioxide. *Carbon*, 5(2):93–105, 1967. ISSN 00086223. doi: 10.1016/0008-6223(67)90063-2.

[60] R. Soltani, M. A. Rosen, and I. Dincer. Assessment of CO2 capture options from various points in steam methane reforming for hydrogen production. *International Journal of Hydrogen Energy*, 39(35):20266–20275, 2014. ISSN 03603199. doi: 10.1016/j.ijhydene.2014.09.161. URL http://dx.doi.org/10.1016/j.ijhydene.2014.09.161.

[61] I. Suelves, M. J. Lázaro, R. Moliner, B. M. Corbella, and J. M. Palacios. Hydrogen production by thermo catalytic decomposition of methane on Ni-based catalysts: Influence of operating conditions on catalyst deactivation and carbon characteristics. *International Journal of Hydrogen Energy*, 30(15):1555–1567, 2005. ISSN 03603199. doi: 10.1016/j.ijhydene.2004.10.006.

[62] I. Suelves, J. L. Pinilla, M. J. Lázaro, and R. Moliner. Carbonaceous materials as catalysts for decomposition of methane. *Chemical Engineering Journal*, 140(1-3):432–438, 2008. ISSN 13858947. doi: 10.1016/j.cej.2007.11.014.

[63] Takayuki Takarada, Yasukatsu Tamai, and Akira Tomita. Reactivities of 34 coals under steam gasification. *Fuel*, 64(10):1438–1442, 1985. ISSN 00162361. doi: 10.1016/0016-2361(85)90347-3.

[64] P. A. Tesner, T. D. Smegiriova, and V. G. Knorre. Kinetics of dispersed carbon formation. *Combustion and Flame*, 17(2):253–260, 1971. ISSN 00102180. doi: 10.1016/S0010-2180(71)80168-2.

[65] United Nations. Paris agreement, 2015. URL https://unfccc.int/process-and-meetings/the-paris-agreement/the-paris-agreement.

[66] a. Van Der Drift, R Van Ree, H Boerrigter, and K Hemmes. Bio-Syngas : Key Intermediate for Large Scale Production of Green Fuels and Chemicals. *The 2nd World Conference and Technology Exhibition on Biomass for Energy, Industry and Climate Protection*, (May):10–14, 2004. URL https://www.ecn.nl/docs/library/report/2004/rx04048.pdf.

[67] Angayle Vasiliou, Mark Nimlos, and G. Barney Ellison. Mechanism of the thermal decomposition of furan. In *ACS National Meeting Book of Abstracts*. ACS Publications, 2009. ISBN 9780841224414.

[68] O. Vohler, P. L. Reiser, and E. Sperk. Deposition of pyrolytic carbon in the pores of graphite bodies - I. Introduction to and results of deposition experiments using methane. *Carbon*, 6 (3), 1968. ISSN 00086223. doi: 10.1016/0008-6223(68)90035-3.

[69] Irving Wender. Reactions of synthesis gas. *Fuel Processing Technology*, 48(3):189–297, 1996. ISSN 03783820. doi: 10.1016/S0378-3820(96)01048-X.

[70] D.J. Wilhelm, D.R Simbeck, A.D Karp, and R.L Dickenson. Syngas production for gas-to-liquids applications: technologies, issues and outlook. *Fuel Processing Technology*, 71(1-3):139–148, 6 2001. ISSN 03783820. doi: 10.1016/S0378-3820(01)00140-0. URL https://linkinghub.elsevier.com/retrieve/pii/S0378382001001400.

[71] Alvin E Witt. A PRELIMINARY INVESTIGATION OF THE FORMATION OF CARBON BLACK BY THE PYROLYSIS OF RESIDUAL FUEL OIL FE 2 1I2S IBARs State University. 1966.

[72] Alvin E Witt. *A PRELIMINARY INVESTIGATION OF THE FORMATION OF CARBON BLACK BY THE PYROLYSIS OF RESIDUAL FUEL OIL FE 2 1I2S IBARs State University*. PhD thesis, Massachusetts Institute of Technology, 1966.

[73] D. P. Ye, J. B. Agnew, and D. K. Zhang. Gasification of a South Australian low-rank coal with carbon dioxide and steam: Kinetics and reactivity studies. *Fuel*, 77(11):1209–1219, 1998. ISSN 00162361. doi: 10.1016/S0016-2361(98)00014-3.

2 The deposition of carbon on nonporous media

This chapter has been published as: Kreuger, T., van Swaaij, W. P. M., Bos, A. N. R., & Kersten, S. R. A. (2022). Methane decomposition kinetics on unfunctionalized alumina surfaces. Chemical Engineering Journal, 427, 130412.

Table 2.1: Symbol list for chapter 2

Symbol	Description	Unit
ρ_p	Density	$kg \cdot m^{-3}$
S	Selectivity	
C	Concentration	$mol \cdot m^{-3}$
C	Loading	$g \cdot m^{-2}$
t	Time	s
R_x	Reaction rate x	
k	Rate constant	
Ea	Activation energy	$kJ \cdot mol^{-1}$
T	Temperature	K
R	Gas constant	$J \cdot mol^{-1} \cdot K^{-1}$
P	Polynomial constant	
D	Diameter	m
A	Surface	m^2
τ	Residence time	s
F	View factor	
ΔH_r	Reaction enthalpy	$J \cdot mol^{-1}$
ϵ	Emissivity	
ω	Stefan-Boltzmann constant	$J \cdot m^{-2} \cdot K^{-4}$
E	Energy	J
U	Heat transfer coefficient	$W \cdot m^{-2} \cdot K^{-1}$

Abbr.	Description	Unit
Abbr.	Abbreviation	
ID	Inner diameter	m
OD	Outer diameter	m
TOS	Time on stream	s
AS	Available sites	
nuc	Nuclei	
C	Carbon	

Subscript	Description
p	Particle, Product
M	Methane
ex	External
0	Initial
dec	Decomposition, Pyrolysis
mod	Model
exp	Experimental
int	Internal
HE	Heating element
$H1$,$H2$	Heater 1, 2
HL	Heat loss
gas	Gas
tot	Total
eff	Effective
Δ	Difference
avg	Average
b	Bulk

Abstract

The pyrolytic conversion of methane for the production of hydrogen and carbon was investigated over nonporous α-Al_2O_3 surfaces in the range of 900 - 1300 °C. Two devices were used: i) a single particle reactor to determine the carbon deposition rate at various temperatures and ii) a fixed bed in which both methane conversion and carbon deposition were measured.

It was observed that at 1000 °C and below, the selectivity towards carbon (and hydrogen) was initially low over fresh α-Al_2O_3 (e.g. 38% at 250 s reaction time), increasing to 100% over time. Methane conversion was constant at 20% during this period. These observations point towards the presence of an activation process for the formation of carbon and hydrogen from the intermediates products (e.g. benzene) of methane pyrolysis. A temperature dependent maximum in carbon loading was observed. When this maximum carbon loading was reached, methane conversion also stopped completely, indicating 100% selectivity towards carbon and hydrogen.

Two kinetic models for carbon deposition were derived and applied. After parameterization of these models using single particle data, they were able to predict carbon growth and CH_4 conversion as function of temperature, specific bed area, carbon loading and gas composition in the new data set from the fixed bed.

2.1 Introduction

Recently, the decarbonization of fossil fuels has received increased interest[24]. The pyrolysis of CH_4 into carbon and hydrogen is an example of a decarbonization reaction:

$$CH_4 \rightarrow C + 2H_2 \qquad \Delta H_r = +75.6\text{kJ}\cdot\text{mol}^{-1}, 298\text{K} \tag{2.1}$$

Deposition of solid carbon means that no CO_2 is emitted, and the carbon is readily separated. The pyrolysis of methane occurs at elevated temperatures[15, 17]. Typical decomposition temperatures range from 500-1000 °C for metallic catalysts[6, 32] and 850-1300 °C for unfunctionalized ceramic carriers[20, 35]. Pressures range from 1 bar CH_4 and higher. The solid carbon may be gasified again to CO to yield synthesis gas.

Three types of catalysts are reported upon in literature: metal based[2, 11, 29, 36], carbon based[1, 3, 4, 25, 27, 28] and unfunctionalized carriers[1, 4]. Literature is widely available for metal and carbon catalysts. These works show a decrease in required temperature to achieve methane conversion. However, a large part of these works show a relatively fast deactivation of the catalyst, either during carbon deposition or after gasification of the deposited carbon[3, 4, 11, 27, 28, 36]. In other cases, up to 10 carbon deposition-gasification cycles are reported without significant activity loss[2].

The main advantage of unfunctionalized carriers is the stability, being inert up to high temperatures in a large range of atmospheres. This work will focus exclusively on the decomposition part, however. Because a large variety of carrier materials is present, a selection had to be made. An initial choice was made for Al_2O_3 as it is a common carrier that is widely available. Other materials are evaluated in future work.

During the pyrolysis of methane, carbon is deposited on a surface in the reactor. It is generally accepted that the formation of solid carbon from methane is achieved via the formation of acetylene and benzene[17, 18, 33]. The simplified reaction network is a stepwise dehydrogenation: $CH_4 \rightarrow C_2H_6 \rightarrow C_2H_4 \rightarrow C_2H_2 \rightarrow C_6H_6 \rightarrow C$. Several authors have proposed more expanded reaction networks consisting of hundreds of reactions[23, 33, 38].

Analysis of the carbonaceous deposits after CH_4 pyrolysis showed that numerous polyaromatic hydrocarbons are present in the deposited material[9]. Many authors report on the decomposition kinetics, [4, 8, 10, 16, 17, 19, 21, 22, 30, 31]. However, the majority of those focuses on the first steps of the methane decomposition and designed the experiments so that little to no carbon was formed in the system, they exclusively studied the step towards gaseous hydrocarbons. To advance process development a kinetic model describing carbon deposition as function of temperature, pressure, gas composition and particle characteristics is required. As far as we know, such a model is not available. This chapter describes an attempt to develop a kinetic model for carbon deposition during methane pyrolysis on non-porous α-Al_2O_3 . The model is based on experimental data of carbon deposition collected for this chapter, and reported mechanistic studies[12, 16, 22, 30, 37, 42]. Non-porous particles offer the advantage that internal mass transfer effects can be excluded. In upcoming work, we will report on various porous particles. It was our strategy to use a single particle reactor and a fixed bed reactor. The single particle reactor was designed so that carbon deposition was not hindered by mass transfer limitations and it allowed precise control of the reaction temperature. Next to that, interpretation of the single particle reactor data was not

hindered by heating and cooling trajectories of the particle, spatial gradients in gas composition or wall effects. In the fixed bed, the coupling between carbon deposition and methane conversion could be studied. The fixed bed was also used to investigate if the kinetics derived from single particle data could predict results obtained in the fixed bed.

2.2 Materials and methods

2.2.1 Materials

Two types of nonporous α-alumina particles were used in this work. Particle A (1.5 mm diameter, 99% Al_2O_3 , ρ_p = 3740 kg $\cdot$ m$_p^{-3}$) was obtained from Saint-Gobain NorPro. Particle B (3 mm diameter, 99% Al_2O_3 , ρ_p = 3688 kg $\cdot$ m$_p^{-3}$) was obtained from Baan Machines. Si_3N_4 precision spheres (Nonporous, 3 mm diameter, Ra surface roughness 12 nm) were obtained from Ceratec Technical Ceramics. In this work, all the particles were used as received, additional details on the used particles are presented in table B.8 in the appendix accompanying this chapter. Methane (99.999%) was supplied by Linde. Nitrogen (99.999%) was supplied by Nippon Gasses. Calibration gasses, hydrogen, oxygen and shielding gas (95% Ar, 5%H_2) were supplied by Linde. All gasses used in this work were used as received.

2.2.2 Heating unit

Heating of the reactors was facilitated by an in-house constructed radiation oven (max. temperature 1500 °C). The temperature was controlled using Eurotherm P116 controllers in the 2 heaters (16 cm axial length each) individually. A cross section of the heating unit internals is presented in figure 2.1b. Heating was provided by heating wires (1.5 mm diameter, SuperKanthal A1, Salomons Metalen) wrapped around a cylindrical radiation element (99.7% Al_2O_3, Haldewanger). The inner diameter of the radiation element was 30 mm. The radiation element was placed inside the oven vertically. The reactor tube was placed inside this element, so that radiation reached the reactor tube all around. In this reactor tube the single particle reactor (section 2.2.3) or the fixed bed (section 2.2.4) was placed. The controlling type S thermocouples were placed on the outside of the reactor tube wall, inside the radiation element. The axial height of the controlling thermocouples depended on the experimental configuration used and is discussed in the following sections. All the internals were isolated with alumina wool (Morgan Ceramics) and placed in an aluminium enclosure. A detailed list of construction materials is included in the appendix, table B.7.

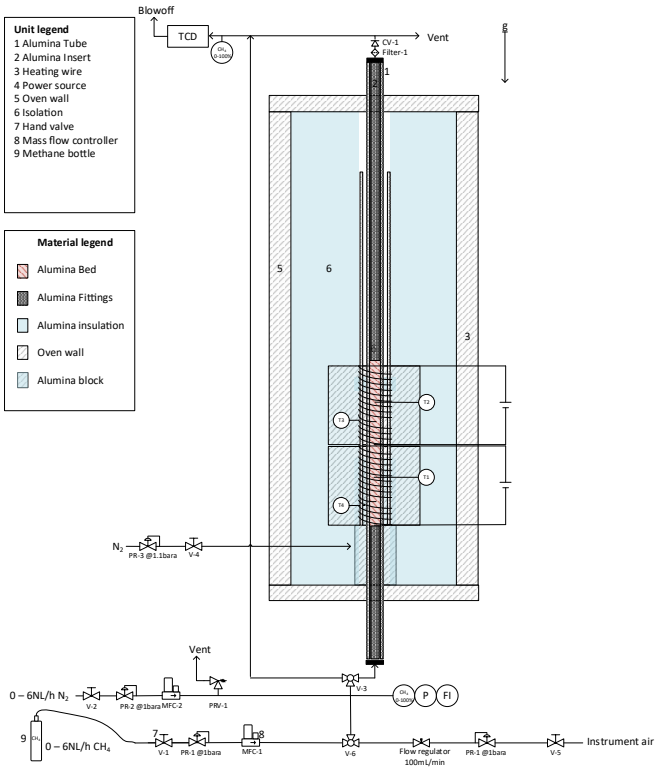

(a) PID of setup in fixed bed configuration

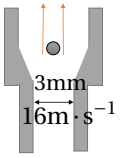

(c) Schematic of singleparticle reactor

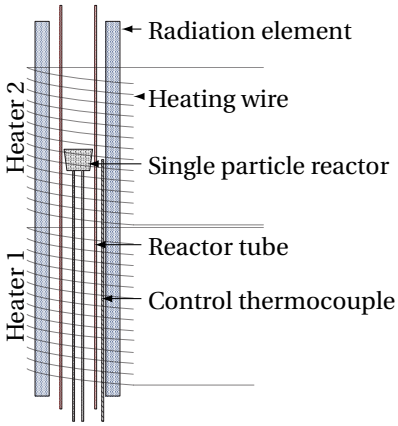

(b) Cross section of heating unit internals in single particle reactor configuration

Figure 2.1: Overview of the experimental setup

2.2.3 Single particle configuration

In the single particle reactor an Al_2O_3 particle was suspended in a CH_4 flow by placing it in a conical reactor. A reactor tube (11 mm ID, 99.9% Al_2O_3 , Haldewanger) was placed inside the oven. The conical Al_2O_3 reactor was placed inside this reactor tube, as presented in figure 2.1b. In figure 2.1c a schematic of the cone itself is presented. At the bottom of the cone the local gas velocity equaled the terminal velocity of the particle, thereby suspending the particle inside the cone.

To check the mass transfer around the particle, the carbon deposition rate was compared to the carbon oxidation rate, which is most likely mass transfer limited. To measure the oxidation rate a carbon loaded particle was suspended at 1000 °C in air. The oxidation rate measured was a factor 100 faster than the carbon deposition rate during pyrolysis, therefore the carbon deposition rate cannot be mass transfer limited. An additional study into the mass transfer in the cone has been performed using the sublimation of a copper particle, this is presented in the appendix of this chapter and supports that the methane decomposition is not mass transfer limited.

The temperature was controlled by placing the type S control thermocouple at the height of the cone. The controlling thermocouple for this first heater was placed halfway along the axial length of the first heater. For measurement accuracy it was important to know the particle temperature. For

this, an energy balance was made, taking into account energy consumption by the decomposition reaction and energy inflow via radiation. This energy balance assumes the gas had reached the setpoint temperature before it reached the particles height within the cone, and therefore no energy was transferred between gas and particle. The energy balance is presented in appendix B of this chapter, and shows that the particle temperature does not deviate from the setpoint temperature significantly. Hence, the decomposition reaction is not heat transfer limited.

To ensure the gas had heated up to the setpoint temperature, the energy consumption of the second heater was monitored with and without gas flowing through the cone. A detailed explanation of this is presented in appendix B of this chapter. If the second heaters power consumption did not change when the gas was turned on, the gas had reached setpoint temperature when it reached the cone. This was ensured by gradually increasing the setpoint of the first heater, thereby increasing the gas temperature. The difference in power consumption of the first heater with and without gas flow was approximately 70 W, in agreement with the theoretical power required to heat the CH_4 stream to setpoint temperature.

When the particle was contacted with methane, a carbonaceous material was deposited on the particle, increasing its mass. Since this particle was not in contact with any reactor wall, effects of surfaces other than the particle were ignored. Via the mass change over time the carbon deposition rate was obtained. As gas residence time was in the order of 1 ms and the surface to volume ratio was very low, the measured CH_4 conversion was negligible, as confirmed by GC.

The deposited carbonaceous material will contain a small amount of hydrogen. Literature on pyrolytic graphite deposited from methane at higher temperatures than this work show a H/C ratio of 0.0004 $mol \cdot mol^{-1}$[5]. The carbon in this work is deposited at lower temperature, and should therefore have a higher H/C ratio[5, 34]. However, the H/C ratio would have to be 3 orders of magnitude higher than this literature value in order to significantly change the mass of our deposited material. Therefore, the hydrogen in the carbonaceous material is neglected.

For more enhanced experimentation, it was investigated whether it was possible to introduce up to 3 particles simultaneously into the reactor. In appendix A of this chapter, table B.10 it is shown that comparable carbon loadings are found, regardless of the number of particles. Therefore, for most of the experiments 3 particles were used simultaneously.

Experimental procedure

With the cone present in the reactor tube the system was heated to setpoint (Heating rate 10 $K \cdot min^{-1}$) under nitrogen. When setpoint was reached, the CH_4 flow was turned on. Inflowing gas had a flow rate of 1600-1800 NmL/min. This was controlled by a mass flow controller (Brooks) and was varied depending on the setpoint temperature. Superficial gas velocity through the cone base was kept constant over all experiments. After passing through the reactor the gas was vented. When the system had reached steady state (as measured by heater power consumption) a particle was introduced by opening the top valve. The particle fell into the cone and remained there until the desired time was reached. This was confirmed visually via an observation port in the top of the setup. The addition of carbon onto the particle did not affect the suspension of the particle, as the deposited amounts were relatively small. After an experiment the gas flow was turned off. The particle fell through the Al_2O_3 tube and was collected in a 5 ml sample glass connected to the reactor. The particle cooled down in ± 1 s, as confirmed by measurements using an IR camera, no active cooling was required. Afterwards the carbon content was calculated via the weight

difference and the sample was stored.

Reproducibility of experiments

To test reproducibility and to establish the measurement uncertainty, two test series were done. The first series composed of repeating a deposition test under identical conditions a number of times using different particles from the same batch. The found standard deviation on the mean was 6%. In the second series, three particles were suspended in a CH4 flow at 1100 °C for 20 minutes. The carbon mass fraction was measured, and the carbon was burnt off under pure oxygen at 1100 °C for 6 hours. This was repeated 5 times. The results of this series are listed in table 2.2. Also for this series, the standard deviation on measurement mean was 6%.

Hence, repeated usage of a single particle compared to single use of multiple particles did not increase accuracy. It was decided, for efficiency reasons, to repeat each condition several times using different particles. Because of the large spread each measurement was repeated 12 times or more, to obtain an acceptable confidence interval.

Table 2.2: Carbon loading after repeated experiments in the single particle reactor, particle A

	Measured loading $[g \cdot m_{p,ex}^{-2}]$				
Run number	1	2	3	4	5
Particle 1	17.9	20.9	17.9	19.4	16.4
Particle 2	24.8	26.1	24.8	24.8	23.4
Particle 3	18.0	22.1	21.1	21.1	21.1

2.2.4 Fixed bed configuration

The fixed bed was placed inside the reactor tube (figure 2.1a). The axial location of the controlling thermocouples was the axial middle of heater 2 which coincided with the axial middle of the bed. The control thermocouple was placed outside the reactor tube, within the heating element, as in figure 2.1b. During some experiments, temperature measurements were performed inside the reactor. For this, an Al_2O_3 insulated type S thermocouple (3 mm OD, 600 mm length) was inserted into the reactor tube. At the controlling thermocouple axial height, measured temperature did not deviate from the setpoint temperature by more than 2 °C , which is less than the accuracy of the used thermocouple at this temperature. Moreover, along the complete axial length temperature did not deviate over time. Therefore, temperature is regarded as constant over time, but not over axial length, as a temperature profile is present throughout the bed (presented in figure 2.5). For the experiments where internal temperature measurements were performed, a reduction in bed volume and area occurred because of the thermocouple, therefore these datapoints were not included in the final dataset.

Inflowing gas was CH_4 and N_2 with flow rates ranging from 0-100 $NmL \cdot min^{-1}$. These were controlled individually by mass flow controllers (Brooks). By changing the gas flow rate residence times in the bed were varied between 0.2 and 2.5 s. Gas entered the reactor through the bottom coupling. Before and after the bed, cylindrical (OD 10 mm) Al_2O_3 inserts were placed in the reactor, decreasing dead volume outside the bed. Total axial bed length was 40 cm and kept constant over all experiments.

Methane fractions were measured every 1.2 s using IR sensors (0-100%vol CH_4, MIPEX). The CH_4 sensors were placed before and after the reactor. Hydrogen fraction was measured using a TCD (Caldos 5G-Ex), at the reactor outlet. Both the CH_4 and H_2 sensors were calibrated using pre-mixed gasses (Linde). Pressure was measured at the reactor inlet (Brooks SolidSense II), the reactor outlet was at atmospheric pressure at all times. All relevant measurements were corrected for changes in atmospheric pressure over time. Inlet flow was measured using a brooks mass flow meter. After analysis the reactor offgas was vented. For GC measurements, samples were taken by hand using a 50 ml syringe during selected experiments.

Experimental procedure

Before each experiment, the inner reactor wall was cleaned with a steel brush. The reactor was then rinsed with acetone and demineralized water, and dried by blowing compressed air through the tube. The reactor was filled with the inserts and fresh bed particles. The bed was flushed with a 100 $NmL \cdot min^{-1}$ N_2 flow during heating and cooling of the reactor.

The heating rate was 10 $K \cdot min^{-1}$ for all experiments. When the setpoint temperature was reached, a CH_4 or CH_4-N_2 flow was applied. The total duration of this gas flow depended on process conditions. After the desired time on stream had been reached, the CH_4 flow was shut off. Nitrogen kept flushing the system at all times. At this point the heating was gradually decreased to ensure the cooling rate of the reactor did not exceed 10 $K \cdot min^{-1}$.

After the reactor had cooled down overnight bed samples were retrieved layer-by-layer. This was done by gradual removal of the top most fraction, using a custom made steel tool. Carbon weight fractions were then measured in a LECO A200 carbon analyzer. A tungsten accelerator (LECO, Lecocel -20 40) was added to ensure complete oxidation of the present carbon. Afterwards the remains were discarded.

Reproducibility of experiments

To check reproducibility of measured CH_4 conversion, 10 experiments were performed in duplicate during the research. Average deviation between measured CH_4 conversion was 1.1 percent point, with a maximum of 2.0 percent point, well within the calculated 95% confidence deviation of 3.5 percent point, which was based on the precision of the CH_4 sensors. For the measured carbon profiles, the calculated 95% confidence deviation was in the order of 0.1%. However, a larger variation was observed (12%) experimentally. This was attributed to the method of retrieving samples from the bed. Since a large axial temperature gradient (up to 10000 $K \cdot m^{-1}$) was present, a large axial gradient in carbon mass fraction could be expected. In the ideal measurement, the particles in a single sample obtained from the bed have an identical carbon fraction. To be able to meet this uniform fraction the obtained samples have to be significantly smaller than a monolayer of particles removed from the bed. Average sample weight obtained was 1.1g, corresponding to 4 monolayers.

To obtain a reproducible carbon weight fraction of the obtained samples from the bed, it was found that the sample size fed into the analyzer should be 100 mg at minimum. All carbon measurements were performed in duplo with a sample size between 100 and 150 mg, if enough sample was obtained from the bed. Obtained carbon fractions were taken as average for the layer location of the original bed sample. Obtained carbon profiles were found to be reproducible, results are presented in appendix A of this chapter. Furthermore, burning off the carbon in pure

oxygen at 1100 °C for 6 h yielded a comparable carbon profile, validating the result obtained from the LECO analyzer. Concluding, the resulting errors were caused predominantly by random variations in the experiment and the bed sampling method.

To check the overall H_2 and C balance, both CH_4 and H_2 were measured. To be able to use the TCD signal, no CH_4 could be present in the reactor outflow, therefore it is required to operate at 100% CH_4 conversion. To realize this, an experiment was performed at 1350 °C and a CH_4 residence time of 1.0 s. Furthermore, since the TCD had an upper detection limit of 50% H_2 in N_2 an inlet CH_4 fraction of 0.2 was used. To measure to total carbon deposition, all setup components were weighed before and after the run. The overall carbon and hydrogen balances are presented in table 2.3. For this calculation it was assumed that no hydrogen is present in the deposited carbon. The errors denote the calculated absolute percent point errors on the measured value and were based on the errors of the individual components used during each of the measurements.

Table 2.3: Overall mass balance for C and H measured in the fixed bed at 1350 °C

	Measured	Expected	Closure	Unit
Carbon	0,803	0,857	94% ±5 pp	g
Hydrogen	30,2	30,5	99% ±7 pp	vol%

2.2.5 Analysis equipment

Particle surface area measurements were performed by gas adsorption measurement (Gemini VII 2390 Surface Area Analyzer, Micrometrics). Trace compound gas measurements were performed using a Varian 450-GC refinery gas analyzer. Methane fractions were measured using MIPEX IR sensors. Hydrogen concentration was measured using a Caldos 5G-Ex TCD. Carbon mass fractions on used particles was measured using a LECO A200 carbon analyzer.

2.3 Results and discussion

2.3.1 Carbon deposition measurements in the single particle reactor

Using the single particle reactor, carbon loading over time was measured for several temperatures. For all the data presented in the results section, particle A was used. To measure kinetics, mass and and energy transfer limitations should be negligible. Energy and mass transport in the single particle reactor has been discussed in section 2.2.3 and appendix B of this chapter and was found to not limit the decomposition reaction.

Results are presented in figure 2.2a. Error bars denote the 95% confidence interval based on the standard deviation of the measurement mean. With increasing temperature the carbon loading over time increases faster. For the 950 and 1000 °C data, a sigmoid curve is observed. An induction period where carbon is deposited slowly is also observed. A possible explanation for this may be given via a surface activation mechanism, where a nucleus first has to form on the surface before decomposition can occur. After the slow nucleation step the decomposition rate accelerates and carbon is deposited more rapidly. This has been discussed in literature[12, 21, 37], and shown in experiments comparable to these for short gas residence time systems operating at low CH_4 conversion. This is discussed further in section 2.3.4.

Additionally, a temperature-dependent maximum loading was observed for the measurements of 1000 °C and up. Near maximum loading the deposition of carbon onto the surface stops or becomes very slow. The likely reason for this has not been established. It was also found that a smooth particle (Si_3N_4, RA surface roughness 12 nm) did not gather a measurable amount of carbon (total mass increase < 0.01 mg) after 1 h TOS at 1050 °C. Furthermore, it was found that this maximum loading was reached after a longer time when the methane concentration was lowered via a dilution with nitrogen. In appendix A of this chapter, figure 2.15 it is shown that the carbon deposition speed is first order in methane concentration.

To put the measured decomposition rate into perspective, assuming a reactor operating isothermally at 1100 °C , without mass or energy transfer limitations would correspond to a volumetric productivity of 35 mol C·$m_r^{-3}\cdot s^{-1}$ (1500 kg C ·$m_r^{-3}\cdot h^{-1}$). This assumes a fluidized bed with 50 µm porous particles, and a total available area of 10^4 $m_p^2\cdot m_r^{-3}$, internal and external area combined. Comparing this productivity to a typical value of 4 mol C·$m_r^{-3}\cdot s^{-1}$ for methane steam reforming shows that the potential realizable volume based production rate of C and H_2 from methane pyrolysis is high[26, 43].

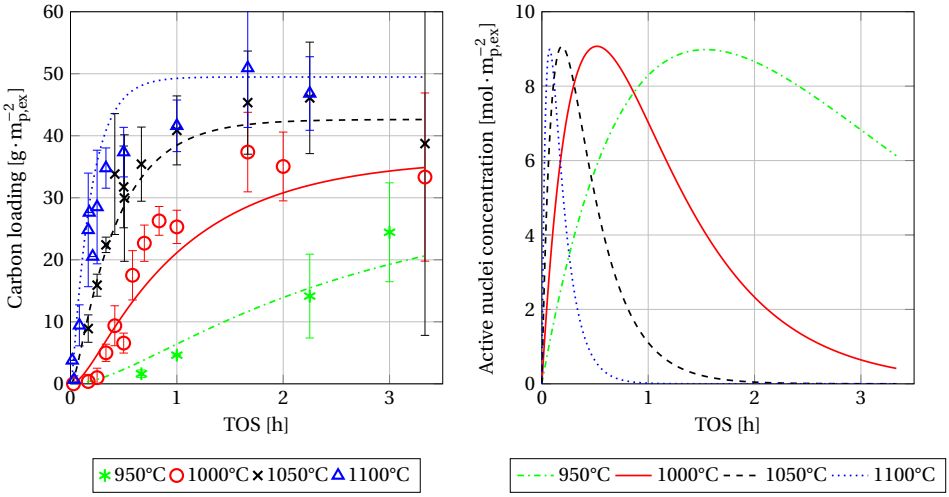

(a) Carbon loading over time. Lines denote accompanying modelling results using nucleation modeldata in figure *a* (see section 2.3.4). *(b)* Nuclei concentration over time accompanying data in figure *a*

Figure 2.2: Experimental carbon loading over time obtained in the single particle reactor and prediction of nucleation kinetics model, various temperatures, particle A

2.3.2 Carbon deposition and methane conversion

In the previous section, results on carbon deposition were presented under differential conditions, i.e. very low methane conversion. Therefore, no link between methane conversion and carbon deposition could be made. This section reports the data obtained using the fixed bed reactor, providing data of methane conversion, and selectivities towards gaseous hydrocarbons and solid

carbon, and solid carbon deposition data as function of both time and location.

For the data presented in figure 2.3 temperature was 1000 °C, particle A was used, gas inlet was 100% CH_4 and the gas residence time was 1.0 s. To measure momentary selectivities towards gaseous intermediates, gas samples were taken using a syringe. The total sample time was in the order of seconds, therefore the gaseous products in the sample syringe reflect the rate towards gaseous intermediates during this period. Via equation 2.2 the momentary selectivity was obtained.

$$S_p = \frac{C_{\text{intermediates}}}{C_{M,in} - C_{M,out}} \left[\frac{\text{mol} \cdot \text{s}^{-1}}{\text{mol} \cdot \text{s}^{-1}} \right] \tag{2.2}$$

For the selectivity towards solid carbon, carbon profiles were measured at several points in time. Since the bed has to be removed from the reactor and is consumed during carbon analysis in the LECO machine, a total of 4 tests were done, one for each solid selectivity data point. The amount of carbon produced since the previous measurement was then calculated. From this change in amount of carbon, a time-averaged decomposition rate was obtained and used in equation 2.3. This allowed comparison of the selectivities towards gaseous hydrocarbons and solid carbon under the same conditions and at the same time. The momentary selectivity S towards phase p is defined as:

$$S_p = \frac{\text{production rate of C in phase p}}{\text{total } CH_4 \text{ conversion rate}} \left[\frac{\text{mol} \cdot \text{m}_\text{r}^{-3} \cdot \text{s}^{-1}}{\text{mol} \cdot \text{m}_\text{r}^{-3} \cdot \text{s}^{-1}} \right] \tag{2.3}$$

In figure 2.3 the obtained selectivities and overall CH_4 conversion are plotted over time.

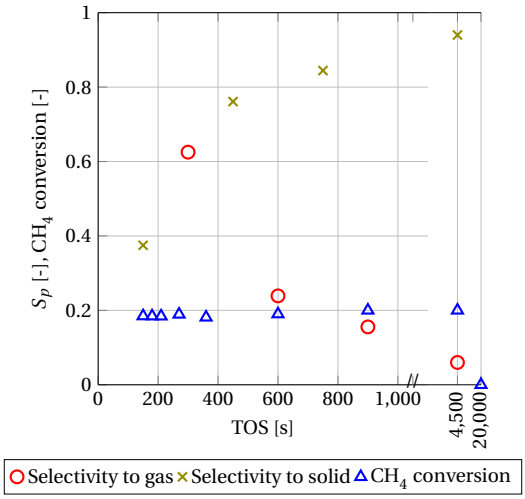

Figure 2.3: Methane conversion and momentary selectivity towards gaseous and solid products, measured in a fixed bed at 1000 °C. Gas residence time 1.0 s, Inlet 100%CH_4 , Particle A

Methane conversion over time was constant at approximately 0.2 for all but the last (t=20000 s) measurements. Next to CH_4 and H_2, the intermediate decomposition products C_2H_4, C_2H_2 and C_3H_6 were detected. It can therefore be concluded that the conversion of methane towards gaseous intermediates is independent of the induction period observed for carbon deposition, observed in the single particle reactor. In figure 2.4 this is shown conceptually, as function of loading. The rest of the observations discussed in this section are also present in this figure.

The selectivity towards solid carbon increases over time. This is in line with the observed induction period observed for solid carbon deposition. Some solid carbon was found at t=300 s. This result might seem to conflict with the single particle results, where no carbon was measured in this initial period. This difference is caused by the detection limits of the used methods. The detection limit for carbon of the LECO used for fixed bed measurements is much lower (equivalent to 0.005 $g \cdot m_{p,ex}^{-2}$) than the carbon loading detectable by the weight difference method used in the single particle experiments (equivalent to 1.2 $g \cdot m_{p,ex}^{-2}$). The observed loading measured at 300 s in the fixed bed was 0.4 $g \cdot m_{p,ex}^{-2}$.

For the longer TOS the observed fixed bed loadings correspond to the measured single particle loadings. The observed volume fractions of intermediates decreased over time, in line with the increased solid carbon deposition and reduced selectivity to gaseous hydrocarbons. For longer TOS (20000 s), the conversion of methane reduced to effectively 0. The loading at this point corresponds to the maximum loading observed in the single particle reactor, and no carbon was being deposited in the bed at this point. A gas phase measurement confirmed that no methane was being converted to gaseous intermediates at this point, either.

The observation that CH_4 conversion to the first decomposition products, such as ethylene and acetylene, is not related to the induction period observed for carbon deposition implies that methane conversion and carbon deposition are initially, over fresh α-Al_2O_3 , two different processes. At 20000 s however, carbon deposition as well as methane conversion appear to stop almost completely. The only difference between t=0 s and t=20000 s is the amount of carbon deposited on the particles. Therefore, near the maximum loading, the amount of deposited carbon on the available surface does influence the conversion of methane towards gaseous intermediates. Note that the maximum loading is dependent on the temperature and is therefore a function of axial location along the reactor, visualized in figure 2.4.

The observed phenomena are summarized in figure 2.4. The point of maximum loading is temperature dependent, a lower temperature results in a lower maximum carbon loading. The point where the selectivity towards carbon becomes 100% is not known exactly, but appears to occur at a certain carbon loading and appears to be temperature independent.

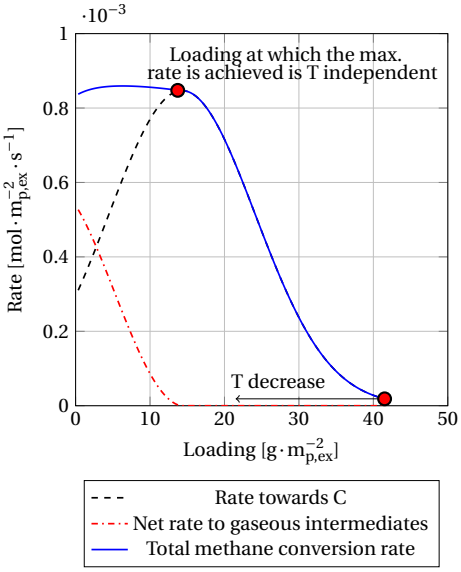

Figure 2.4: Methane conversion and carbon deposition rate as function of loading, 1000 °C

To further investigate the effect of available surface on the conversion of methane towards gaseous intermediates, the experiment was repeated in a empty tube. Gas residence time and setpoint temperature were kept the same as the original experiment by increasing the CH_4 flow. The total run time was 300 s. CH_4 conversion to gaseous intermediates was 0.2%, only a trace (0.06%vol) of C_2H_4 was detected, this was near the detection limit of the GC. This low CH_4 conversion indicates that the rate of methane conversion is also aided by a surface.

If the desired product is either hydrogen or syngas, from a process development perspective, the production of gaseous intermediates should be minimized. At 1000 °C the gaseous intermediates are mostly formed in the first ±1000 s, where relatively little carbon is being deposited. After these first 1000 s the production of gaseous intermediates remains low. From figure 2.4, the net production of gaseous intermediates occurs at loadings below ±15 g$\cdot$m$^{-2}_{p,ex}$. For a process with high carbon efficiency operating at 1000 °C , working below this loading should be avoided. The loading, at which the production of gaseous intermediates stops, appears to be temperature independent. As higher temperatures result in a higher rate, the loading of ±15 g$\cdot$m$^{-2}_{p,ex}$ is achieved much earlier. In table 2.4 the measured selectivities to solid carbon are presented for TOS=250 s, for various temperature setpoints. Almost no gaseous products were found at these higher temperatures.

2.3.3 Further fixed bed data

In this section further fixed bed data is presented. Some model results are also incorporated. These model results are discussed in section 2.3.5. For all data presented in this section a 50%CH_4 - 50%N_2 inlet was used, gas residence time in the hot zone was 0.6 s, and particle A was used. Conversion over time is presented in figure 2.6. In agreement with figure 2.3 the methane conversion over time is not constant. First, a slight acceleration is observed, thereafter followed by a decrease over time. The decrease and eventual stop of methane conversion is explained by the carbon

Table 2.4: Measured differential selectivities of methane towards solid carbon at several temperatures, fixed bed, gas residence time 1 s, TOS = 250 s, Particle A.

Setpoint T [°C]	S_{solid} [-]
1300	0.999
1200	0.976
1100	0.967
1000	0.375

deposition on the bed, as shown in section 2.3.5.

Interestingly, the slight acceleration in overall conversion also means that more intermediates are being formed, as intermediates must be formed before carbon can deposit. This implicates that the initial rate of intermediate formation at t=0 is slower than the intermediate formation rate at maximum methane conversion. A reason for this initially slow intermediates production rate has not been identified. It is speculated that the thermodynamic equilibrium between methane and the intermediates is reached[14], thereby limiting the initial intermediates production rate.

The bed temperature varies significantly over the axial reactor coordinate, therefore the overall CH_4 conversion is a result of decomposition processes at a wide range of temperatures. A temperature and corresponding carbon profile is presented in figure 2.5. Regardless of setpoint temperature used, the first carbon from the inlet side was always found around the point where the local temperature was 850 °C. In figure 2.7 the growth of carbon over time was visualized by measuring three carbon profiles after different runtimes. It is seen here that the growth over time is not linear, as can be expected from the single particle measurements.

In section 2.3.5 the model predictions also visible in these figures are discussed.

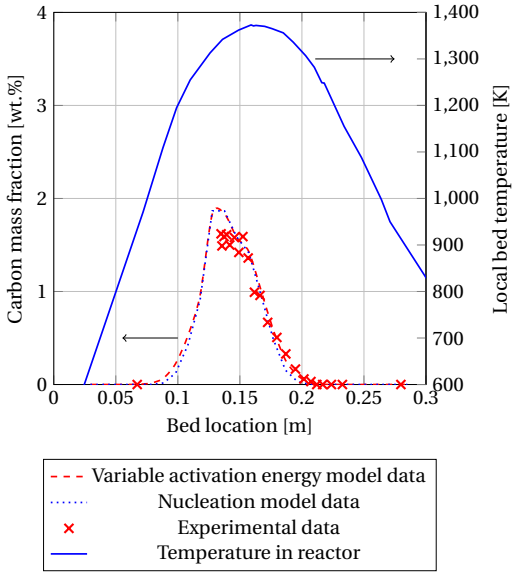

Figure 2.5: Carbon and temperature profile measured in fixed bed reactor. Setpoint 1100 °C, total runtime 1800 s, Gas residence time 0.6 s, Inlet fraction CH_4 = 0.5, particle A

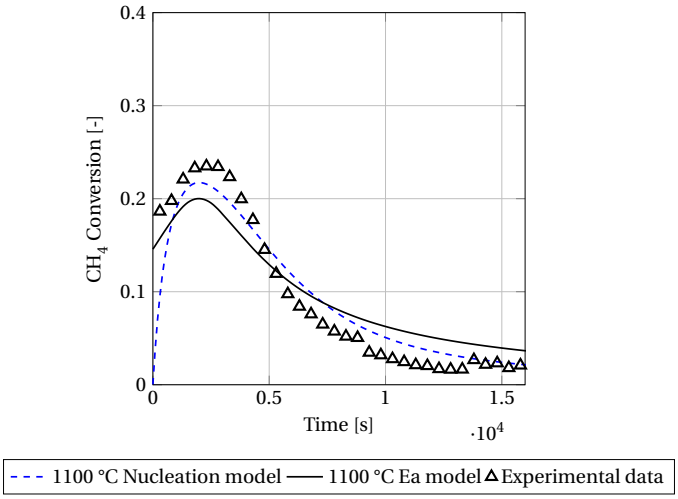

Figure 2.6: CH_4 conversion over time measured in fixed bed at 1100 °C , gas residence time 0.6 s, Inlet fraction CH_4 = 0.5, particle A

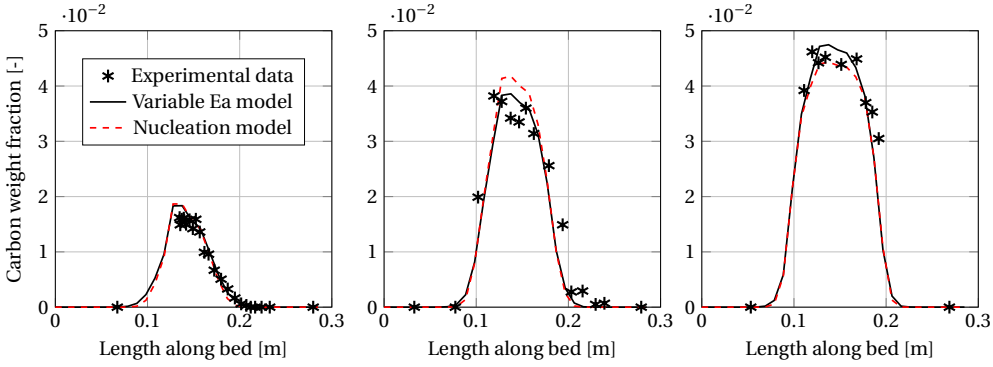

(a) 1800 s *(b)* 7200 s *(c)* 16700 s

Figure 2.7: Carbon profiles in fixed bed measured at different time on stream values, 1100 °C , Gas residence time 0.6 s, Inlet 50%CH_4 - 50% N_2, Particle A

2.3.4 Mechanism and modeling

In the experimental data presented earlier, several phenomena are observed to occur during methane pyrolysis for fresh, carbon free α-Al_2O_3 :

1. An initial induction period during which no carbon is deposited.
2. During this period, methane is already being converted to gaseous intermediates.
3. Effects 1 and 2 are most pronounced for temperatures up to 1000 °C. For higher temperatures the deposition starts much earlier and little gaseous intermediates are produced overall.
4. A temperature dependent maximum carbon loading occurs. When this loading is reached, methane is not converted to solid carbon nor to gaseous intermediates anymore.

All these key phenomena should be incorporated into a model in order to be useful for reactor design and optimalization. To predict phenomenon 1, the model needs to have some sort of initiation for carbon deposition. To predict phenomenon 4, the model needs to have a termination mechanism for carbon deposition.

From a process development perspective, the formation of gaseous intermediates should be avoided. The decomposition reactor should be designed so that little gaseous species are produced, for example by increasing the decomposition temperature. Therefore, and for sake of simplicity, phenomenon 2 is not incorporated in either of the models, and gas phase intermediates are not taken into account. This still enables prediction of phenomena 1, 3 and 4 whilst reducing the complexity of the models. Note that this means that this model is not able to make correct predictions for short solids residence time applications, especially for temperatures below 1100 °C.

The first model is a nucleation model based on literature (e.g. [12, 16, 22, 30, 37, 42]), where a nucleus has to form on the surface in order for carbon to deposit. The second model uses a variable activation energy to describe the acceleration and eventual stop in carbon deposition, using fewer parameters.

Nucleation model

The data presented in the previous sections may be indicative of a nucleation mechanism for carbon deposition. If the formation of this nucleus is the limiting step at low temperature this can explain the observed acceleration of carbon deposition. After these nuclei are formed the faster carbon deposition reaction becomes dominant and carbon is deposited faster. The published nucleation models do not include a termination mechanism. We included this termination by incorporating a maximum number of nuclei that can be formed and setting the stoichiometry between nuclei and deposited carbon.

The nucleation model takes into account three species: available sites (AS), nuclei (nuc) and deposited carbon (C). In this model, a nucleus can be formed only on an available site. These available sites are consumed when a nucleus forms and are incorporated to limit the number of nuclei that can be formed. Kinetics reported in literature do not limit the growth of nuclei and, by extension, the growth of carbon. It was shown experimentally that the carbon deposition does stop, therefore this addition was made. The conceptual working of the model is presented in figure 2.8.

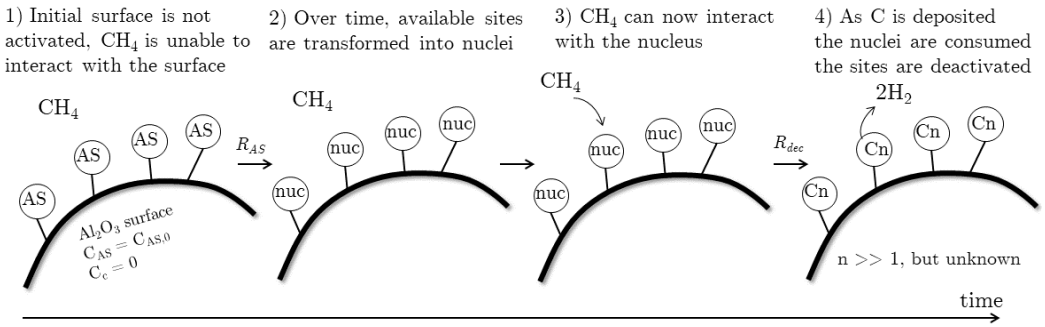

Figure 2.8: Nucleation model visualized in steps

The amount of available sites (AS) is a particle characteristic, and is temperature dependent. The change from available site to nuclei is described by equation 2.4. It is an exponential decay dependent on temperature and has unit $\text{mol} \cdot \text{m}^{-2}$. This part functions as the initiation to predict phenomenon 1 by an increasing amount of nuclei in the induction period. Additionally, this serves as a brake to limit the amount of carbon that can be deposited. When the amount of available sites is consumed no more carbon can be deposited.

$$R_{AS} = -k_{AS} \exp\left(\frac{-E_{a,AS}}{RT}\right) C_{AS} \tag{2.4}$$

The initial amount of available sites is given by equation 2.5. It does not need to represent a real quantity of a species and can be regarded as a measure for the energy level of the surface. The initial amount of available sites ($\text{mol} \cdot \text{m}^{-2}$) equals the maximum carbon loading at that temperature. Hence, it causes the carbon deposition to stop.

$$C_{AS,0} = k_{AS,II} \exp\left(\frac{-E_{a,AS,II}}{RT}\right) \tag{2.5}$$

For nuclei a generation rate and a consumption rate are formulated. Nuclei generation is dependent on the amount of available sites C_{AS}. The nuclei generation rate serves as the initial induction period, and accelerates the carbon deposition in these moments. In this model, it is assumed nuclei do not consume methane. In reality the nuclei likely consists of carbonaceous material, and should therefore originate from methane. This has not been incorporated for simplicity sake: the (molar) mass of a nucleus cannot be measured and was therefore taken as 0. Nuclei consumption is dependent on the carbon deposition rate, it is assumed that every carbon atom deposited consumes a nucleus. Since no data is available on the amount of nuclei present on the surface, it is unknown how much carbon can be deposited per nucleus, for simplicity this stoichiometry was then taken as 1. One could change this stoichiometry to any arbitrary value, provided that the amount of available sites is also changed accordingly. Since the nucleus is removed when a carbon atom is deposited, this model implies the formation of a monolayer of carbon. In reality, this is not possible as the amount of carbon deposited is much larger than one monolayer on the Al_2O_3 surface. Therefore, the real amount of nuclei must be smaller than presented in the model and secondly, more carbon can be deposited per nucleus. The nuclei balance is presented as equation 2.6.

$$R_{nuc} = R_{AS} - R_{dec} = k_{AS} \exp\left(\frac{-E_{a,AS}}{RT}\right) C_{AS} - C_M C_{nuc} k_{dec} \exp\left(\frac{-E_{a,dec}}{RT}\right) \tag{2.6}$$

For the carbon deposition, from experimental results it is known that the decomposition rate is first order in available area (tables B.9 and B.10 in appendix A of this chapter). Furthermore, it is shown that the carbon deposition rate is first order in methane pressure (figure 2.15 in appendix A). From section 2.3.2 it is known that for the first steps in the decomposition mechanism towards gaseous intermediates, no nuclei are required. As stated before, the gaseous intermediates are not taken into account. It is assumed that the total methane reaction rate is dependent on the nuclei concentration. Although this is not correct in the initiation period. This will only negatively affect predictions in the initial periods for temperatures below 1000 °C. This is incorporated in equation 2.7:

$$R_{dec} = C_M C_{nuc} k_{dec} \exp\left(\frac{-E_{a,dec}}{RT}\right) \tag{2.7}$$

The equations mentioned above were fitted to the experimental data presented in figure 2.2a by minimizing the difference between model and experimental values in MATLAB using the fmincon, fminunc and nlinfit routines. Equation 2.8 was used for the minimalization of the error σ for j datasets of temperature T_j consisting of N datapoints, with C being the model or experimental carbon loading:

$$\sigma = \sum_{T=T_1}^{T_j} \sum_{i=1}^{N_j} \frac{1}{N_j} (C_{mod,j,i} - C_{exp,j,i})^2 \tag{2.8}$$

In figure 2.2a model results are presented. Modeled loading over time approximates experimental values. The sigmoid curves are observed for the lower 2 temperatures. The initial slow deposition of carbon is explained by the lack of nuclei, which are presented in figure 2.2b. At lower temperatures the nuclei generation rate (equation 2.4) is relatively slow. The sigmoid curve is therefore most visible at lower temperatures. At higher runtime and higher loadings the number of available sites approaches zero (figure 2.16 in appendix A). From figure 2.2b and equation 2.6 this is seen as the decrease in available nuclei eventually leading to a stop in carbon deposition.

Table 2.5: Kinetic parameters

	Ea $[kJ \cdot mol^{-1}]$	Error Ea $[kJ \cdot mol^{-1}]$	k	Error k	unit k
Dec	324	±3	$1{,}42 \cdot 10^{8}$	$\pm 4.8 \cdot 10^{6}$	$m_g{}^{3} \cdot mol^{-1} \cdot s^{-1}$
AC	243	±3	$3.45 \cdot 10^{6}$	$\pm 2.4 \cdot 10^{4}$	s^{-1}
AC_0	45	±4	$2{,}54 \cdot 10^{4}$	$\pm 2.0 \cdot 10^{2}$	$mol \cdot m_p{}^{-2} \cdot s^{-1}$

Parameter values are presented in table 2.5. Errors present 95% confidence intervals. The rate constant does not accurately represent the turnover frequency of the hydrocarbons on the Al_2O_3 surface. The relevant component in equation 2.7 is taken as methane since this concentration is known. In reality this will most likely be some larger hydrocarbon formed as an intermediate during methane decomposition. Since this intermediate will be present in a lower concentration the true turnover frequency will be higher. Methane is used in the equation as the concentration of this component is known and secondly because the concentration of the relevant intermediate reactant(s) will be directly proportional to the CH_4 concentration.

Correlation coefficients were calculated to range from 0.93 to 1 across all parameters. This strong cross-correlation can be expected because available sites and nuclei concentration could not be measured.

It is known that the particle surface has a (or multiple) characteristic(s) that influence the carbon deposition rate. All kinetic data here were obtained using particle A, however experiments with a smooth (RA surface roughness 12 nm) resulted in no deposited carbon after 1 h at 1050 °C. Therefore the parameters presented here need to be determined for each particle type.

Variable activation energy model

Variable activation energy models are used to describe a large set of paralel and consecutive reactions[7, 39–41]. The effect of the complex reaction network is lumped in the variable activation energy. In this work, the variable activation energy uses a change in activation energy to describe the observed acceleration and eventual stop of carbon deposition. As is the case with the nucleation model presented in the previous section, methane is taken to be the reactive molecule. In reality this will be an intermediary larger molecule. The formation of this intermediary molecule is not taken into account.

The model workings are visualized in figure 2.9. It is assumed that the deposition of the first carbon is relatively slow. This is comparable to the formation of the nucleus of the first model and is incorporated via a relatively high activation energy. When the initial carbon has been deposited it becomes easier to deposit additional carbon. This translates to a lower activation energy. With further increasing carbon loading the activation energy increases again. The activation energy

as function of carbon loading will therefore have a parabolic shape, as visualized conceptually in figure 2.9.

The use of a variable activation energy in kinetics is seen by some as indicative of an overly simplistic or overall incorrect kinetics approach[7, 39, 40]. In this work, no detailed fundamental study into the decomposition steps has been performed, nor was it aimed to do so. We merely evaluated if such a model could describe experimental results. A variable activation energy cannot be regarded as an activation energy in the fundamental sense, but is a result of an interplay between several simultaneously occurring reaction steps or processes[7, 39–41]. For methane pyrolysis, the reaction network is simplified in the sense that several intermediate species are not regarded.

The carbon deposition is described by equation 2.9. The parameter k_{dec} incorporates the particle particle dependent characteristic of the amount of available sites. Therefore, only a single equation is needed. The activation energy is a function of carbon loading and is described by equation 2.10.

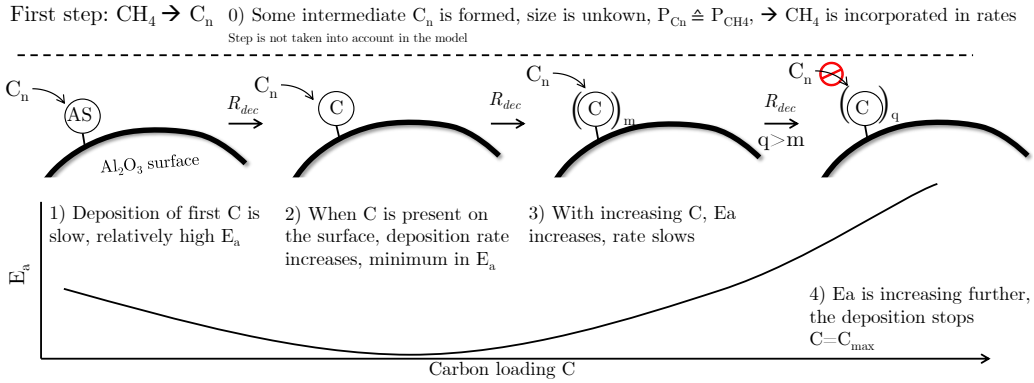

Figure 2.9: Variable activation energy model visualized in steps

$$\frac{dC_c}{dt} = R_{dec} = C_M k_{dec} \exp\left(\frac{-E_{a,dec}}{RT}\right) \tag{2.9}$$

$$E_{a,dec} = p_2 \cdot C_c^2 + p_1 \cdot C_c + p_0 [\mathrm{J \cdot mol^{-1}}] \tag{2.10}$$

Combination of equation 2.9 and 2.10 yields:

$$\frac{dC_c}{dt} = C_M k_{dec} \exp\left(\frac{-(p_2 \cdot C_c^2 + p_1 \cdot C_c + p_0)}{RT}\right) \tag{2.11}$$

Which has the analytical solution:

$$k_{dec} C_M t = \frac{\sqrt{\pi RT} \exp\left(\frac{p_1^2 - 4p_0 p_1}{4p_2 RT}\right)\left(\mathrm{erfi}\left[\frac{p_1 + 2p_2 C_c}{2\sqrt{p_2 RT}}\right] - \mathrm{erfi}\left[\frac{p_1}{2\sqrt{p_2 RT}}\right]\right)}{2\sqrt{p_2}} \tag{2.12}$$

Equation 2.12 was used to calculate loading over time. The fitting routine was the same as the first model, using equation 2.8 describing the error. Fit parameters were k_{dec} and the 3 polynomial coefficients. The obtained fit is presented in figure 2.10. The corresponding activation energy as function of carbon loading is presented in figure 2.12.

After parameterization this model describes the experimental data. The sigmoid curves are present in the modeled loading. For all temperatures, the deposition speed has reached a maximum at $C_c = 15\ \mathrm{g \cdot m_{p,ex}^{-2}}$, being the inflection point in the sigmoid curve and the minimum of the E_a parabola.

In table 2.6 the the fitted parameters are presented. Calculated correlation coefficients indicate a strong (0.9-1) cross correlation between all the polynomial parameters, but not between the polynomal parameters and the rate constant (0-0.3).

Table 2.6: Fitted parameters for activation energy distribution model

	Value	Error	Unit
k_{dec}	$1{,}97 \cdot 10^{9}$	$6.7 \cdot 10^{6}$	$\mathrm{m_g{}^3 \cdot m_p{}^{-2} \cdot s^{-1}}$
p_0	$3{,}3 \cdot 10^{5}$	$6{,}3 \cdot 10^{2}$	$\mathrm{J \cdot mol^{-1}}$
p_1	$-18.5 \cdot 10^{3}$	$3.6 \cdot 10^{2}$	$\mathrm{J \cdot m^2 \cdot mol^{-2}}$
p_2	$7.9 \cdot 10^{3}$	64	$\mathrm{J \cdot m^4 \cdot mol^{-3}}$

As is the case with the nucleation model, these parameter values are only valid for particle A. An adaption of these parameters needs to be made for usage of other particles.

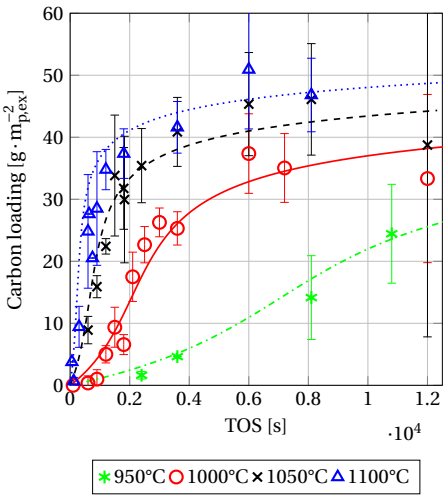

Figure 2.10: Carbon loading over time in the single particle reactor with activation energy distribution results, several temperatures, particle A.

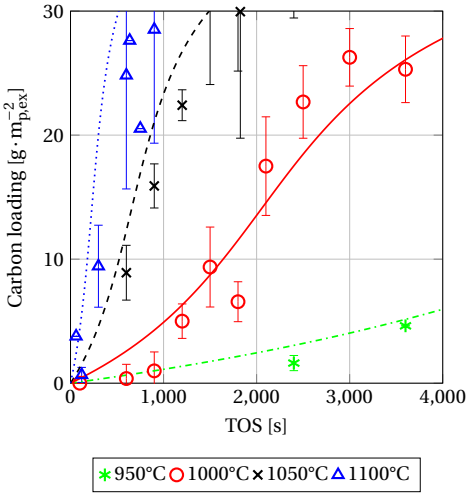

Figure 2.11: Carbon loading over time in the single particle reactor with activation energy distribution results, several temperatures, particle A. Zoomed in from figure 2.10

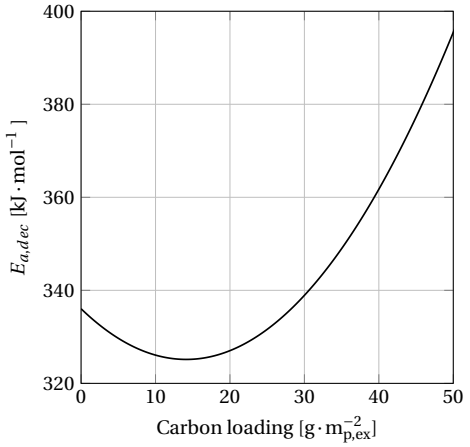

Figure 2.12: Fitted activation energy as function of carbon loading, corresponding to the results in figure 2.10

Comparing both models

Comparing both models, the overall accuracy of the fit, as measured by equation 2.8, is slightly better for the first model (total deviation over all datapoints 418 g · m$^{-2}_{p,ex}$for model 1 versus 477 g · m$^{-2}_{p,ex}$for model 2). The accuracy for both models is comparable to the error estimates on the experimental data (summing to 405 g · m$^{-2}_{p,ex}$), and it is argued that both models predict the

experimental loading with comparable accuracy. However, there are a few other aspects that vary between both models. The first model uses more parameters (6 vs. 4), which (as a result) have a higher cross correlation. For a process design it is mainly desired to describe carbon deposition, which both models are able to do.

2.3.5 Verification of kinetics in a fixed bed

In this work a fixed bed was chosen because it is a relatively simple system that could be evaluated without changes to the used setup. From a process development perspective there are numerous other reactors that may be more suitable for this process, as well as the option of porous particles. This will be evaluated in a separate publication.

In this section fixed bed results are compared to model predictions 2.3.4. Both the kinetics were incorporated in a fixed bed model. In this model it is assumed that the total methane conversion rate is equal to the carbon deposition rate, meaning that the net formation of intermediates is not taken into account, as discussed earlier. In the fixed bed model, the measured axial temperature profiles were used as input and were taken as constant over time. More details on the model and the differential equations describing this system are presented in appendix D of this chapter. The bed temperature varies significantly over the axial reactor coordinate, therefore the overall CH_4 conversion is a result of decomposition processes at a wide range of temperatures. The induction period will play a role for temperatures below ±1050 °C .

The model prediction for CH_4 conversion over time is in reasonable agreement with the experimental results. For the nucleation model the predicted conversion at $t = 0$, is 0. This is because no available sites have been transformed into nuclei at this point. Even though accurate measurement of CH_4 conversion in the first ±100 s is complicated because the remaining nitrogen is still being flushed out by the newly introduced methane, it is clear that some methane is already being converted. In section 2.3.2 this is also described. For the variable activation energy model this difference is not present as the initial reaction rate is nonzero for these kinetics.

A large part of the bed has a lower temperature than the setpoint temperature, however the carbon deposition is slow here. The lower temperature areas of the bed do not contribute significantly to the total carbon deposition. A test was carried out with a setpoint of 1000 °C . Here, the production of gaseous intermediates becomes much more relevant. The required loading of $\pm 15\ g \cdot m_{p,ex}^{-2}$ takes significantly longer to reach, see figure 2.19. Neither of the models is able to accurately predict methane conversion for this temperature, evident from figure 2.19 in appendix A. Concluding, at lower temperatures the production of gaseous intermediates is much more pronounced and for accurate methane conversion predictions, should be taken into account. At 1100 °C and above, this is not the case.

In figure 2.7 the measured and predicted carbon profiles are presented for three different total runtimes, so that the growth of the carbon profile is visible. The experimental results show that the growth over time is not linear, as can be expected from the single particle results and the total CH_4 conversion over time. For all three run times the predictions of both models are in good agreement with the experimental results. Both kinetic models therefore accurately predict when, and where carbon is deposited. This, and the prediction of CH_4 conversion over time provides confidence that the kinetics obtained in the single particle reactor can be used to predict CH_4 conversion and carbon deposition in a fixed bed. Hence, the kinetics can be used as a rational basis for reactor design and process development.

2.4 Conclusions

This work describes a first attempt to quantitatively describe carbon deposition from methane pyrolysis on nonporous particles in a way useful for reactor design and process development. A method was developed to characterize carbon deposition on a specific single particle. Using this method, an accurate prediction of the carbon deposition behavior of many particles in a fixed bed was possible.

Detailed data on carbon deposition as function of time and temperature is reported. It was found that carbon deposition accelerates in the first moments after first contacting with methane. Additionally, a maximum carbon loading was found on the used nonporous particles. For 1000 °C, it was shown that even though carbon deposition does not occur directly after first contacting with methane, methane is being converted to gaseous intermediates. Over time, as carbon deposition starts and accelerates, the selectivity to gaseous intermediates greatly reduces. This effect is most pronounced at temperatures below 1100 °C. For a hydrogen or syngas production process the formation of gaseous hydrocarbons should be avoided, therefore a sufficiently high temperature and solids residence time in the decomposition reactor is required so that the net production of intermediates is largely avoided.

Two types of kinetic models were presented. In neither of these models, the gaseous intermediates were included. Both models accurately predict carbon deposition and methane conversion at 1100 °C over time in a fixed bed system. Therefore, for a decomposition reactor operating at 1100 °C it is sufficient to only describe the solid deposition to accurately describe methane conversion.

Bibliography

[1] A. Abánades, E. Ruiz, E. M. Ferruelo, F. Hernández, A. Cabanillas, J. M. Martínez-Val, J. A. Rubio, C. López, R. Gavela, G. Barrera, C. Rubbia, D. Salmieri, E. Rodilla, and D. Gutiérrez. Experimental analysis of direct thermal methane cracking. *International Journal of Hydrogen Energy*, 36(20):12877–12886, 2011. ISSN 03603199. doi: 10.1016/j.ijhydene.2011.07.081.

[2] Rita Aiello, Jeffrey E. Fiscus, Hans Conrad Zur Loye, and Michael D. Amiridis. Hydrogen production via the direct cracking of methane over Ni/SiO2: Catalyst deactivation and regeneration. *Applied Catalysis A: General*, 192(2):227–234, 2000. ISSN 0926860X. doi: 10.1016/S0926-860X(99)00345-2.

[3] J. Ashok, S. Naveen Kumar, A. Venugopal, V. Durga Kumari, S. Tripathi, and M. Subrahmanyam. CO free hydrogen by methane decomposition over activated carbons. *Catalysis Communications*, 9(1):164–169, 1 2008. ISSN 15667367. doi: 10.1016/j.catcom.2007.05.046. URL `https://linkinghub.elsevier.com/retrieve/pii/S1566736707002452`.

[4] Zongqing Bai, Haokan Chen, Baoqing Li, and Wen Li. Catalytic decomposition of methane over activated carbon. *Journal of Analytical and Applied Pyrolysis*, 73(2):335–341, 2005. ISSN 01652370. doi: 10.1016/j.jaap.2005.03.004.

[5] L C Blackman, G Saunders, and A R Ubbelohde. Defect structure and properties of pyrolytic carbons. *Proceedings of the Royal Society of London. Series A. Mathematical and Physical Sciences*, 264(1316):19–40, 1961. ISSN 0080-4630. doi: 10.1098/rspa.1961.0183.

[6] Vladimir V Chesnokov and Alexandra S Chichkan. 1-s2.0-S036031990900144X-main.pdf. *international journal of hydrogen energy*, 34(7):2979–2985, 2009.

[7] F Hurn Constable. The mechanism of catalytic decomposition. *Proceedings of the Royal Society of London. Series A, Containing Papers of a Mathematical and Physical Character*, 108 (746):355–378, 1925. ISSN 0019-7866. doi: 10.1021/ie50602a034.

[8] Gilles H. Denis and Thomas E. Daubert. Application of quasilinearization to methane pyrolysis. *AIChE Journal*, 20(4):720–727, 1974. ISSN 15475905. doi: 10.1002/aic.690200413.

[9] Alan M. Dunker, Sudarshan Kumar, and Patricia A. Mulawa. Production of hydrogen by thermal decomposition of methane in a fluidized-bed reactor - Effects of catalyst, temperature, and residence time. *International Journal of Hydrogen Energy*, 31(4):473–484, 2006. ISSN 03603199. doi: 10.1016/j.ijhydene.2005.04.023.

[10] B Eisenberg and H Bliss. Kinetics of methane pyrolysis. In *Chem. Eng. Prog. Symp. Ser.*, volume 63, pages 3–17. Yale Univ., New Haven, CT, 1967. URL `http://www.osti.gov/energycitations/product.biblio.jsp?osti_id=5142124`.

[11] M. A. Ermakova, D. Yu Ermakov, and G. G. Kuvshinov. Effective catalysts for direct cracking of methane to produce hydrogen and filamentous carbon. Part I. Nickel catalysts. *Applied Catalysis A: General*, 201(1):61–70, 2000. ISSN 0926860X. doi: 10.1016/S0926-860X(00)00433-6.

[12] D. V. Fedoseev, S. P. Vnukov, and B. V. Derjaguin. Physico-chemical theory of graphite growth from hydrocarbons. *Carbon*, 17(6):453–458, 1979. ISSN 00086223. doi: 10.1016/0008-6223(79)90033-2.

[13] F. Geiger, C. A. Busse, and R. I. Loehrke. The vapor pressure of indium, silver, gallium, copper, tin, and gold between 0.1 and 3.0 bar. *International Journal of Thermophysics*, 8(4):425–436, 1987. ISSN 0195928X. doi: 10.1007/BF00567103.

[14] Christophe Guéret, Michel Daroux, and Francis Billaud. Methane pyrolysis: Thermodynamics. *Chemical Engineering Science*, 52(5):815–827, 1997. ISSN 00092509. doi: 10.1016/S0009-2509(96)00444-7.

[15] Ling Han, Tae Ki Lim, Young Jun Kim, Hyun Sik Hahm, and Myung Soo Kim. Hydrogen production by catalytic decomposition of methane over carbon nanofibers. *Materials Science Forum*, 510-511(2):30–33, 2006. ISSN 16629752. doi: 10.4028/0-87849-995-4.30.

[16] Peter Harris. 'Chemistry and physics of carbon'. *Materials Science and Technology*, 13(12): 1066–1066, 1997. ISSN 0267-0836. doi: 10.1179/mst.1997.13.12.1066.

[17] A. Holmen, O. A. Rokstad, and A. Solbakken. High-Temperature Pyrolysis of Hydrocarbons. 2. Naphtha to Acetylene. *Industrial and Engineering Chemistry Process Design and Development*, 18(4):653–657, 1979. ISSN 01964305. doi: 10.1021/i260072a014.

[18] Anders Holmen. Direct conversion of methane to fuels and chemicals. *Catalysis Today*, 142 (1-2):2–8, 2009. ISSN 09205861. doi: 10.1016/j.cattod.2009.01.004.

[19] J. Lahaye, G. Prado, and J. B. Donnet. Nucleation and growth of carbon black particles during thermal decomposition of benzene. *Carbon*, 12(1):27–35, 1974. ISSN 00086223. doi: 10.1016/0008-6223(74)90037-2.

[20] Aik Chong Lua and Hong Yan Wang. Hydrogen production by catalytic decomposition of methane over Ni-Cu-Co alloy particles. *Applied Catalysis B: Environmental*, 156-157(6):84–93, 2014. ISSN 09263373. doi: 10.1016/j.apcatb.2014.02.046.

[21] K. I. Makarov and V. K. Pechik. Kinetics of methane thermal decomposition on the carbon surface in transient regime. *Carbon*, 7(2):279–285, 1969. ISSN 00086223. doi: 10.1016/0008-6223(69)90110-9.

[22] K. I. Makarov and V. K. Pechik. Kinetics of methane pyrolysis under conditions of pyrolytic carbon formation. *Carbon*, 12(4):391–403, 1974. ISSN 00086223. doi: 10.1016/0008-6223(74)90004-9.

[23] David M. Matheu, Anthony M. Dean, Jeffrey M. Grenda, and William H. Green. Mechanism generation with integrated pressure dependence: A new model for methane pyrolysis. *Journal of Physical Chemistry A*, 107(41):8552–8565, 2003. ISSN 10895639. doi: 10.1021/jp0345957.

[24] Jonas Meckling, Thomas Sterner, and Gernot Wagner. Policy sequencing toward decarbonization. *Nature Energy*, 2(12):918–922, 2017. ISSN 20587546. doi: 10.1038/s41560-017-0025-8.

[25] R Moliner, I Suelves, M J Lázaro, and O Moreno. Thermocatalytic decomposition of methane over activated carbons: influence of textural properties and surface chemistry. *International Journal of Hydrogen Energy*, 30(3):293–300, 2005.

[26] Jacob A Moulijn, Michiel Makkee, and Annelies E Van Diepen. *Chemical process technology*, volume 51. John Wiley & Sons, 2013. doi: 10.5860/choice.51-2107.

[27] N. Muradov. Catalysis of methane decomposition over elemental carbon. *Catalysis Communications*, 2(3-4):89–94, 2001. ISSN 15667367. doi: 10.1016/S1566-7367(01)00013-9.

[28] Nazim Muradov, Franklyn Smith, and Ali T-Raissi. Catalytic activity of carbons for methane decomposition reaction. *Catalysis Today*, 102-103:225–233, 2005. ISSN 09205861. doi: 10.1016/j.cattod.2005.02.018.

[29] Nazim Z. Muradov. CO2-free production of hydrogen by catalytic pyrolysis of hydrocarbon fuel. *Energy and Fuels*, 12(1):41–48, 1998. ISSN 08870624. doi: 10.1021/ef9701145.

[30] H. B. Palmer, J. Lahaye, and K. C. Hou. On the kinetics and mechanism of the thermal decomposition of methane in a flow system. *Journal of Physical Chemistry*, 72(1):348–353, 1968. ISSN 00223654. doi: 10.1021/j100847a068.

[31] J. L. Pinilla, I. Suelves, M. J. Lázaro, and R. Moliner. Kinetic study of the thermal decomposition of methane using carbonaceous catalysts. *Chemical Engineering Journal*, 138(1-3):301–306, 2008. ISSN 13858947. doi: 10.1016/j.cej.2007.05.056.

[32] Nazanin Rahimi, Dohyung Kang, John Gelinas, Aditya Menon, Michael J. Gordon, Horia Metiu, and Eric W. McFarland. Solid carbon production and recovery from high temperature methane pyrolysis in bubble columns containing molten metals and molten salts. *Carbon*, 151:181–191, 2019. ISSN 00086223. doi: 10.1016/j.carbon.2019.05.041. URL `https://doi.org/10.1016/j.carbon.2019.05.041`.

[33] Sylvain Rodat, Stéphane Abanades, Julien Coulié, and Gilles Flamant. Kinetic modelling of methane decomposition in a tubular solar reactor. *Chemical Engineering Journal*, 146(1): 120–127, 2009. ISSN 13858947. doi: 10.1016/j.cej.2008.09.008.

[34] P. Sander. Surface and in-depth analysis of hydrogenated carbon layers on silicon and germanium by mass and electron spectroscopy. *Journal of Vacuum Science & Technology B: Microelectronics and Nanometer Structures*, 7(3):517, 1989. ISSN 0734211X. doi: 10.1116/1.584778.

[35] Stefan Schneider, Siegfried Bajohr, Frank Graf, and Thomas Kolb. State of the Art of Hydrogen Production via Pyrolysis of Natural Gas. *ChemBioEng Reviews*, 7(5):150–158, 2020. ISSN 21969744. doi: 10.1002/cben.202000014.

[36] I. Suelves, M. J. Lázaro, R. Moliner, B. M. Corbella, and J. M. Palacios. Hydrogen production by thermo catalytic decomposition of methane on Ni-based catalysts: Influence of operating conditions on catalyst deactivation and carbon characteristics. *International Journal of Hydrogen Energy*, 30(15):1555–1567, 2005. ISSN 03603199. doi: 10.1016/j.ijhydene.2004.10.006.

[37] P. A. Tesner, T. D. Smegiriova, and V. G. Knorre. Kinetics of dispersed carbon formation. *Combustion and Flame*, 17(2):253–260, 1971. ISSN 00102180. doi: 10.1016/S0010-2180(71)80168-2.

[38] Angayle Vasiliou, Mark Nimlos, and G. Barney Ellison. Mechanism of the thermal decomposition of furan. In *ACS National Meeting Book of Abstracts*. ACS Publications, 2009. ISBN 9780841224414.

[39] S. Vyazovkin. On the phenomenon of variable activation energy for condensed phase reactions. *New Journal of Chemistry*, 24(11):913–917, 2000. ISSN 11440546. doi: 10.1039/b004279j.

[40] Sergey Vyazovkin. Variable Activation Energy-1.Pdf. *Thermochimica acta*, 397(1-2):269–271, 2003.

[41] Sergey Vyazovkin. Reply to "What is meant by the term 'variable activation energy' when applied in the kinetics analyses of solid state decompositions (crystolysis reactions)?". *Thermochimica Acta*, 397(1-2):269–271, 2003. ISSN 00406031. doi: 10.1016/S0040-6031(02)00391-X.

[42] Alvin E Witt. *A PRELIMINARY INVESTIGATION OF THE FORMATION OF CARBON BLACK BY THE PYROLYSIS OF RESIDUAL FUEL OIL FE 2 1I2S IBARs State University*. PhD thesis, Massachusetts Institute of Technology, 1966.

[43] M Zanfir and A Gavriilidis. Catalytic combustion assisted SMR in a plate reator. *Chemical Engineering Science*, 58(17):3947–3960, 2003.

Appendix A - Supplementary data

Appendix A contains all the supplementary data is summarized. In table B.7 a detailed list of used materials for the heating unit is presented. In table B.8 additional details on the two used particle types is presented. Note that the vast majority of the results presented in this chapter use particle A. Particle B was only used for the measurement on external area influence, the results of which are presented in table B.9.

Table B.7: Detailed overview of used materials in heating unit

Part	**Material**	**Supplier**
Heating wire	SuperKanthal A1	Salomons Metalen
Electrical wire	6mm stainless steel cable	
Screw terminal	Al_2O_3 block	RS Components
Radiation element	99,7%Al_2O_3	Haldewanger
Reactor tube	99,9%Al_2O_3	Haldewanger
Thermal cement	48%Al_2O_3 , 48% SiO_2	ThermAll b.v.
Isolation block	Foamed Al_2O_3	Pizzaoven.shop
Isolation wool	Morgan Al_2O_3 Superwool	Morgan Ceramics
Oven wall	6mm Aluminium plate	

Table B.8: Properties of particles and packed bed of particles. ^{a}-taken from manufacturer datasheet, ^{b} measured

Particle	D_p [mm]	ρ [kg · m^{-3}]	Sphericity [-]	A_{int} [m^2 · kg^{-1}]	A_{ex} [m^2 · kg^{-1}]	Void fraction [m^3_g · m$^{-3}_r$]
A	1,5^a	3740^a	1^a	0^b	0.88	0,55
B	3.0^a	3688^a	1^a	0^b	0.41	0,57

Table B.9: Measured fixed bed reactor averaged decomposition rate for two different particle types

Particle	Area in reactor $[m^2 \cdot m^{-3}]$	Fixed bed reactor averaged rate $[mol \cdot m^{-2} \cdot s^{-1}]$
A	1716	1,23E-08
B	1206	1,19E-08

In table B.10 the carbon loading is presented for the case of 1, 2 or 3 particles present in the cone, for various temperatures and TOS. The variation between the cases for 1, 2 or 3 particles is comparable to the variation between all experiments with 3 particles present in the cone. Therefore, the number of particles in the cone does not affect the measured loading. It was decided to measure with 3 particles almost all of the experiments to increase number of samples taken.

Table B.10: Data on amount of particles present in the cone of the single particle reactor.

TOS [s]	T [°C]	Loading obtained $[g \cdot m_{p,ex}^{-2}]$		
		3 particles	2 particles	1 particle
900	1050	18,4	18,0	
1200	1050	22,6		21,4
1200	1100	34,7		37,2
1200	1000	4,9	5,1	
3600	1050	40,1	40,3	38,0

In figure 2.13 measurement data on the heating unit is presented. The two data series denote the temperature profiles measured along the axial length of the reactor tube. The wider profile uses both heaters, the narrow profile uses only heater 2. The triangle and asterisk denote the location of the controlling thermocouples for heater 1 and heater 2, respectively. The black line denotes the location of the fixed bed, note that in this case only heater two is used. The asterisk (control thermocouple 2) is also the location of the single particle reactor cone, in this case both heaters are used in order to sufficiently heat the gas. Note that for single particle operations the current setpoints do not reflect the actual setpoints.

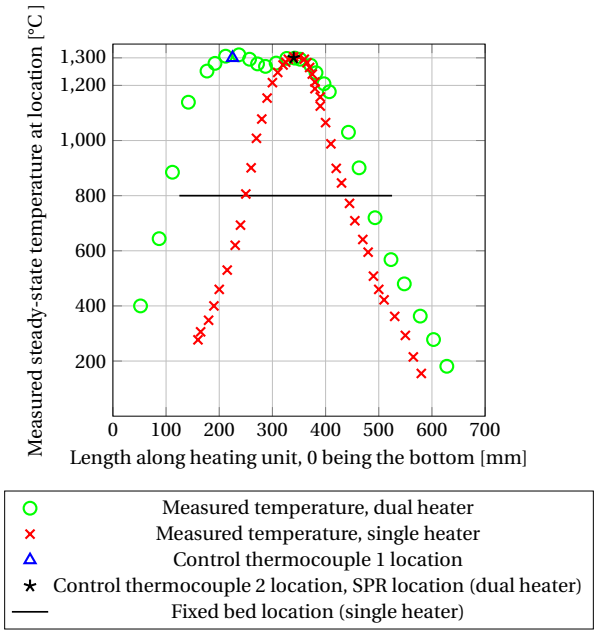

Figure 2.13: Steady state temperature profile of the heating unit. Setpoint was 1300°C. measurements taken with Type S thermocouple in fixed bed configuration.

In figure 2.14 data on the reproducibility of carbon profile measurements is presented. Using the LECO analyzer on a sample thrice obtained a similar profile. When burning off the carbon of this sample in an oxygen atmosphere at 1100°C for 6h obtained a comparable profile, confirming reproducibility of carbon measurements.

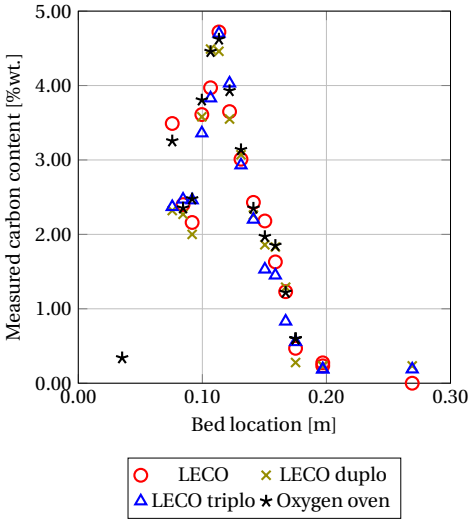

Figure 2.14: Reproducibility of measured carbon profiles in fixed bed. T = 1100°C , Inlet CH_4 fraction = 0.5, $\tau = 0.6s$

In figure 2.15 the measured deposition rate (expressed in $g \cdot m_{p,ex}^{-2} \cdot s^{-1}$) measured at 1000°C is presented as function of methane pressure. From the single particle data (figure 2.2a) it is known that the carbon deposition rate is not a constant, and varies over the carbon loading. To make a fair comparison, the presented rate was measured at a carbon loading of 11 $g \cdot m_{p,ex}^{-2}$, being the inflection point of the sigmoid carbon deposition curve. It was found that a linear relation between carbon loading and deposition rate exists, indicating a first order dependence on methane concentration.

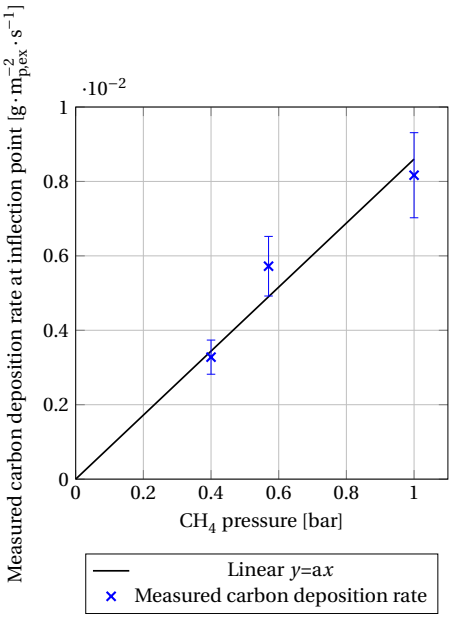

Figure 2.15: Measured carbon deposition rate measured at inflection point of the deposition curve for various CH_4 gas fractions

In figure 2.16 the modeled concentration of active sites is presented. The concentration over time follows an exponential decay. The decay is faster at higher temperature, in agreement with the increased reaction rate over time. The initial amount of active sites is proportional to the maximum carbon loading that can be obtained at that specific temperature and is therefore increasing with temperature.

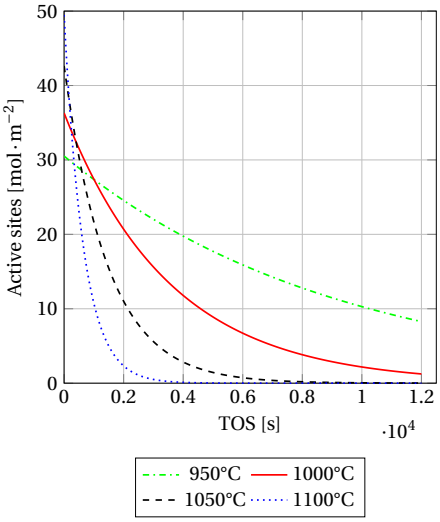

Figure 2.16: Concentration of active sites

In figures 2.17 and 2.18 SEM images of particle A before and after carbon deposition are presented. The rough edges present in figure 2.17 appear to be smoothed out to some extent by the deposited carbon in figure 2.18.

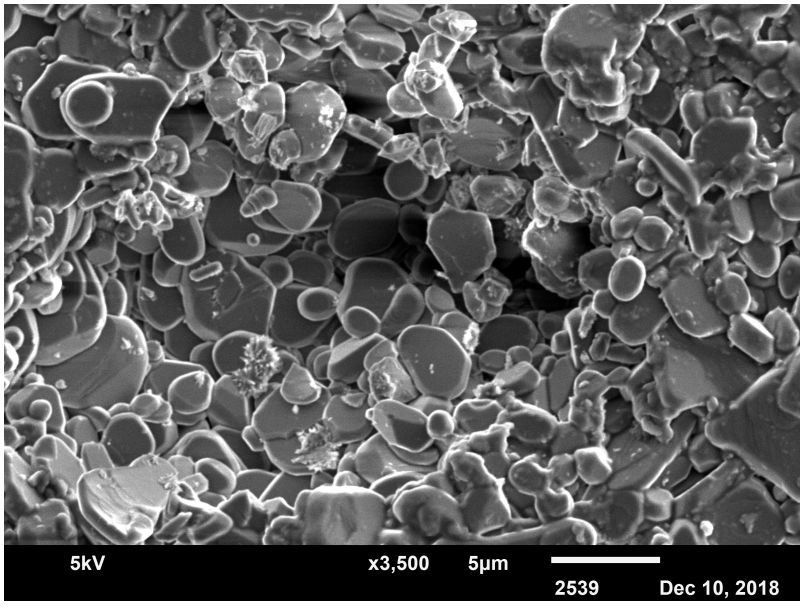

Figure 2.17: SEM image of particle A before exposure to methane

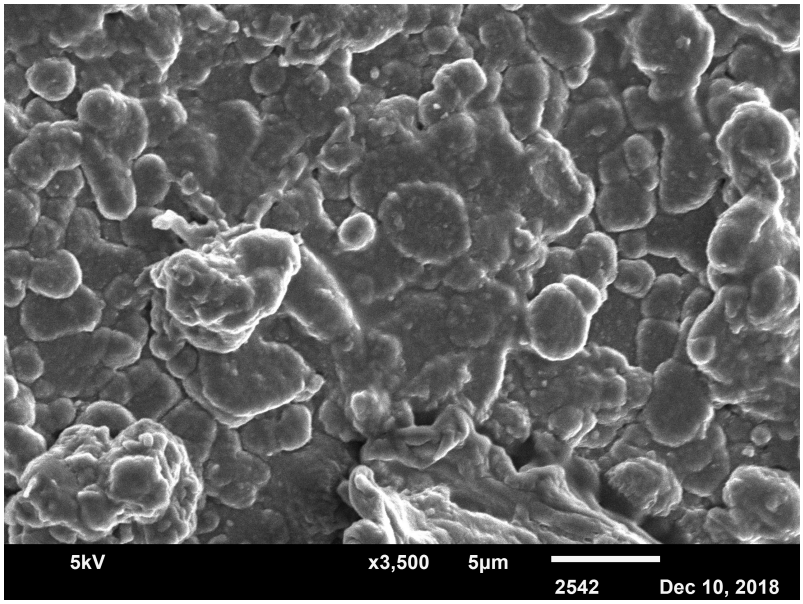

Figure 2.18: SEM image of particle A after methane decomposition, 1300°C 50%CH_4 - 50%N_2

In figure 2.19 the measured methane conversion and model predictions are presented for the fixed bed. One can see that the model predictions do not agree with the measured data. This is explained via the assumption, made in the models, that the total methane conversion rate is equal to the carbon deposition rate. In reality there exists a period where a significant selectivity to gaseous product occurs, see figure 2.4. At 1000 °C this is a relatively long period, at 1100 °C this period is relatively short. Therefore, at 1000 °C the model does not accurately predict methane conversion.

In figure 2.19 the measured methane conversion and model predictions are presented for the fixed bed. One can see that the model predictions do not agree with the measured data. This is explained via the assumption, made in the models, that the total methane conversion rate is equal to the carbon deposition rate. In reality there exists a period where a significant selectivity to gaseous product occurs, see figure 2.4. At 1000 °C this is a relatively long period, at 1100 °C this period is relatively short. Therefore, at 1000 °C the model does not accurately predict methane conversion.

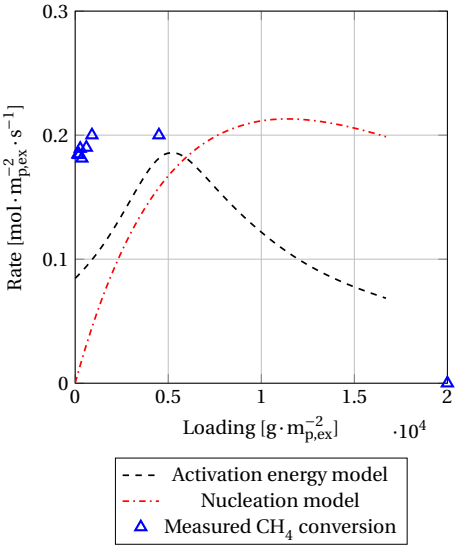

Figure 2.19: Measured and predicted methane conversion for the fixed bed, gas residence time 1 s, setpoint 1000 °C , Particle A.

Appendix B - Energy balances over reactor cone single particle

Single particle

In this section a temperature balance over the single particle is presented. It is assumed the particle is suspended in a gas flow equal to the particle temperature, therefore no heat transfer occurs between particle and gas. The energy balance over the particle is then composed of ingoing heat via radiation and heat consumption via the methane decomposition reaction. In an equation:

$$F_{1,2}\epsilon\sigma(T_{HE}^4 - T_p^4) = R_{dec}\Delta H_{dec}[\mathrm{W}\cdot\mathrm{m}^{-2}] \tag{B.13}$$

In which $F_{1,2}$ is the view factor (1 for a particle suspended in a significantly longer tube), ϵ the emissivity of alumina, σ the Stefan-Boltzmann constant, T_{HE} the heating element temperature in K, T_p the particle temperature in K, R_{dec} the methane decomposition rate in mol $\cdot$ m$^{-2}_{\mathrm{p,ex}}$ and ΔH_{dec} the reaction enthalpy of the decomposition reaction.

Rearranging equation B.13 for T_p yields:

$$T_p = \left(T_{HE}^4 - \frac{R_{dec}\Delta H_{dec}}{F_{1,2}\epsilon\sigma}\right)^{0.25} \tag{B.14}$$

Filling in the maximum measured reaction rate yields:

$$T_p = (O(12) - O(10))^{0.25} \tag{B.15}$$

with a calculated temperature difference between T_{HE} and T_p of 2°C , which is comparable to the inherent accuracy of the used type S thermocouple at operation temperatures.

Reactor cone

To ensure the gas temperature equals the setpoint temperature in the cone, an energy balance was derived for the heating unit. It was aimed to relate the power consumption of both the heaters to the gas temperature in the cone. The temperature during experiments did not vary over time, therefore all balances in this section are for steady state. The energy balance is given for each of the two heaters for a case with zero gas flow in the reactor. In this the total heat loss though the external heating unit surface is the sum of its components HL_{H1} provided by heater 1 and HL_{H2} supplied by heater 2. Since no gas flows though the reactor, the heat loss is the power consumption E of either of the heaters:

$$E_{H1} = HL_{H1} \qquad \text{and} \qquad E_{H2} = HL_{H2} \tag{B.16}$$

When an arbitrary gas flow ϕ_g is introduced, the gas temperature is increased by the heating unit. The energy consumption of the heaters increases via heat exchange with the gas. The total energy increase of the gas is given by:

$$E_{gas,tot} = U_{eff} A_{tot} \Delta T_{avg} \tag{B.17}$$

If we incorporate that total gas heating energy consumption into the total energy balance:

$$E_{H1} = HL_{H1} + U_{eff} A_{H1} \Delta T_{avg,H1} \text{ and } E_{H2} = HL_{H2} + U_{eff} A_{H1} \Delta T_{avg,H2} \tag{B.18}$$

Note that both of the power consumptions E_{H1} and E_{H2} could be read from the setup. When we set the requirement that the gas temperature in the cone equals the setpoint (heater) temperature, one can see that $\Delta T_{avg,H2} = 0$. The energy consumption of the second heater then equals once again $E_{H2} = HL_{H2}$. Experimentally, this was ensured by setting the temperature in the first heater to a sufficiently high temperature. Note that the temperature of the first heater was dependent on the setpoint temperature of the cone, and that this routine needs to be repeated for each unique temperature, as the respective heat losses were also a function of cone setpoint temperature.

Appendix C - Mass transfer in the cone

To investigate the mass transfer to and from the particle suspended in the cone, a 1.5mm diameter copper particle (99.999%) was suspended in a 95% Ar, 5% H_2 flow at 1000°C. The particle was cast to match the diameter of Al_2O_3 particle A. At this temperature Cu has a vapor pressure[13], causing the particle to gradually lose mass. A H_2 containing gas was used to ensure the particle was not oxidized by trace oxygen. All other process conditions, including the particle size, were equal to the methane decomposition experiments. The mass over time is presented in figure 2.20.

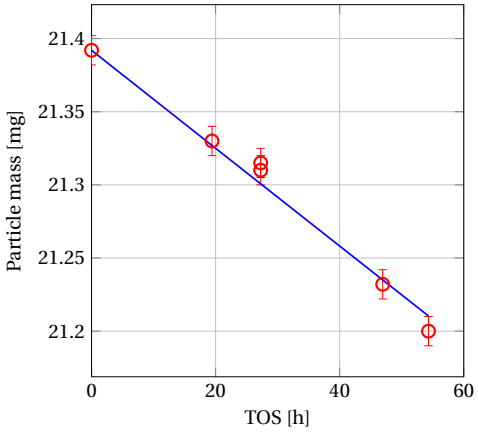

Figure 2.20: Cu particle mass over time, T=1000°C

The mass over time decreases linearly, this is expected as the radius of the particle did not change significantly. The measured mass transfer coefficient at 1000°C k_m is 2.19 $m \cdot s^{-1}$. To find out if the process is mass transfer limited the following mass balance was solved:

$$k_m \left(C_{M,b} - C_{M,s} \right) = R_{dec} \tag{B.19}$$

in which $C_{M,b}$ and $C_{M,s}$ are the bulk and surface concentrations of CH_4 , respectively and R_{dec} is the maximum measured methane decomposition rate. It was found that $C_{M,b}$ and $C_{M,s}$ differ by approximately 0.5%. Therefore it is concluded that the methane decomposition in the cone is not mass transfer limited, in agreement with experimental observations for the much faster oxidation reaction.

3 Predicting gasification rates of pyrolytic graphite deposited from methane

This chapter has been published as: Kreuger, T., A. N. R. Bos, and S. R. A. Kersten. "Predicting gasification rates of pyrolytic graphite deposited from methane." Chemical Engineering Journal (2022): 135487.

Table 3.1: Symbol list for chapter 3

Symbol	Description	Unit
ρ	Density	$kg \cdot m^{-3}$
S	Selectivity	
C	Concentration	$mol \cdot m^{-3}$
C	Loading	$g \cdot m^{-2}$
t	Time	s
R_x	Reaction rate x	
k	Rate constant	
Ea	Activation energy	$kJ \cdot mol^{-1}$
T	Temperature	K
R	Gas constant	$J \cdot mol^{-1} \cdot K^{-1}$
D	Diameter	m
A	Surface area	m^2
τ	Residence time	s
F	View factor	
ΔH_r	Reaction enthalpy	$J \cdot mol^{-1}$
ϵ	Emissivity	
ω	Stefan-Boltzmann constant	$J \cdot m^{-2} \cdot K^{-4}$
E	Energy	J
U	Heat transfer coefficient	$W \cdot m^{-2} \cdot K^{-1}$
r	Radius	m
u	Molar mass, Superficial velocity	$g \cdot mol^{-1}$,$m^3 \cdot m^{-2} \cdot s^{-1}$
m	Mass	kg

Abbr.	Description	Unit
Abbr.	Abbreviation	
ID	Inner diameter	m
OD	Outer diameter	m
TOS	Time on stream	s
SPR	Single particle reactor	
C	Carbon	

Subscript	Description
p	Particle, Product
M	Methane
ex	External
0	Initial
dec	Decomposition, Pyrolysis
mod	Model
exp	Experimental
int	Internal
gas	Gas, Gasification
tot	Total
eff	Effective
Δ	Difference
avg	Average
b	Bulk

Abstract

This work describes the gasification of carbon produced during the pyrolysis of methane. Carbon was deposited on nonporous $\alpha-Al_2O_3$ at temperatures ranging between 950 and 1150 °C. The time $\alpha-Al_2O_3$ was in contact with methane was varied between 60 and 8400 seconds. Gasification tests were performed in the range of 1000 to 1100 °C and steam, CO_2 and air were used as oxidizer.

It was observed that the gasification rate cannot be described by only parameters related to the gasification conditions (temperature, pressure, gas composition). In fact, it became clear that information about the carbon is needed in the gasification rate equation. The H/C ratio and the peak oxidation temperature, as reactivity measures, turned out not to relate uniquely to the gasification rate and are thus not suited as completing parameters. However, it was possible to relate the gasification reactivity of the carbon to the pyrolysis conditions (temperature, contact time between $\alpha-Al_2O_3$ and CH_4) under which it was produced. After parameterization of the thus obtained rate equation using data obtained in a single particle reactor, an adequate prediction on the gasification of carbon deposited by pyrolysis of methane in a fixed could be made. The developed method is therefore a suitable way of predicting gasification rates for reactor design purposes.

3.1 Introduction

The pyrolysis of methane may be a suitable reaction route towards carbon efficient syngas production. The pyrolysis of methane produces hydrogen and solid carbon via reaction 3.1

$$CH_4 \rightarrow H_2 + C \tag{3.1}$$

In previous work the carbon deposition kinetics on unfunctionalized, nonporous α-Al_2O_3 were reported[16]. This work regards the gasification of the deposited carbon via the following reactions:

$$C + H_2O \longrightarrow CO + H_2 \tag{3.2}$$

$$C + CO_2 \rightleftharpoons 2\,CO \tag{3.3}$$

$$C + \frac{1}{2}O_2 \longrightarrow CO \tag{3.4}$$

An industrial process using methane pyrolysis is able to produce hydrogen and synthesis gas. To produce CO, any of the above gasification reactions may be used. Depending on the gasification option chosen, the resulting syngas ratio may be varied between 1 and 3. Hence, the gasification rates of these reactions are investigated.

On the formation and characteristics of deposited carbon

The characteristics of the carbonaceous material deposited (hereafter denoted as carbon) depend on the pyrolysis conditions such as pyrolysis temperature, hydrocarbon pressure, gas flow rates and substrate material. Characteristics of the deposited carbon that may vary with these parameters are, among others, H/C ratio, crystallinity, graphite plate size, density, and various mechanical properties [6, 12, 13, 21, 23, 30].

Generally, with increasing pyrolysis temperature, the deposited carbon increases in crystallinity and decreases in H/C ratio[4, 13, 35]. At conditions, comparable to the ones studied in this work, the carbon is deposited as pyrolytic graphite with a molar H/C ratio of 0.1 after approximately 4200 s of contact with 50/50 methane/hydrogen at 1200 °C[12]. It is one of the aims of this work to investigate the correlations between carbon characteristics and pyrolysis conditions. Carbons produced at different pyrolysis temperature (1000, 1050, 1100 °C) and time (60 – 8400 s) were used, where pyrolysis time is defined as the contact time of the α-Al_2O_3 particles with methane at elevated temperature. Pyrolysis/Decomposition temperature (T_{dec}) and time (τ_{dec}) were included in the design of experiments, because they are key design variables of a process based on CH_4 pyrolysis

On the gasification of the deposited carbon

Gasification of numerous types of carbonaceous materials ranging from activated carbon to graphite is extensively reported in literature[5, 10, 11, 17, 25, 33], and is generally well understood. In this work, reactions of carbon with steam, CO_2 and air were studied at 1 bar and between 950 and 1150 °C. Hereafter, all these reactions will be called gasification.

Typically, the rate equations used to describe the measured data include a proportionality to the concentration of the gasification agent and an Arrhenius term. Obviously, the activation energy and pre-exponential factor of the Arrhenius term are not generic parameters. They are different for each carbonaceous material considered.

To the best of our knowledge, no kinetics are available on the gasification of carbon deposited by the pyrolysis of CH_4. This paper presents our attempt to develop a semi-empirical rate equation for the gasification of such carbon that includes: 1) measurable properties of the carbon or 2) the conditions under which the carbon was produced.

It was found that the measured carbon characteristics did not correlate uniquely to the measured gasification rates, making these carbon characteristics unsuitable to incorporate in a model. Therefore, a model predicting the reactivity of the deposited carbon as function of pyrolysis parameters was developed. This parameterized model was incorporated into a fixed bed model and the predictions of this model were compared with experimental data.

3.2 Materials and methods

3.2.1 Materials

Nonporous α-Al_2O_3 particles were obtained from Saint-Gobain Norpro. The particles were used as received, further information on the used particles is presented in table 3.2 . Nitrogen (99.999%) was supplied by Nippon gases. Methane (99.999%), calibration gases, shielding gas (95% Ar, 5%H_2), CO_2 (99.999%) were supplied by Linde. All gases in this work were used as received. Steam was generated from Milli-Q water obtained from a Water Purification System (Merck).

Table 3.2: Properties of particles and packed bed of particles. ^{a}-taken from manufacturer datasheet, ^{b} measured ^{c} calculated

Particle	D_p [mm]	ρ [kg·m^{-3}]	Sphericity [-]	A_{int} [m^2·kg^{-1}]	A_{ex} [m^2·kg^{-1}]
A	1,5^b	3740^a	1^a	0^b	0.88^c

The particle internal area was measured using gas physisorption measurements. The particle outer diameter was measured using calipers (Mitutoyo, accuracy 0.01 mm).

3.2.2 Experimental setup

The experimental setup is presented in figure 3.1a. It consists of a heating unit and the gas management system. The heating unit has been described in detail in previous work[16]. The heating control thermocouples for each of the two heating coils present in the heating unit were placed in the axial middle of each heating coil. Within the heating unit a reactor tube (11 mm ID, 99.9% Al_2O_3 , Haldewanger) was placed. Within this tube, the conically shaped single particle reactor (SPR, figure 3.1c) was placed. The axial location of the SPR cone was the middle of the second heating coil, at the height of the controlling thermocouple.

To deposit carbon on the particles, methane was pyrolyzed. For gasification, either steam, CO_2 or air was used. For steam, the experimental setup and procedure were slightly different than when

either methane, air or CO_2 was used. Therefore, these two cases are discussed separately. The experimental procedure was identical for CH_4, CO_2 and air experiments.

Setup modifications for steam gasification

The measurement procedure for steam gasification experiments was modified from the CO_2 and air gasification experiments. This was to prevent condensation of steam in the feed and outflow lines of the reactor tube. For this, the feed and outflow lines were heated to 120 °C using a tracing heater (Horst). Controlling thermocouples for (Type K, RS Components) were placed on the outside of the bottom and top valves, respectively for either tracing. Steam was generated by pumping milli-Q water trough a steam generator (T=250 °C , in house constructed) using a HPLC pump (Instrument Solutions). The tracings and steam drum were controlled with Eurotherm P116 controllers individually. A condensation drum was placed at the outlet of the reactor, where condensed liquid water was separated from the gaseous part of the reactor outflow. Afterwards the liquid water was discarded. The gaseous products were vented. In all cases the used gas was not diluted with another gas during single particle experiments. All other parts of the experimental procedure were identical to CH_4, CO_2 and air experiments.

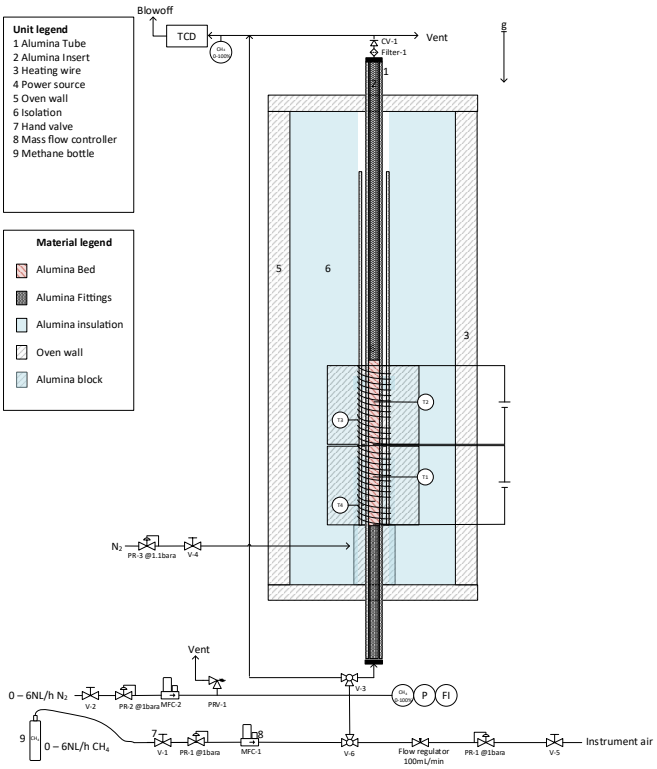

(a) PID of setup in fixed bed configuration

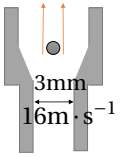

(c) Schematic of single particle reactor

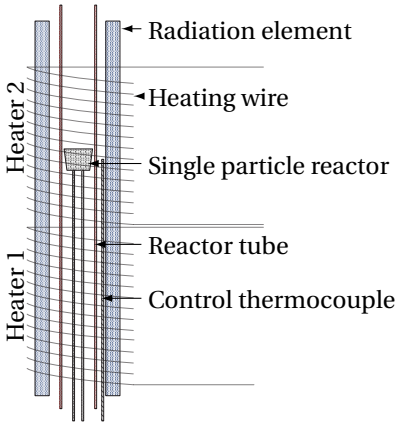

(b) Cross section of heating unit internals in single particle reactor configuration

Figure 3.1: Overview of experimental setup

3.2.3 Modification for fixed bed experiments

For verification of the obtained reactivity model a fixed bed configuration was used. It was operated and configured identically as presented in earlier work[16]. For this, the single particle reactor was removed from the reactor tube. The same reactor tube was used for fixed bed experiments. The bed consisted of the same particle A. The bed had a total length of approximately 30 cm and was placed along the second heater. It was kept in place by two Al_2O_3 inserts. The fixed bed configuration is presented in figure 3.1a. All other parts of the setup were unchanged when a fixed bed measurement was performed.

3.2.4 Mass and energy transport in the single particle reactor

Knowledge on the mass and energy transport characteristics of the reactor is required to accurately measure reaction kinetics. It has been shown that mass and energy transfer are not limiting the deposition of carbon in the used single particle reactor, see appendix C of chapter 2. In this work, steam and CO_2 gasification are shown not to be mass transfer limited as measured air gasification rates were over 1 order of magnitude higher. Air gasification was of the same order of magnitude as the mass transfer rate. Therefore it is concluded that the gasification of carbon in air is mass transfer limited. Because of the extremely fast mass transfer in the cone (k_m = 2.2 m$\cdot$s^{-1}, Sh $\approx$ 20), it is safe to conclude that carbon gasification using air will be mass transfer limited in almost all conventional reactor types.

Additionally, the assumption is made that the temperature of the particle is constant during its residence time in the reactor. The heating time of the particle is in the order of 1 second, as verified by IR measurements. The particle residence times during CO_2 and steam gasification experiments are in the order of minutes, therefore, this assumption is justified.

3.2.5 Experimental method

Experimental procedure for particle loading and gasification of carbon using CO_2 or air

The experimental procedure is identical for particle loading using methane and for carbon gasification using air or CO_2. The heating unit was brought up to the desired temperature with a heating rate of 10 K$\cdot$min^{-1}. CO_2 or CH_4 was taken from a gas cylinder, air and nitrogen were taken from the laboratory utility system. Gas flow was controlled using mass flow controller (brooks). Over all experiments, the superficial gas velocity was kept constant at approximately 16 m$\cdot$s^{-1} at the bottom of the cone. Therefore, the flow rates of the gases were altered depending on temperature. Gas flow rates ranged between 1600-2200 NmL$\cdot$min^{-1}.

Particles with a known diameter were weighed before each experiment, and introduced to the SPR by opening the top valve. After the desired time had passed, the gas flow was turned off. The particle fell out of the cone and was collected at the bottom sample glass. Via the weight difference a reaction rate could be obtained. To increase output of data from the system, three particles were introduced simultaneously. It has been confirmed in previous work that the measured results are not affected when three or fewer particles are used[16].

Experimental procedure modification for steam gasification

In addition to the method presented in the previous section, for steam the following procedure was followed. To prevent steam condensation the in- and outgoing feed lines were heated using

tracing set at 120°C. On the HPLC pump a liquid flow was set, depending on the temperature. The superficial steam velocity on the cone was set to be identical to the superficial gas flow speeds, at identical temperature. Steam was condensed in the latter parts of the outgoing reactor line, here it was collected in a condensation drum. No active cooling was required. Periodically the condensation and liquid water feed drums had to be emptied or filled, respectively. No further gases were used during steam experiments.

Experimental procedure modification for fixed bed measurements

Some fixed bed measurements were performed. The method used was identical to one described earlier[16]. Approximately 35 g of particle A was loaded into the bed so that 30 cm of bed was present centered around the second heater. The bed diameter was 1.1 cm. Controlling thermocouples were present at identical locations as the single particle experiments. The heating rate and operation was also identical to the single particle experiments.

Carbon was deposited by contacting a 300 $\mathrm{NmL \cdot min^{-1}}$ flow with the bed at set point temperature. After a set time, the methane flow was turned off. Gasification experiments were then done by contacting the carbon loaded bed with either CO_2 or steam for a desired time. A 20-100 $\mathrm{NmL \cdot min^{-1}}$ nitrogen flow was added during gasification experiments. Gaseous outflow was analyzed periodically using gas chromatography. Samples were taken by syringe from the manual sample point at the reactor outlet.

The heater was then turned down so that the cooling rate did not exceed 10 $\mathrm{K \cdot min^{-1}}$. The reactor was cooled down overnight. The reactor tube was removed, and carbon samples were taken layer-by-layer. The carbon mass fraction was measured using a LECO carbon analyzer. The reactor tube was cleaned using a steel brush and placed back into the reactor.

Reproducibility of experiments

To test reproducibility of obtained data, a set of particles was subjected to multiple carbon loading - gasification cycles. Four particles were selected at random. These particles were loaded with carbon for 1200 s at 1100 °C. After this, they were gasified with steam at 1050 °C for 10 minutes. After this the carbon was removed by air at 1100 °C for 600 s. During each run the mass loss during steam gasification was noted. This was repeated 5 times for all the particles.

In figure 3.2, results of the reproducibility test are presented. It is concluded that the gasification measurement is reproducible, although some variation is observed. The absolute amounts of carbon gasified are small, approximately 0.05-0.08 mg for all the tested samples. The used balance has a sensitivity of 0.01 mg. The variance observed in the repeated result of the reproducibility test falls within this value for all individual particles. Concluding, the experimental error on all measurements is dominated by the accuracy of the balance. This is more pronounced for samples with a lower absolute amount of C deposited. For more on this see appendix B of this chapter.

Another take on the measured data is to look not at the absolute amount of carbon gasified, but at the measured rate, unit ($\mathrm{gm_{p,ex}^{-2}/s}$). Where the absolute amount of carbon gasified per particle is influenced by the total surface area, and therefore the particle radius, the measured rate takes this into account. This also explains why the variation in total absolute carbon loading [mg] between the samples exceeds 0.01 mg. This is caused by the difference in particle surface area. In figure 3.2 the measured rates are also presented. One can see the rate varies significantly between the particles (standard deviation on measurement mean 5%). This has been observed before during

the carbon deposition tests. It is speculated that some characteristic of the particle affects the gasification rate.

To exclude the assumed effect of this particle characteristics and find a representative value for a gasification rate, each experiment was repeated 12 times per datapoint, and averaged. The experimental error was in almost all cases still dominated by the accuracy of the balance, however.

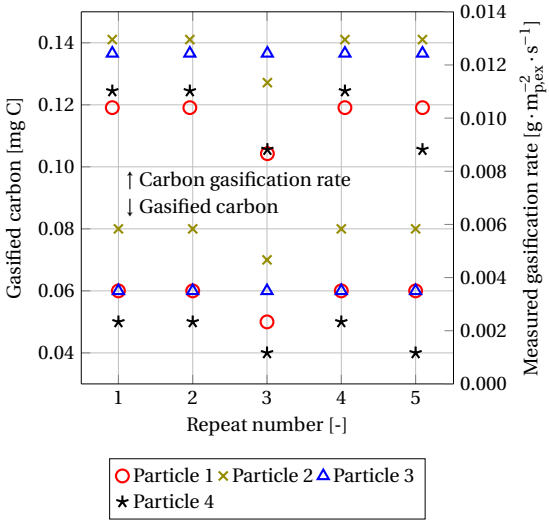

Figure 3.2: Reproducibility of steam gasification test on 4 particles, T_{dec}= 1100 °C, τ_{dec}=1200 s, T_{gas}=1050 °C , particle A

3.2.6 Analysis methods

In this work, the deposited carbon was analyzed for several characteristics. The H/C ratio was investigated using ToF-SIMS (IONTOF). Gasification mass loss over time and temperature in oxygen was measured via TGA coupled to a DSC (NETZSCH STA 449F3). Specific area was measured via surface adsorption measurements (Gemini VII 2390 Surface Area Analyzer, Micrometrics). A Raman measurement was performed on a SENTERRA instrument (figure A.10 in appendix A). Gas was analyzed using a GC (Varian 450-GC). Carbon mass fractions were measured using a LECO A200 carbon analyzer, for selected single particle experiments and all the fixed bed experiments. XPS was attempted (PHI Quantera XPS) but yielded no additional information. This analysis was greatly complicated by the noncrystallinity of the deposited carbon.

3.3 Results and discussion

3.3.1 Gasification

Air, steam and CO_2 gasification was studied in the single particle reactor at gasification temperatures T_{gas}ranging from 950 to 1150 °C. For all data in this section, particle A was used, unless mentioned otherwise. In figure 3.3 the measured carbon loading over time is presented. The

carbon loading was calculated using equation 3.5, in which Δm is the mass change measured before and after loading with carbon [g] and r_p is the particle radius [m].

$$C_c = \frac{\Delta m}{4\pi r_p^2} \qquad \left[\mathrm{g \cdot m_{p,ex}^{-2}}\right] \tag{3.5}$$

Over time the surface decrease from carbon loss is negligible (as the radius of the particle does not change significantly), which means mass transfer characteristics remain the same during gasification. Over time the mass decreases, as carbon is gasified. It is observed that the mass decrease over time is linear and is therefore not dependent on the carbon loading. Two plausible explanations for this observation are presented 1) a gasification rate that is zeroth order in carbon loading or 2) complete external mass transfer control. The latter was discussed in section 3.2.4, and can be excluded, because the observed air gasification rates are over 1 order of magnitude faster than the steam gasification rate in figure 3.3. Moreover, no correlation between particle diameter or mass loss flux [$\mathrm{g \cdot m_{p,ex}^{-2} \cdot s^{-1}}$] was observed. Hence, it is concluded that the steam gasification rate is zeroth order in carbon. This zeroth order dependence is explained via the constant availability of surface covered with carbon. As neither gas phase characteristics nor mass transfer characteristics change over time a constant mass loss rate is observed. Additionally, the linear mass decrease also implies that the carbonaceous material does not undergo changes significantly affecting the gasification rate, during the gasification step.

For all measured data, Arrhenius plots are presented in figure 3.4. For this, the rate constant was assumed to be described by equation 3.6. The first order dependence on oxidant concentration was based on literature [8, 18, 29].

$$R_{gas} = k_{gas} C_{ox} \qquad \left[\mathrm{mol \cdot m_{p,ex}^{-2} \cdot s^{-1}}\right] \tag{3.6}$$

$$k_{gas} = \frac{\Delta m}{\tau_{gas} 4\pi r_p^2 u_c C_{ox}} \qquad \left[\mathrm{{m_g}^3 \cdot m_{p,ex}^{-2} \cdot s^{-1}}\right] \tag{3.7}$$

From the measured data, k_{gas} was then calculated via equation 3.7. It is observed that for all the used oxidants, a large spread, approximately a factor 10, is found in the rate constants at fixed temperature. However, when a random particle is subjected to several loading-gasification cycles the measured values are reproducible (see section 3.2.5). It is noted that this occurs at all temperatures, and cannot be caused by a different order in oxidant. Within the set of measurements performed at each $\mathrm{T_{gas}}$, samples of various pyrolysis temperatures $\mathrm{T_{dec}}$and pyrolysis time τ_{dec}were used. It is known that the pyrolysis parameters affect some unknown characteristic(s) of the deposited carbonaceous material, and it is assumed that this in turn affect(s) the gasification rate measured. The next section shows our attempt of measuring such characteristics, and subsequently correlating this to the measured gasification rates.

Because of this large spread it is speculated that a pre-exponential factor and activation energy obtained from these Arrhenius plots are unable to predict gasification correctly. This is verified (see section 3.3.6 for the method used to verify this), by fitting these constants to the steam gasification data obtained in the single particle reactor The predicted result for the fixed bed reactor (figure 3.10) did not agree with the measured data. Concluding, the gasification of this type of carbon cannot be described by gasification parameters only. Additional information is required

to correctly describe the gasification rates. Note that this result can be expected, as it is known that the characteristics of the deposited carbon are affected by the conditions under which it is deposited [6, 12, 13, 21, 23, 30].

The gasification rates of steam and CO_2 differ by a factor 5, approximately. This is good agreement with literature [20, 31, 34]. The obtained reaction rates are significantly lower than reported values for char[14], but significantly higher than values reported for pure graphite [22]. Therefore, it is speculated that the carbon deposited in this work has a degree of graphitization in between these two types of carbon found in literature.

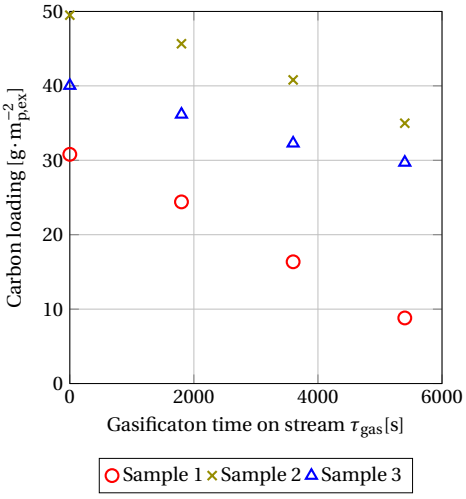

Figure 3.3: Measured carbon loading in the single particle reactor as function of time under steam τ_{dec}= 1100 °C, T_{gas}=1000 °C , various τ_{dec}, particle A

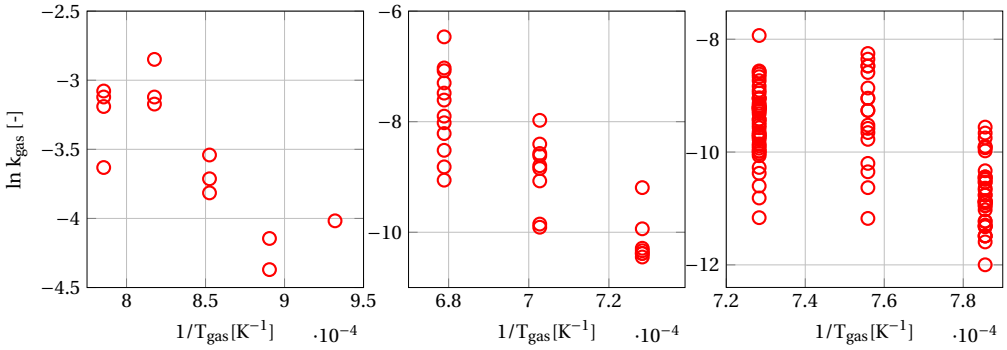

(a) Air gasification *(b)* Steam gasification *(c)* CO_2 gasification

Figure 3.4: Arrhenius plots of measured gasification rate [$mol \cdot m_{p,ex}^{-2} \cdot s^{-1}$] constants for a) air, b) steam and c) CO_2 gasification. T_{gas} ranged between 950 and 1150°C, various T_{dec}, various τ_{dec}, Particle A.

3.3.2 Notes on air gasification

Although a large spread is present in the measured air gasification rate, the highest measured mass loss rates were in the order of $5\ g \cdot m_{p,ex}^{-2} \cdot s^{-1}$. This is comparable to the calculated maximum flux, established from mass transfer experiments [16]. This is over 1 order of magnitude faster than steam and CO_2 gasification, proving that both of these are not mass transfer limited.

No kinetic model is developed for air gasification. This is justified by the fact that, if the air gasification is mass transfer limited in the single particle reactor, it will be mass transfer limited in (almost) all other reactor systems. Therefore, the air gasification rate of this carbon is dictated exclusively by oxygen feed rate and mass and energy within the reactor. No further depth was added to this part of the study.

3.3.3 Carbon analysis

In this section, the carbon characteristics H/C ratio and peak oxidation temperature are discussed. It is aimed to investigate whether the pyrolysis temperature T_{dec} and/or pyrolysis time τ_{dec} affect the properties of the carbon.

SIMS

The H/C ratio was investigated using ToF-SIMS. This analysis technique has been used numerous times to analyze the composition of carbonaceous materials. For pyrolytic graphite, analyses reported in literature comparable [3, 7, 19, 32, 36] or identical[2, 9, 26] to the analysis performed in this work are well established. As is the case in literature, the presented data in this work denotes the ratio in intensity of the CH^- over the C^- signal. This is not a measure of the absolute molar H/C ratio but is a linear function of the H/C ratio[26, 32]. Therefore, in this work, the terms CH^-/C^- signal intensity and H/C ratio are used interchangeably. The H/C ratio is a measure of the relative amount of edges present in the carbon. However numerous graphite plates can be drawn,

satisfying the same H/C ratio[35]. Therefore, it is speculated that the average plate geometry is influenced by the decomposition/pyrolysis temperature.

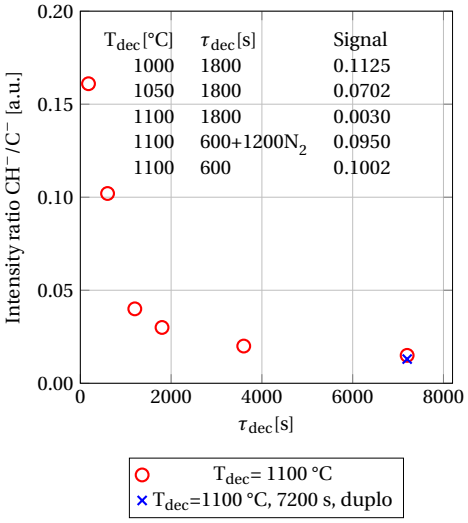

Figure 3.5: Measured intensity ratio CH^-/C^- as function of τ_{dec}. Various decomposition temperatures

The obtained signal intensities are presented as function of pyrolysis time τ_{dec}. In figure 3.5 the obtained CH^-/C^- signal is presented for various samples. For a pyrolysis temperature of 1100 °C several pyrolysis times were tested. One can see the decrease of H/C ratio over time. This indicates that the material becomes more graphitic over time. This must mean that the average crystal size or graphite plate size increases over time, which is in good agreement with observations reported in literature[4, 13, 35]. The data suggests that the H/C value at long τ_{dec}approaches an asymptote. It is speculated that this is some kind of equilibrium H/C characteristic for the used pyrolysis temperature. The effect of $T_{dec}$is also visible from the table in figure 3.5, for the samples at τ_{dec}=1800 s. Again as expected it is observed that at higher temperature a more graphitic carbon is deposited.

Literature values on the real values of H/C of graphite deposited from methane is sparse. Blackmann et. al. report a a H/C value of 0.00045 for carbon deposited at 1600 °C[4]. Gueret reports a H/C value of 0.1 at temperatures comparable to this work, albeit with a 1:1 CH_4 :H_2 in the feed[12]. This gives an upper and a lower range of real H/C for the carbon in this work. Without additional data a more accurate estimation is unfortunately not obtainable.

In the table of figure 3.5, a separate sample created at T_{dec}=1100 °C for 600 s under methane is included. After this it was contacted with nitrogen for 1200 s at 1100 °C, also in the single particle reactor. It was aimed to investigate whether this particle had the characteristics of a 600 s particle or a 1800 s particle in a CH_4 -rich atmosphere. It is observed that the H/C ratio did not change significantly under nitrogen, compared to the original 600 s sample. This means that the decrease in H/C is not an effect of temperature and residence time exclusively. It is speculated that the

exchange of hydrogen towards the gas phase atmosphere, leading to a decrease in H/C, is only possible when a hydrocarbon is present in a certain fraction.

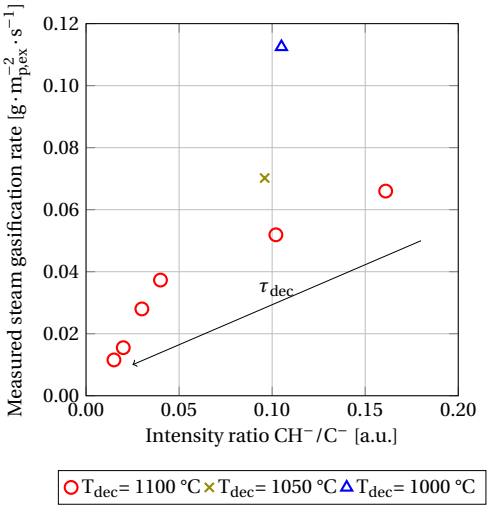

Figure 3.6: Measured steam gasification rate as function of measured dimensionless H/C ratio

In figure 3.6 the obtained H/C ratio from figure 3.5 is plotted over the measured steam gasification rate. It is observed that the gasification rate measured is a monotonic function of the H/C rate for the T_{dec}=1100 °C . A lower H/C rate corresponds to a lower gasification rate. This can be expected as a more graphitic material is more stable, and less prone to gasification by any oxidant [14, 22].

However, when including more pyrolysis temperatures in the analysis it turns out that the gasification rate is not a (unique) function of the H/C ratio. For the same H/C of approximately 0.1, different rates were found. Since the H/C ratio is not a unique parameter to describe the gasification rate, kinetics can not be based on this parameter alone.

TGA-QMS

A set of particles coated with carbon under identical conditions as the SIMS set was analyzed in a TGA-QMS. The trends observed in the measured results were strongly comparable to the results presented in the previous section. For brevity, the TGA-QMS results are included in appendix A of this chapter.

3.3.4 Gasification rate as function of pyrolysis parameters

In the previous two sections, it was shown that the gasification of carbon deposited by methane pyrolysis is not described by simple first order kinetics. It was also shown that two measured characteristics of the carbon are unsuitable parameters to describe the measured gasification rate. In this section, the calculated gasification rate is presented as function of the pyrolysis parameters. In figure 3.7 the measured gasification rates for steam and CO_2 in the single particle reactor are

presented. Three series were tested, varying the decomposition temperature between 1000 and 1100 °C. The contact time of the deposited carbon with oxidant τ_{gas}ranged from 60 s to 600 s, increasing in length with the respective pyrolysis time. Additional data on gasification rates for steam and CO_2 is included in appendix A of this chapter.

The measured reactivity has an initial sharp decrease with pyrolysis time, which then approaches a constant value for the longer τ_{dec}. Even though the experimental error is larger for the lower pyrolysis times, the observed increase in reactivity is significant. This effect is mostly visible for the T_{dec}=1100 °C series presented in figure 3.7, however this has also been observed for other gasification temperatures, see figures A.4-A.8 in appendix A. A porous particle was also tested using the same method, (figure A.9). The a similar shape was obtained, albeit at a different absolute gasification rate. These observations support the theory that this gasification phenomena is caused by properties of the carbon and not by a particle characteristic. The utilization of porous media will be studied in detail in upcoming work.

To further test the effect of pyrolysis time, a particle was loaded with carbon at 1100 °C for 600 s. Afterwards this particle was placed back into the single particle reactor and contacted with pure nitrogen for 1200 s. It was aimed to investigate what effect this had on carbon characteristics and gasification rates. This data point is presented in table 3.3. The gasification rate is comparable to the 600 s sample. Therefore it is concluded that this carbon was not affected by the high temperature nitrogen. The same observation was made in section 3.3.3. Additionally, a particle was loaded with carbon at 1100°C for 600 s and subsequently contacted with a 9:1 N_2:CH_4 flow for 1200 s. It was found that the gasification rate of this particle had decreased slightly and approached the gasification rate of the conventional 1800 s particle. This supports the theory that a hydrocarbon needs to be present in some fraction in the atmosphere for this carbon to undergo changes in reactivity.

The measured reactivity of the carbon decreases with increasing pyrolysis temperature. The measurements performed at τ_{dec}=1800 and 3600 s are presented in figure 3.8. Due to this observation, carbon samples at 1150 °C were added to the data set. It was aimed to obtain carbon deposited at 1200 °C , however this was not possible in the single particle reactor. At temperatures above 1150 °C a carbon dust appeared in the reactor, blocking the tubing. An interesting case arises at this temperature, where the reactivity of the carbon further decreases. It is not known whether the reactivity of this carbon reaches zero or plateaus at a non-zero value.

The measured reactivity for CO_2 is much lower than for steam, in agreement with literature consensus for the used temperatures. The observation that the same two phenomena are present for CO_2 and steam supports the theory that the gasification rate is influenced by some characteristic(s) of the carbon. When comparing the steam and the CO_2 set, the gasified carbon has been deposited at identical conditions and should therefore have the same characteristics. Therefore, one could expect similar gasification behaviour from these two carbon sets.

Table 3.3: Overview of gasification experiments. Steam, T_{gas}= 1100 °C

T_{dec}	τ_{dec}	Gasification rate $[g \cdot m_{p,ex}^{-2} \cdot s^{-1}]$
1100	600 s CH_4	0.055
1100	1800 s CH_4	0.026
1100	600 s CH_4 + 1200 s N_2	0.080
1100	600 s CH_4 + 1200 s N_2:CH_4 9:1	0.035

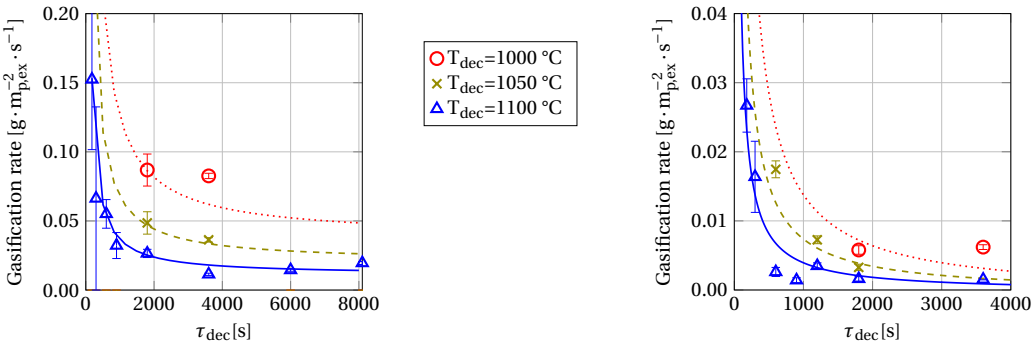

(a) Steam gasification

(b) CO_2 gasification

Figure 3.7: Measured steam (a) and CO_2 (b) gasification rate in the single particle reactor as function of decomposition τ_{dec}, T_{gas}=1100 °C (steam), 1050 °C (CO_2), various T_{dec}, particle A. Lines denote gasification model predictions (section 3.3.6)

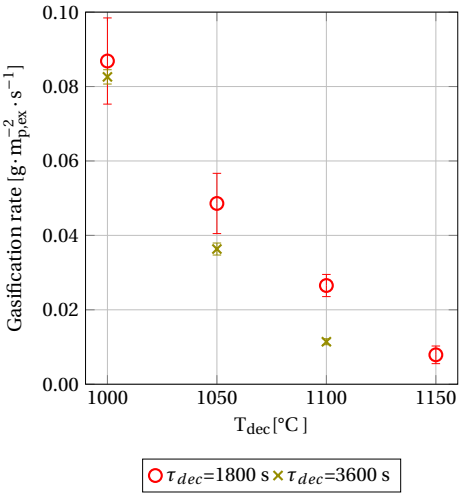

Figure 3.8: Measured steam gasification rate as function of T_{dec} in the single particle reactor, T_{gas}=1100 °C , various τ_{dec}, particle A

3.3.5 Predicting the gasification rate

This section presents our attempt to develop a method to describe the gasification rate during steam and CO_2 gasification for a given gasification temperature. It has been shown previously that neither a conventional first order nor carbon characteristics are suitable pathways towards description of the measured gasification rates. In this section an attempt is made to use the the pyrolysis parameters in a gasification model.

From section 3.3.4 it is known that several phenomena were observed during gasification measurements. As these phenomena should also be included in a model describing gasification, they are summarized here:

- The gasification rate is initially high for short τ_{dec} carbon deposition. With increasing τ_{dec} this gasification rate rapidly decreases. Here, the pyrolysis time is defined as the time the particle is in contact with CH_4 at pyrolysis temperature T_{dec}.
- After a set τ_{dec} the gasification rate approaches a constant value.
- With increasing T_{dec}, the gasification rate decreases.
- The observed phenomena occur for steam and CO_2 .

The available process parameters are temperature, solids residence time, gas composition and pressure, all of those for both the pyrolysis as for the gasification step. In this and previous work[16], the effects of pyrolysis & decomposition temperature and residence time was investigated in detail. In this work, the effect of decomposition gas composition on reactivity was touched upon briefly. No effects of pressure have been investigated. Because by far the largest amount of data is available for the parameters T_{dec}, τ_{dec}, T_{gas} and τ_{gas}, these will be used in the gasification model.

Model outline and assumptions made

The model can be considered to be merely a mathematical tool, derived from measured observations, useful for the engineering purpose to design a reactor. Though, some parts of the model might be linked to mechanistic aspects, as will be discussed later.

The following assumptions are made:

- The data presented in section 3.3.4 suggests that the decrease in gasification rate with $\tau_{\mathrm{dec}}$is present and of comparable shape for both CO_2 and steam. Therefore, it is attempted to use the same model equations for both gasification gases. The numerical values of the fitted parameters will differ between the two gases, however.
- The observed decrease in gasification rate with $\tau_{\mathrm{dec}}$for T_{dec}=1100 °C is also present at lower T_{dec}. This could not be measured using the SPR for nonporous particles, see appendix B of this chapter for further details on this. This effect was observed at 1050 °C for a porous particle.
- All the gasification rates are taken to be first order in oxidation concentration, based on literature [8, 18, 29].

From figure 3.7 it is known that the gasification rate at long τ_{dec}approaches a constant value. This value appears pyrolysis temperature dependent. The gasification rate of this carbon is then given by:

$$R_{gas} = k_0'(T_{dec}) \cdot \exp\left(\frac{-E_{a,gas}}{RT_{gas}}\right) C_{ox} \qquad \left[\mathrm{gm}_{\mathrm{p,ex}}^{-2}/\mathrm{s}\right] \tag{3.8}$$

Equation 3.8 only describes the gasification rate for long τ_{dec}. In figure 3.7 it can be seen that the measured gasification rate increases for shorter τ_{dec}carbon. This means the rate constant k_0 is also a function of τ_{dec}. The simplest function describing the increase at lower $\tau_{\mathrm{dec}}$is given as an extra component for k_0:

$$k_0(T_{dec}, \tau_{dec}) = k_0'(T_{dec}) + k_0''(\tau_{dec}) \tag{3.9}$$

$$k_0''(\tau_{dec}) = \frac{k_1}{\tau_{dec}} \tag{3.10}$$

The effect of T_{dec}may be seen in figures 3.7 and 3.8. From this, a decrease with $T_{\mathrm{gas}}$is clearly visible. The equation describing this is chosen so that no negative gasification rate could be obtained. One simple form describing this is given by

$$k_0'(T_{dec}) = k_2 \cdot \exp(-k_3 \cdot (T_{dec} - 1373)) \tag{3.11}$$

Combination of equations 3.8-3.11 yields the corresponding overall gasification equation:

$$R_{gas} = \left(\frac{k_1}{\tau_{dec}} + k_2 \exp(-k_3 \cdot (T_{dec} - 1373))\right) \cdot \exp\left(\frac{-E_{a,gas}}{RT_{gas}}\right) C_{ox} \tag{3.12}$$

A mechanistic interpretation of this equation is as follows. The lowest reactivity for any given gasification temperature, which is obtained at high pyrolysis time, corresponds to the reactivity of equilibrated carbon at the used pyrolysis temperature. Equilibrated is meant here as having achieved a final composition (see figure 3.5 in which the H/C ratio of the carbon is shown versus the pyrolysis time) which corresponds to the lowest reactivity.

The equations are fitted to the measured data by minimization of equation 3.13 using MATLABs nlinfit routine. ϵ_i denotes the experimental error of data point i. 95% Confidence intervals and cross correlation coefficients were obtained using the nlparci function.

$$\Delta = \sum_{i=1}^{N} \left(\frac{R_{gas,measured,i} - R_{gas,predicted,i}}{\epsilon_i} \right)^2 \tag{3.13}$$

Notes on cross correlation

Some notes are made on parameter estimation using rate equations described by the Arrhenius equation, or more generally exponential functions. The mathematical form of these equations dictate that the exponent in some form is present in the derivative of these functions. The derivatives are used in the estimation of the correlation coefficients during parameterization. Hence, usually a high correlation between parameters is observed.

To reduce this correlation, numerous other forms of the Arrhenius equation can be used in the fitting process[15, 24, 27, 28]. All of these variations use a reference temperature in the equation. Analogies are noted between these and the reference temperature proposed by Svante Arrhenius[1]. In this work, the cross correlation is reduced via the method proposed in [28].

Fitting results and discussion

The parameters were fitted on the complete data sets of CO_2 and steam gasification, spanning 260 points for steam and 143 for CO_2 . The obtained fit (figure 3.7 and table 3.4) approaches the measured data within the confidence interval of the experimental data. The presented model shows that, using 4 parameters, 3 of which are fitted on the decomposition process conditions, it is possible to accurately predict gasification behaviour. In this work, the model was tested only on the used particle. To extend this, the equations will need to be reparameterized for other particles. The obtained numerical values for the activation energy indicate that indeed no mass transfer control exists.

Table 3.4: Fitted parameter values for steam and CO_2 gasification

	Steam		CO_2	
Parameter	Value	95% CI	Value	95% CI
k_1	$2.40 \cdot 10^{12}$	$1.75 \cdot 10^{11}$	$2.30 \cdot 10^{12}$	$3.68 \cdot 10^{11}$
k_2	$1.25 \cdot 10^{9}$	$8.00 \cdot 10^{7}$	$3.90 \cdot 10^{8}$	$2.73 \cdot 10^{7}$
k_3	$1.83 \cdot 10^{-2}$	$1.83 \cdot 10^{-3}$	$2.80 \cdot 10^{-2}$	$7.28 \cdot 10^{-3}$
E_a	$2.90 \cdot 10^{5}$	$1.02 \cdot 10^{4}$	$3.01 \cdot 10^{5}$	$1.57 \cdot 10^{4}$

Calculated correlation coefficients indicate a weak correlation between the fitted parameters, ranging from 0.0001 to 0.1. One exception to this is a correlation of 0.5 between k_1 and k_3. The weak correlation indicates that the data suffices to make an independent fit for each of the incorporated phenomena. However, it should be mentioned that the presented values cannot be interpreted as (a) meaningful rate constant(s). The overall rate constant is now incorporated into the parameters in equation 3.9. The fitting functions were chosen by the shapes of the data presented in figures 3.7a and 3.8. It is speculated that numerous other equations will yield a comparable or even better fit. This model was developed to investigate whether it is possible to describe gasification rates using only parameters from the decomposition step. The obtained results indicate this is possible. In the next section, this model is verified using a fixed bed setup. The predictive capability of this model will be tested against a separate experimentally obtained data set.

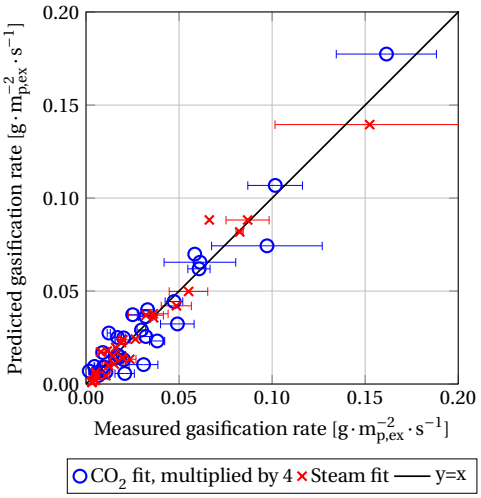

Figure 3.9: Measured and predicted steam and CO_2 gasification rate in the single particle reactor. T_{gas} range from 1000 to 1100 °C , τ_{dec} between 60 and 8100 s, T_{dec} between 1000 and 1100 °C, particle A

3.3.6 Verification of both gasification models

To verify the applicability and test the predictive power of the developed gasification model, a test was performed in a fixed bed setup. This separate data set is used only to test the model, it has not been used for the fitting process. A fixed bed was filled with particle A. Over the bed length, an axial temperature gradient caused an axial carbon profile to be formed. This carbon profile is a measure of the reaction rates at temperatures ranging between 850 and 1100 °C. An example of the temperature profile is presented in figure 3.10, note that this was not the exact temperature profile at which these carbon profiles were deposited.

By measuring the amount of carbon present in the bed, before and after gasification, the gasification rate as function of reactor length was obtained. By incorporating the gasification kinetics

obtained in the single particle reactor in a numerical fixed bed model, a prediction for the resulting carbon profile was made. The numerical model uses the method of lines to solve the carbon mass fraction in the bed as function of location and time. This model is comparable to the model used in previous work, it has been modified only to include gasification. In this work we showed that this model is able to predict carbon growth over time and location[16].

Carbon was deposited at 1100 °C set point, and a total decomposition time on stream of 1800 s. A 300 $NmL \cdot min^{-1}$ CH_4 flow was used during carbon deposition. After this 100 $NmL \cdot min^{-1}$ nitrogen and a 0.1 $mL \cdot min^{-1}$ liquid H_2O were fed into the reactor for a set time. After this the water flow was turned off and the bed was cooled down over night.

The measured and modeled carbon profiles are presented in figure 3.10. The first half of the carbon profile could not be measured experimentally, as it was not possible to retrieve layer-by-layer samples without mixing the solids. Therefore this data was omitted. Additionally, it was not possible to obtain usable carbon samples for beds that were gasified to lower carbon weight fractions, also due to mixing during retrieval.

It is observed that the predicted carbon profile agrees well with the measured carbon profile. This means that the gasification kinetics satisfactorily predict gasification rates across the entire temperature range of 850 to 1100 °C. This temperature range might seem a significant extension of the single particle data used to fit the kinetics. However, at these lower temperatures a relatively small amount of carbon is deposited, and therefore are not of large importance for this case.

In figure 3.11 the results of a test performed at shorter decomposition time is presented. In figure 3.12 CO_2 was used. The predictions made by the model agree with experimental data for both cases. The prediction can take into account the effects of $\tau_{dec}$and is also suitable for CO_2. It is noted however, that in figure 3.10 the deviation for relatively unreactive carbon under CO_2 has a large deviation.

The kinetic models were developed under negligible gas phase conversion conditions in the single particle reactor. In the fixed bed, the gas phase steam conversion was approximately 12%. This is a relatively low conversion, it is therefore expected that a higher concentration will affect the accuracy of the prediction negatively. The kinetics should be expanded to take this into account.

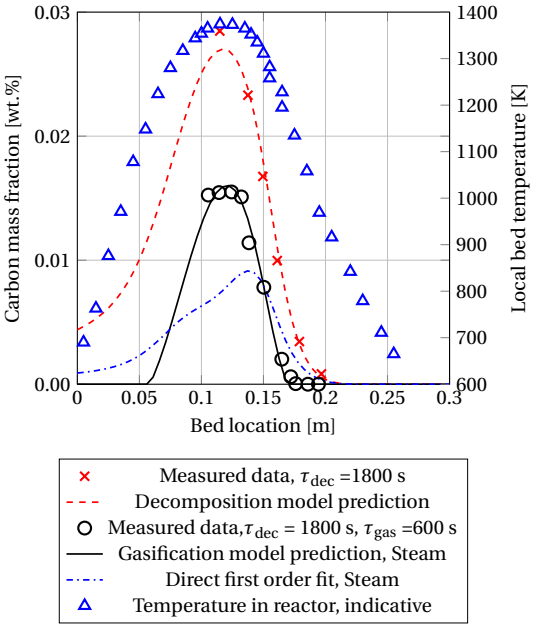

Figure 3.10: Carbon and temperature profile measured in fixed bed reactor. Setpoint 1100 °C, total runtime 1800 s, Gas residence time 0.6 s, Inlet fraction CH_4 = 0.5, particle A

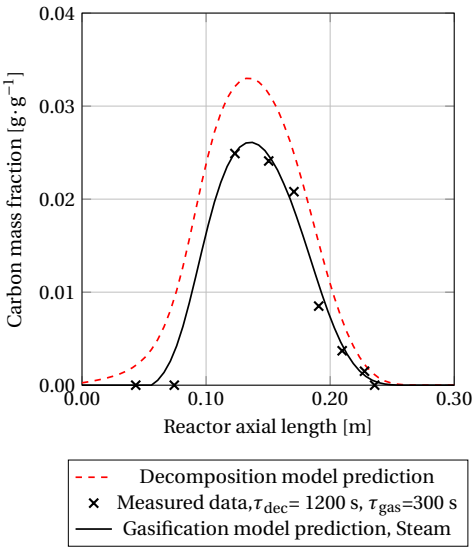

Figure 3.11: Measured and predicted carbon profiles in the fixed bed reactor. Carbon deposition: T_{dec}=1100 °C , τ_{dec}=1200 s. Gasification: Steam, T_{gas}=1100 °C, τ_{gas}=300 s. Note that the used methane flow used in this experiment is 1 order of magnitude higher than the one used in figure 3.10

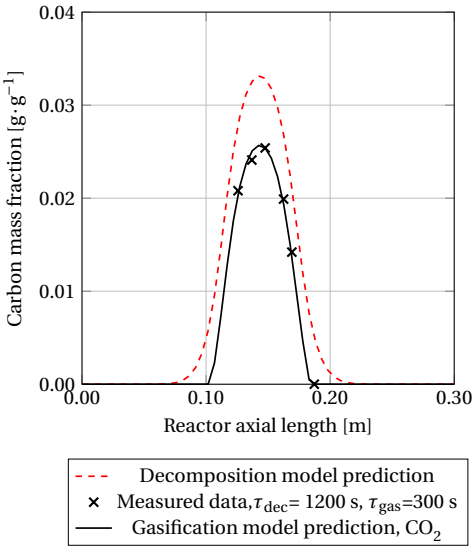

Figure 3.12: Measured and predicted carbon profiles in the fixed bed reactor. Carbon deposition: T_{dec}=1050 °C , τ_{dec}=1800 s. Gasification: CO_2 , T_{gas}=1050 °C, τ_{gas}=1800 s.

3.4 Industrial scale design considerations

Although the focus of this work is not process or reactor design oriented, several implications of the results are noted. These are discussed briefly in this section.

The initial decrease of gasification reactivity with pyrolysis time is relatively large. From a process development perspective, for a higher volumetric gasification rate [$mol_c \cdot m_r^{-3} \cdot s^{-1}$], more reactive carbon is desired over the relatively nonreactive obtained at higher pyrolysis times. Perhaps more importantly, from figure 3.7a, one can conclude that carbon produced at long pyrolysis time is difficult to gasify using steam (or CO_2). Therefore, should these gases be used to gasify the carbon, the residence time of the solids during pyrolysis cannot be too long. This also means that the solid residence time should be controllable, (e.g. little solids residence time distribution should occur during pyrolysis). Therefore one can conclude that the solids phase should have low mixing and behave like a PFR as much as possible, during decomposition, should either steam or CO_2 be used as an oxidant exclusively. Note that this statement is only valid for CO_2 and steam gasification. Should air be used, no effect of $\tau_{dec}$is present.

The selection and conceptual design of an optimal reactor and process is beyond the scope of this thesis. The observation that a high gasification rate can be realized using a low solids residence time during decomposition is only part of the process optimization. The highest overall productivity, regardless how this productivity is defined, will have both a gasification and a decomposition component. This will be studied further in upcoming work.

3.5 Conclusion

In this work, the gasification of carbon deposited on non-porous $\alpha-Al_2O_3$ particles by the pyrolysis of methane was studied. Using a single particle reactor, carbon was deposited on nonporous

α-Al_2O_3 and subsequently gasified. It is concluded that the pyrolysis conditions affect both the characteristics of the carbon as well as the subsequent gasification rate of this carbon. Hence, information on the pyrolysis conditions is required to describe the gasification rate. Measured gasification rates were used to formulate a rate equation. In this rate equation, components describing the carbon reactivity as function of the pyrolysis residence time and temperature were required. This parameterized equation was then used to successfully predict carbon gasification in a fixed bed system.

Bibliography

[1] Svante Arrhenius. Über die Reaktionsgeschwindigkeit bei der Inversion von Rohrzucker durch Säuren. *Zeitschrift für Physikalische Chemie*, 4U(1):226–248, 1889. ISSN 0942-9352. doi: 10.1515/zpch-1889-0416.

[2] Kan Ashida, Kenji Ichimura, and Kuniaki Watanabe. Two different species of deuterium implanted into a pyrolytic graphite observed by XPS–SIMS. *Journal of Vacuum Science & Technology A: Vacuum, Surfaces, and Films*, 1(3):1465–1468, 1983. ISSN 0734-2101. doi: 10.1116/1.572169.

[3] J. F. Barrenechea, F. J. Luque, D. Millward, L. Ortega, O. Beyssac, and M. Rodas. Graphite morphologies from the Borrowdale deposit (NW England, UK): Raman and SIMS data. *Contributions to Mineralogy and Petrology*, 158(1):37–51, 2009. ISSN 00107999. doi: 10.1007/s00410-008-0369-y.

[4] L C Blackman, G Saunders, and A R Ubbelohde. Defect structure and properties of pyrolytic carbons. *Proceedings of the Royal Society of London. Series A. Mathematical and Physical Sciences*, 264(1316):19–40, 1961. ISSN 0080-4630. doi: 10.1098/rspa.1961.0183.

[5] T.H. BLAKELEY. the Gasification of Carbon in Carbon Dioxide and Other Gases At Temperatures Above 900°C. *Carbon*, 4th Editio:95–105, 1960. doi: 10.1016/b978-1-4831-9835-4.50017-3.

[6] J. C. Bokros. The structure of pyrolytic carbon deposited in a fluidized bed. *Carbon*, 3(1): 17–29, 1965. ISSN 00086223. doi: 10.1016/0008-6223(65)90023-0.

[7] Qingyun Chen and Greg M. Swain. Structural characterization, electrochemical reactivity, and response stability of hydrogenated glassy carbon electrodes. *Langmuir*, 14(24):7017–7026, 1998. ISSN 07437463. doi: 10.1021/la980907z.

[8] X. Chu and L. D. Schmidt. Reactions of NO, O2, H2O, and CO2 with the basal plane of graphite. *Surface Science*, 268(1-3):325–332, 1992. ISSN 00396028. doi: 10.1016/0039-6028(92)90972-9.

[9] Alec Deslandes, Marek Jasieniak, Mihail Ionescu, Joe G. Shapter, Callie Fairman, J. Jystin Gooding, D. Brynn Hibbert, and Jamie S. Quinton. ToF-SIMS characterisation of methane- and hydrogen-plasma-modified graphite using principal component analysis. *Surface and Interface Analysis*, 41(3):216–224, 2009. ISSN 01422421. doi: 10.1002/sia.3010.

[10] Initial Distribution, I S Limited, F O R Additional, Copies See, and Back Cover. Reactions between Gases and Solids. *Agard*, (32), 1970.

[11] Sabri Ergun. Kinetics of the reaction of carbon dioxide with carbon. *Journal of Physical Chemistry*, 60(4):480–485, 1956. ISSN 00223654. doi: 10.1021/j150538a022.

[12] C. Guéret, F. Billaud, B. Fixari, and P. Le Perchec. Thermal coupling of methane, experimental investigations on coke deposits. *Carbon*, 33(2):159–170, 1995. ISSN 00086223. doi: 10.1016/0008-6223(94)00120-O.

[13] Christophe Guéret, Michel Daroux, and Francis Billaud. Methane pyrolysis: Thermodynamics. *Chemical Engineering Science*, 52(5):815–827, 1997. ISSN 00092509. doi: 10.1016/S0009-2509(96)00444-7.

[14] Muhammad F. Irfan, Muhammad R. Usman, and K. Kusakabe. Coal gasification in CO2 atmosphere and its kinetics since 1948: A brief review. *Energy*, 36(1):12–40, 2011. ISSN 03605442. doi: 10.1016/j.energy.2010.10.034.

[15] R. E.W. Jansson. *Electrochemical reaction engineering*, volume 35. 1980. ISBN 047125424X. doi: 10.1016/0009-2509(80)80138-2.

[16] T. Kreuger, W. P.M. van Swaaij, A. N.R. Bos, and S. R.A. Kersten. Methane decomposition kinetics on unfunctionalized alumina surfaces. *Chemical Engineering Journal*, 427(June 2021):130412, 2022. ISSN 13858947. doi: 10.1016/j.cej.2021.130412. URL `https://doi.org/10.1016/j.cej.2021.130412`.

[17] Milton Levy. Oxidation of pyrolytic graphite in air between 1250° and 1850°F. *Industrial and Engineering Chemistry Product Research and Development*, 1(1):19–23, 1962. ISSN 01964321. doi: 10.1021/i360001a005.

[18] Martin A. Mayers. The Rate of Oxidation of Graphite by Steam. *Journal of the American Chemical Society*, 56(9):1879–1881, 1934. ISSN 15205126. doi: 10.1021/ja01324a015.

[19] Randell Mills, Jayasree Sankar, Paresh Ray, Bala Dhandapani, and Jiliang He. Spectroscopic characterization of the atomic hydrogen energies and densities and carbon species during helium-hydrogen-methane plasma CVD synthesis of diamond films. *Chemistry of Materials*, 15(6):1313–1321, 2003. ISSN 08974756. doi: 10.1021/cm020817m.

[20] Alejandro Molina and Fanor Mondragón. Reactivity of coal gasification with steam and CO 2. *Fuel*, 77(15):1831–1839, 1998. ISSN 00162361. doi: 10.1016/S0016-2361(98)00123-9.

[21] S. M. Oh and Jai Young Lee. A study on the formation of soot in pyrolytic carbon deposited in a tumbling bed and its effects on mechanical properties. *Carbon*, 24(4):411–415, 1986. ISSN 00086223. doi: 10.1016/0008-6223(86)90260-5.

[22] K. Otto, L. Bartosiewicz, and M. Shelef. Catalytic steam gasification of graphite: Effects of calcium, strontium, and barium with and without sulfur. *Carbon*, 17(4):351–357, 1979. ISSN 00086223. doi: 10.1016/0008-6223(79)90008-3.

[23] H. O. Pierson and M. L. Lieberman. The chemical vapor deposition of carbon on carbon fibers. *Carbon*, 13(3):159–166, 1975. ISSN 00086223. doi: 10.1016/0008-6223(75)90226-2.

[24] D. J. Pritchard and D. W. Bacon. Statistical assessment of chemical kinetic models. *Chemical Engineering Science*, 30(5-6):567–574, 1975. ISSN 00092509. doi: 10.1016/0009-2509(75)80028-5.

[25] Daniel E. Rosner and Joseph P. Strakey. High-temperature kinetics of pyrolytic graphite gasification by fluorine atoms and molecules. *Journal of Physical Chemistry*, 77(5):690–699, 1973. ISSN 00223654. doi: 10.1021/j100624a027.

[26] P. Sander. Surface and in-depth analysis of hydrogenated carbon layers on silicon and germanium by mass and electron spectroscopy. *Journal of Vacuum Science & Technology B: Microelectronics and Nanometer Structures*, 7(3):517, 1989. ISSN 0734211X. doi: 10.1116/1.584778.

[27] Marcio Schwaab and José Carlos Pinto. Optimum reference temperature for reparameterization of the Arrhenius equation. Part 1: Problems involving one kinetic constant. *Chemical Engineering Science*, 62(10):2750–2764, 2007. ISSN 00092509. doi: 10.1016/j.ces.2007.02.020.

[28] Marcio Schwaab, Lívia P. Lemos, and José Carlos Pinto. Optimum reference temperature for reparameterization of the Arrhenius equation. Part 2: Problems involving multiple reparameterizations. *Chemical Engineering Science*, 63(11):2895–2906, 2008. ISSN 00092509. doi: 10.1016/j.ces.2008.03.010.

[29] M. Shelef and P. L. Walker. Transient phenomena in the gasification of graphite by high-purity carbon dioxide. *Carbon*, 5(2):93–105, 1967. ISSN 00086223. doi: 10.1016/0008-6223(67)90063-2.

[30] P. A. Tesner, T. D. Smegiriova, and V. G. Knorre. Kinetics of dispersed carbon formation. *Combustion and Flame*, 17(2):253–260, 1971. ISSN 00102180. doi: 10.1016/S0010-2180(71)80168-2.

[31] Satoshi Umemoto, Shiro Kajitani, and Saburo Hara. Modeling of coal char gasification in coexistence of CO2 and H2O considering sharing of active sites. *Fuel*, 103:14–21, 2013. ISSN 00162361. doi: 10.1016/j.fuel.2011.11.030. URL `http://dx.doi.org/10.1016/j.fuel.2011.11.030`.

[32] John C Vickerman. 1 ToF-SIMS — An Overview. (January), 2016.

[33] O. Vohler, P. L. Reiser, and E. Sperk. Deposition of pyrolytic carbon in the pores of graphite bodies - I. Introduction to and results of deposition experiments using methane. *Carbon*, 6 (3), 1968. ISSN 00086223. doi: 10.1016/0008-6223(68)90035-3.

[34] P. L. Walker, Frank Rusinko, and L. G. Austin. Gas Reactions of Carbon. In *Advances in Catalysis*, volume 11, pages 133–221. Elsevier, 1959. doi: 10.1016/S0360-0564(08)60418-6.

[35] Xin Xiao, Zaiming Chen, and Baoliang Chen. H/C atomic ratio as a smart linkage between pyrolytic temperatures, aromatic clusters and sorption properties of biochars derived from diverse precursory materials. *Scientific Reports*, 6(February):1–13, 2016. ISSN 20452322. doi: 10.1038/srep22644. URL `http://dx.doi.org/10.1038/srep22644`.

[36] Wenjing Xie, Lu Tao Weng, King Lun Yeung, and Chi Ming Chan. Repair of defects created by Ar+ sputtering on graphite surface by annealing as confirmed using ToF-SIMS and XPS. *Surface and Interface Analysis*, 50(9):851–859, 2018. ISSN 10969918. doi: 10.1002/sia.6487.

Appendices

Appendix A - Supplementary data

In this appendix, additional data is presented. In figure A.1 the CO_2 signal obtained in the TGA measurements is presented. It is observed that lower τ_{dec}carbon is gasifed to CO_2 at a lower temperature than higher τ_{dec}carbon. This onset temperature of gasification can be seen as a reactivity indicator. A lower gasification onset temperature indicates that a material is more prone to gasification. This is in good agreement with the other results presented in this work. In figures A.1 and A.2 additional TGA results are presented. Figure A.2 shows that the sample aged under

nitrogen for 1200 s has a comparable oxidation curve as the original 600 s sample. Figure A.1 shows the effect of T_{dec}. Both of these trends are observed in the SIMS section, hence the TGA data is included here, for reference.

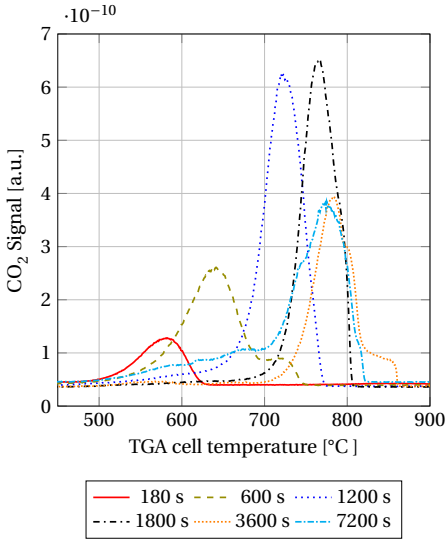

Figure A.1: Obtained CO_2 signal of QMS as function of TGA temperature. Several τ_{dec}. T_{dec}= 1100 °C.

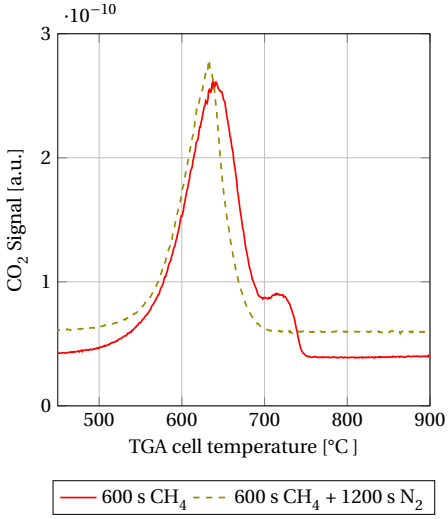

Figure A.2: Obtained CO_2 signal of QMS as function of TGA temperature. Several τ_{dec}. T_{dec}= 1100 °C.

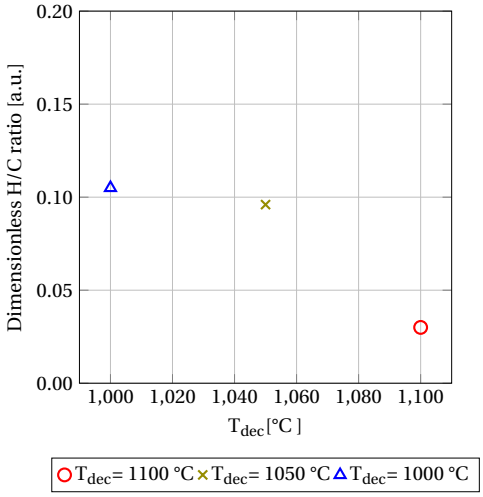

Figure A.3: Measured dimensionless H/C ratio as function of decomposition temperature. $\tau_{dec}$was 1800 s for all samples.

In figures A.4 - A.8 additional gasification data is presented. The trends observed and discussed in the main text are partially visible here, as not all datasets have been expanded sufficiently. Note that all this data has been used in the kinetics section. Since no further knowledge could be gained from these plots, they were included in the appendix for further reference.

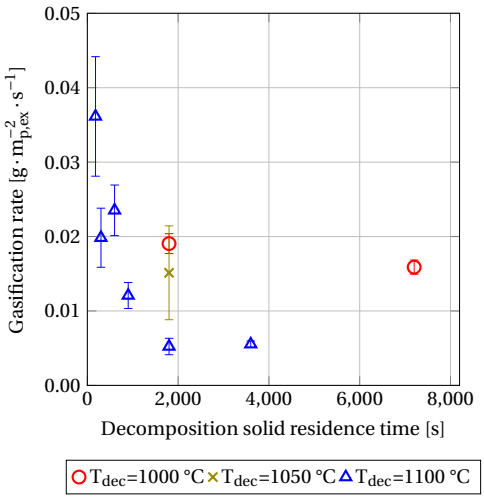

Figure A.4: Measured steam gasification rate in the single particle reactor, T_{gas}=1050 °C, various decomposition T, particle A

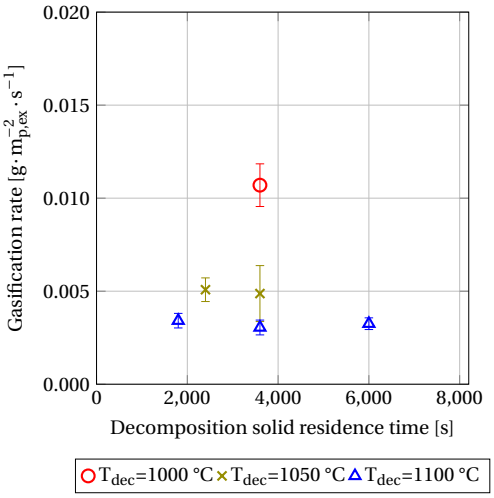

Figure A.5: Measured steam gasification rate in the single particle reactor, T_{gas}=1000 °C, various decomposition T, particle A

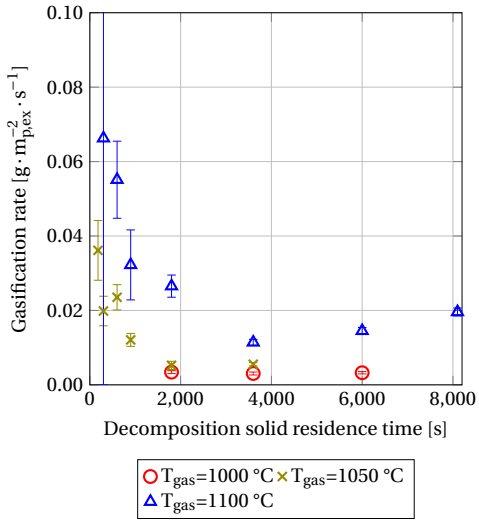

Figure A.6: Measured steam gasification rate in the single particle reactor, T_{dec}= 1100°C, various gasification T, particle A

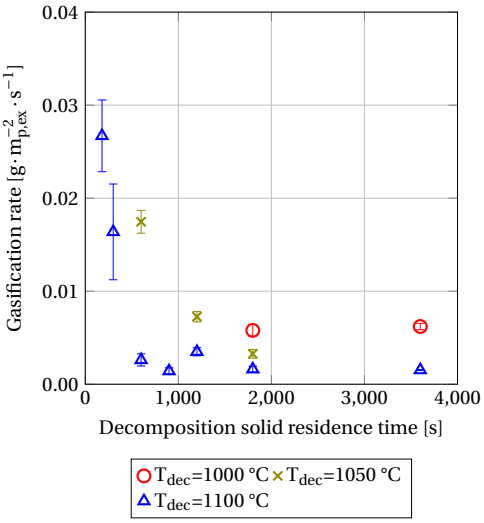

Figure A.7: Measured CO_2 gasification rate in the single particle reactor, T_{gas}=1050 °C, various decomposition T, particle A

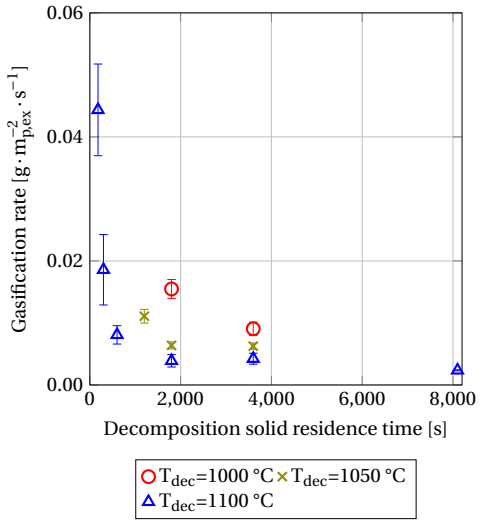

Figure A.8: Measured CO_2 gasification rate in the single particle reactor, T_{gas}=1100 °C, various decomposition T, particle A

In figure A.9 gasification data for a porous particle is included. τ_{dec}has been varied. It is observed that a strongly comparable trend in gasification rate exists for this porous particle, when compared to the nonporous particle. This result indicates that the measured trends in gasification rate are not caused by some particle characteristic but rather by characteristics of the carbon deposited.

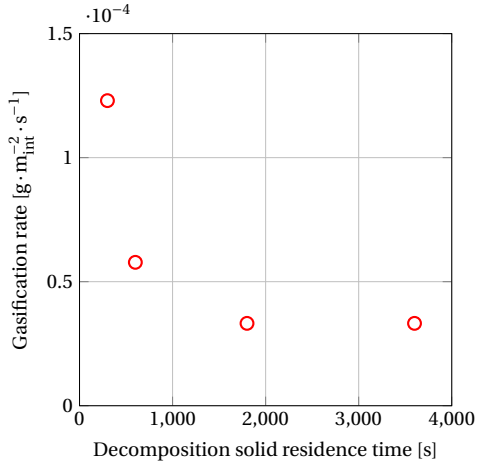

Figure A.9: Measured steam gasification rate in the single particle reactor, T_{gas}=1050 °C, various decomposition T, porous particle B

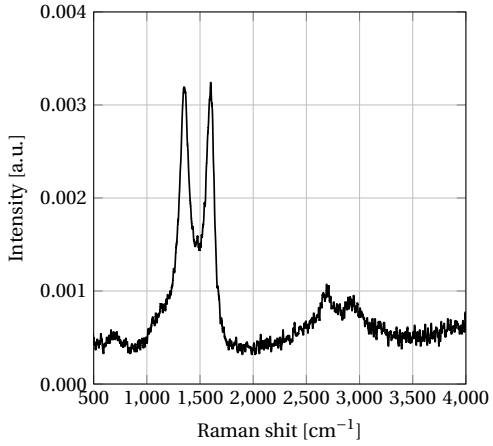

Figure A.10: Obtained raman spectrum of deposited carbon, T_{dec}=1100 °C, τ_{dec}=7200 s.

In figure A.10 an obatained raman spectrum is presented. From this spectrum it may be concluded that the carbon is graphitic in nature. This data has been included for completeness. It soon was found that various other techniques were more suitable for our purposes, hence raman was not pursued further.

A set of particles coated with carbon under identical conditions as the SIMS set was analyzed in a TGA-QMS. The peak temperature, defined as the TGA cell temperature where mass loss over time is fastest, is presented in figure A.11. For the samples with τ_{dec}below 3600 s the peak temperature increases with τ_{dec}. At higher $\tau_{dec}$the peak temperature occurs at approximately the same cell

temperature.

It is noted that the behaviour of peak temperature shows similarities to the H/C ratio measured in the SIMS. This is explained by the identical pyrolysis conditions under which these particles were treated, which in turn yields identical carbon between the two sets.

A sample was prepared by depositing carbon at 1100 °C for 600 s. After this, this sample was kept in the single particle reactor at 1100 °C under nitrogen for 1200 s. It was aimed to investigate whether this particle has characteristics of a 600 s carbon or 1800 s carbon. In figure A.11 this datapoint shows strong similarities to the 600 s sample. The 1200 s spent at 1100 °C under nitrogen did not affect the gasification behaviour of the sample. Therefore, it is concluded that the degree of graphitization is not an effect of temperature and residence time only. It is speculated that the material needs to be contacted with gaseous hydrocarbons in order to exchange H and C atoms, and become more graphitic. An identical observation was made in section 3.3.3 and in the gasification section.

A total of 10 species (2, 4, 14, 16, 17, 18, 28, 32, 40 and 44 u) were traced in the QMS. No species other than CO_2 (44) were detected in significant quantities. It is speculated that the effects of surface adsorbents and general noise on the signal were of a same order of magnitude as the H_2 and H_2O signals, as some difference over time was observed for these signals. This means that the total amount of hydrogen in the carbon must be extremely low. This is in line with the observation that the carbon deposited is graphitic and the results of the SIMS analysis. Note that SIMS is significantly more suitable to detect elements present in low concentrations, and can therefore detect hydrogen in these samples.

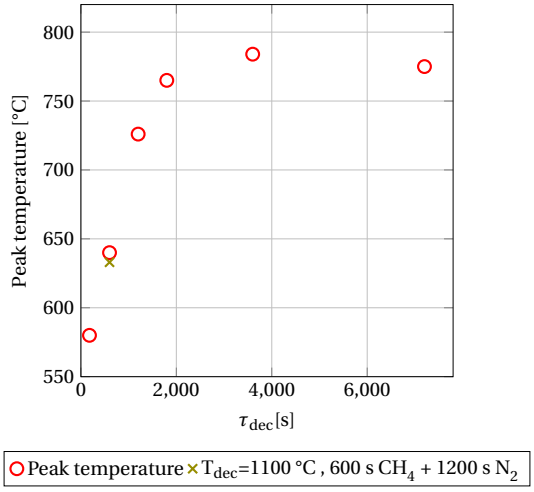

Figure A.11: Measured peak oxidation temperature as function of τ_{dec}, T_{dec}=1100 °C, Particle A.

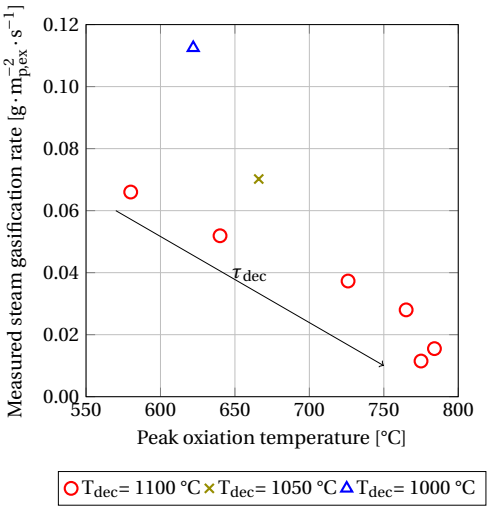

Figure A.12: Measured steam gasification rate as function of measured peak temperature. Various $\tau_{dec}$and T_{dec}, particle A.

In figure A.12 the relation between measured peak temperature and measured steam gasification rate is presented. Three series are shown. Between the series, the decomposition temperature is the varied parameter. For the 1100 °C series, the decomposition solids residence time has been varied. Several observations are made.

For part of the T_{dec}=1100 °Cseries, a crude relation between peak oxidation temperature and gasification rate is observed. A higher oxidation temperature corresponds to a slower steam gasification rate. It can be expected as higher peak oxidation temperature materials are more stable and thus gasify slower. This statement is not universally true. Where the peak oxidation temperature has a maximum around 780 °C the steam gasification rate still decreases.

For the series measured at T_{dec}= 1000 and 1050 °C, a different dependence is found. The lower temperature measurements clearly differ from the 1100 °C series. Therefore it can be concluded that the peak oxidation temperature is not an independent variable related to gasification behaviour.

In the single particle reactor, using air as oxygen source, it was confirmed that during oxygen gasification no effect of $\tau_{dec}$and T_{dec}could be observed. In figure A.11 a clear effect of both $\tau_{dec}$and T_{dec}can be seen. The TGA is able to measure much more accurate than the single particle reactor. Adding to this, the lowest temperature tested in the single particle reactor was 900 °C, making the gasification rates in the single particle reactor much higher, and the timescales much shorter, compared to the TGA. It therefore stands to reason that the effects of $\tau_{dec}$and $T_{dec}$are not observable in the single particle reactor, or more general, when oxygen is used as oxidant at high temperature.

As an improvement, it might be worthwhile to repeat the TGA test, using steam instead of oxygen. We know from this work that steam does show these effects, and may therefore have a peak oxidation rate useful for incorporation in a kinetic model.

Appendix B: Constraints on measuring low T_{dec}, low τ_{dec} carbon

As stated in the experimental method, the carbon mass fraction and gasification rates are obtained via a mass change of the particle. The used balance had a sensitivity of 10 µg. The gasification rate was also calculated from data obtained using this balance. To accurately measure the gasification rate, one could not completely remove all carbon from the particle. The demand that some carbon should remain on the particle after gasification measurements increased the minimum amount of deposited carbon that is required for a reproducible measurement. It was found that 40 to 50 µg of initially deposited carbon were required, at minimum.

Adding to this, in previous work it was reported that the deposition of carbon did not start immediately after a particle was contacted with methane. Especially at temperatures below 1100 °C, an induction period ranging into the thousands of seconds was observed[16]. This prevents measuring of short solids residence time carbon at lower temperature, as none is deposited at this time. In figure B.1 the minimum τ_{dec} (to deposit 10 µg of carbon) and the preferred τ_{dec} (to deposit 40 µg of carbon) is presented as function of the used T_{dec}. Simply put, measuring at τ_{dec} below the black line is not possible using our current experimental method.

These two phenomena are also the reason a relatively large error is present for the shorter τ_{dec} measurements throughout this work.

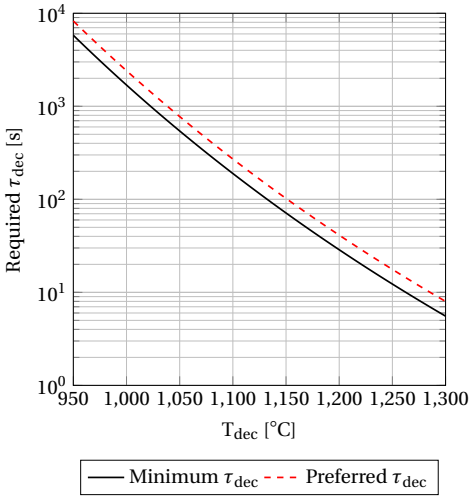

Figure B.1: Minimum and preferred τ_{dec} as function of T_{dec} for a possible gasification measurement. Minimum is defined as time to deposit 10 µg of carbon. Preferred is defined as time to deposit 40 µg

Appendix C: Energy balance calculation

In this appendix it is shown that the gasification reactions are not heat transfer limited. It is experimentally verified that the gas has heated up to set point temperature by the time it reached the particle. Therefore no energy is exchanged between particle and gas, when the particle is also

at this temperature. The method used is identical to the energy balance calculation in[16]. The energy balance is given by:

$$F_{1,2}\epsilon\sigma(T_{HE}^4 - T_p^4) = R_{dec}\Delta H_{dec}[\mathrm{W}\cdot\mathrm{m}^{-2}] \tag{B.14}$$

In which $F_{1,2}$ is the view factor (1 for a particle suspended in a significantly longer tube), ϵ the emissivity of alumina, σ the Stefan-Boltzmann constant, T_{HE} the heating element temperature in K, T_p the particle temperature in K, R_{dec} the methane decomposition rate in $\mathrm{mol}\cdot\mathrm{m}_{\mathrm{p,ex}}^{-2}$ and ΔH_{dec} the reaction enthalpy of the decomposition reaction.

Solving this equation for the highest steam and CO_2 gasification rate measured yields temperature differences of 4 and 0.8 K, respectively. This is smaller than the accuracy of the thermocouple and can therefore be ignored.

4 The deposition of carbon on porous media

Table 4.1: Symbol list for chapter 4

Symbol	Description	Unit
ρ	Density	$kg \cdot m^{-3}$
C	Concentration	$mol \cdot m^{-3}$
C	Loading	$g \cdot m^{-2}$
t	Time	s
R_x	Reaction rate x	
k	Rate constant	
Ea	Activation energy	$kJ \cdot mol^{-1}$
T	Temperature	K
R	Gas constant	$J \cdot mol^{-1} \cdot K^{-1}$
D	Diameter, Diffusion coefficient	m,$m^2 \cdot s^{-1}$
A	Surface area	m^2
τ	Residence time	s
F	View factor	
ΔH_r	Reaction enthalpy	$J \cdot mol^{-1}$
ϵ	Emissivity	
ω	Stefan-Boltzmann constant	$J \cdot m^{-2} \cdot K^{-4}$
U	Heat transfer coefficient	$W \cdot m^{-2} \cdot K^{-1}$
r	Radius	m
u	Molar mass, Superficial velocity	$g \cdot mol^{-1}$,$m^3 \cdot m^{-2} \cdot s^{-1}$
χ	Fraction of volume filled	
β	Dampening factor	

Abbr.	Description	Unit
Abbr.	Abbreviation	
ID	Inner diameter	m
OD	Outer diameter	m
TOS	Time on stream	s
SPR	Single particle reactor	
C	Carbon	

Subscript	Description
p	Particle, Product
M	Methane
ex	External
0	Initial
dec	Decomposition, Pyrolysis
mod	Model
exp	Experimental
int	Internal
gas	Gas, Gasification
tot	Total
eff	Effective
Δ	Difference
avg	Average
b	Bulk
ox	Oxidant
∞	Infinite (time)

Abstract

The deposition of carbon from methane pyrolysis on various porous media was investigated at 950 - 1100 °C. 7 Types of unfunctionalized carriers were used, with pore sizes varying between 4 nm and 250 μm. Carbon deposition over time was measured in a single particle reactor.

It was found that the porous samples can exhibit both an induction period as well as a gradual stop in carbon deposition. An induction period was observed for α-Al_2O_3 samples, but not for γ-Al_2O_3 , SiC and C carriers. Hence, the slow start of the carbon deposition may be caused by substrate material.

Furthermore, for all samples, an apparent maximum carbon loading was observed. It was confirmed that this is not caused by pore blockage, as significant surface area remains in these samples at the point of maximum carbon loading. In fact, it was found that fraction of pore volume filled at maximum loading, is a function of the initial pore diameter. The smaller pores fill to a lesser extent than the bigger pores.

This maximum achievable carbon fraction was incorporated in a particle model. Using only the fraction of volume filled as a single parameter, the measured loading over time could be described.

4.1 Introduction

This chapter presents our efforts to study carbon deposition from methane pyrolysis in various porous media. In previous work, kinetics describing carbon deposition for a single nonporous α-Al_2O_3 were presented. In this work, it is aimed to create understanding of the process of carbon deposition in porous media, and what information is required to make predictions on carbon deposition.

Work regarding carbon deposition in or on various porous media has been published[1, 2, 6, 7, 10, 11, 13–16]. It is reported that the initial decomposition rate is related to surface area, and the concentration of high energy groups such as defects and various oxygenated groups, and that the amount of carbon that can be deposited before carbon deposition stops is dependent on pore volume, pore size, pore area and surface groups[1, 10, 11, 13, 15]. It is found that the initial pore volume scales with the amount of carbon that can be deposited[15].

In previous work[8, 9] decomposition and gasification kinetics were obtained for a nonporous $\alpha-Al_2O_3$ carrier. This work can be seen as a continuation of this work, where the obtained kinetics are expanded to various porous media. It was concluded that porous particles may result in a larger vollumetric reaction rate [$mol_c \cdot m_r^{-3} \cdot s^{-1}$], due to the larger amount of area present[8]. Hence, porous media are investigated in this work.

It was found that the deposition of carbon on a nonporous surface is a nonlinear process[8]. After first contacting a nonporous α-Al_2O_3 particle with methane, an induction period was observed. During this period, no carbon was deposited on the particle, however methane was being converted to gaseous intermediates. After some time, carbon deposition started, at this point the net production of gaseous intermediates greatly reduced and the selectivity towards solid carbon became 1. Additionally a temperature dependent maximum carbon loading (unit: $g \cdot m_{p,ex}^{-2}$) was observed. When this carbon loading was approached, carbon deposition and methane conversion to gaseous intermediates ceased. These phenomena were described mathematically but not fully understood. In this work, it is aimed to gather more insight into both the observed phenomena via testing of a larger variety in particle types and materials. The various materials might exhibit different behaviour in terms of these phenomena, hopefully yielding additional insight.

Various particle characteristics were measured and related to the activity during CH_4 pyrolysis. A kinetic model was developed, taking into account these particle characteristics.

4.2 Materials and methods

The experimental method developed in earlier work for nonporous particles is able to test porous particles as well[8]. This experimental setup and experimental method were slightly adapted for this work, but furthermore remain unchanged. For brevity, only the adaptions are presented here. In total, two modifications were made; first, an increased diameter of the single particle reactor, to accommodate the larger particles used in this work. Second, the linear gas speed was increased to ensure the larger particles could be kept inside the cone. The modifications are presented in table 4.2. No further adaptions were made to setup or method.

Table 4.2: Overview of changed parameters in experimental setup

	Nonporous work[8]	This work	
Superficial gas velocity	16	19	$m \cdot s^{-1}$
Methane flow	1.6-1.8	11-15	$NL \cdot min^{-1}$
Inner cone diameter, bottom	3	8	mm

Note that the density of the used particles is significantly lower than the nonporous particles, hence the linear gas velocity does not increase by a lot.

A selection of porous particles was procured. These 7 types were selected, to create a set spanning large pore sizes (5 orders of magnitude). Moreover, several material types (α- and $\gamma-Al_2O_3$, SiC and C) were included. Two sets with comparable internal characteristics but varying radii were also included. Lastly, 1 particle type with a trimodal pore volume distribution was included. Complete specifications of the used particles and their characteristics is presented in table 4.3.

The Al_2O_3 samples were purchased at NORPRO - Saint-Gobain, the SiC and C samples were purchased from SICAT. All particles were used as received. Nitrogen (99.999%) was supplied by Nippon gases. Methane (99.99%), was supplied by Linde. All gasses in this work were used as received. Physisorption measurements were performed on a Micrometrics Gemini VII.

Table 4.3: Overview of used particles in this work. ^{a} trimodal pore volume, ^{b} cylindrical particles, ^{c} spherical particles, ^{d} average

Name	SA5262	SA52124	SA6273	CE2	CE3	SiC E2	SiC E3
Material	α-Al_2O_3	α-Al_2O_3	γ-Al_2O_3	C	C	SiC	SiC
Surface area, $m^2 \cdot kg^{-1}$	0.75	6.7	200	171	166	27.7	26.2
Pore volume, $cm^3 \cdot g^{-1}$	0.53	0.3	0.6	0.23	0.24	0.19	0.18
Pore size, µm	$1/10/250^a$	0.15	0.007	0.004^d	0.004^d	0.027^d	0.028^d
Part. Diameter, m	0.0048^c	0.0052^c	0.003^c	0.002^b	0.003^b	0.002^b	0.003^b

It is known that γ-Al_2O_3 is thermodynamically unstable at elevated temperatures. To test the applicability of γ-Al_2O_3 for these experiments, a γ-Al_2O_3 SA6723 sample was contacted with nitrogen at 1100 °C for 18 h. By measuring pore area and volume, before and after this test, it was confirmed that this sample did not loose significant area or pore volume during this time. Hence, it is assumed that for all measurements presented in this work, no area or volume is lost. All measurements in this work had high temperature contact times significantly less than 18 h.

Reproducibility of experiments

To test reproducibility of experiments, 5 particles of each type were selected at random. Under equal conditions, the particles were loaded with carbon in the SPR. It was found that a spread in loading of approximately 10% exists between particles of the same type. A similar observation was made for nonporous particles. To accurately estimate error margins, on these samples each particle type was tested at minimum 9 times in the SPR, and averaged.

A SA5262 sample was subjected to multiple carbon deposition cycles, by removing the carbon using air in the SPR. Over these repetitions, the deviation in this set was approximately 3%. Two conclusions are drawn. It is concluded that the variation on the measured carbon loading in the set of 5 random particles is a result of some particle characteristic. Secondly it is concluded that the carbon loading measurements are reproducible.

For each physisorption measurement, a large number of particles was required. Hence, the spread of these samples caused by variations between individual particles is expected to be small. Here, a duplo was also tested. The relative difference in pore volume was 3%.

4.3 Results and discussion

4.3.1 Carbon deposition

Carbon deposition on a SA6723 γ-Al_2O_3 particle is presented in figure 4.1. This is a particle with a 7 nm average pore size. It is observed that the loading curves of this particle have a slightly different shape than the nonporous data [8]. Most notably, the induction period is absent. This is also discussed further in section 4.3.2, as this is also observed for other particles. It is further observed that the carbon loading seems to cease when a certain loading is reached, analogue to the nonporous data. It is yet unknown whether this is due to pore blockage or due to other effects. This is reported further upon in section 4.3.2. Furthermore, it is noted that the absolute amount of carbon deposited on these porous particles is one order of magnitude higher than the highest obtained loading on nonporous particles. To illustrate this, a data set of nonporous measurements performed in the SPR at 1050 °C is included in figure 4.1. The increased loading is a result of the internal area.

Carbon deposition curves measured at various temperatures are presented in figure 4.2 for particle type SA5262. This is a particle with a trimodal pore size distribution. It is observed that the shape of the loading curve shows some interesting characteristics. First, the data shows an induction period (most significantly for the lower temperature), as was observed in earlier work[8]. At the end of the curve, one does not observe a clear stop in mass increase. Instead, a change of slope is observed, most notable for the 1050 and 1000 °C series. This is deviation from the observations in previous chapters as well as data in this chapter. In section 4.4 it is shown that this is a result of the trimodal pore size distribution combined with the orders of magnitude larger pores present in this particle.

Comparing the carbon deposition rate of the porous particles to nonporous data under equal conditions yields a factor 10 higher productivity ($kg_C \cdot m_r^{-3} \cdot s^{-1}$) for the SA5262 particle. Hence, it is concluded that the utilization of porous particles is beneficial for the productivity of a decomposition reactor.

Looking at the data in figures 4.1 and 4.2, it is noted that the overall shapes show strong similarities with the nonporous data. Some slight differences are noted, but the overall characteristics are comparable. From this data alone it is not possible to conclude anything with respect to the effect of the internal characteristics of the particle on the deposition, Hence, further investigation is presented in the next section.

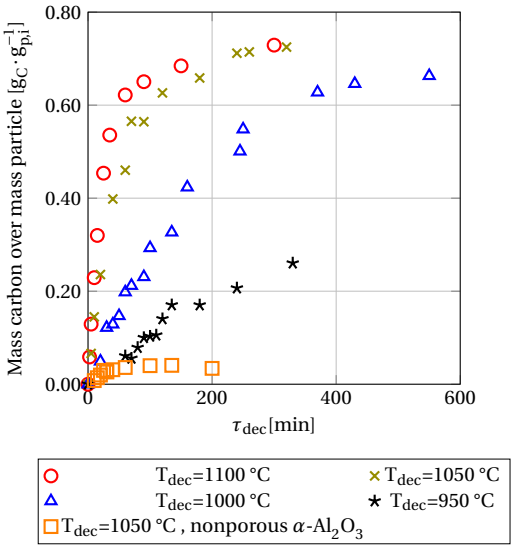

Figure 4.1: Measured mass of carbon over mass particle as function of τ_{dec}in the single particle reactor, various T_{dec}, particle SA6723. Nonporous data (particle A) measured under equal conditions, taken from [8]

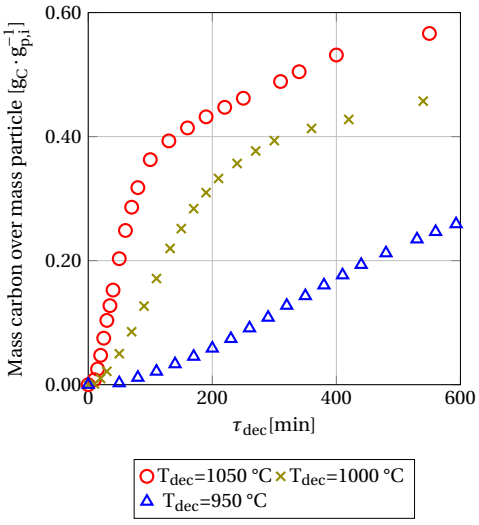

Figure 4.2: Measured mass of carbon over mass particle as function of τ_{dec}in the single particle reactor, various T_{dec}, particle SA5262

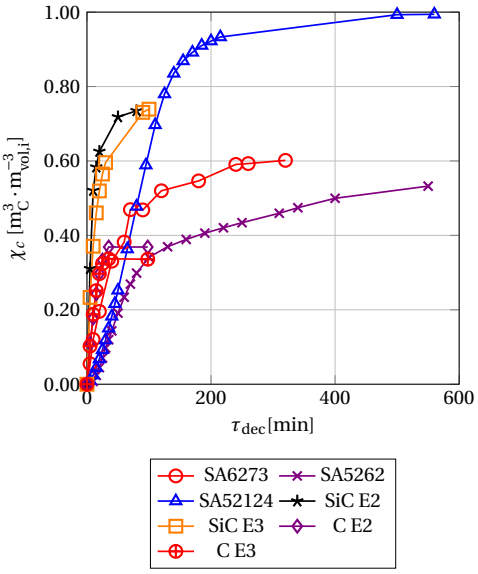

Figure 4.3: Measured carbon loading of τ_{dec}in the single particle reactor, T_{dec}=1050 °C , various particles

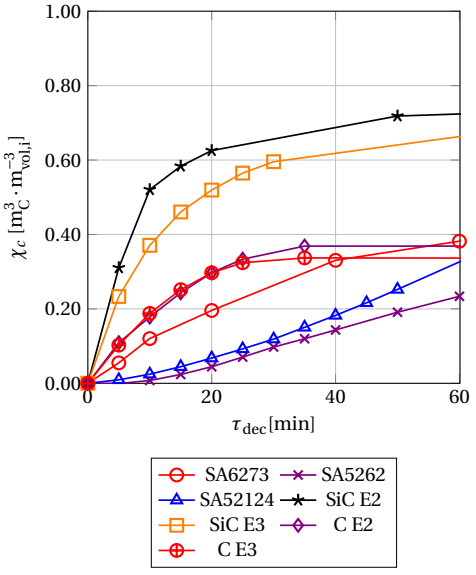

Figure 4.4: Measured carbon loading of τ_{dec}in the single particle reactor, T_{dec}=1050 °C , various particles

4.3.2 Internal particle characteristics

To be able to compare between particles with varying characteristics (diameter, density, pore-volume, -radius and -area), a suitable unit of measurement is required. In this work, the fraction of initial volume filled with deposited material, χ_c (unit $m_C^3 \cdot m_{vol,i}^{-3}$) is used. This parameter is the ratio of pore volume filled with carbon V_c over the initial pore volume $V_{p,i}$:

$$\chi_c = \frac{V_c}{V_{p,i}} = \frac{V_{p,i} - V_{p,t}}{V_{p,i}} = \frac{m_c \rho_c}{V_{p,i}} \tag{4.1}$$

Two pathways to obtain $\chi_c$are available, either via volume or mass measurement. The former can be measured directly using gas physisorption via the pore volume before and after carbon deposition, the reduction in volume is attributed to the deposited carbon. It is noted that measurement of the volume via physisorption measurement is not applicable when the pores are blocked, as the true remaining pore volume cannot be measured in this case. The second pathway, via mass measurement of the deposited carbon can be related to the carbon volume via the density of pyrolytic graphite[3, 4, 17].

In figure 4.3, $\chi_c$over time is presented for various particles at a deposition temperature of 1050 °C. Figure 4 shows the same data, enlarging the initial 60 minutes. Several observations are presented. First, the initial part of the loading curves have different shapes. As was already noted before, for γ-Al_2O_3 the induction period is not present, we now show that it is also not present for the SiC and C carriers. It is therefore concluded that the induction period is, at least, partially dependent on the substrate material. More high energy sites present on the surface of the material, might help overcome the activation energy of carbon deposition. This is also noted in literature[10, 15], where it was concluded that the initial rate is dependent on the surface concentration of oxygenated groups in a carbonaceous carrier.

On the end of the curve, all samples show an eventual stop of carbon deposition. It is noted that the pair of SiC and the pair of C samples approach comparable carbon loadings. These pairs have, next to the same substrate material, comparable pore size (distribution) and total pore volume. One of these or a combination of these parameters affects the final fraction of volume filled. It is concluded that the substrate material is not affecting the final loading, as the α-Al_2O_3 (samples SA52124 and SA5262) have different final loadings, evident from figure 4.3. Note that this is not directly visible in figure 4.5, as the trimodal particle does not have a known value for $\chi_{c,\infty}$ for each of the pore sizes present in this trimodal particle.

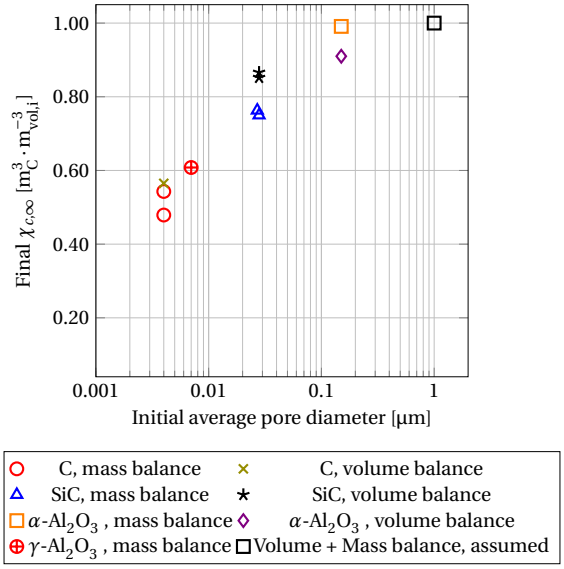

Figure 4.5: Obtained χ_c at maximum loading, data from figure 4.3, T_{dec}=1050 °C , various particles

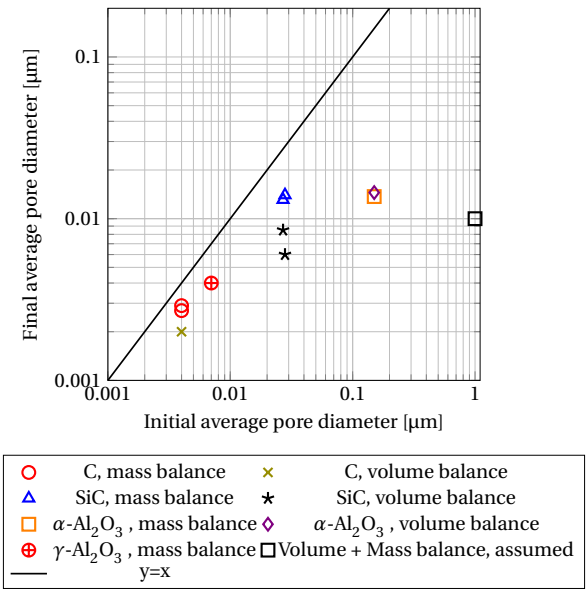

Figure 4.6: Measured and calculated final pore size over initial pore size, evaluated at maximum carbon loading, data from figure 4.3, T_{dec}=1050 °C , various particles

In figure 4.5 the final fraction of pore volume filled with carbon at a deposition temperature of 1050 °C is plotted over the initial pore diameter. A clear trend is observed: the smaller pores are only fractionally filled, at maximum loading. The larger pores are filled almost completely. The trimodal particle (SA5262) was excluded from this graph, as for this particle, no accurate data is available on internal characteristics after carbon deposition. These larger pores were unable to be measured in the available physisorption apparatus, and hence the value of $\chi_c$cannot be calculated.

Another important observation is that the calculation of $\chi_c$using the mass increase yields comparable results to calculation of $\chi_c$via physisorption measurements. This means that the pore volume after carbon deposition is still available (reachable) for the physisorption gas. Hence, no significant pore blockage could have occurred in any of the particles.

Moreover, this means that internal area is still available for the carbon to be deposited on. All these samples were kept in the reactor for extended periods of time (figure 4.3), confirming that carbon deposition had (very nearly) ceased. For the SA52124, SA6723, CE2 and CE3 samples it was confirmed carbon deposition had completely ceased by keeping the particle in the reactor overnight. No additional mass was deposited during this time. Hence, carbon deposition stopped, while area was still available. This identical observation was made for nonporous particles[8].

The exact mechanism for this stop in carbon deposition is not known. It was previously speculated that this is related to the surface roughness of the material[8]. For the porous particles, this could also be the case for the larger pores. If a (sufficiently) smooth layer of carbon is deposited it might become impossible for new carbon to be deposited. It was measured (figure 4.6) that the smaller pores get reduced to approximately 2 nm. For these smaller pores, another reason for the stop in deposition may be plausible. If the carbonaceous intermediate is sterically hindered by the pore wall, this intermediate will not be able to form or penetrate the pores, and carbon deposition will cease. Although the exact size of a polyaromatic intermediate that is eventually deposited is not known, intermediates ranging the the order of a nanometer are possible[6]. Hence, it is speculated that carbon deposition from these intermediates in small pores will be slow.

In figure 4.7 the obtained pore volume distribution for a SiC sample is presented. It is noted that the initial pore size has a relatively wide distribution ranging between 20 and 100 nm. The average measured diameter is 27 nm. After depositing carbon, the pore volume in the bigger pores decreases. For the smaller pores the pore volume increases. This is explained via the deposition of carbon, decreasing the diameter of the pores, thereby increasing the number of smaller pores and the total volume of this diameter. For the SiC sample, it is noted that the final pore distribution approaches a monomodal distribution. Hence, all pores get reduced to a similar final size. It is concluded that the final pore size is a function of the initial pore size.

The trimodal particle was also analyzed. From mass increase measurements (figure 4.3) it followed that approximately 50% of the total initial available volume of this particle is filled with C, at maximum loading. From the pore volume measurements, it follows that at least some pores are reduced to the nm scale, this is presented in appendix A. By combination of these two experimental observations, it is assumed that the smaller pores are filled completely. This is in line with the trend observed in figure 4.3, but still an assumption. From the mass and volume balance, it then follows that the larger pores are filled to a much lower extent. This is supported as follows: from a certain pore size, the inner pore surface on the molecule length scale is essentially flat. Hence, for these pores, the carbon deposition should be described by the external surface carbon deposition kinetics. It is known that carbon deposition on these surfaces stops relatively quickly and hence, the pores do not fill to a large extent.

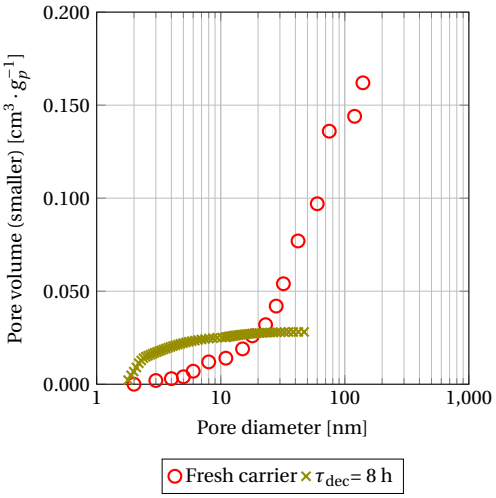

Figure 4.7: Measured pore volume, SiC2 carrier. µm

4.3.3 Modelling results

In this work, it is aimed to create understanding of the process of carbon deposition in porous media, and what information is required to make predictions on carbon deposition. Instead, a combined experimental and modelling approach, focusing on the porous characteristics is presented. Ideally, one is able to make predictions on the behaviour of a particle type without the need for a large amount of experiments.

First, it is emphasised that no mass transfer limitations are present. From experimental data, this was also concluded. At no time could a radial gradient in carbon be detected . Moreover, when two particles with almost identical characteristics (SiC E2 & SiCE3 and CE2 & CE3) but different radii were tested, equal loadings [$g_C \cdot g_{p,i}^{-1}$] were obtained (see figure 4.3), this can only be expected when internal (and external) limitations are absent. A complete particle model was developed. The results of this calculation also indicate that no radial gradients in carbon or in gas phase composition are present. The workings of this detailed model, including the radial particle coordinate, is presented in appendix B of this chapter. A complete analysis of the mass transfer is presented in appendix A of this chapter.

Because of the lack of mass transfer control, a detailed particle model is not required to make accurate predictions of the carbon loading. The absence of internal gradients yield an identical solution to both models. Hence, a model describing the reaction rate over the whole particle at once is presented. The loss of area and volume are taken into account, however.

From the experimental data, several observations are made that need to be incorporated in the porous deposition model for correct predictions:

- The model needs to be able to predict an eventual stop in carbon deposition.
- Smaller pores get filled to a lesser extent than larger pores.

It is known that the deposition of carbon decreases the area available within the particle. This loss of area leads to a decrease in overall carbon deposited within the particle. However, the decrease in area does not explain the stop in carbon deposition. Should the stop in carbon deposition be an effect of area alone, this would mean that the internal area is either completely gone, or completely inaccessible. However, it is known that area is still available, from physisorption measurements. Hence, the stop in carbon deposition is caused by some other phenomena, and needs to be incorporated into the model in some other way. The simplest equation describing carbon deposition is given by:

$$R_{dec} = k_{dec} C_m \beta \tag{4.2}$$

in which β_r is a dampening factor related to χ_c, the fraction of pore volume filled with carbon, on reactor (particle) level this is described by:

$$\beta_r = 1 - \frac{V_c}{V_{c,\infty}} = 1 - \frac{\chi_c(t)}{\chi_{c,\infty}} \tag{4.3}$$

The value of β decreases with carbon loading. Eventually this approaches zero, thereby stopping the carbon deposition. In figure 4.5 the fraction filled volume at (near) infinite residence time is presented. Hence, the parameter $\chi_{c,\infty}$ can be determined experimentally in a single measurement. This kinetic model then uses only 1 fitting parameter to describe carbon deposition on porous media at a certain T_{dec}, being the rate constant k_{dec}. When the model is expanded to other temperatures, this would also add an activation energy.

The experimental and model results are presented in figures 4.8 and 4.9 for the mono-modal samples. A satisfactory agreement between the model and the experimental data is observed for all cases.

It is noted that the induction period of carbon deposition visible in figure 4.8b is not predicted using these simple models. Incorporation of this phenomena would increase the number of parameters. However, from figure 4.8 and 4.9 it is evident that even 1 parameter generally suffices. Depending on the exact prediction and the accuracy required, this 1 parameter approximation may not suffice for this particular case. An expansion of the kinetics analogue to the nonporous kinetics may be able to incorporate this induction period. It is concluded that even a simple model is able to predict carbon loading over time for various nonporous particles spanning a large range of pore sizes and materials.

In figure 4.10 the experimental and detailed particle model data for the trimodal particle is presented. The individual pore contributions are split out over the three pore diameters present in the particle. It is observed that the majority of carbon is deposited in the small pores, this is expected as these hold virtually all of the pore area. The larger pores contain a smaller area, and hence take a long time to fill. This also explains the steady increase in overall loading at long τ_{dec}, not observed for the smaller pored samples. To make a prediction for any particle with multiple pore sizes, the pore volume or pore area distribution needs to be known.

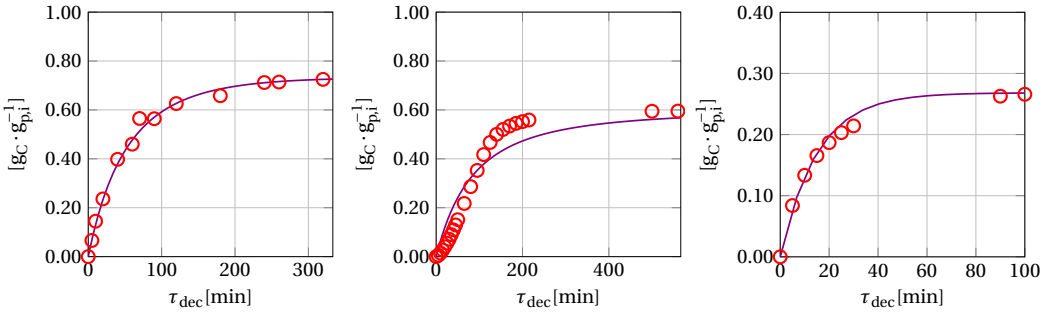

(a) SA6723, γ-Al_2O_3 *(b)* SA52124, α-Al_2O_3 *(c)* SiCE3

Figure 4.8: Experimental (circles), particle model (solid line) and shortcut model (dashed line) loading results, various particles. T_{dec}=1050 °C. Y axis: Mass carbon over initial mass particle.

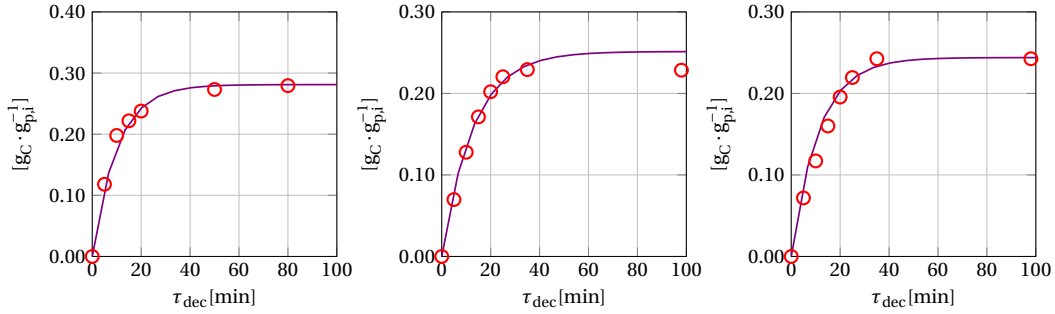

(a) SiCE2 *(b)* CE3 *(c)* CE2

Figure 4.9: Experimental (circles) and particle model (solid line) loading results, various particles. T_{dec}=1050 °C. Y axis unit: mass carbon over initial mass particle.

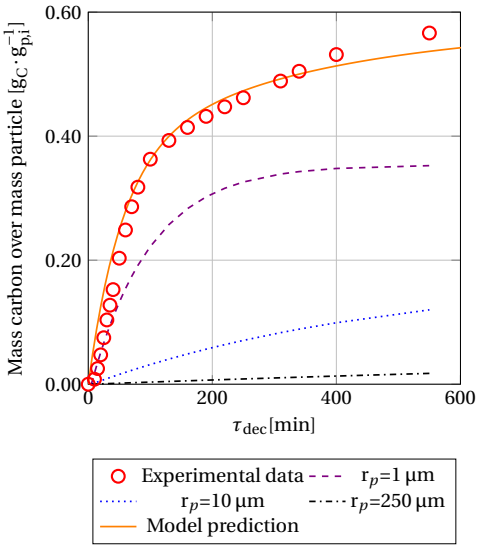

Figure 4.10: Measured carbon loading of τ_{dec}in the single particle reactor, T_{dec}=1050 °C , trimodal particle

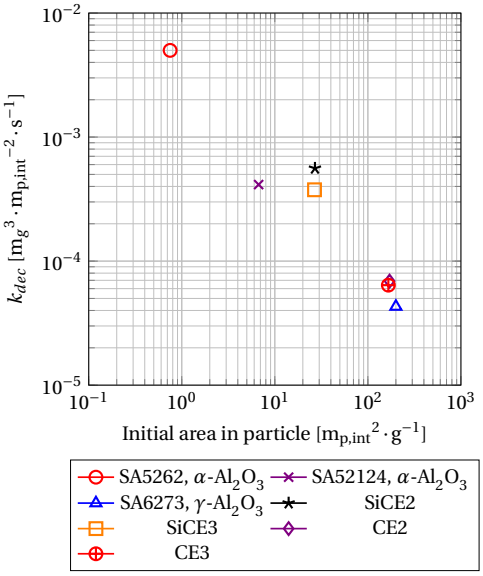

Figure 4.11: Fitted rate constants as function of the initial area present in the particle

In table 4.4 the fitted parameters are presented. The fitted values correlate to the initial particle area, at least to some extent. A larger internal area results in a smaller rate constant, this is

visualized in figure 4.11. It is observed that significant spread still exists in this data. Therefore, the rate constant is not related only to internal area and substrate material. It is speculated that the pore radius itself might affect the rate constant, as well. To investigate this, the studied set of monomodal particle types should be expanded to include more variation in pore sizes per substrate material.

Furthermore, it is noted that the product of the rate constant and initial internal area A_p appears to group, for all the individual materials. The variation in this product, observed within pairs of carrier material is at most 58% (SiC), (α-Al_2O_3 35% and C 12%). Hence, it is speculated that this product may be a characteristic dependent only on substrate material. For this, additional particle types should be evaluated. Should this product be known, one could make a rough prediction of the pyrolysis reaction rate of any particle, without the need to perform experiments.

Table 4.4: Overview of fitted parameters

	k_{dec} [$m_g{}^3 \cdot m_{p,int}{}^{-2} \cdot s^{-1}$]	$k_{dec} \cdot A_p$ [$m_g{}^3 \cdot kg^{-1} \cdot s^{-1}$]
SA5262	$5.00 \cdot 10^{-3}$	$3.75 \cdot 10^{-3}$
SA52124	$4.14 \cdot 10^{-4}$	$2.77 \cdot 10^{-3}$
SA6273	$4.30 \cdot 10^{-5}$	$8.60 \cdot 10^{-3}$
SiCE2	$5.64 \cdot 10^{-4}$	$1.56 \cdot 10^{-2}$
SiCE3	$3.76 \cdot 10^{-4}$	$9.85 \cdot 10^{-3}$
CE2	$6.95 \cdot 10^{-5}$	$1.19 \cdot 10^{-2}$
CE3	$6.41 \cdot 10^{-5}$	$1.06 \cdot 10^{-2}$

4.4 Conclusion

In this work, carbon was deposited from methane in various porous media. It was found that porous media exhibit a maximum achievable loading, and that this is not a result of pore blockage. Moreover, it was found that smaller pores are not filled to the same extent as larger pores. It is speculated that the smaller pores prevent the carbonaceous intermediate from forming in or being transported into the pore. The larger pores might suffer from a deactivation mechanism comparable to nonporous α-Al_2O_3 particles[8].

Various porous materials (C, SiC, α and γ -Al_2O_3) were evaluated. All these show loading curves near identical to the nonporous particles tested earlier. It is therefore concluded that the overall shape of the carbon loading curve over time is not influenced strongly by substrate material or surface morphology. A minor difference is seen in the presence of the induction period. The low energy α-Al_2O_3 exhibits this more strongly than all other materials.

No data supporting internal mass transfer limitations were found, meaning the internal area of the particles can be used efficiently. It is concluded that porous particles are greatly beneficial for processes by increasing vollumetric carbon conversion rates [$mol_c \cdot m_r{}^{-3} \cdot s^{-1}$] up to two orders of magnitude compared to nonporous particles.

A simple particle model was found to adequately predict carbon loading over time. For correct description, knowledge on the particle pore size (distribution) is required. Only a rate constant as fitting parameter sufficed for satisfactory predictions.

Bibliography

[1] J. Ashok, S. Naveen Kumar, A. Venugopal, V. Durga Kumari, S. Tripathi, and M. Subrahmanyam. CO free hydrogen by methane decomposition over activated carbons. *Catalysis Communications*, 9(1):164–169, 1 2008. ISSN 15667367. doi: 10.1016/j.catcom.2007.05.046. URL `https://linkinghub.elsevier.com/retrieve/pii/S1566736707002452`.

[2] Zongqing Bai, Haokan Chen, Baoqing Li, and Wen Li. Catalytic decomposition of methane over activated carbon. *Journal of Analytical and Applied Pyrolysis*, 73(2):335–341, 2005. ISSN 01652370. doi: 10.1016/j.jaap.2005.03.004.

[3] A. R.C. Brown, D. Clark, and J. Eastabrook. Some interesting properties of pyrolytic carbon. *Journal of The Less-Common Metals*, 1(2):94–100, 1959. ISSN 00225088. doi: 10.1016/0022-5088(59)90046-3.

[4] Francis Crick and James Watson. Density of deposited carbon. *Nature*, 1953.

[5] DD Do. *Fundamentals of Diffusion and Adsorption in Porous Media*. Imperial College Press London, 2 edition, 1998. doi: 10.1142/9781860943829{_}0007.

[6] Alan M. Dunker, Sudarshan Kumar, and Patricia A. Mulawa. Production of hydrogen by thermal decomposition of methane in a fluidized-bed reactor - Effects of catalyst, temperature, and residence time. *International Journal of Hydrogen Energy*, 31(4):473–484, 2006. ISSN 03603199. doi: 10.1016/j.ijhydene.2005.04.023.

[7] Ling Han, Tae Ki Lim, Young Jun Kim, Hyun Sik Hahm, and Myung Soo Kim. Hydrogen production by catalytic decomposition of methane over carbon nanofibers. *Materials Science Forum*, 510-511(2):30–33, 2006. ISSN 16629752. doi: 10.4028/0-87849-995-4.30.

[8] T. Kreuger, W. P.M. van Swaaij, A. N.R. Bos, and S. R.A. Kersten. Methane decomposition kinetics on unfunctionalized alumina surfaces. *Chemical Engineering Journal*, 427(June 2021):130412, 2022. ISSN 13858947. doi: 10.1016/j.cej.2021.130412. URL `https://doi.org/10.1016/j.cej.2021.130412`.

[9] Tomas Kreuger, Kersten, S.R.A, and A.N.R. Bos. Predicting gasification rates of pyrolytic graphite deposited from methane. *Chemical Engineering Journal*, 2022.

[10] R Moliner, I Suelves, M J Lázaro, and O Moreno. Thermocatalytic decomposition of methane over activated carbons: influence of textural properties and surface chemistry. *International Journal of Hydrogen Energy*, 30(3):293–300, 2005.

[11] N. Muradov. Catalysis of methane decomposition over elemental carbon. *Catalysis Communications*, 2(3-4):89–94, 2001. ISSN 15667367. doi: 10.1016/S1566-7367(01)00013-9.

[12] Nazim Muradov and others. Thermocatalytic CO2-free production of hydrogen from hydrocarbon fuels. In *Proceedings of the 2000 Hydrogen Program Review, NREL/CP-570-28890*. Citeseer, 2000.

[13] Nazim Muradov, Franklyn Smith, and Ali T-Raissi. Catalytic activity of carbons for methane decomposition reaction. *Catalysis Today*, 102-103:225–233, 2005. ISSN 09205861. doi: 10.1016/j.cattod.2005.02.018.

[14] Nazim Z. Muradov. CO2-free production of hydrogen by catalytic pyrolysis of hydrocarbon fuel. *Energy and Fuels*, 12(1):41–48, 1998. ISSN 08870624. doi: 10.1021/ef9701145.

[15] I. Suelves, J. L. Pinilla, M. J. Lázaro, and R. Moliner. Carbonaceous materials as catalysts for decomposition of methane. *Chemical Engineering Journal*, 140(1-3):432–438, 2008. ISSN 13858947. doi: 10.1016/j.cej.2007.11.014.

[16] O. Vohler, P. L. Reiser, and E. Sperk. Deposition of pyrolytic carbon in the pores of graphite bodies - I. Introduction to and results of deposition experiments using methane. *Carbon*, 6 (3), 1968. ISSN 00086223. doi: 10.1016/0008-6223(68)90035-3.

[17] S. Yajima, T. Satow, and T. Hirai. Microstructure and density of pyrolytic graphite. *Journal of Nuclear Materials*, 17(2):127–135, 1965. ISSN 00223115. doi: 10.1016/0022-3115(65)90029-2.

Appendix A - Supplementary data

Mass transfer analysis

To understand the carbon deposition within porous media, knowledge on mass transfer characteristics are required. From previous work it is known that external mass transfer does not limit the deposition reaction in the case of nonporous media. For this work, the particles are both porous, and significantly bigger, not favouring mass transfer limitations. However, comparing the maximum measured carbon deposition rate ($6\,\mu g_C \cdot s^{-1}$, SiC 2 mm particle) to the calculated maximum flux for this particle (order of $1000\,\mu g_C \cdot s^{-1}$) indicates that the porous media are also not externally mass transfer limited.

The internal mass transfer is equally if not more important. From literature it is known that the effective internal diffusion of a species in porous media is dominated by Knudsen diffusion if the pore diameter is smaller than the mean free path of the species. At 1050 °C, the mean free paths of CH_4 and H_2 are 311 and 811 nm, respectively. Hence, for a large part of the particles studied in this work, the internal diffusion is described by Knudsen diffusion.

Using this, the particle model discussed in appendix B indicates no internal mass transfer limitations. This means that the particle does not have an internal carbon gradient, and that the deposition is described equally well without the internal mass transfer equations. Increasing the carbon deposition rate with a factor 100 does not change this.

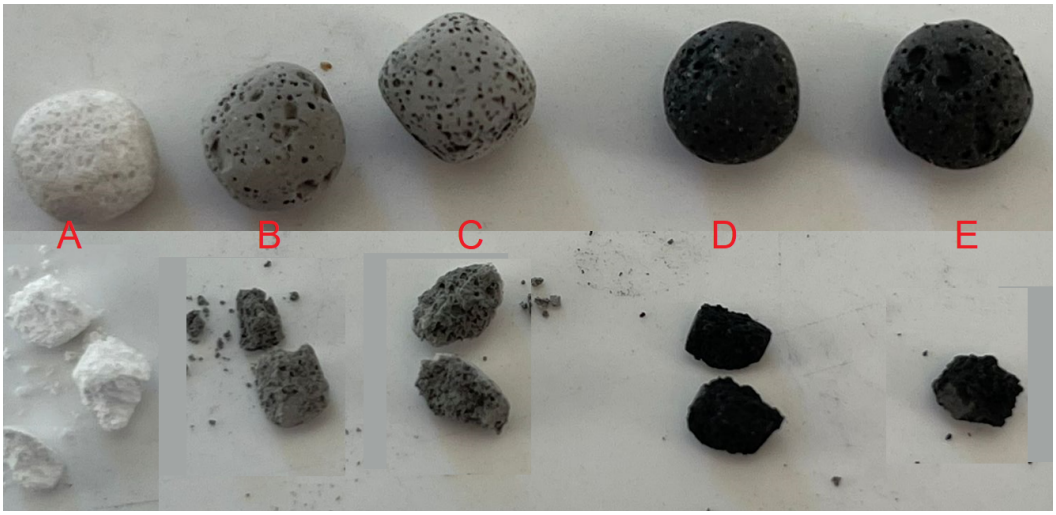

Figure A.1: Photo of particles loaded with carbon from SPR. Top lines: as received. Bottom line: same particles as top, cracked open. Letters denote varying residence times A: 60 s, B: 120 s, C: 180 s, D: 240 s, E: 300 s.

It was also attempted to investigate the internal mass transfer using measurements. Loaded particles at very short τ_{dec}were cracked open to investigate the presence of a carbon gradient along the radial direction, which would be visible as a change in color, this is visualized in figure A.1. It was found that no carbon gradient could be identified in any case. Another measurement supporting an equal carbon loading throughout the radius was performed using gas adsorption. This is discussed in section 4.3.2.

Lastly, two pairs of porous carriers with near identical characteristics were evaluated. The difference within these two pairs was a varying particle diameter. No variation in carbon loading was found within the set. Hence, the change in diameter did not affect the carbon loading per particle volume. This is only possible when no significant mass transfer limitations exist.

All these calculations and measurements support the claim that mass transfer rates do not limit the decomposition reaction of the tested porous particles.

BET data trimodal particle

A large spread (1, 10 and 250 µm exists in the pore diameters present in the SA5262 sample. A BET measurement is presented in figure A.2. For the control (blanco) sample, all these pores fell outside the suitable range for physisorption measurements, and are therefore not visible in the presented results. The carbon loaded samples of this particle do contain (smaller) pores that can be measured. This does not mean that all the pores in this sample get reduced to the measured 1-10 nm size, however. The larger pores could be measured with Hg intrusion measurements, however this unit was unavailable to us.

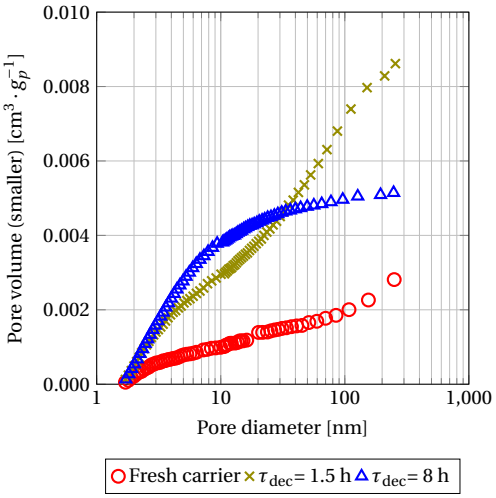

Figure A.2: Measured pore volume, SA5262 trimodal sample. Initial pore sizes 1/10/250 µm

Appendix B: Particle model used in this work

Complete particle model

To accurately predict the behaviour of a porous particle, the internals of the particle should be taken into account. The total pore volume is incorporated into a numerical model. The following parameters are described over radius r time t:

- The mass and/or volume fraction of carbon, unit [$g_C \cdot g_{p,i}^{-1}$ or $m_C^3 \cdot m_{vol,i}^{-3}$]
- The average pore radius, unit [m]
- The gas phase volume fractions
- The local gas pressure [Pa] needs to be incorporated to account for the net production of moles in the pore

Assumptions made:

- The particle characteristics are valid over the complete particle volume.

The mass balance for a gaseous component i over a particle with radius r and J different pore sizes is presented:

$$\frac{\partial\left(C\epsilon_p\right)}{\partial t}4\pi r^2\Delta r = 4\pi\left(J_{in}r^2 - J_{out}(r+\Delta r)^2\right) - \sum_j^J R_{dec}A_{p,j}\rho_p 4\pi r^2\Delta r \tag{B.4}$$

Division by $dV = 4\pi r^2\Delta r$ and taking lim r=0:

$$\frac{\partial\left(C\epsilon_p\right)}{\partial t} = -\frac{1}{r^2}\frac{\partial}{\partial r}\left(J_i r^2\right) - \sum_j^J R_{dec} A_{p,j} \rho_p \tag{B.5}$$

The flux J_i is composed of a diffusional and a convective term:

$$\frac{\partial\left(C\epsilon_p\right)}{\partial t} = \frac{1}{r^2}\frac{\partial}{\partial r}\left(r^2 D_{i,eff}\frac{\partial C_i}{\partial r} + r^2 C_{tot}\frac{B_0}{\mu_g}\frac{\partial P}{\partial r}\right) - \sum_j^J R_{dec} A_{p,j}\rho_p \qquad \left[\mathrm{mol}\cdot \mathrm{m_p}^{-3}\cdot \mathrm{s}^{-1}\right] \tag{B.6}$$

The concentration and void fraction of the particle are solved together, as both are changing over time and place. The concentration can be calculated from this via the total deposited volume.

The term $C_{tot}\frac{B_0}{\mu_g}\frac{\partial P}{\partial r}$ describes the viscous flow caused by the net production of molecules during decomposition[5]. The parameter B_0 characterizes the nonporous medium and is given by:

$$B_0 = \frac{\epsilon_p r_p^2}{8\tau_p} \tag{B.7}$$

The total pore volume occupied by carbon is given by:

$$V_{c,tot} = \int_0^{r_p}\int_0^t R_{dec} M_c \frac{\rho_p}{\rho_c} A_p(r,t)\,dt\,dr \qquad \left[\mathrm{m_c}^3\cdot \mathrm{m_p}^{-3}\right] \tag{B.8}$$

The change in pore diameter can be deducted from this by assuming the carbon is deposited equally along the radial coordinate of each pore. The change in area is given by:

$$A_p(t) = A_{p,0}\frac{r_p(t)}{r_{p,0}} = A_{p,0}\sqrt{1-\chi_c} \tag{B.9}$$

For the reaction rate in this model, the definition of dampening factor β is slightly different, as it needs to be evaluated at each radial coordinate of the particle:

$$\beta_p = 1 - \frac{V_c}{V_{c,\infty}} = 1 - \frac{r_{p,0}^2 - r_{p,t}^2}{r_{p,0}^2 - r_{p,\infty}^2} \tag{B.10}$$

For the Thiele modulus, the reaction rate is lumped into a quasi first order rate constant by incorporating all the constants:

$$k'' = k_{dec} A_{p,int}\rho_p\epsilon_p \qquad \left[\mathrm{s}^{-1}\right] \tag{B.11}$$

The thiele modulus θ is then given by:

$$\theta = r_p\sqrt{\frac{k''}{D_{eff}}} \tag{B.12}$$

The effective diffusion will for the nanoporous particle be strongly dominated by Knudsen diffusion, as the pores are two orders of magnitude smaller than the mean free paths of CH_4 and H_2. Because of the high temperature D_{eff} is still in the order of 10^{-5} $m^2 \cdot s^{-1}$.

$$D_{eff} = \frac{r_p}{3}\sqrt{\frac{8RT}{M_g \pi}} \tag{B.13}$$

From the thiele modulus the effectiveness factor η_p is obtained. Even for the nanopourous particle the obtained effectiveness factor approaches 1. This means that the presented particle model returns the same result as directly calculating the loading from the carbon deposition kinetics.

This high effectiveness factor also implies that little to no carbon gradient over the particle radius can be expected. This was confirmed with experimental observations. In all cases, the nanoporous particle was black throughout the particle volume. No gradient in this could be observed by eye.

Simple particle model

The simple particle model does not contain a radial coordinate. The reaction rate, gas concentration and particle internals are evaluated over the radius of the particle. This is justified by the fact that mass transfer limitations can be ignored, and therefore no radial gradients are present.

The following assumptions are made:

- The gas phase concentration in the particle is equal to the bulk gas concentration (pure methane for the SPR).

The reaction rate summed over J different pore sizes and corresponding area is described by:

$$\frac{dC_c}{dt} = \sum_j^J R_{dec} A_{p,j}(t) \rho_p \tag{B.14}$$

The change in internal area is given by equation B.9. β is defined by equation 4.1.

Appendix C: Literature summary

Numerous authors report on the deposition of carbon from methane within porous media. The majority of these regard either supported metal catalysts or unfunctionalized porous carbonaceous carriers. A brief summary is presented.

A wide range of maximum achievable loadings is reported, varying with substrate material. In excess of 6 times the carrier mass can be deposited on certain commercial carbon blacks[15]. This seems dependent on various characteristics. It is suggested that the amount of carbon that can be deposited on a porous carrier is partially related to the total initial pore volume[12, 15].

Pore size distribution of various porous carriers before and after carbon deposition also indicate that the majority of carbon is deposited in the smallest pores[2, 16]. This is then attributed to the vast area present in these pores. This is in good agreement with results of this work.

The induction period has also been observed for Al_2O_3 in literature [14]. It is suggested that for carbonaceous carriers, the induction period is dependent on surface chemistry[10, 15]. The

presence of high energy groups, such as oxygenated groups on activated carbon or alumina, strongly increase the initial carbon deposition rate. For carbonaceous carriers, most notably activated carbon, it is further observed that the methane conversion rate is decreasing quickly (in the order of minutes) after initial contact with methane.

5 Continuous methane pyrolysis & carbon gasification in a lab scale setup

Table 5.1: Symbol list for chapter 5

Symbol	**Description**	**Unit**
T	Temperature	K
D	Diameter, Diffusion coefficient	m,$m^2 \cdot s^{-1}$
A	Surface area	m^2
τ	Residence time	s
N	Number of partitions	

Subscript	**Description**
0	Initial
dec	Decomposition, Pyrolysis
mod	Model
exp	Experimental
int	Internal
gas	Gas
tot	Total
avg	Average
ox	Oxidant

Abstract

This chapter documents the results of a continuous methane pyrolysis – carbon gasification setup. The design of this setup was based on experimental data from chapters 2-4, as well as numerous numerical models and is presented in appendix B. Using the constructed continuous setup, it was shown that the amount of carbon that can be deposited is related to the amount of carbon that was gasified in the previous cycle. This point was discovered in the modelling stage of the design, and of importance for further development of continuous processes. Additionally, this setup allows deposition of carbon at temperatures significantly lower than used in the previous chapters. It is found that this carbon is very reactive during gasification. Hence, this might open up possibilities for a methane pyrolysis – gasification process operating at a relatively low temperature.

5.1 Introduction

In this chapter, a continuous lab scale pyrolysis – gasification setup is described, and first results are presented. The goal of this setup is two fold. First, it was aimed to demonstrate the continuous application of the pyrolysis and gasification reactions integrated in a single unit. Until this point, in chapters 2-4, the vast majority of the work considered separated parts (reactions) of this system. This chapter can therefore be seen as a continuation of the earlier work presented in this thesis. To the best of our knowledge, we are the first to present a fully continuous system where CH_4 pyrolysis, steam gasification and air oxidation are incorporated.

The second goal of this system was to gather information related to the continuous operation of the process. From the data gathered previously, the existence of several phenomena important for continuous operation were observed experimentally, or via modelling. The increased operating range and continuous operating of this setup allows, for the first time, to experimentally investigate these phenomena in an integrated system. A brief summary on this is presented in section 5.2.2 and appendix B.1-B.4 in detail. It should be emphasized that this setup is not designed for a specific production target. As stated, this has been constructed for research purposes only. Hence, at no point it is claimed that this design is optimal for production purposes.

Using the data from this setup, the verification of assumptions made for continuous models can be tested. For the industrial analysis presented in chapter 6, both of these points are of great value.

5.2 Materials and methods

5.2.1 Materials

Porous α-Al_2O_3 particles were obtained from Saint-Gobain NorPro. (D_p=4.8 mm, ρ_p = 1431 $kg \cdot m^{-3}$, A_{int}=$4.1 \cdot 10^5$ $m^2 \cdot kg^{-1}$). These particles were used in earlier chapters work [1]. Kinetics were experimentally obtained for these particles and are used without modification.

All the particles were used as received. Methane (99.999%) was procured from Linde. Nitrogen (99.999%) from Nippon Gasses. All gasses used in this work were used as received. Steam was generated using Miili-Q water obtained from a purification system (Merck).

5.2.2 Experimental design

The experimental setup is discussed. Next to the conventional discussion of constructional and operational aspects of the setup, a summary of the design process is presented.

Some notes on the design philosophy and method

This section summarizes appendix B.1 and B.2. The complete design process is presented in appendix B.

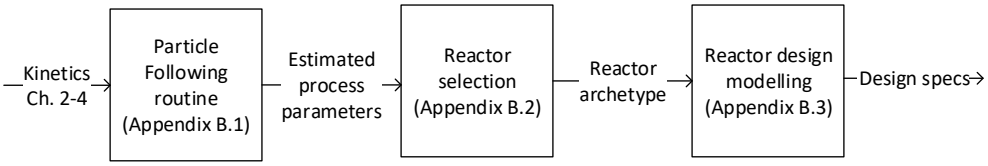

Figure 5.1: Schematic of method used to reach the design of the continuous lab scale setup.

The basis of this design are the kinetics measured in chapters 2-4. Two important points are identified, based on these kinetics. First, it was experimentally observed that the pyrolysis conditions (strongly) affect the gasification rates of the deposited carbon. A higher pyrolysis temperature yielded a slower gasification, and a longer pyrolysis solids residence time yielded a slower gasification. Hence, a connection exists between the pyrolysis and the gasification conditions. To further investigate the effect of this on the operation of a continuous process, the kinetics were incorporated in numerical model, following a single particle through an arbitrary pyrolysis- – gasification process.

Using this particle following routine, presented in appendix B.1, it was found that an optimal operating window exists. Operating at this configuration yielded the highest productivity [$mol_c \cdot m_r{}^{-3} \cdot s^{-1}$]. Two points important for this design were then identified. First, it was concluded that the gasification required a higher temperature than the pyrolysis step. Secondly, an upper limit exists for the pyrolysis solids residence time. These two together imply the temperature change velocity [$°C \cdot s^{-1}$] in the reactor should be high. Moreover, from this it is deduced that the pyrolysis temperature needed to be accurately controllable. This is discussed in detail in section B.1.

For the technical implementation of this, various options were analysed. Unsuitable reactor archetypes were excluded. The process is documented in appendix B.2. After these selection steps and consulting with multiple experts, it was decided to create a system where a physically moving heater was the basis for temperature change. Using different set points, the temperature in the reactor will be influenced by the rotational speed.

As stated in the introduction, it was aimed to create a system that was as flexible as possible. Practically this means that the overall possible operating window is as large as possible, meaning a large possible variation in input parameters. Important here is that steady state operation should remain possible in this window. Examples why this is not possible include a net carbon buildup over time. For this, a numerical model study was performed. This study is presented in appendix B.3.

Experimental setup

A schematic is presented in figure 5.2. The heating equipment, shown partially in orange, is rotating along the axial length. Six heating units are used in the constructed setup, placed around the reactor. The reactor itself is stationary (shown as a tube in yellow). Gas flows from bottom to top, the in and outlets are shown in purple.

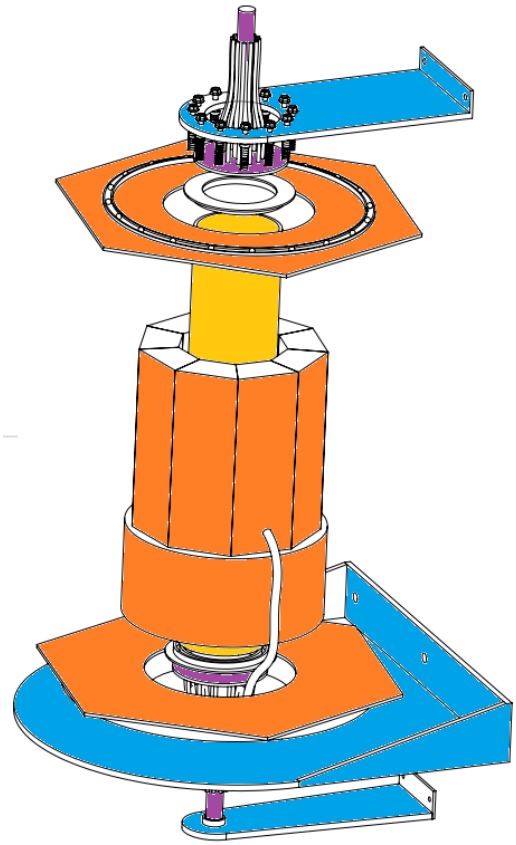

Figure 5.2: Schematic of experimental setup. Orange parts: Oven, rotating along the axial coordinate. Not shown: external isolation and temperature controllers. Blue: support structure, stationary. Yellow: location of ceramic reactor, stationary. Purple: gas inlet, stationary.

The reactor is divided into six partitions (angular width 60°). In each of the partitions a certain process phase occurs. This can be pyrolysis, steam gasification, oxygen gasification, or flushing (using nitrogen). The timing of these phases is a set parameter. Each of the phases has a corresponding heater set point temperature. Over time, partitions cycle through all the phases. At the end of each phase, the heater rotates to match the temperature to the phase in each partition. The gasses are switched using valves. A complete cycle of a random partition is then Pyrolysis → Flush → Steam gasification → Flush (→ Oxygen gasification → Flush). The total cycle time is also the time for 1 complete heater rotation. Not all the partitions start in a pyrolysis step, this is depending on the setup configuration.

For completeness it is mentioned that two methods op heater rotation were tested. First it was attempted to continuously rotate the heater. However, it was found this temperature change is

unfavourable. The step-wise rotation was found to work significantly better.

Heating unit

Heating of the reactors was facilitated by an in-house constructed radiation oven. The bulk of the oven is constructed from ceramic bricks. In these, a heating wire was placed (1.5 mm diameter, SuperKanthal A1, Salomons Metalen). The heating wires were kept in place by a high temperature cement. Temperature was controlled using Jumo Dtron temperature controllers. The thermocouples (ceramic insulated, type S) measuring the heater temperature for controller feedback were placed in the axial middle of the heating unit, on the inner surface of the heating block. The six heaters form a hexagon when placed side to side in the axial length, the minimum inner diameter was 150 mm, the heater height was 700 mm. Inside this hexagon the reactor was placed.

Power was supplied from a 10 kW, 55 V transformer. This low voltage power was fed through a in-house constructed slip ring and then moved to the respective heaters. This power was also used for the temperature controllers. The heating unit was isolated using 300 mm of ceramic wool (Morgan ceramics). An outer shell made out of aluminium kept the heater in place. The rotational position of the heater could be measured by a magnetic detector (RS components). That the oven position was detected at a constant point in the rotation. This was used to ensure the oven was at the correct position at the start of experiments.

Reactor

The reactor was in-house constructed out AISI 310 steel (1.5 mm, Salomons metalen). The length of the partitions was 300 mm, the outer diameter of the reactor 140 mm. To each of the partitions a gas feed and outlet pipe (ID 10 mm, AISI 310) was welded. It was aimed to construct the reactor out of ceramics, to facilitate higher temperatures. This proved to be difficult, hence a first attempt using a steel reactor was used. This proved to be stable enough to run the desired experiments. Hence, it was decided to continue with the steel version, for this work.

The reactor was kept in place using a steel support. The height of the reactor in the oven could be changed freely.The axial reactor middle was placed at 550 mm height, measured from the bottom of the heater.

The reactor partitions were filled with the porous Al_2O_3 particles, per partition this was approximately 420 gram of particles. No solid samples could be retrieved from this system. Moreover, no thermocouple was present in the reactor. This is because we wanted to limit the amount of welds on the reactor, increasing structural stability. Hence, no openings were present.

Notes on reactor construction material

Initially it was aimed to construct the reactor out of Al_2O_3 . This would have resulted in a system capable of operating at temperatures up to 1400 °C and allow evaluation of the complete operating area tested in the particle following method. However, construction of this ceramic system was met with numerous setbacks. In view of available time, the decision was made to construct the reactor out of AISI 310 steel. This reduced the operating window to max. 1200 °C. As a result, the effect of $T_{dec}$was more challenging to measure. It was predicted this effect is most pronounced at 1200 °C and above (appendix B.1). Secondly, the plausible catalytic effect of a metallic surface on

the pyrolysis and gasification reactions falls outside the scope of this work, and has therefore not been characterized. It was found that the used steel (AISI 310) was stable enough to be used for numerous experiments spanning several weeks.

Gas preparation

A PID of the gas inlet section is presented in figure A.1. Gas flows (methane, air and nitrogen) are controlled via Bronkhorst mass flow controllers (MFC 1-3, 2-100 $NL \cdot min^{-1}$). Steam was generated using in-house constructed steam generators (SG 1-6). Steam flow was controlled using a liquid water pump (SP 1-6, 0.2-20 $mL \cdot min^{-1}$ liquid, KNF Verder). All the ingoing steam lines were heated to 200 °C using tracing heaters (Horst), this is coloured red in figure A.1. Each of the partitions has an own ingoing feed line. The flowing gas is controlled by opening and closing magnetic valves (P1x-P6x, Eriks). Each of the lines has 3 ingoing and 3 outgoing valves. The pressure drop across the 6 partitions of the reactor was balanced using rotatmeters (P 1-6, Brooks). All the flows, valves and oven rotation were controlled using LABVIEW software combined with the National Instruments communications equipment. This was also used for data monitoring and logging.

Gas outlet and analysis section

The outgoing section of the setup is presented in figure A.2. The outgoing gasses are cooled using a heat exchanger (HEX 1-6), cooled with tap water (approximately 10 °C). The remaining water is separated off in phase separators (SEP 1-6). Any remaining contaminants are filtered out using 20 micron filters. The outgoing flows are then recombined into the correct stream using valves (V1x-V6x, Eriks). The flow size is measured using mass flow meters (0-100 $NL \cdot min^{-1}$, Bronkhorst). The composition of the three outgoing flows is analyzed using a 0-100 %vol CO, 0-100 %vol CO_2 , and 0-100 %vol CH_4 NDIR sensors, (Gascard, Edinborough Sensors). The outgoing flows correspond to Pyrolysis, Steam gasification and Air gasification. The flush stream is divided over the three streams, during switching of valves, to prevent a combustible mixture from forming.

5.2.3 Experimental procedure

The oven was heated up to the required set points ($10\ °C \cdot min^{-1}$) over night. During heating and cooling, nitrogen was used as a flush gas in all partitions ($2\ L \cdot min^{-1}$, per partition) and the oven was stationary. The required parameters were configured in the control software. An overview of the available experimental parameters is presented in table 5.2. The oven rotational speed is dictated by the total cycle time, which is the sum of all the residence times of the respective used phases.

Table 5.2: Overview of available process parameters. Flows are flows per partition, the total number of partitions must equal 6.

Parameter	Indicative range	Unit
Methane flow	2000-8000	$NmL \cdot min^{-1}$
Steam flow	2-10	$mL \cdot min^{-1}$, liquid
Oxygen Flow	2000-4000	$NmL \cdot min^{-1}$
Flush flow	8000-12000	$NmL \cdot min^{-1}$
τ_{dec}	300-1000	s
τ_{gas}	300-1200	s
τ_{flush}	100-500	s
T_1 - T_6	1000-1200	°C
N_{dec}	1-3	Number of pyrolysis partitions
N_{gas}	1-3	Number of steam gasification partitions
N_{ox}	0-3	Number of air gasification partitions
N_{cy}	1-30	Number of cycles in experiment

When the set point temperatures were reached the experiment could commence. For this, the oven rotation was started. When the oven had reached the correct position, flows and data-logging were started. In- and outgoing flows, temperatures, gas compositions were logged every 1 second. When the setup was running, no further action was required.

After a set number of cycles, the experiment finished. All partitions were fed nitrogen (2 L/min, per partition) and oven rotation stopped. The next experiment could commence at this point. Alternatively a cleaning step could be used. For this, the flows are switched to air (2 L/min, per partition) for a short time (order of minutes) to completely burn off all the remaining carbon. Cleaning progress could be checked via the CO and CO_2 sensors in the gas outlet section, when these were not detected anymore, the bed was void of carbon, as verified by opening up the reactor (opening the reactor was done once after completely switching the reactor and is not normal experimental procedure, as the reactor is destroyed).

5.2.4 Reproducibility of experiments

To test reproducibility, two experiments using 10 cycles were ran. Outgoing gas flows, flow rate and reactor temperature show good reproducibility over the cycles, although some variation is observed in the initial cycles. This is presented in figure 5.3. This was observed during every first experiment of the day. Hence, this is attributed to the temperature in the oven reaching a quasi-steady state. It is most likely caused by the increased energy consumption inside the oven, due to heating of gasses and the endothermic reactions. If an experiment was performed immediately after, this effect was not observed. It is concluded that measurement are reproducible.

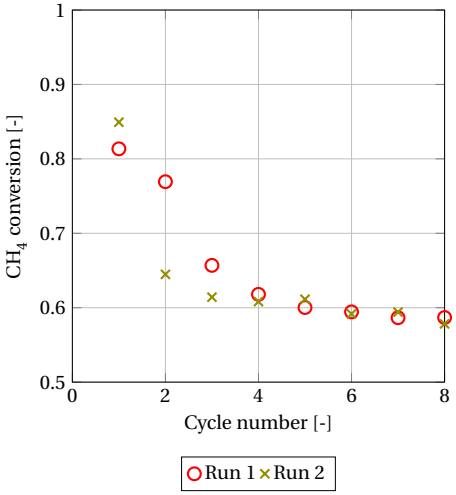

Figure 5.3: Obtained methane conversion for two runs under identical conditions, presented in table 5.3, base case.

5.3 Results and discussion

Effect of τ_{dec}

First, the effect of deposition residence time on gasification rate is verified. For this, three experiments were ran, at varying τ_{dec} (300, 500 and 900 s). The further experimental parameters are presented in table 5.3. Note that the flows are reported as flows per partition. At all times, an excess of steam was fed (moles of steam compared to moles deposited C). This was done to ensure the gasification of carbon did not stop, due to insufficient steam.

The measured CO production rate over time is presented in figure 5.4a. These data were chosen because it best shows the trends expected. For all three experiments, it was observed that as soon as the steam entered the system, a large CO stream left the reactor. This was short lived, as the CO production soon stopped, even though steam was still being fed to the reactor, and was observed condensing out of the system. At all times, the peak CO production rate was significantly lower than the total steam feed rate. Hence, the height of this peak was not limited by steam feed. Furthermore, it is observed that the CO peaks are slightly wider for the 900 s run than for the 300 s run, but that the 300 s runs have a higher CO peak production than the 900 s run. From the gasification kinetics measurements, it is known that the gasification rate is zeroth order in carbon loading. It is concluded that the height of the peak is then a result of the reactivity of the carbon. The width of the peak is then related to the amount of carbon present on the bed.

The obtained average CO production rate over the whole reactor (figure 5.4b) is presented. It was observed that the average CO production rate scales inversely with τ_{dec}. From the kinetic analysis this was expected: older carbon less prone to gasification. Therefore, a lower peak (and average) gasification rate are observed. Note that in figure 5.4b the rate is evaluated over the whole reactor, whereas in figure 5.4a the rate is observed as 3 out of 6 partitions, over time. This explains the approximate factor 2 difference between both figures.

The shape of the data presented in figure 5.4b is observed for all three datasets, and is a result of two effects. First, for cycle 1, the average CO production rate is relatively low. This is because the bed is initially void of carbon. Hence, the partitions starting with a gasification step do not produce any CO. The second effect is related to a temperature decrease observed at every 'cold start' and is discussed in section 5.2.4.

The CO production rate is observed to be relatively fast, being comparable to the obtained pyrolysis rates. The carbon was deposited at relatively low T_{dec}, when compared to the temperatures evaluated in the particle following routine and chapters 1-3. In previous work, we were unable to deposit enough carbon at low temperature, complicating analysis of this low temperature carbon. In this setup, using the significantly larger gas flows, this is possible. It is concluded that this high gasification rate might open up possibilities for a lower temperature pyrolysis process.

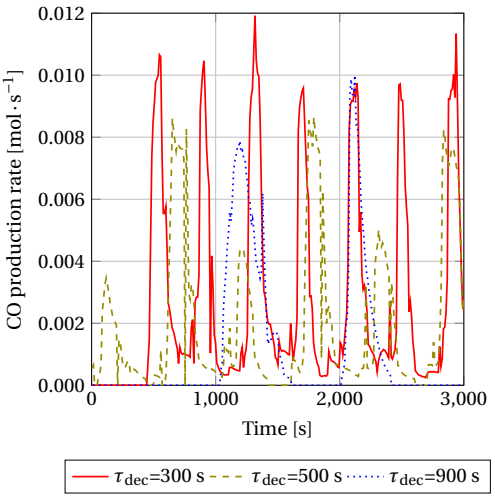

(a) Obtained CO production rate over time, for various τ_{dec}.

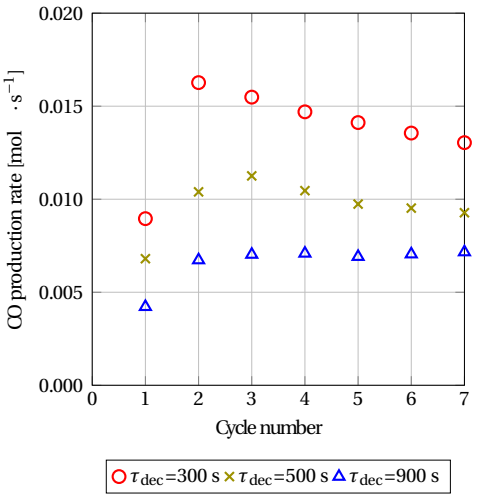

(b) Averaged C gasification rate over cycle number, corresponding to figure 5.4a

Figure 5.4: Results of the τ_{dec}effect experiments.

Table 5.3: Used parameters for the residence time experiments. Flows denote flows per partition.

	Base	Long	Short	Unit
τ_{dec}	500	900	300	s
τ_{gas}	200	500	150	s
Flush	400	600	350	s
N_{dec}	3	3	3	-
N_{gas}	3	3	3	-
CH_4 flow	4000	4000	4000	N mL $\cdot$ min^{-1}
	2.73	2.73	2.73	mmol $\cdot$ s^{-1}
	1.50	2.46	0.82	mol total
Steam flow	0.10	0.10	0.10	mL $\cdot$ min^{-1}, liquid
	5.46	5.46	5.46	mmol $\cdot$ s^{-1}
	1.09	2.73	0.82	mol total

Notes on the effect of T_{dec}

A separate experiment was performed to test the effect of T_{dec}. For this, a control experiment was performed, during this all the heaters were set to 1000 °C. Then, a second experiment was performed, where the heaters corresponding to the decomposition phase were lowered to 950 °C. The hypothesis was that the lower decomposition temperature resulted in more reactive carbon, enhancing the gasification rate of the system.

Unfortunately, at this time the setup was partially fouled near the heat exchangers. Although attempts were made to remedy this, the fouling could not be removed without removing the complete reactor from the system. This is a risky task, as the reactor is prone to damage when removed from the oven and would almost certainly be damaged, requiring a new unit. This was not available. Hence, these experiments were unfortunately not performed.

Longer demonstration of the process

A longer test was performed on the setup. The goal of this was two fold. First, to demonstrate this process at longer run time. Second, to investigate the longer run time behaviour of this system, where more loading cycles are performed. Up until this work the longest continuous amount of pyrolysis-gasification cycles performed on a single particle were in the order of 10 cycles. It is noted that this is not a true long term stability test, spanning months and thousands of cycles. This was unfortunately not possible in the current setup and available time.

The experimental configuration is presented in table 5.4. No air oxidation step was included in the experiment. The reason for this is because the effect of carbon buildup over cycles could then be investigated. Initially, the bed was confirmed to be void of carbon, via oxidation with air.

Table 5.4: Used parameters during the long experiment, and for the model calculations

	Cycle 1-19	From cycle 19	Unit
τ_{dec}	1000	1000	s
τ_{gas}	400	300	s
τ_{flush}	200	300	s
N_{dec}	3	3	-
N_{gas}	3	3	-
T_{dec}	1100	1100	°C
T_{gas}	1000	1000	°C
CH_4 flow	4000	4000	$\text{NmL} \cdot \text{min}^{-1}$
	2.73	2.73	$\text{mmol} \cdot \text{s}^{-1}$
	2.73	2.73	mol total
Steam flow	0.10	0.10	$\text{mL} \cdot \text{min}^{-1}$, liquid
	5.46	5.46	$\text{mmol} \cdot \text{s}^{-1}$
	2.19	1.64	mol total

The obtained cycle averaged CH_4 conversion is presented in figure 5.5a. The experiment spanned 3 days, hence the data is presented in three series. At every restart, the startup effect is observed. It is noted that at the second and third restart, the effect appears to be less pronounced. This can be explained by the carbon loading. Initially, the bed is void of carbon, and at slightly elevated temperature, resulting in a higher pyrolysis rate. From the second restart, the bed is loaded with carbon, and at (equal) slightly elevated temperature. Hence, the pyrolysis rate is enhanced less and the effect is observed less clearly.

Over time, after approximately 5 cycles after both restarts, a comparable CH_4 conversion is observed. The first 19 cycles appear to converge to a methane conversion of almost 60%. At the end of cycle 19, the experimental configuration was changed. The gasification time was reduced by 30%, thereby reducing the amount of carbon gasified. It was aimed to increase the amount of carbon on the bed. In figure 5.5, the estimated loading over time is presented. This loading was calculated by summing the mass balance over time. Up until 40 ks, the configuration was that of cycle 1-19. Afterwards, the shorter gasification time was used. With the change in gasification time, two observations are made. First, according to expectations, the bed loading increases faster (figure 5.5) after the configuration change.

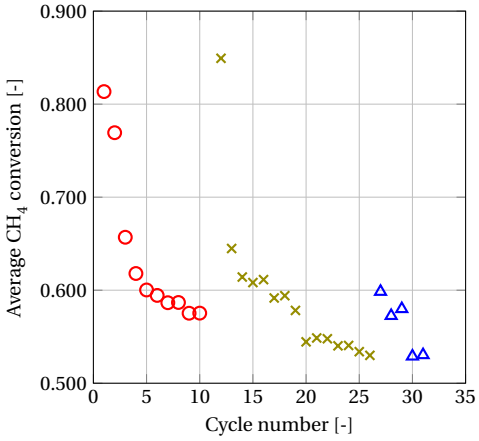

(a) Obtained CO production rate over time, for various τ_{dec}accompanying figure 5.5b

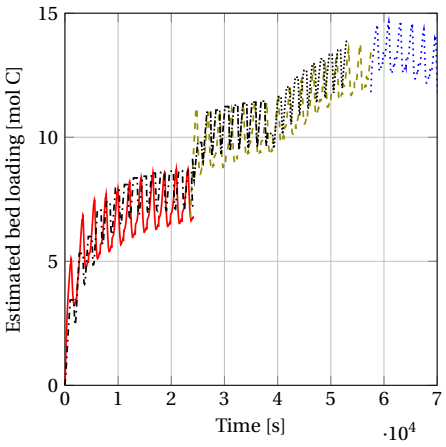

(b) Averaged C gasification rate over cycle number, model data in dashed black.

Figure 5.5: Results of the τ_{dec}effect experiments.

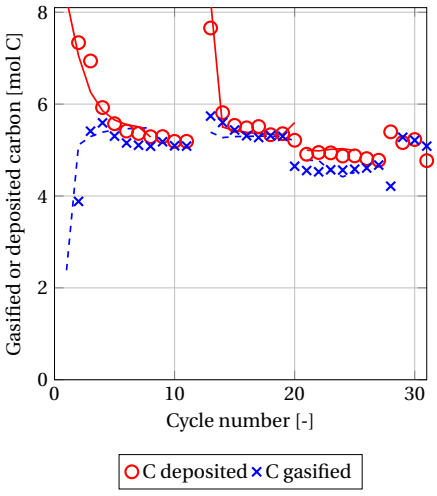

(a) Moles of carbon deposited and gasified over cycle number, lines denote the model predictions.

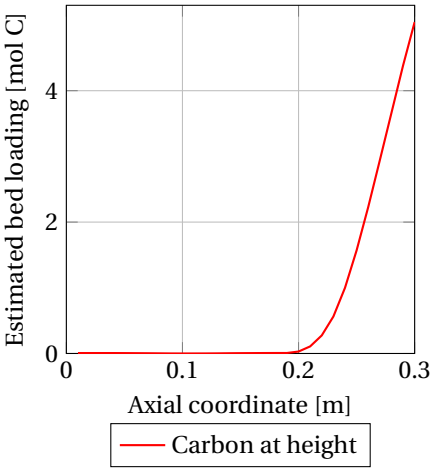

(b) Modelled axial carbon profile along the reactor. Data taken from the long run, after cycle 1. Values denote the total amount of moles present at the presented height.

Figure 5.6: Results of the τ_{dec}effect experiments.

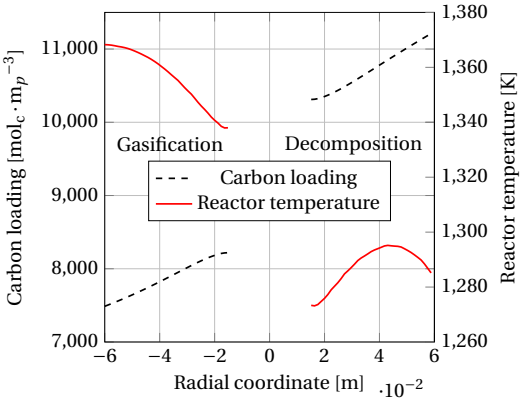

(a) Modelled radial reactor temperature and carbon loading profile. The left hand part is at the end of a gasification step. The right hand side is at the end of a pyrolysis step.

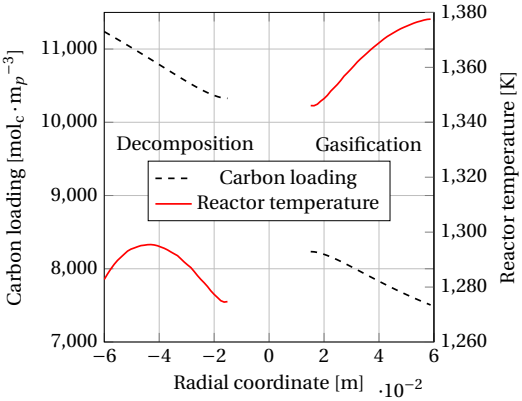

(b) Modelled radial reactor temperature and carbon loading profile. The right hand side is at the end of a gasification step. The left hand side is at the end of a pyrolysis step.

Figure 5.7: Modelling results, radial temperature and carbon loading profile for cycle number 25, various times, further configuration data in table 5.4.

Second, the CH_4 conversion (figure 5.5a) is reduced slightly. From cycle 20 on, the conversion is reduced to 54%. Hence, by reducing the amount of gasified carbon, the amount of deposited carbon is also reduced. To further investigate this, the amounts of carbon deposited and gasified are presented in figure 5.6a. Over time, they indeed appear to converge. In other words, the amount of carbon that can be deposited is limited by the amount that is gasified in the previous cycle. It is concluded that, at the used parameters, the system was operating at a quasi steady state. More importantly, it is concluded that a reduced gasification capability eventually reduces the complete productivity of the system, by limiting the deposition of fresh carbon. This was first predicted in the particle tracking analysis, and now experimentally shown. The observation that gasified carbon eventually limits the ability to deposit carbon is important for the design of continuous processes. Concluding, it is important to control the buildup of carbon in the system, in order to be able to control steady state productivity.

It is concluded that the used α-Al_2O_3 particles are stable over extended times. Over the course of the performed testing and experiments, 450-500 cycles were performed on the vast majority of the used carrier. Some was added between the second and third version of the reactor (75 gram on a total of approximately 2500 g, hence this is neglected). During this, no degradation could be detected via measured parameters, or by visual inspection. For definitive data, a physisorption measurement is required. No literature data on carbon deposition is reported after this amount of cycles.

5.3.1 Modelling results

A numerical model of the continuous reactor has been constructed in matlab. The goal of this model is to better understand the internal properties of the reactor. From previous work, it was

concluded that the developed kinetic models are able to describe carbon deposition and methane conversion in a simple fixed bed. These kinetics are also used in this model. The detailed model workings are presented in Appendix B.3.

Before the results are presented, it is important to critically evaluate this modelling. From the experimental data, only gas conversions, external wall temperature and pressure drop are available. From within the reactor, no directly measured information could be obtained, due to the reactor design. Hence, no direct verification of the model prediction can be made. The model results should be interpreted with this in mind.

The results of the long run are presented in figure 5.5b. Three points are observed. First, good agreement exists between the model prediction and the – estimated – experimental bed loading. The overall amount of carbon on the bed is predicted correctly.

The second point observed from figure 5.5b is the shape of the loading curve. Because in the model, everything is perfect plug flow, no (back)mixing occurs. In reality, significant gas mixing and dead reactor volume affect the shape of the experimental curves. Therefore, the differential conversion or reaction rates are not predicted correctly. Over a complete cycle, the large gas volumes mitigate this, and the overall balance is predicted correctly.

Third, the "step" in the carbon loading after the first restart is also predicted. The experimentally measured external reactor wall temperature is input for the model, hence this is incorporated via this. This also shows the effect is indeed (partially) an effect of temperature.

The change in operating parameters after cycle 19 is incorporated into the model. The predicted increase in carbon loading matches with the experimental estimation. This supports the observation that the decrease in deposited moles of C is related to the reduced gasification step. It is concluded that the measured kinetics are able to predict a decrease in productivity due to this interplay.

Although we cannot verify the predicted internal properties, some preliminary conclusions can be drawn from this, mainly for the heat balance. It is proposed that the predicted internal temperature cannot deviate much from the real temperature. A big deviation would have yielded a significantly different reaction rate and carbon loading. Hence, it is concluded that the simple heat transfer model is accurate enough for this type of modeling.

A radial temperature and concentration profile is included in figure 5.7. Two points are noted. First, no large temperature difference exists within a partition. This is desired, as the whole partition is then participating in the process at a comparable level. Secondly, the temperature difference between the partitions, evaluated over the whole reactor diameter is almost 100 °C. This is in good agreement with the experimentally set temperature swing. It is again emphasized that these model results are not substantiated with experimental results, and can therefore be seen as indications only. An axial profile is presented in figure 5.6b. It can be seen that the lower part of the reactor does not contribute to the productivity. This has been qualitatively observed experimentally, by opening a defective reactor. The particles near the bottom of the system were white, the top particles were black. This is attributed to a lower temperature near the bottom of the reactor. Hence, it is concluded that the temperature profile was not optimal during the long run.

5.4 Conclusion

A fully continuous methane pyrolysis – carbon gasification process was demonstrated. Using the kinetics obtained in chapters 2-4, a design of this continuous setup was made (see appendix B). The constructed setup was tested and found to perform in agreement with expectations.

It was found that the amount of carbon that can be deposited is related to the amount of carbon that was gasified in the previous cycle. Hence, it is concluded that in order to control productivity of the system, it is vital to control the total amount of moles C gasified. This is a major point for further development of continuous systems.

Furthermore, it is concluded that separately measured pyrolysis and gasification kinetics are able to correctly predict behaviour of fully continuous systems.

It is concluded that pyrolytic graphite produced at relatively low temperature (850-950 °C) offers possibilities for a relatively low temperature methane pyrolysis process. The fast gasification allows high productivity, whilst reducing the overall required temperature. This brings benefits for energy efficiency and heat exchange.

Bibliography

[1] T. Kreuger, W. P.M. van Swaaij, A. N.R. Bos, and S. R.A. Kersten. Methane decomposition kinetics on unfunctionalized alumina surfaces. *Chemical Engineering Journal*, 427(June 2021): 130412, 2022. ISSN 13858947. doi: 10.1016/j.cej.2021.130412. URL https://doi.org/10.1016/j.cej.2021.130412.

Appendix A - PFD of continuous setup

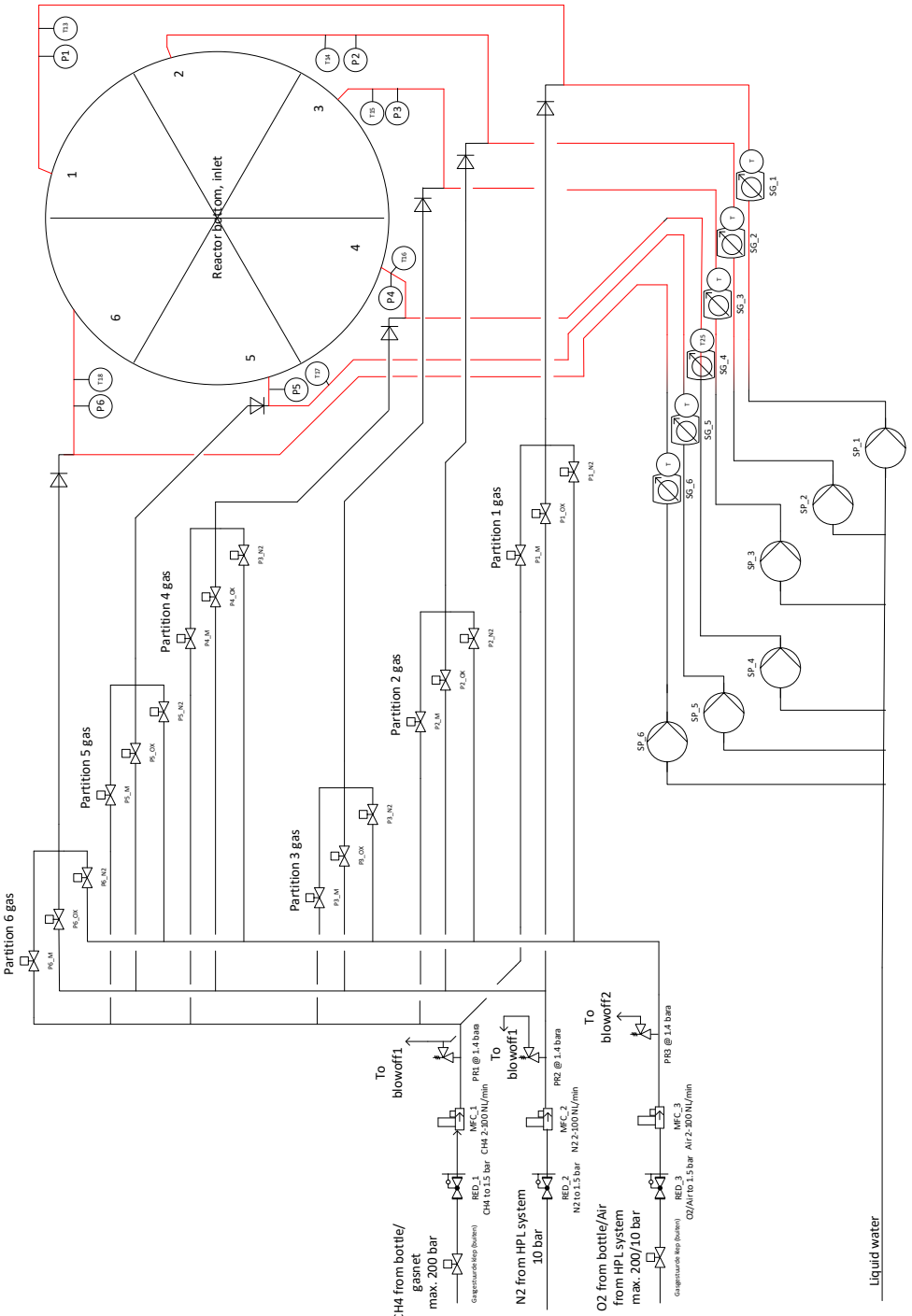

Figure A.1: Schematic of the gas inlet section.
The red lines denote a tracing is present.

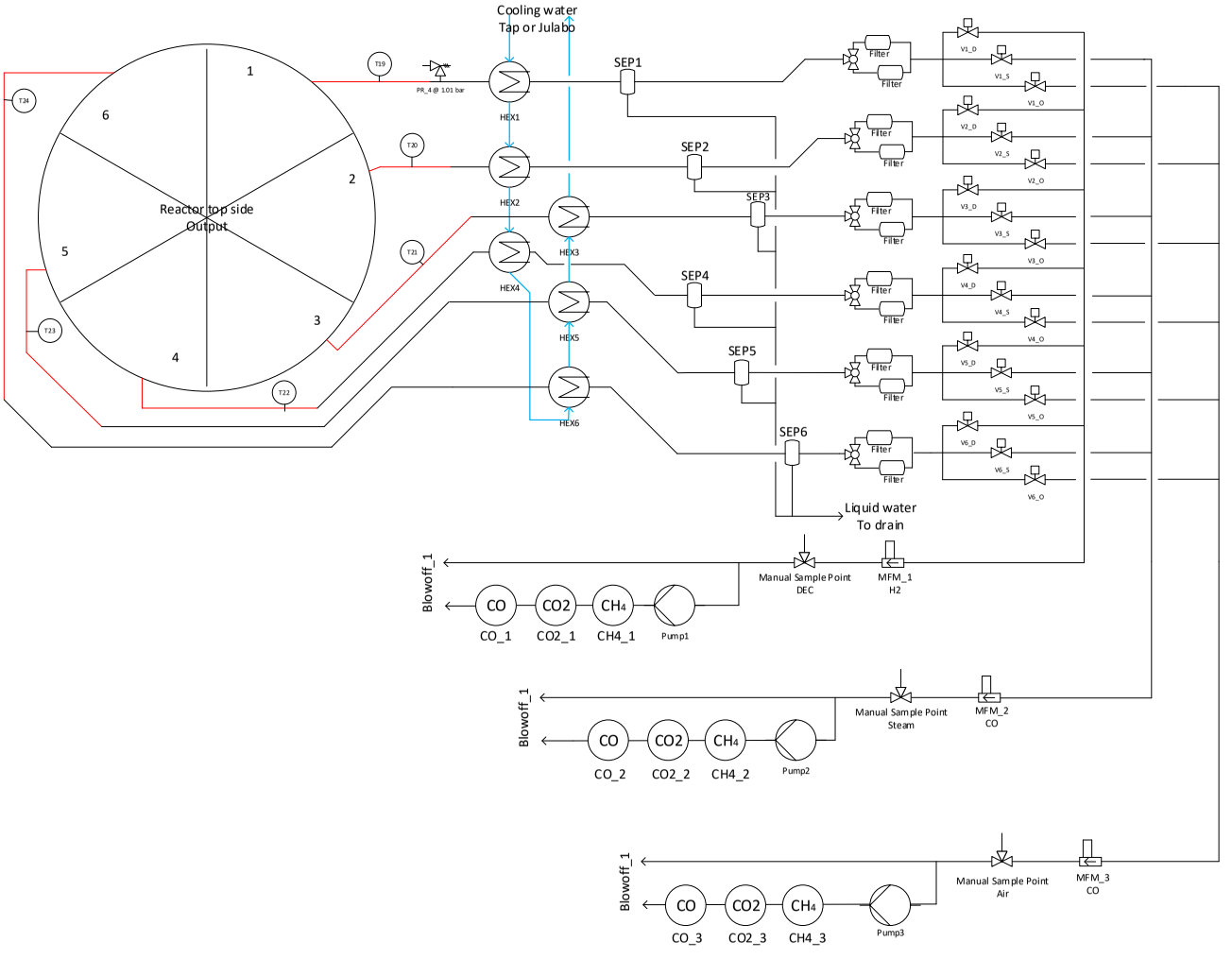

Figure A.2: Schematic of the gas outlet section.
The red lines denote a tracing is present.

6 An evaluation of the industrial application of methane pyrolysis

Table 6.1: Symbol list for chapter 6

Symbol	**Description**	**Unit**
ρ	Density	$kg \cdot m^{-3}$
η, κ	Efficiency	
C	Loading	$g \cdot m^{-2}$
t	Time	s
ϕ	Mass flow	$kg \cdot s^{-1}$
x	Mass fraction	
λ	Gas solid ratio	$kg \cdot kg^{-1}$
T	Temperature	K, °C
R	Gas constant	$J \cdot mol^{-1} \cdot K^{-1}$
D	Diameter	m
N	Amount of material	g
τ	Residence time	s
ΔH_r	Reaction enthalpy	$J \cdot mol^{-1}$
r	Radius	m
u	Superficial velocity	$m^3 \cdot m^{-2} \cdot s^{-1}$
L	Length	m
E	Energy	kJ
V	Volume	m^3

Abbr.	**Description**	**Unit**
Abbr.	Abbreviation	
C	Carbon	
LHV	Lower heating value	kJ

Subscript	**Description**
p	Particle, Product
M	Methane
ex	External
0	Initial
dec	Decomposition, Pyrolysis
mod	Model
exp	Experimental
int	Internal
gas	Gas
tot	Total
eff	Effective
fix	Fixed bed
fl	Fluidized bed
b	Bulk
ox	Oxidant
∞	Infinite (time)

6.1 Abstract

This chapter documents our analysis of the industrial application of methane pyrolysis. It is aimed to investigate the possibilities of a methane pyrolysis process in an industrial application. Numerous process configurations are evaluated at various level of detail. From this, general important points for an arbitrary methane pyrolysis process are identified, as well as positive negative aspects of various process configurations. It is also determined which points are important for future development.

First, a reactor level analysis was used to determine mixing states and heating methods. Internally heated systems, where deposited carbon is oxidized to CO, were found to be very attractive in terms of heat transfer. For all configurations, fluidized bed systems offer a higher productivity than their fixed bed counterparts.

In a process level analysis, it was confirmed that heating via the recycling of hot solids is not effective. The most suitable configurations were compared using numerous KPI, focusing on carbon and energy efficiency. The most suitable design was evaluated at 30 bar to better reflect the industrial conditions.

6.2 Introduction and goals in this section

This section discusses the industrial methane pyrolysis process. It is aimed to investigate the important parameters affecting the viability of a CH_4 pyrolysis and gasification process. Using the knowledge obtained in the earlier chapters of this thesis, an analysis of this process is presented. It is not aimed to present the most optimal or viable industrial design. It is argued that at this stage of development, it is more beneficial to attempt to gather as much knowledge as possible for the design of an industrial case and to investigate the potential of a methane pyrolysis process for industrial application.

This chapter features four levels of analysis. In each step, more detail is added to the analysis. First, a reactor level analysis is presented. Numerous possible process configurations are available, these are presented in the next section and are compared to each other in section 6.4.3. Various characteristics are compared, in order to find out positive and negative aspects of these configurations. Examples of these characteristics can be reactor size operating temperature and methane conversion. This first level functions as an investigative step, to get an idea of what these processes could look like, and what mixing states are preferable.

The second level of analysis regards a process for the production of 100 ktpa hydrogen. A parameter sweep is performed over the available process parameters. For all configurations, approximate reactor and flow sizes are determined. Conclusions are drawn on the characteristics of these processes, and methane pyrolysis in general. The goal of this step is to reduce the number of configurations for further evaluation,

In the third level the configurations selected in section 6.4.3 are evaluated using defined KPI. Again general conclusions are drawn on the industrial application of methane pyrolysis. The best performing configuration is selection for evaluation in level four.

The fourth level of analysis regards a comparison to the industrial standard, acting as a benchmark. Additionally, it is proposed that an industrial methane pyrolysis process is years away from large-scale industrial application. Optimistically a full scale industrial process could operate between 2030 and 2040. Hence, it is argued we should try to compare the pyrolysis process to the industrial benchmark of 2040. It is envisioned this will be some adapted version of the current industrial benchmark, for example an electrically heated steam reformer with carbon capture. The long term goals of these hypothetical processes is to operate with a net carbon emission of 0 $gCO_{2,e} \cdot MJ^{-1}$.

After this last step, final conclusions, remarks on this study and recommendations for future study are presented.

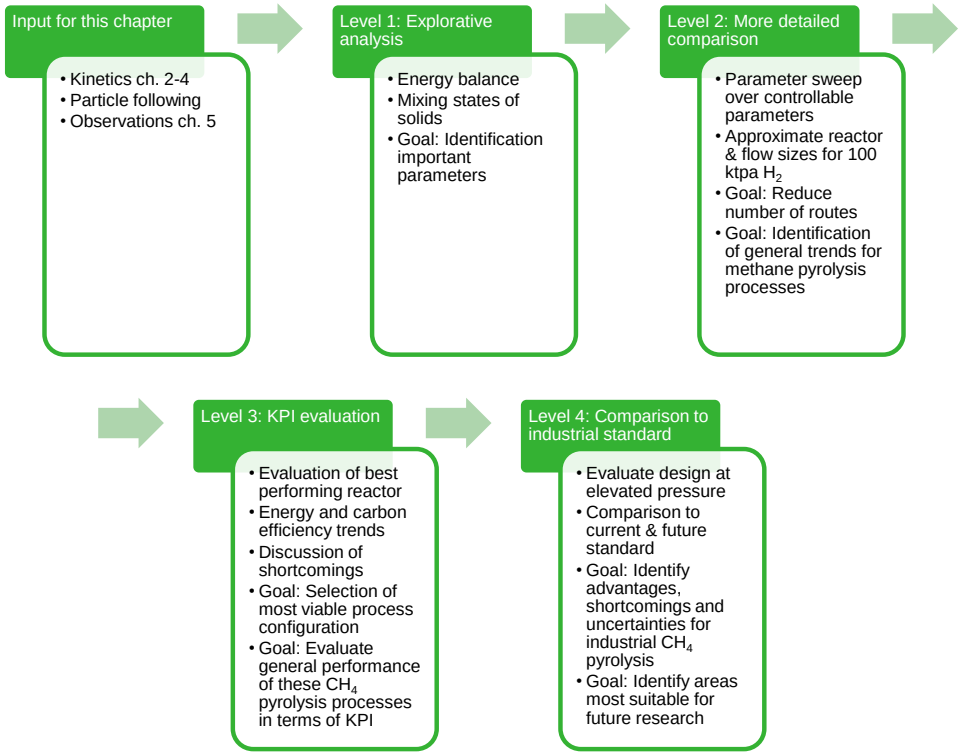

Figure 6.1: Work flow diagram of this chapter

6.3 Process configurations taken into consideration

A process involving methane pyrolysis and subsequent gasification needs to be defined more stringently in order to be analyzed. Multiple options can be identified. In this work, the selected design parameters are the gasification agent (oxygen, CO_2 and steam) and the heating method. An overview of evaluated configurations is presented in table 6.2 and the accompanying PFDs in figures 6.2-6.6.

External fuel may be conventional combustion of methane, carbon, or heating via electricity. The combustion of carbon is the oxygen gasification of the deposited graphite, and yields CO. The combustion of methane is external of the reactor volume and yields CO_2 .

Table 6.2: Overview of studied configurations

Configuration	Gasification	Heating	PFD figure
1	Steam/CO_2	External fuel	6.2
2	Steam/CO_2	Carbon combustion	6.3
3	None	External fuel	6.4
4	None	Carbon combustion	6.5
5	None	Complete carbon combustion	6.6

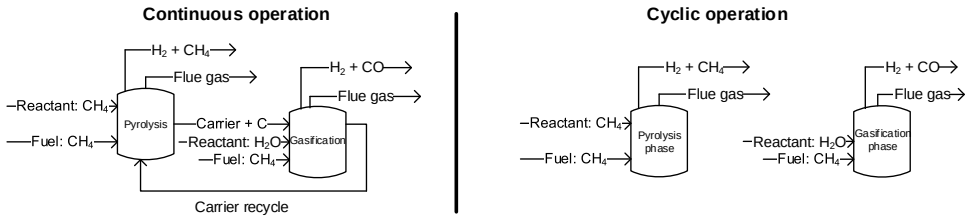

Figure 6.2: PFD of configuration 1, two options are evaluated. The cyclic option denotes a single unit switching the operating phase over time.

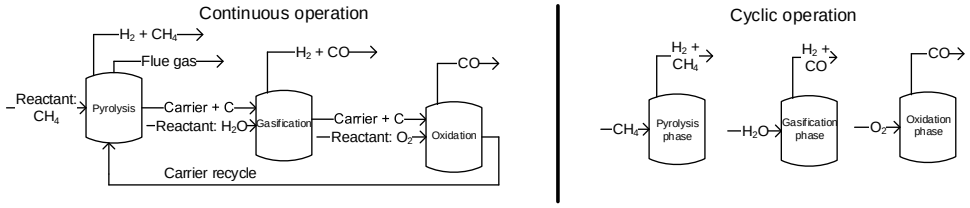

Figure 6.3: PFD of configuration 2, two options are evaluated. The cyclic option denotes a single unit switching the operating phase over time.

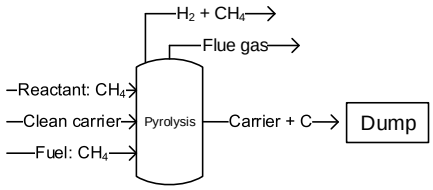

Figure 6.4: PFD of configuration 3

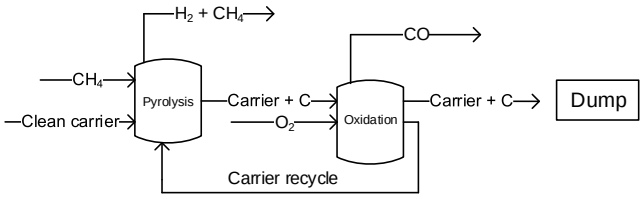

Figure 6.5: PFD of configuration 4

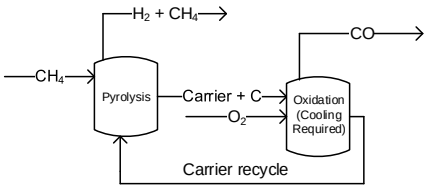

Figure 6.6: PFD of configuration 5

6.4 Level 1: Reactor analysis

In this section, the various reactor options and corresponding solids mixing states are discussed. The overall goal of this section is to select a suitable reactor archetype for each of the process configurations. At the same time, it is aimed to identify important parameters for each of the configurations presented. These parameters are important for the further development of these processes. To investigate this, reactor models have been developed for each of the configurations.

6.4.1 Reactor models & background

In this chapter, a fixed and fluidized bed reactor are evaluated. It is aimed to estimate the characteristics, such as reactor size, operating temperature or gas phase conversion, of a reactor within

these processes. In this section, only the reactor is evaluated. In the next section these models are incorporated into a process model.

In the lab scale design chapter, it was discovered that energy transport may play a vital role in the reactor design. To further analyze this, in this section, simple numerical models are used to investigate the approximate temperature profile present in a reactor. Furthermore, from the particle following analysis, it was found that for some process configurations the mixing state of the solids is an important parameter, for example via the effects of a residence time distribution. In table 6.3 the mixing states of both the models are presented.

Table 6.3: Overview of mixing states in the used models

Phase	Fixed bed	Fluid bed
Gas	Plug flow	Plug flow
Solid	Not mixed	Perfectly mixed

In figure 6.7 the calculation scheme of both models is presented. The reactor model consists of two steps, one for the energy balance and one for the mass balance. First, the input parameters are transferred to the energy balance model. This model calculates the radial temperature profile present in the reactor. For this an initial carbon loading guess C_{ig} is used. The obtained radius-averaged temperature is then used in a mass balance calculation. From this, a calculated carbon loading C_c is obtained, and the calculation is repeated with C_{ig}=C_c. The energy and mass balance then iterate to equate both of these carbon loadings, yielding a quasi-2D model of these reactors.

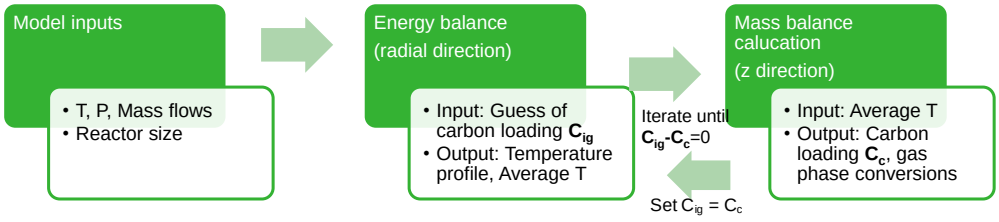

Figure 6.7: Calculation scheme for the models in this chapter

The energy balance model has been used in the design of the continuous setup. The fixed bed model for mass has been used for the verification of decomposition and gasification kinetics in chapter 1. The fixed bed, fluidized bed and energy balance models are presented in appendix A at the end of this thesis.

6.4.2 General findings

The general findings of the reactor model study are presented. These are valid for each of the configurations, but may be more pronounced for some of the configurations. They are discussed

separately to prevent double presentation of results. After the general findings, configuration-specific points are briefly discussed.

1. For the heating method, external heating and internal heating are varied between the various configurations. It was found that all process configurations using external heating require relatively small (0.05 - 0.3 m) diameters. The internal radial temperature gradient prevents effective use of larger systems at a controlled temperature. This was also found in the lab scale setup and is explained in detail in appendix A.3.
2. For all configurations, a fluidized bed yields a system with a higher productivity [$mol_c \cdot m_r{}^{-3} \cdot s^{-1}$] and better temperature control. This because the mixing of solids effectively removes internal temperature gradients, thereby creating a system that more efficiently uses the carrier throughout the reactor volume. This is visualized in figure 6.8. Moreover, due to the increased internal heat transport, the external wall temperature is lower, increasing the external heat transport as well. The added benefit is this is that larger diameter reactors are possible to be used, simplifying construction.
3. Using the combustion of deposited carbon as a heating source puts no constraint on reactor size, in fact larger systems are preferred due to the lower heat loss to the environment. This is a very efficient method of heating, as the heat is created where it is consumed.
4. Using a combination of carbon combustion and moving solids as a heating mechanism is technologically challenging. From thermodynamics only, it was calculated that relatively high solids to gas ratio (approximately 10-30 $\frac{kg_s}{kg_g}$) is required to ensure sufficient energy is present, for a high methane conversion. There is also a kinetic aspect to this, which will be discussed in the initial process analysis. It is noted that this phenomena is affected by particle characteristics.

From this, a general conclusion is that fixed bed reactors do not offer major advantages, compared to fluidized beds, for these cases. The increased constructional simplicity and easier operation of fixed beds are two noted advantages. However, for all of the configurations, two major points (internal heat transfer and solids mixing) are significantly better for a fluidized bed. Therefore, for all these configurations, a fluidized option is seen as preferable.

6.4.3 Configuration 1: Gasification & External heating

From the particle following model (section B.1), it was concluded that 2 important constraints are present for this configuration. First, the decomposition temperature should be controlled at (ideally exactly) 1130 °C. Second, the decomposition solids residence time should be in the order of minutes.

This configuration allows operation in a single reactor (switching the gasses) or multiple reactors (by transporting the solids between the systems). This is a choice not made trivially. Hence, both options are taken to the process level. The accompanying PFD are presented in figure 6.2. For both configurations, a (externally circulating) fluidized bed type is seen as the most likely candidate. In this work, for an externally circulating fluidized bed the definition of van Swaaij is used[14], meaning the solids are transported continuously in and out of one or more fluidized beds. A complete overview of van Swaaijs definitions is included in appendix B.

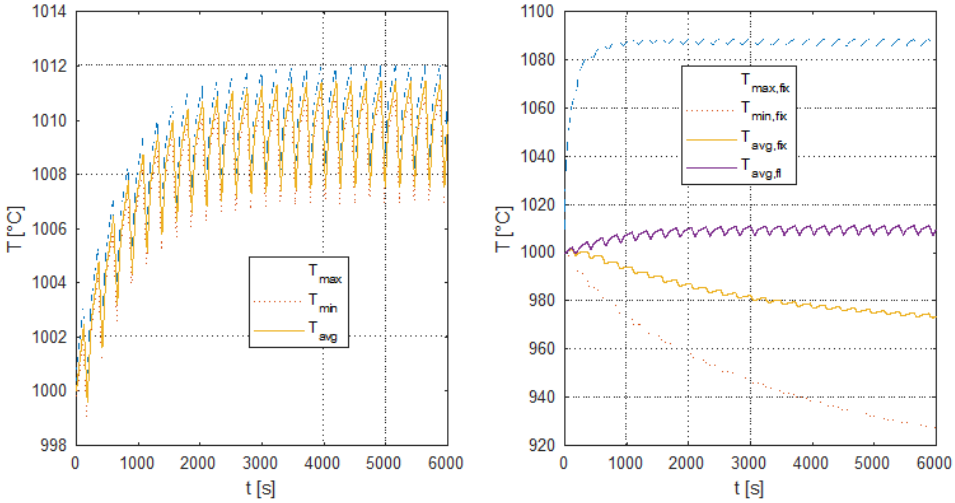

Figure 6.8: Left: fluidized bed temperatures, right: fixed bed temperatures. Reactor radius: 0.25 m, Heater temperature 1100 °C , all conditions equal between the two options. $T_{max,min,avg}$, denote the maximum, minimum and radius averaged temperatures. Subscripts $_{fix,fl}$ denote either a fixed or fluidized bed. Periodic variations over time due to cyclic operation of the reactors.

6.4.4 Configuration 2: Gasification & Internal heating

It is noted that this configuration allows excellent temperature control. One can vary the fraction of carbon that is gasified with steam, thereby decreasing the fraction of combusted C. This allows precise control of the temperature within the reactor(s).

For this configuration, no large internal radial temperature profiles are foreseen. However for fixed bed systems, temperature profiles could still be present, caused by a non uniform loading of carbon. Hence, there are situations possible where the reactor might not be heated satisfactory. In a fluidized system this is mitigated via mixing of solids. Hence, a fluidized system is seen as the only option for this configuration.

This configuration allows operation in a single reactor (switching the gasses) or multiple reactors (by transporting the solids between the systems). The accompanying PFD are presented in figure 6.3. This is also a choice not made trivially. Hence, both options are taken to the process level. Again, a (externally circulating) fluidized bed type is seen as the most likely candidate.

6.4.5 Configuration 3: Deposition only

As no gasification is used, no constraints are present on the decomposition conditions. Hence, for productivity purposes the deposition temperature will likely be as high as possible and the solids residence time short. As a consequence of carbon not being removed from the carrier, fresh carrier will need to be supplied to the system. Hence, fixed bed family reactors are seen as unsuitable for this configuration. An externally circulating fluidized bed is seen as the most likely candidate.

Heat transfer limitations might still be present, however moving solids will mitigate this partly. Nevertheless, models indicate a diameter above 0.2 m will greatly reduce the vollumetric productivity. Note that the operating temperature of this system is taken at approximately 1400 °C, being 200 °C higher than configurations 1 and 2. Therefore, the obtained productivity and the vollumetric energy consumption are relatively high for this configuration. The high temperature and short solids residence times point towards a riser, fast fluidized bed, or cyclone archetype reactor.

The ratio of gas to solids fed to the reactor has a maximum value. This occurs at the point where at 100% CH_4 conversion, the carrier is completely filled with carbon. This is given by equation 6.1, in which ϕ_g denotes a mass flow of gas or dense, $x_{c,g}$ the mass fraction of carbon in methane and $C_{c,d,max}$ the maximum carbon loading achievable. For the used particles, the maximum feed ratio is 0.37 kg_g/kg_d. Any higher gas to solid ratio will not be able to reach 100% CH_4 conversion.

$$\frac{\phi_{g,m}}{\phi_{g,d}} = \frac{C_{c,d,max}}{x_{g,c}} = \frac{0.29}{0.75} = 0.37 \tag{6.1}$$

It is noted that it is possible to operate this process cyclically, as well. This option has not been evaluated in this work, because it is known that a carrier fills up in the order of hours. Since the carbon cannot be gasified in this route, this then means all the solids need to be removed from this reactor every hour, which is seen as impractical.

6.4.6 Configuration 4 & 5: (Complete) oxidation of carbon

As these cases are comparable, they are discussed together. The complete oxidation of carbon (configuration 5) is a unique process configuration, as it is the only one having a net production of energy. Hence, the regeneration reactor volume will need to be cooled to prevent excessive temperature from occurring. Meanwhile, for the decomposition unit, heat is supplied via addition of the hot carrier, coming from the regenerator. No external heating is required.

For the energy balance, the solids to gas ratio is an important parameter. In appendix A of this chapter a calculation is presented, relating the solids to gas ratio with the temperature difference between the hot incoming solids and the pyrolysis reactor. The result of this calculation is presented in figure 6.9. From the energy balance, is concluded that a high solids to gas ratio is required to heat this system. The high solids to gas ratio may be problematic, since these solids need to be moved whilst at (extremely) high temperatures. It is noted that although the solids to gas ratio is on the high end, it is not unrealistically high[13]. It is concluded that this configuration is technologically challenging to realize. Since solids are transported from an oxygen combustion step to a pyrolysis reactor, an externally circulating fluidized bed is seen as the most likely candidate.

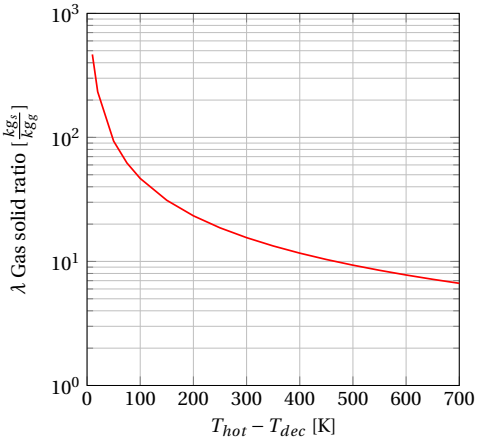

Figure 6.9: Calculated gas solid ratio and required temperature difference for an arbitrary reactor

Adding to this, a maximum operating temperature exists. This is either dictated by the used carrier or the used reactor materials, and is assumed to be in the order of 1400 °C. This, combined with the data in figure 6.9 also puts constraints on T_{dec}, which in turn affects the reaction rate. Concluding, this process is not easily characterized and will be investigated in detail in the next step.

6.4.7 Conclusion

The 5 different configurations have been characterized. An overview of the results is presented in table 6.4. It was found that the externally heated options are limited by internal heat transport. Therefore, large diameter reactors will be inefficient for these configurations. The options where the system is heated internally by combustion of carbon do not have this limitation. The heat is supplied there where it is consumed. Hence, it is concluded that internal heating is a very effective heating method, as little to no transfer limitations exist for this. Furthermore, it is noted that this heating method scales very well.

It is noted that a multitubular fixed bed is able to be used, due to the thin tubes. These will be able to be used effectively. The constructional complexity of this reactor is high, however.

The mixing state of the solids is partly related to the heating method. Should external heating be used it is preferred that the solids are mixed. In fact, a fluidized system is preferred for all configurations. However, for configuration 1 a residence time distribution effect exists. If a stabiliser, where the remaining carbon is combusted with oxygen is added, this effect can be mitigated. The selected reactors are now taken to a process level.

Table 6.4: Overview of findings in reactor analysis step

Process configuration	Proposed reactor	General findings (sec. 6.4.2)	Important characteristic
1	(Ext. circulating) fluidized bed	1	Reactor diameter Single or multiple units Stabiliser required
2	(Ext. circulating) fluidized bed	3	Single or multiple units
3	Externally circulating fluidized bed	1	Reactor diameter Solids to gas ratio
4	Externally circulating fluidized bed	3,4	Solids to gas ratio Operating temperature
5	Fluidized bed	3,4	Solids to gas ratio Operating temperature Cooling required

6.5 Level 2: Process analysis

6.5.1 Goal

In this section, the reactor models developed in the previous section are incorporated in simulations taking into account the whole process. It is aimed to reduce the number of configurations for the final analysis. All the reactors selected in the previous step will be evaluated. Characteristics such as flow magnitude, reactor size or achievable conversion will be compared in this stage. The least suitable configurations are excluded. By keeping the level of detail relatively low, this large amount of process options can still be compared.

In this section, a parameter sweep will be performed for each of the process configurations. A comparison is made on process characteristics such as required reactor volume for 100 ktpa H_2 production, or flow sizes.

First, the process boundaries, assumptions and reporting method are presented. This is also valid for the third and forth analysis levels.

Methodology

Before any comparison between the configurations is made it is important to establish how the processes are modeled. In this section it is discussed what is included in the analyses. Furthermore, it is presented how various estimations on heat exchange and gas separation are made. The following assumptions are made for the process analyses.

- The operating, inlet and outlet pressure is initially set at 1 bar. This is because all the kinetic data gathered in this work was obtained at this pressure. For industrial purposes, an elevated

pressure is more realistic. Therefore, the most viable process configuration will be evaluated at 30 bar in a second analysis.

- Pure methane is available at the plant.
- Pure oxygen is available at the plant.
- SA5262 is used as a carrier.
- The highest allowable temperature is 1400°C . This value is based on the specified continuous operating temperature of the used carrier
- The combustion of carbon using oxygen yields only CO.

The process boundaries set for this analysis are presented in figure 6.10. The possible process operations and streams are presented, but not present for all of the studied configurations. The production of reactants is not taken into account, nor are any required gas separations. It was found that all used reactors are able to produce products well into the 99% purity range. Hence, all configurations will require comparable separation steps, in terms of equipment or duty. Hence, it is argued that the separations will not make a meaningful difference for this comparison, and are excluded from the analysis.

Heat exchange is also presented as a step, how this is incorporated is discussed in section 6.8. The exact definitions of the KPI are presented in the next section.

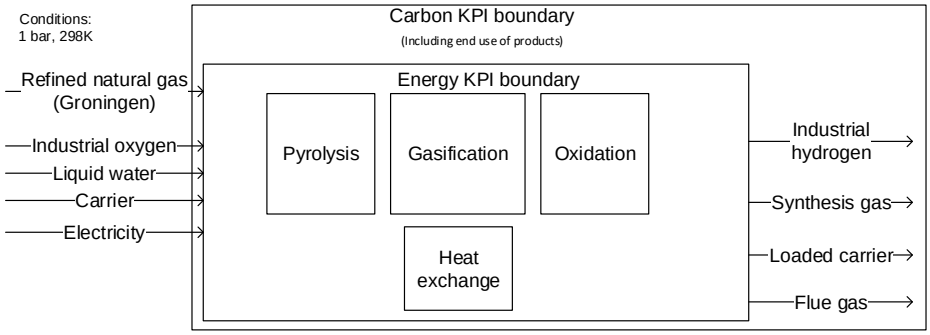

Figure 6.10: Schematic of defined process boundaries. Note that not all these operations and streams exist for every studied configuration.

Optimization routine

For both analysis level 2 and 3, a optimization method is used. This is not a traditional optimization. Instead, it is opted to perform a parameter sweep over (a selection of) the available process parameters. Whilst this might not guarantee the most optimized point is found, this does visualize trends. In the end, such a parameter sweep yields more information on which parameters are important for this design. Since it is not our goal to design the most optimal process, but instead to gather as much information as possible, it is argued this is the more suitable method.

In the process analysis, the parameter sweep will include all available parameters. This adds up to many combinations, however, since the reactor models are relatively simple, the computational time is manageable (order of 12 hours per sweep). Thus, many evaluations are possible.

6.5.2 Results

In this section, various parameters are incorporated into a parameter sweep. Various of these parameters can be chosen freely, such as reactor length. Some parameters are not able to be chosen freely, such as the superficial gas velocity. At high temperature, the minimum fluidization velocity u_{mf} increases[3, 16]. From this literature it is estimated u_{mf} is 3 $m \cdot s^{-1}$. Operating at 10 u_{mf} then yields an upper limit of 30 $m \cdot s^{-1}$for the gas in the reactor.

Configuration 1: Gasification + External heating

Two options of this configuration are evaluated, one continuous where pyrolysis and gasification occur in separate units and the solids are cycled between. The second options uses a single unit cycling through feed gasses over time. A risk identified in the reactor model analysis was that the gasification might not be able to remove all carbon deposited, thereby creating a net increase of carbon over time. This effect is amplified by a possible residence time distribution. A buildup of carbon will lead to bed deactivation. A remedy for this is the periodic oxidation using oxygen, which is known to remove all carbon in a short time. It is decided that this option should be present in an industrial configuration, as it is the only way to guarantee process stability.

Cyclic operation

A mass, mole and energy balance were constructed. Using this, a parameter sweep was performed. The varied parameters are presented in table 6.5. It was found that a high methane conversion is obtained with gas residence times in the order of 0.1 s and an inlet velocity of 30 $m \cdot s^{-1}$. This is in good agreement with experimental fixed bed data presented in chapter 2. Since these high conversions are achievable in these systems, only designs with a methane conversion above 90% were used in this analysis.

A large number (10-230) of reactor units are required for the range of reactor radii (r=0.1-0.2 m). The small diameters do lead to a high vollumetric productivity (order of 100 $mol_c \cdot {m_r}^{-3} \cdot s^{-1}$). This is expected, as identical figures were found in the heat transfer study presented in Appendix A.3. Larger diameters require fewer reactors, but have a lower productivity and therefore a higher total reactor volume for the production of 100 ktpa H_2 . This consideration will be strongly dependent on the capital costs of these reactors, which is foreseen to be high.

Therefore, it is concluded that the larger diameter reactors are more preferable. The selected size is manageable, and requiring fewer or only one unit simplifies this process. The achieved productivity in these systems is still in the order of 10 $mol_c \cdot {m_r}^{-3} \cdot s^{-1}$.

Table 6.5: Overview of model parameters for configuration 1, cyclic option

Parameter	Type	Range	Unit
L_{dec}	Input	1-5	m
r_{dec}	Input	0.1-0.6	m
$u_{g,methane}$	Input	10-30	$m \cdot s^{-1}$
$T_{dec,i}$	Input	1403	K
τ_{dec}	Input	150	s
τ_{gas}	Solved for steady state		s
T_{gas}	Solved for steady state		K
$u_{g,steam}$	Solved for steady state		$m \cdot s^{-1}$

Continuous operation

A parameter sweep comparable to the cyclic process has been performed for the continuous process (parameters shown in table 6.6). The gasification reactor volume was optimized as the minimum volume where the carbon conversion was 99%.

Table 6.6: Overview of model parameters for configuration 1, continuous option

Parameter	Type	Range	Unit
L_{dec}	Input	1-4	m
r_{dec}	Input	0.1-0.6	m
$u_{g,methane}$	Input	10-30	$m \cdot s^{-1}$
$u_{g,steam}$	Input	10-30	$m \cdot s^{-1}$
T_{heater}	Input	1473-1673	K
λ	Input	1-6	$\frac{kg_s}{kg_g}$
L_{gas}	Solved for min. vol.		m
r_{gas}	Solved for min. vol.		m

In this configuration, the total volume is the sum of a pyrolysis and gasification reactor, and for the units, each of these is counted individually. A stabiliser is assumed to be present, but the found loadings going into this stabiliser is small (order 1% total deposited carbon), hence the volume and addition of this single unit is neglected. Moreover, no net buildup of carbon then needs to be taken into account.

As was done with the cyclic process, the designs with a CH_4 conversion above 90% are selected. The same trends were observed for the continuous process as for the cyclic option. The required solids to gas ratio λ found for these designs is approximately 3-5 $[\frac{kg_s}{kg_g}]$. Lower ratios were also tested and are ineffective, as the solid fills up with carbon, lowering productivity. It is noted that albeit this ratio is not uncommon, the challenge of moving hot solids between reactors is technologically challenging.

Table 6.7: Comparison of the two configurations for configuration 1. The total required volume is given for a H_2 production of 100 ktpa.

Configuration	Approximate reactor size [m^3]
Continuous	36
Cyclic	15

Comparing continuous and cyclic configurations

In table 6.7 the key findings presented in this section are compared. The total required reactor volume for a production of 100 ktpa H_2 is presented. Because of the relatively low level of detail, these values are presented as indications. First and foremost it is observed that 100 ktpa H_2 can be reached in a single reactor for volumes that are feasible. One would realistically not consider constructing multiple smaller units. The continuous process reaches a 100 ktpa H_2 production at significantly lower volume. This has two reasons. First, by constantly circulating carrier, the average loading in the pyrolysis reactor is approximately 50% lower in the continuous process than it is in the cyclic process. Hence, the pyrolysis rate is enhanced. Secondly, the continuous process has two separate units, which are slightly smaller than the single unit of the cyclic process. This significantly enhances heat transfer into the system, allowing greater reaction rates in both systems.

From this data, one could conclude that the continuous process is desired. However, it must be noted that the continuous process requires transport of a large amount of solids, at high temperature. It is concluded that the cyclic process is the technologically easier of the two options to realize. Furthermore, it is concluded that the that the continuous process has a greater potential, should these technological challenges be overcome. It is noted that the required volumes are not unrealistically big for any of the configurations.

For the detailed analysis level, the cyclic process is evaluated, as this is the technologically simpler process and still has an acceptable reactor size.

Configuration 2: Gasification + internal heating

For this configuration, it was also decided to evaluate continuous and cyclic processes. These configurations are heated by combustion of the deposited carbon. In contrast to configuration 1, no external heat transfer limitations are present here. Therefore, much larger diameters are viable. From thermodynamic calculations it is known that approximately 14% of the carbon is available for steam gasification. The rest is combusted to supply energy for the pyrolysis and steam gasification steps. Should the in-going gases be fed at a lower temperature, the share of steam gasified carbon decreases.

Cyclic operation

The cyclic operation consists of a single unit, the PFD is analogue to figure 6.3. Over time, the inlet gas is changed periodically. The available parameters and swept ranges are presented in table 6.8. The fraction of steam gasified carbon is indirectly solved by changing τ_{gas}, to guarantee steady

state operation. The measure for this are the carbon loading and temperature at the beginning and end of the cycle.

Table 6.8: Overview of process parameters for cyclic configuration 2

Parameter	Type	Range	Unit
L_r	Input	1-10	m
r_r	Input	0.1-0.5	m
u_g Methane	Input	10-30	$m \cdot s^{-1}$
u_g Steam	Input	10-30	$m \cdot s^{-1}$
u_g Oxygen	Input	10-30	$m \cdot s^{-1}$
T_0	Input, initial condition	1673	K
τ_{dec}	From kinetic analysis	130	s
τ_{gas}	Solved to guarantee steady state		s
τ_{ox}	Dependent on U_g Oxygen		s

It was found that no effect of r_r on the conversion exists. Under the tested conditions. The required reactor radius for a 100 ktpa H_2 production is 1.5 m (u_g=30$m \cdot s^{-1}$, total volume 41 m^3). It is noted that relatively high carbon loadings are achieved (0.2 of the maximum loading).

Continuous operation

For the continuous option, the available parameters are presented in table 6.9. The recycle temperature is treated as input, as this effectively controls the decomposition and gasification reactor temperature. To guarantee steady state, the size of the gasification reactor is solved, indirectly solving the fraction of gasified carbon to be 14%. The measure for this is the recycle temperature.

The recycle temperature is set at the maximum acceptable value of 1400 °C. Based on the reactor model section and the thermodynamic analysis, the solid/gas mass ratio is set at 0.05. Note that this implies an extremely large solids flow. However, it was found that sufficiently heating the system is difficult, hence the high recycle temperature and large solids flow.

Table 6.9: Overview of process parameters for cyclic configuration 2

Parameter	Type	Range	Unit
$L_{r,d}$	Input	1-5	m
$r_{r,d}$	Input	0.1-0.6	m
$L_{r,g}$	Solved for steady state		m
$r_{r,g}$	Input	0.1-0.6	m
u_g Methane	Input	10-30	$m \cdot s^{-1}$
u_g Steam	Input	10-30	$m \cdot s^{-1}$
u_g Oxygen	Input	10-30	$m \cdot s^{-1}$
T_{recyle}	Input	1673	K
λ	From thermodynamic analysis		$[\frac{kg_g}{kg_s}]$

Comparing continuous and cyclic operation

When comparing both process options, differences are observed. First, in the required reactor volume. The continuous process requires a significantly smaller volume than the cyclic process (23 m^3 vs. 41 m^3), for a H_2 production of 100 ktpa.

This is caused by the fact that the cyclic process, during gasification and oxidation steps, does not have an inflow of methane. Therefore, to reach a H_2 production of 100 ktpa, a larger reactor radius is required. A minor difference in favour of the continuous process is caused by the lower loading (13-20% of max. loading, respectively) for the continuous process.

However, for the continuous operating system, the biggest challenge lies in the transportation of a large solids flow (at minimum 20 $\frac{kg_g}{kg_s}$) at high temperatures. This is a technological challenge, is seen as a showstopper for this option. Hence, the cyclic process is taken to a detailed analysis level.

Configuration 3: Pyrolysis only + External heating

As with the previous configurations, a parameter sweep was performed, varying r_r, L_r and λ. No parameter values, such as a reactor size or residence time, is solved in this configuration. The system is fully described by the in- and outlet flows, reactor temperature and reactor size. The inlet gas velocity was set at 30 $m \cdot s^{-1}$. For a radius of 1 m, the results are presented in figure 6.11. The gas to solid ratio λ was varied. It was found that this is an interesting parameter: it is observed that achieving a simultaneous high methane conversion and high solids loading is difficult, requiring large reactor sizes to reach this. A trade-off exists between the solids loading (cost of new solids) and the CH_4 conversion (cost of methane, energy efficiency) or reactor size (captial expense). Note that this trade-off is strongly dependent on the maximum achievable loading. For this configuration, it therefore makes sense to use a carrier with a high maximum loading, or a carbonaceous carrier that can be reused.

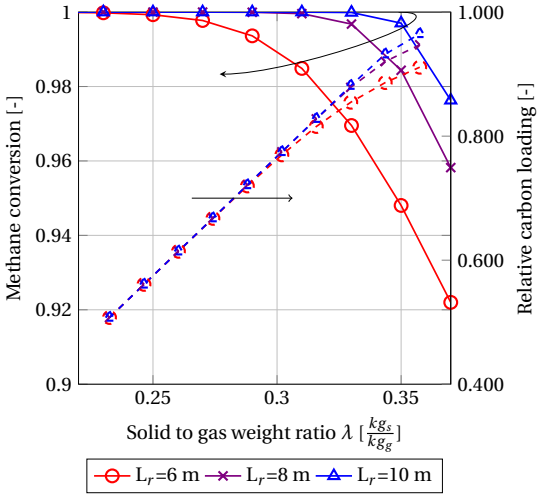

Figure 6.11: Results of parameter sweep for case 3. Data for r_r=1 m. Dashed lines: achieved loading. Solid line: CH_4 conversion.

Because the solids need to be replaced for this process, a fluidized bed type is seen as the only option.

Configuration 4& 5: (Complete) oxidation of carbon

A mass and energy balance were also constructed for configurations 4 and 5. Because of the similarity between these two, they are discussed together. The energy balance is most important for these configurations. As shown in the reactor modelling section, a complicated equilibrium exists between gas/solid ratio, reactor volume and reactor temperature. It was found that a large amount of solids $[\frac{kg_s}{kg_g}]$ is required to sufficiently heat the system and obtain a high CH_4 conversion. This was also observed via the reactor model calculations.

The kinetic component of this system is now included in the analysis. A solid/gas mass ratio lower than 10 is not able to achieve CH_4 conversions higher than 70% whilst keeping a plausible regenerator exit temperature, irrespective of reactor volume. Hence, higher solid to gas ratios are required, or the regenerator exit temperature should be increased. A ratio of 20 $[\frac{kg_s}{kg_g}]$ is able to sufficiently heat the system. However, as noted in all the other configurations, transport of this large solids flow is seen as problematic.

Should the solids flow and temperature ensure enough heat is supplied to the system, productivity in the order of 100 $mol_c \cdot m_r^{-3}$ are achieved. Therefore the decomposition reactor volume itself is relatively small and still able to achieve a high methane conversion.

For configuration 4, only a fraction of the carbon or carrier is combusted for heat. As a result, the recycle of hot carrier decreases in size. However, with this decrease, also a lower amount of energy is transported towards the pyrolysis reactor. Hence, the pyrolysis reactor cannot reach sufficient temperature. As a result either low CH_4 conversions or impractically large reactor volumes are required.

Concluding, the connection between the maximum allowable regenerator exit temperature, and desired high methane conversion results in a high solid/gas ratio of at least 20 $kg \cdot kg^{-1}$. Moreover, the exit temperature of the regenerator is high (max. 1400 °C), even for methane pyrolysis standards. Because of the high solid/gas ratio, the solids flow is also very large. This further complicates the technological feasibility of this process.

The remedy for this is the reduction of the solids flow and temperature. To still ensure a sufficiently hot pyrolysis reactor one would have to heat this unit externally as in configuration 3. One could still add and remove some part of the solids. Alternatively, a solid with a higher C_p could make this process more viable.

It is concluded that combustion of only a fraction of the carbon is not beneficial, as the energy balance will become increasingly unfavourable. The required solids flow, for both configurations, are seen as too big for these configurations to be feasible. Therefore, configuration 4 and 5 are not taken to the next design iteration.

6.5.3 Conclusion of this design iteration

In this section, a parameter sweep was performed for each of the process configurations. A comparison was made on process characteristics such as required reactor volume for 100 ktpa H_2 production, or flow sizes. Several trends were observed and discussed.

The configurations where solids need to be transported from between reactors were excluded. It was found that the required pyrolysis reactor temperature could only be achieved with a large solids to gas ratio. These large solids streams are seen as problematic. Since an alternative to this is present, and very effective, the configurations where moving solids facilitate heating are excluded. It is concluded that the benefit of solids transportation (a reduced carbon loading in the pyrolysis reactor) does not outweigh this technological challenge in realizing this. The configurations taken to the next design iteration are presented in table 6.10.

Table 6.10: Overview of configurations evaluated in the detailed step

configuration	Description	Operation mode	Vr [m^3]
1	Gasification+External heating	Cyclic	34
2	Gasification+Internal heating	Cyclic	42
3	Decomposition only + Ext. heat	Continuous	31

The indicative reactor volumes are also reported here. It is noted that all of these are comparable, at least within the accuracy of this analysis. Hence, at this point no conclusion is drawn on which of the three remaining configurations is the most preferable.

6.6 Level 3: Comparison of KPI

Definition of KPI

Several key performance indicators will be used in this work. In this section the definitions of these are presented.

Carbon intensity

The definition of carbon intensity has been based on the definition given in the carbon intensity targets of Shell (version January 2022[2]). To calculate carbon intensity, all emissions including production, processing, transport and end-use are summed. This definition is modified slightly for this work, as not every aspect of the production process is included.

The carbon intensity KPI is defined by equation 6.2 below. Note that all the non-offset ($N_{\text{reactants}} + N_{\text{ext}}$) carbon going in to the process is counted as emission, in agreement with the inclusion of end use of the product being a fuel in this KPI. N denotes a mass of carbon.

$$\kappa_c = \frac{\text{Total carbon emitted}}{\text{Total energetic production}} = \frac{N_{\text{reactants}} + N_{\text{ext}} - N_{\text{offset}}}{\text{LHV}_{\text{products}} - E_{\text{ext}}} [\text{gCO}_{2,e} \cdot \text{MJ}^{-1}] \tag{6.2}$$

Looking at the goal of a net zero CO_2 emission by 2050, the desired value for κ_c is 0. If natural gas from a well is used, this means an equal amount of C must be offset. A note is made that the carbon that is deposited but not further used, such as in process configurations 3 and 4 is considered as captured.

A representative benchmark value for κ_c is 75 $\text{gCO}_{2,e} \cdot \text{MJ}^{-1}$, this was the average net carbon footprint of shells activities in 2020[1]. Note that this value reflects all the activities along the production chain, making a comparison with κ_c values obtained in this work is nontrivial. Another take on an industrial benchmark may be via the CertifHy programme[5]. Here, a different definition for carbon intensity is used. The carbon present in the products is not taken into account for these values, only that emitted during production is included. To make a comparison to the values reported in this work, a second carbon KPI is defined:

$$\kappa_{c,prod} = \frac{\text{Total carbon emitted during production}}{\text{Energy in products}} = \frac{N_{\text{emitted}} + N_{\text{ext}} - N_{\text{offset}}}{\text{LHV}_{\text{products}}} [\text{gCO}_{2,e} \cdot \text{MJ}^{-1}] \tag{6.3}$$

The CertifHy is used to certify the origin of green hydrogen in the EU. The benchmark value for carbon emitted during low-emission hydrogen production is 36.4 $\text{gCO}_{2,e} \cdot \text{MJ}^{-1}$ for hydrogen. The benchmark value for current hydrogen production using gas fired steam reforming is 91 $\text{gCO}_{2,e} \cdot \text{MJ}^{-1}$. Interestingly, a value is also given for thermal methane decomposition (36 $\text{gCO}_{2,e} \cdot \text{MJ}^{-1}$). Although no detailed calculation was reported, for these LCA it is clearly defined what is (not) part of the analysis[5], possibly making comparison more feasible.

Energy efficiency

Energetic efficiency is evaluated via equation 6.4. External energy not part of the reactants may be a heating duty or electricity consumption. Note that this KPI does not consider integrated heat. For this, a secondary energy KPI η_{hex} is defined in equation 6.5. In this, E_{ext} is the same as in equation 6.4, the integrated heat is removed from this. Methane steam reforming has an LHV based energy efficiency of approximately 75 %[10, 15].

$$\eta_{\text{heat}} = \frac{\text{LHV}_{\text{products}}}{\text{E}_{\text{in,net}}} = \frac{\text{LHV}_{\text{products}}}{\text{LHV}_{\text{reactants}} + \text{E}_{\text{ext}}} [\text{kJ} \cdot \text{kJ}^{-1}] \tag{6.4}$$

$$\eta_{hex} = \frac{LHV_{products}}{E_{in,net}} = \frac{LHV_{products}}{LHV_{reactants} + E_{ext} - E_{integrated}} [kJ \cdot kJ^{-1}] \tag{6.5}$$

External heat supplied to the reactor can be sourced from electricity, methane or hydrogen. In this work, it is assumed it is supplied by CH_4 combustion.

The second analysis iteration will focus on the defined KPI. The method of analysis is comparable to the initial analysis and briefly discussed. Instead of using some optimization routine, it is opted to again perform a parameter sweep. This is because by sweeping numerous parameters, the (initially unknown) effects of these parameters on the KPI may be visualized. Not only does this then show the characteristics of the optimal design, also further knowledge on the important process parameters is obtained. Note that it is possible to evaluate thousands of different process configurations because the computational time is relatively short.

Initially the energy KPI is evaluated, as the carbon KPI is not applicable for all process (e.g. no CO is produced). The following assumption is made for this analysis step:

The feed rate of CH_4 is limited by the inlet gas velocity, set at max. 30 $m \cdot s^{-1}$. If the total CH_4 inflow would then produce an excess of 100 ktpa product, the inlet speed is decreased to match the production of 100 ktpa of product. Regardless of process configuration, at a radius of approximately 1.5 m and an inlet velocity of 30 $m \cdot s^{-1}$, the total production reaches 100 ktpa of H_2 (at 100% CH_4 conversion), and the linear gas velocity is decreased, to prevent excess of 100 ktpa H_2 production. This allows more effective utilization of larger diameter systems, by lowering the gas residence time. Lower inlet velocities are also evaluated for the designs under 1.5 m radius, thus requiring multiple units.

6.6.1 Configuration 1

For configuration 1, a selection of the optimization results are presented in figure 6.12. The individual lines denote various inlet gas speeds. The subfigures denote an increasing T_{heater}. These parameters were chosen as they most clearly show the observed trends. These results indicate the maximum energy efficiency reached at these points, occurring at various reactor length and diameters. This is a selection of the obtained results. Three points are noted.

First, the lower temperatures (fig. 6.12a) have a low energy efficiency, because they operate at incomplete CH_4 conversion. Only at the lowest inlet velocity, the single pass conversion approaches 100% (10 $m \cdot s^{-1}$in figure 6.12b). At higher T_{heater}, more cases approach 100% CH_4 conversion, and have an increased energy efficiency. It is concluded that at low temperatures, low inlet speeds are required.

Secondly, with increasing temperature, a maximum in efficiency can be observed. For all radii, this is the minimum temperature at which (near) 100% CH_4 conversion occurs. This occurs at 1473-1523 K, depending on the radius, feed rate and reactor length. Hence, the optimal heater temperature will lie in this range. Increasing the temperature further only yields a larger energy loss.

Concluding, for these diameters (0.5-1.4 m), operating at a total production of less than 100 ktpa H_2 , the only action to increase production is to use multiple units, or a higher inlet velocity. The other option is to use a larger reactor radius. In this configuration, the feed can be set to equal a production of 100 ktpa H_2 . This has the advantage that the gas speed decreases with diameter,

whilst reaching the required production. This has been evaluated for reactor radii ranging between 1.5 and 2 m. The maximum obtained efficiency and corresponding H_2 production are presented in figure 6.13. Note that various radii and lengths are present in this data.

From this, it is concluded that 100 ktpa can be reached in a single system. The energy efficiency again has a maximum. It is observed that this maximum occurs at a higher $T_{heater}$for the large diameter set (fig. 6.13), than for the low diameter set (fig. 6.12c). This was expected, as large diameters are inefficient to heat this system. The final design in presented in the comparison section.

Comparing these energy efficiencies to the current industrial standard of 65-75% for steam reforming[6], does not favour configuration 1. It is noted that various aspects (oxygen generation, gas separation, flush gas and heat loss) are currently not taken into account for the energy efficiency calculation. Hence, the reported value will decrease further. Hence, based on current knowledge, it it expected that configuration 1 will have a lower energy efficiency than SMR.

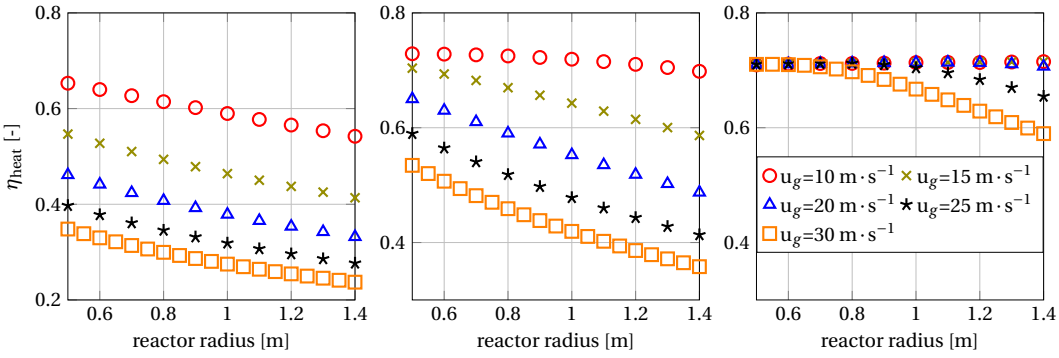

(a) 1323 K *(b)* 1373 K *(c)* 1473 K

Figure 6.12: Selection of case 1 optimization results. Energy efficiency as function of reaction length for various reactor radii. Per subfigure, the initial temperature is varied.

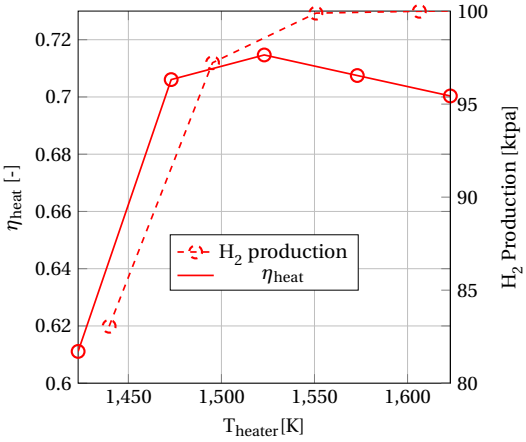

Figure 6.13: Max hydrogen production (dashed, right axis) and max. energy efficiency (solid, left axis) for case 1. Various radii (1.5-2 m), various lengths

6.6.2 Configuration 2

The results for configuration 2 are presented in figure 6.14. The maximum energy efficiency is presented as function of the initial temperature. The initial temperature is defined to be the solids temperature before pyrolysis starts. The lines represent different gas inlet speeds. No effect of radius is present for this system, hence it can be chosen freely to scale the production, accordingly. Various lengths are included in this analysis, however.

The low efficiency at low initial temperatures is caused by low CH_4 conversion. With increasing temperature, CH_4 conversion rises until it approaches 100%. This is the point of maximum thermal efficiency for any reactor size. After this, the efficiency decreases, due to the larger loss caused by unnecessary heating.

Because no effect of radius exists, one could theoretically reach a 100 ktpa H_2 production with any radius and inlet velocity. However, in this a trade-off can be identified. An increase in productivity $[mol_c \cdot m_r^{-3} \cdot s^{-1}]$ results in a lower energetic efficiency. To illustrate this, in figure 6.15 the obtained productivity $[mol_c \cdot m_r^{-3} \cdot s^{-1}]$ of an arbitrary reactor is presented, as function of initial temperature and gas inlet velocity. One can see the lower inlet velocities result in a less productive system, which achieves a high CH_4 conversion at low temperature. The opposite is also true, the higher inlet velocity results in a high productivity whilst requiring a high temperature and low energy efficiency.

Hence, the reactor size (capital cost) will have to be balanced with the energy cost (operational cost). It is noted that any temperature reduction is favourable for the heat exchange complexity and cost. Moreover, it is noted that the thermal efficiency of this system is significantly higher than that for configuration 1. This is attributed to the fact that in this case, no carbon is lost in the from of CO_2 , thus significantly reducing overall losses.

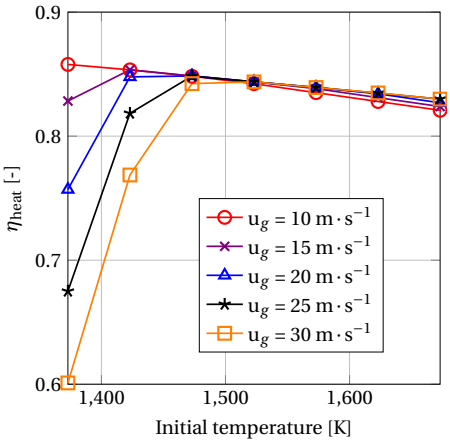

Figure 6.14: Obtained maximal energy efficiency for the case 2 detailed analysis. Initial temperature is the solids temperature at the start of each cycle.

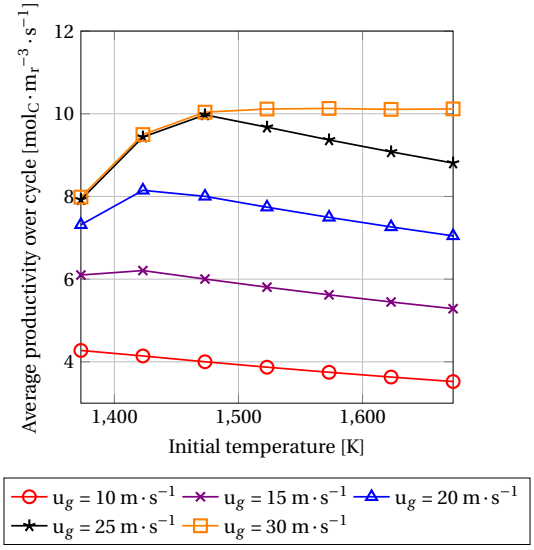

Figure 6.15: Obtained maximal productivity for the case 2 detailed analysis. Initial temperature is the solids temperature at the start of each cycle.

6.6.3 Configuration 3

Configuration 3 is the externally heated - pyrolysis only configuration. Because of the external heating, similarities between this configuration and configuration 1 exist. The trends regarding the effect of radius may be observed. Hence, they will not be presented in detail again. From the initial analysis, a solids to gas ratio (λ, figure 6.11) of 0.33 $kg \cdot kg^{-1}$ is estimated. This balances solids efficiency with high reaction rates.

The highest obtained energetic efficiency as function of heater temperature is presented in figure 6.16. This figure again has strong similarities to figure 6.13. The optimal heat temperature is approximately 1500 K. The biggest difference lies in the much lower efficiency for configuration 3. Because the carbon is not gasified, a large amount of energy is lost. Furthermore, because the carrier is continuously cycled trough the reactor, a large amount of energy is required to heat this carrier. This further reduces the energy efficiency.

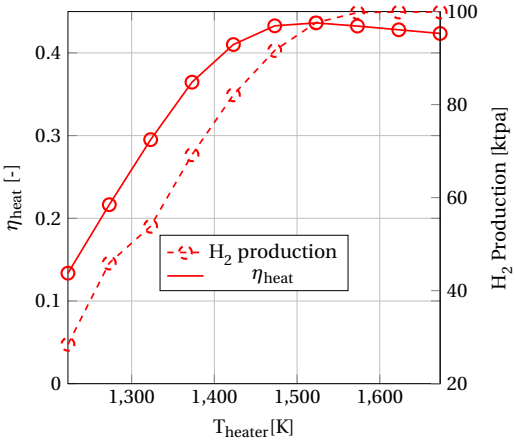

Figure 6.16: Max hydrogen production (dashed, right axis) and max. energy efficiency (solid, left axis) for case 3. Various radii, various lengths

It is noted that the heater temperature is not as high as expected (expected approximately 1700 K, found 1580 K) from the basic modelling calculations. The higher temperatures were evaluated, and resulted in very compact reactors. However, due to the high heating duties, the energetic efficiency of these types was approximately 4 percent points lower than the found optimum. Simultaneously, it is noted that the more efficient designs are not unrealistically big (approximately 70 m^3). Hence, these high temperature designs are not evaluated further.

6.6.4 Conclusion of the KPI comparison

Three possible configurations for an industrial methane pyrolysis process have been compared. Mass and energy balances were constructed, in this a reactor model was incorporated. Key performance indicators were defined, related to energy efficiency and carbon intensity. Significant

variations were found between the configurations. These will first be discussed. This section concludes with some general findings. The results are summarized in table 6.11.

For configuration 1, the energy efficiency is largely reduced via the production of water, from the combusted methane. This explains the slightly reduced energy efficiency, compared to configuration 2. The relatively large fraction of combusted methane is explained by the high amount of hydrogen produced, per methane. This requires a large amount of energy.

Configuration 2 is more efficient in every aspect. Both the heating method and the avoided side product production significantly enhance the performance of the system. A lower amount of hydrogen is produced, per methane, for configuration 2 as compared to configuration 1. Interestingly, because the reactor can be heated more effectively, a smaller reactor is required for configuration 2, to reach 100 ktpa of H_2 . Moreover, options exist to further increase energy efficiency, via a lower temperature. For this, a significantly larger system is required, that operates at approximately 200 °C lower temperature. This benefit for the heat exchange section, combined with the increased efficiency make configuration 2 significantly more attractive than configuration 1.

Configuration 3 suffers from the same shortcoming as configuration 1, as significant amounts of water are produced during the combustion of methane. Moreover, since the process configuration dictates that the carbon cannot be utilized and is effectively captured, this energy is lost too. Although the reaction occurring in this system is the least complex of all the configurations, the technical challenge of this configuration is the most difficult. It is the only configuration where solids movement is strictly required.

However, in contrast to configuration 1, configuration 3 offers a clear advantage. Looking at the carbon emission KPI, configuration 3 has potential. Because the deposited carbon is unused, it may be considered captured. This does not require additional separations, and can therefore be seen as a effective method of carbon emission avoidance. It is concluded that, looking at carbon emissions, configuration 3 is the most promising.

It is noted that all calculated reactors are realistically feasible to construct. The total size of these systems is manageable. Naturally, this process will not be operated at 1 bar. In the final section of this chapter, configuration 2 will be sized to a 30 bar system.

Table 6.11: Results of detailed analysis step [a] final temperature during respective phase, [b] average during phase, [c] average over a cycle, [d] methane only, [e] single pass conversion, [f] including recycle

Configuration	1	2	2	3	2	Unit
Variant		High T	Low T		30 bar	
Lr	10	12	12	8	4	m
Rr	2	1.5	2.75	1.5	1.1	m
Vr	125	85	285	73	15	$m_r{}^3$
η_{heat}	0.68	0.84	0.86	0.43	0.78^f	-
η_{hex}	0.77	0.88	0.91	0.46	0.85^f	-
η_C	0.64	0.94	0.95		0.95^f	-
κ_c	68	59	58	35	63^f	$gCO_{2e}{\cdot}MJ^{-1}$
$\kappa_{c,p}$	33	11	9	35	15^f	$gCO_{2e}{\cdot}MJ^{-1}$
Fraction combusted	0.35	0.07	0.05	0.16	0.07^f	-
Productivity	14.3	16.7	4.9	11.8	81	$mol_c \cdot m_r{}^{-3} \cdot s^{-1}$
u_g	30	30	7.7	15	1.9	$m \cdot s^{-1}$
CH_4 conv.	0.999^b	0.999^b	0.998^b	0.999	$0.78^{b,e}$	-
					0.999^f	-
Steam conv.	0.95^b	0.9^b	0.87^b		0.996^b	-
T_{heater}	1623			1623		K
T_{dec}	1501^a	1518^a	1334^a	1535	1593^a	K
T_{gas}	1502^a	1449^a	1314^a		1426^a	K
T_{ox}		1574^a	1350^a		1700^a	K
Solids flow				42		$kg \cdot s^{-1}$
λ	118^d	56^d	191^d	0.33^d	19^d	$kg_s{\cdot}kg_g$
GHSV	5400	4400	1300	2500	24800	$m_g{}^3 \cdot m_r{}^{-3} \cdot h^{-1}$, STP
GHSV at operating T,P	27100	22500	5800	13100	4400	$m_g{}^3 \cdot m_r{}^{-3} \cdot h^{-1}$

It is noted that for all the designs, a trade off exists between some capital expense, and the energy efficiency. Because no economic analysis is made in this work, the analysis will be left at this point.

6.7 Level 4: Comparison to the industrial standard.

6.7.1 The effect of increased pressure

The industrial design is evaluated at 30 bar, to better reflect the typical pressures in an industrial plant. The three most significant effects of this pressure change are briefly discussed. Starting with the first order pyrolysis and gasification rates, these will be enhanced significantly. For this analysis, it is expected that the system will be energy transfer limited. The challenges of heat

transfer identified in the basic modelling section will be increasingly present, for this case. Hence, the configurations that are heated internally are seen as most promising for the industrial case.

A second effect of the pressure increase is that the equilibrium conversion will be significantly reduced (e.g. CH_4 conversion = 0.77 at 1500 K). Even at 2000 K and 30 bar, single pass CH_4 conversion is barely exceeding 90%. Hence, gas separation and methane recycling will be required to reach specifications. Moreover, this will decrease energy efficiency significantly. For the calculations in this section, it is assumed a recycle is used, increasing the net conversion of CH_4 to near 100%.

A third effect is that the pyrolysis rate may scale with pressure, as far as we know the amount of carbon that can be deposited on the carrier will not. For this, the solid to gas ratio is an important parameter. To supply sufficient energy for the pyrolysis and subsequent steam gasification, the solid to gas ratio should be sufficiently high. However, because of the enhanced carbon deposition rate, it is easier to fill up the carrier. During simulation it was noted that a lower solids to gas ratio is sufficient to achieve high conversion, for the high pressure case. The enhanced pyrolysis rate means that conversion is reached using significantly less carrier. Due to this lower solids to gas ratio the limiting factor then becomes the temperature.

To briefly reflect on configurations 4 & 5, the increased pressure does not solve the observed challenges for these configurations. The increased pressure indeed increases the reaction rates. However, the issue of configurations 4 and 5 comes down to the amount of energy that can be stored (or transported) in a solids flow. This is not a function of pressure. Hence, the problems observed are present to the same extent for a high pressure system.

Concluding from these three points, the most likely candidate is then a system with a relatively short cycle time and relatively low solids to gas ratio. It should be emphasized that the obtained results are strongly dependent on the used carrier. Should a higher loading or vastly different area per volume carrier be used, these results change. Note that increasing the maximum carbon loading of the carrier does not affect the results significantly, as the high loadings are not reached.

Another significant effect lies in the minimum fluidization velocity u_{mf}. With increasing pressure, u_{mf} decreases. Therefore, the calculated maximum of 30 $m \cdot s^{-1}$is not realistic for high pressure systems. However, from the calculations it was found that these high velocities are not preferable. The found value (1.9 $m \cdot s^{-1}$) is assumed to be feasible. Due to the combination of high temperature and elevated pressure, large uncertainties are present.

6.7.2 Industrial design

The high pressure industrial case was modelled using the same models as the 1 bar case. Initial analysis of this system indeed showed the enhanced productivity at relatively low solids to gas ratio. To visualize this, the temperature profile and carbon loading of the industrial and conventional high temperature design are presented in figure 6.17. The increased reaction rates allow a large temperature swing in a short amount of time. This was not possible using the 1 bar kinetics, as the reaction rate could not keep up. One can also clearly observe the increased loading.

The enhanced loading and higher productivity result in a significantly smaller reactor. The obtained results are included in table 6.11. The reactor volume for a 100 ktpa H_2 production is reduced with a factor 5 using the high pressure configuration. At 1 bar, the short gas residence time (0.8 s) has been observed to correspond to a high CH_4 conversion, experimentally. It is concluded that a small unit is able to process large amounts of gas.

The mass and mole balance of the system is presented in table 6.12. Note that no carbon nor Al_2O_3 is visible on the mass balance, as it does not leave the reactor. The temperatures reported are the same as presented in figure 6.17. The incorporation of flows of a cyclic process is discussed in appendix C of this chapter.

The reduced CH_4 conversion reduces the thermal efficiency of this system. The additional required separation will further decrease the efficiency. It is noted that, since gasses are present at elevated pressure in a typical industrial plant, running these processes at 1 bar is not a viable option. Unfortunately this does imply that the efficiency of these processes is reduced. This also implies that, due to the lower conversion, an even larger process stream needs to be fed to the heat exchanger system, further complicating this step. Due to the relatively large energy loss, efficient heat exchange is even more important, for the industrial case.

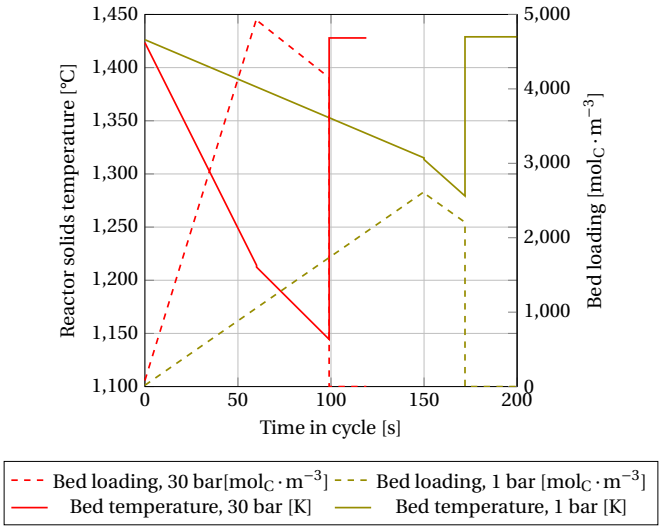

Figure 6.17: Bed loading (dashed, right axis) and reactor temperature (solid, left axis) for case 2. Both the industrial (30 bar) and the conventional (1 bar) are visualized. Air oxidation step assumed to be instantaneous.

Table 6.12: Mass balance for the 30 bar industrial case. [a] initial temperature, [b] average over cycle, [c] final temperature

	Inlet	Gasification in	Oxidant in	Pyrolysis out	Gasification out	Oxidant out
T	1700[a]	1594[b]	1455[b]	1594[b]	1455[b]	1701[c]
			Mass flow [$kg \cdot s^{-1}$]			
CO					3.2	19.8
CO_2						
CH_4	16.8			3.6		
H_2				3.3	0.2	
H_2O		2.0			0.0	
O_2			11.3			
Total	16.8	2.0	11.3	6.9	3.4	19.8
			Mole flow [$mol \cdot s^{-1}$]			
CO					113	708
CO_2						
CH_4	1045			224		
H_2				1643	113	
H_2O		113			0	
O_2			354			

The limiting factor now is the temperature at the end of a cycle. It is noted that the same amount of solids are able to convert significantly more methane, at high temperature. The large amount of solids now mainly functions as a heat storage. Hence, it would be beneficial to utilize a carrier with a higher heat capacity. This can be realized, by mixing in a fraction of nonporous carrier, or using a carrier with a significantly lower porosity (keeping the internal area the same). The contained energy will be supplied to the reactions, whilst the carbon capacity is reduced. This allows operating at a lower initial temperature, yielding energy efficiency benefits.

6.7.3 Comparison to the industrial standard

To conclude this chapter, the calculated KPI will be compared to the industrial standard. It is noted that the amount of data and process steps included in the calculations in this work is relatively small. Because a lower amount of steps or operations are included, the values calculated should be an underestimation when compared to the more complete literature data.

An overview is presented in table 6.13. Starting with the overall κ_c , the calculated values are comparable to the overall κ_c of shells worldwide activities. Two points are noted. First, should a comparable amount of detail be incorporated in these calculations, it is expected that the κ_c for configurations 1 and 2 (all variants) exceeds the benchmark of 75 $gCO_{2,e} \cdot MJ^{-1}$. A figure for steam reforming was also calculated from literature data. This represents a value for κ_c resulting from a complete LCA. Should this also be performed with the pyrolysis process, under equal assumptions, it is likely that the pyrolysis route ends up at a comparable or higher number. Hence, it is not possible to conclude that the pyrolysis processes are more or less energy efficient than the

industrial standard. It is noted that the value of the κ_c is strongly dominated by the end product. Hence, if an equal product is made, this KPI is not the most useful for comparison.

Second, configuration 3 has a clearly lower κ_c . This is because the carbon originating from the methane is considered captured. It is then concluded that the dumping of carbon may be beneficial, in order to meet future emission standards. In fact, any process producing an arbitrary hydrocarbon will have a relatively high carbon intensity, as the carbon in the product itself is counted as emission. Hence, it is concluded that the only method of reducing this intensity is the utilization of non-fossil carbon sources, or offsetting the carbon, as is (partially) done in configuration 3. It is noted that offsetting carbon (via a method other than dumping the carbon, for configurations 1 and 2) is not challenging, as this is already separated from the vast majority of produced hydrogen. It is concluded this might be a major advantage for these process configurations, when compared to SMR.

Table 6.13: Overview of calculated KPI. [a] calculated from reported data, [b] literature value, [c] estimated using literature data, [d] sum of all global activities

Indicator Unit	κ_c $gCO_{2,e} \cdot MJ^{-1}$	$\kappa_{c,p}$ $gCO_{2,e} \cdot MJ^{-1}$ calculated	$\kappa_{c,p}$ $gCO_{2,e} \cdot MJ^{-1}$ literature	η_{heat} $kJ \cdot kJ^{-1}$ calculated	η_{heat} $kJ \cdot kJ^{-1}$ literature
SMR	124[a][11]		91		0.75[10, 15]
Shell[d]	75[b]				
eSMR	25 [c]	3 [c]			0.85[c]
Config. 1	68	33		0.85	
Config. 2, high T	59	11		0.87	
Config. 2, low T	58	9		0.89	
Config. 2, 30 bar	63	15		0.85	
Config. 3	35	35	36	0.46	

A perhaps more fair comparison lies in the production carbon intensity $\kappa_{c,p}$. Only for configuration 3 a value is reported in the CertifHy LCA. Good agreement is found for the calculated value for configuration 3 and the reported value, even though not all aspects are included in our calculation. The exact assumptions behind the values in literature were not reported, making it difficult to assess these numbers.

It is noted that the calculated values for $\kappa_{c,p}$ of configurations 1 and 2 (all variants) are relatively low. The avoided CO_2 via the formation of CO is not accounted as emission, by the CertifHy standard. Hence, the gasification of this carbon is seen as a carbon neutral method of heating. The only emitted CO_2 now is caused by the residual heating of gasses using CH_4 . It is concluded that the CH_4 pyrolysis processes discussed here are suitable to produce low-carbon hydrogen, as measured by the CertifHy standard.

Regarding energy efficiency, a large spread in calculated values is observed. The gasification configurations operating at 1 bar have the highest efficiencies. Again it is expected that these will decrease with a more complete analysis. Hence, with the current knowledge, it cannot be said how

these compare to steam reforming. For the 30 bar configuration 2 and 1 bar configuration 3, it is concluded that these configurations are probably less energy efficient than steam reforming. Even with effective heat exchange, the energy loss remains large. Note that the calculated energy efficiency now includes heat exchange, which is technologically not developed enough for industrial application. It is noted that the low temperature configuration 2 option is not applicable for industrial pressures, due to the significantly lower achievable conversion (0.3 at 1000 °C).

6.7.4 Comparison to eSMR

It is also aimed to compare the pyrolysis processes to a future electrified steam reformer (eSMR). For this, a literature study was performed[8, 17–19]. Some lab scale data is available for electrified SMR. For this comparison it is assumed the electricity is obtained from renewable sources, and hence has a low carbon emission factor.

These electrically heated units deliver the heat to the catalyst itself and operate without heat or mass transport limitations[18], making efficient use of the available catalyst. Therefore, high vollumetric productivity can be achieved. Moreover, no side products are expected, comparable to configuration 2.

Limitations for this system are noted. The reactor designs used in literature compose of thin (6-10 mm OD) tubes, making large scale construction complex. It is noted that this problem is not present for the pyrolysis process, this can occur in a single large volume. It is therefore expected that the pyrolysis process is technologically simpler to construct. This is seen as the largest advantage of pyrolysis over eSMR.

Secondly, it is foreseen that catalyst deactivation might become a more prominent problem for eSMR[18], due to the increased conversion rate per unit of catalyst. This is as far as we know not present for the pyrolysis process.

A major difference between SMR and pyrolysis is that for the steam reforming process, 3 H_2 per CH_4 are produced. Hence, this process makes more efficient use of the feedstock. Due to the efficient heating and relatively high conversion (90 %), this yields a process with a low carbon intensity. Note that no CO_2 is produced in the process itself, as is the case for CH_4 pyrolysis. The increased carbon efficiency is seen as the major advantage for eSMR over pyrolysis configurations.

It was found that for processes operating without side product formation, energy efficiency is dictated by the operating temperature, estimated for eSMR at 1000 °C[18]. The effects of heat exchange are foreseen to be comparable, due to the temperature and gas composition similarities. Hence, it is expected that this will be comparable to the pyrolysis process (0.85).

Lastly, the SMR process is a fully continuous process. No cyclic operating is required. Hence, no time or effort needs to be dedicated to the switching of gasses entering the reactor. This is seen as an advantage for the SMR process.

Concluding from these points, the biggest differences between eSMR and the pyrolysis configurations lie in the constructural complexity and the potential for carbon efficient production. Should the eSMR system be realized, it will theoretically be more carbon efficient than the pyrolysis configurations. Should the construction of the eSMR system be too complex or expensive, pyrolysis can be a viable alternative. Two points are noted. First, at this point it is impossible to foresee which of these points hold true. Secondly, neither of the processes produce CO_2 , hence from this aspect both are viable configurations.

6.8 Conclusion

In this chapter, various process configurations of a methane pyrolysis process were evaluated. It was aimed to investigate the industrial application of this process, and find out which parameters are important for this design. First, it was concluded that the majority of the externally heated systems are severely heat transfer limited, a multitubular reactor being the exception. Internally heated systems were found to be very attractive in terms of heat transfer. Furthermore it is concluded that heating via the combustion of carbon offers attractive scaling opportunities.

In the detailed analysis, it was confirmed that heating via the recycling of hot solids is not effective. The connection between maximum allowable temperature, reactor size and methane conversion dictates that a very large solids to gas ratio is required. It is concluded that recycling of solids is an unsuitable heating method.

Energy efficiency was defined as a KPI. It was found that the internally heated steam gasification process has a high energy efficiency. No side products are produced. Hence, the only energy loss is caused by heat exchange losses. From a literature study, it is found that heat exchange is currently unable to be used at high temperature in an industrial application. Hence, it is concluded that HEX is an important challenge for the viability of the methane pyrolysis process.

Carbon intensity was also defined as a KPI. It was found that the carbon intensity was dominated by the choice of process configuration rather than reactor or process parameters. Should an efficient configuration be chosen, a relatively low carbon emission is obtained. It is concluded that the oxidation of C to CO internally is an attractive heating method in terms of carbon efficiency. Furthermore, it is concluded that CH_4 pyrolysis is able to produce low-carbon H_2 , as per the CertifHy certification scheme.

The most suitable design was evaluated at 30 bar to better reflect the industrial conditions. It was found that this increased pressure allows significantly more efficient use of the carrier, operating at maximum conversion with a much lower solid to gas ratio. However, the pressure increase reduces energetic efficiency, due to the lower conversion. It is concluded that the methane pyrolysis process at elevated pressure is probably less energy efficient than the current industrial standard. The high pressure kinetics are a large uncertainty and must be investigated in future work. Lastly, due to the lower conversion, effective heat exchange becomes more important for the high pressure process.

It is concluded that methane pyrolysis may be a viable way to reduce the carbon intensity of industrial syngas or hydrogen production, should the identified challenges be overcome.

Bibliography

[1] Our net carbon intensity, 2020. URL https://reports.shell.com/sustainability-report/2020/achieving-net-zero-emissions/our-climate-target/our-carbon-intensity.html.

[2] Our net carbon intensity targets, 2020. URL https://reports.shell.com/annual-report/2020/strategic-report/climate-change-and-energy-transition/our-net-carbon-intensity-targets.php.

[3] Aditya Anantharaman, Ray A. Cocco, and Jia Wei Chew. Evaluation of correlations for minimum fluidization velocity (Umf) in gas-solid fluidization. *Powder Technology*, 323:454–485, 2018. ISSN 1873328X. doi: 10.1016/j.powtec.2017.10.016.

[4] A. Banerjee, R. Bala Chandran, and J. H. Davidson. Experimental investigation of a reticulated porous alumina heat exchanger for high temperature gas heat recovery. *Applied Thermal Engineering*, 75:889–895, 2015. ISSN 13594311. doi: 10.1016/j.applthermaleng.2014.10.033. URL http://dx.doi.org/10.1016/j.applthermaleng.2014.10.033.

[5] Frederic Barth, Wouter Vanhoudt, Marc Londo, Jaap C. Jansen, Karine Veum, Javier Castro, Klaus Nürnberger, and Matthias Altmann. CertifHy - Developing a European Framework for the generation of guarantees of origin for green hydrogen. *WHEC 2016 - 21st World Hydrogen Energy Conference 2016, Proceedings*, pages 1022–1023, 2016.

[6] A. Carrara, A. Perdichizzi, and G. Barigozzi. Simulation of an hydrogen production steam reforming industrial plant for energetic performance prediction. *International Journal of Hydrogen Energy*, 35(8):3499–3508, 2010. ISSN 03603199. doi: 10.1016/j.ijhydene.2009.12.156. URL http://dx.doi.org/10.1016/j.ijhydene.2009.12.156.

[7] Masaya Kumada and Yuji Himeji. a Study on the High Performance Ceramic Heat Exchanger for Ultra High Temperatures. pages 107–112, 2019. doi: 10.1615/ihtc11.1390.

[8] Eugenio Meloni, Marco Martino, Antonio Ricca, and Vincenzo Palma. Ultracompact methane steam reforming reactor based on microwaves susceptible structured catalysts for distributed hydrogen production. *International Journal of Hydrogen Energy*, 46(26):13729–13747, 2021. ISSN 03603199. doi: 10.1016/j.ijhydene.2020.06.299. URL https://doi.org/10.1016/j.ijhydene.2020.06.299.

[9] Y. Mori, A. E. Sheindlin, and N. H. Afgan. High Temperature Heat Exchangers. *Journal of Pressure Vessel Technology*, 109(2):264–264, 1987. ISSN 0094-9930. doi: 10.1115/1.3264915.

[10] N. Muradov. *Low-carbon production of hydrogen from fossil fuels*. Number 2013. Elsevier Ltd, 2015. ISBN 9781782423614. doi: 10.1016/b978-1-78242-361-4.00017-0. URL http://dx.doi.org/10.1016/B978-1-78242-361-4.00017-0.

[11] S.L Pamela and K.M Margaret. ., Life Cycle Assessment of Hydrogen Production via Natural Gas Steam Reforming, Technical Report (NREL/TP-570-27637). Technical Report February, National Renewable Energy Lab., Golden, CO (US), 2001.

[12] Jens Schmidt, Matthias Scheiffele, Matteo Crippa, Per F. Peterson, Eugenio Urquiza, Kumar Sridharan, Luke C. Olson, Mark H. Anderson, Todd R. Allen, and Yun Chen. Design, fabrication, and testing of ceramic plate-type heat exchangers with integrated flow channel design. *International Journal of Applied Ceramic Technology*, 8(5):1073–1086, 2011. ISSN 1546542X. doi: 10.1111/j.1744-7402.2010.02573.x.

[13] Thabang W. Selalame, Raj Patel, Iqbal M. Mujtaba, and Yakubu M. John. A Review of Modelling of the FCC Unit—Part II: The Regenerator. *Energies*, 15(1), 2022. ISSN 19961073. doi: 10.3390/en15010388.

[14] W. P.M. Van Swaaij, A. G.J. Van der Ham, and A. E. Kronberg. Evolution patterns and family relations in G-S reactors. *Chemical Engineering Journal*, 90(1-2):25–45, 2002. ISSN 13858947. doi: 10.1016/S1385-8947(02)00066-9.

[15] A. Velazquez Abad and P. E. Dodds. *Production of Hydrogen*, volume 3. Elsevier, 2017. ISBN 9780128046777. doi: 10.1016/B978-0-12-409548-9.10117-4. URL `http://dx.doi.org/10.1016/B978-0-12-409548-9.10117-4`.

[16] Minimum Fluidization Velocity. Minimum Fluidization Velocity at High Temperatures. *Industrial and Engineering Chemistry Process Design and Development*, 20(4):705–707, 1981. ISSN 01964305. doi: 10.1021/i200015a022.

[17] Sebastian T. Wismann, Jakob S. Engbæk, Søren B. Vendelbo, Flemming B. Bendixen, Winnie L. Eriksen, Kim Aasberg-Petersen, Cathrine Frandsen, Ib Chorkendorff, and Peter M. Mortensen. Electrified methane reforming: A compact approach to greener industrial hydrogen production. *Science (New York, N.Y.)*, 364(6442):756–759, 2019. ISSN 10959203. doi: 10.1126/science.aaw8775.

[18] Sebastian T. Wismann, Jakob S. Engbæk, Søren B. Vendelbo, Winnie L. Eriksen, Cathrine Frandsen, Peter M. Mortensen, and Ib Chorkendorff. Electrified Methane Reforming: Understanding the Dynamic Interplay. *Industrial and Engineering Chemistry Research*, 58(51): 23380–23388, 2019. ISSN 15205045. doi: 10.1021/acs.iecr.9b04182.

[19] Qi Zhang, Makoto Nakaya, Tetsuya Ootani, Hiroshi Takahashi, Makoto Sakurai, and Hideo Kameyama. Simulation and experimental analysis on the development of a co-axial cylindrical methane steam reformer using an electrically heated alumite catalyst. *International Journal of Hydrogen Energy*, 32(16):3870–3879, 2007. ISSN 03603199. doi: 10.1016/j.ijhydene.2007.05.031.

Appendix A: Internal heating gas to solids ratio

For the configurations where a reactor is heated via the addition of hot solids coming from a oxygen combustion step, an energy balance calculation is presented. The result of this calculation is presented in figure 6.9. The energy balance for the solid phase in the pyrolysis reactor is:

$$(1-\alpha)\phi_s C_{p,s} T_{makeup} + \alpha\phi_s C_{p,s} T_{hot} - \phi_s C_{p,s} T_{dec} = V_{r,dec} R_{dec} \Delta H_{dec} A_{dec} \tag{B.6}$$

In which α is the fraction of solids sent to the combustor, where it is assumed all the carbon is combusted. For configuration 5, α is set to 1. The inlet temperature T_{hot} (coming from the regenerator) is a function of the carbon loading coming out of the pyrolysis unit:

$$T_{hot} = T_{dec} + \frac{\Delta H_{ox} C_{c,s}}{u_c C_{p_s}} \tag{B.7}$$

By setting the reactive term in moles per second to the methane inflow, the connection between ($T_{hot} - T_{dec}$) and the ratio of gas and solid fed to decomposition reactor can be calculated (figure 6.9). This is then a 100% conversion of said methane flow in a reactor volume. α is set at 1, representing configuration 5. From figure 6.9 it is then concluded that either a large temperature difference or a high solids to gas ratio is required for a high conversion.

Appendix B: Literature study for heat exchange

The current study does not aim to develop an accurate high temperature heat exchange model. Using data published in literature, an estimation of heat exchange efficiency and the approximate required heat exchanger size will be made. It is likely that the margin of error on this estimate is relatively big. Due to the high temperature, effective heat exchange can have a large effect on the thermal efficiency of the process. Hence, this error margin will have a relatively big effect on the final conclusions presented at the end of this chapter. Therefore, one efficiency without, and one efficiency with heat exchange is reported in this work.

High temperature heat exchangers (HTHE) have been a topic of study. Most HTHE are composed of ceramic materials (Al_2O_3 and SiC being most prevalent[4, 7, 9]), as they offer the highest melting point combined with good corrosion and creep resistance. It should be noted however, that these materials are notoriously fragile, making construction of large elements technologically challenging[4, 7].

Published designs include shell and tube[9], plate [12] and finned tube filled with fluidized ceramic particles[7]. Heat transfer coefficients are reported in the range of 30-40 $W \cdot m^{-2} \cdot K^{-1}$ for gas gas HTHE and 50-170 $W \cdot m^{-2} \cdot K^{-1}$ for gas-solid HTHE. Effectiveness up to 60-70 are reported for gas-solid exchange, for gas-gas this is approximately 50%. The measure for efficiency is in these configurations the exchanged heat over the maximum exchangeable heat.

From these various literature sources, it is concluded that a shell and tube heat exchanger is the most suitable to be used in a large industrial process. The estimated heat exchange coefficient is 30 $W \cdot m^{-2} \cdot K^{-1}$ and the assumed heat exchange efficiency is 50%.

It should be noted that this area is currently technologically not developed enough to be used in a large scale process[7, 9]. Moreover, the reported temperatures of high temperature heat exchange (1000-1100 °C, [4, 7]) are on the low end of the processes discussed in this work, complicating the technological feasibility. Adding to this, the total temperature change is in excess of 1000 °C. It is likely that the heat exchange will be split over numerous units in series to reduce the temperature difference in each unit[12]. Lastly, the heat exchange considers the process streams, which are in the order of 100 ktpa. The size of these heat exchangers scales with temperature and stream magnitude.

Concluding, the required heat exchangers are technologically not ready to be used on the proposed industrial scale. Therefore, energy efficiencies are partially measured without heat exchange. A second figure, including an estimated heat exchange efficiency is also reported, but it is noted a large error margin exists on this value.

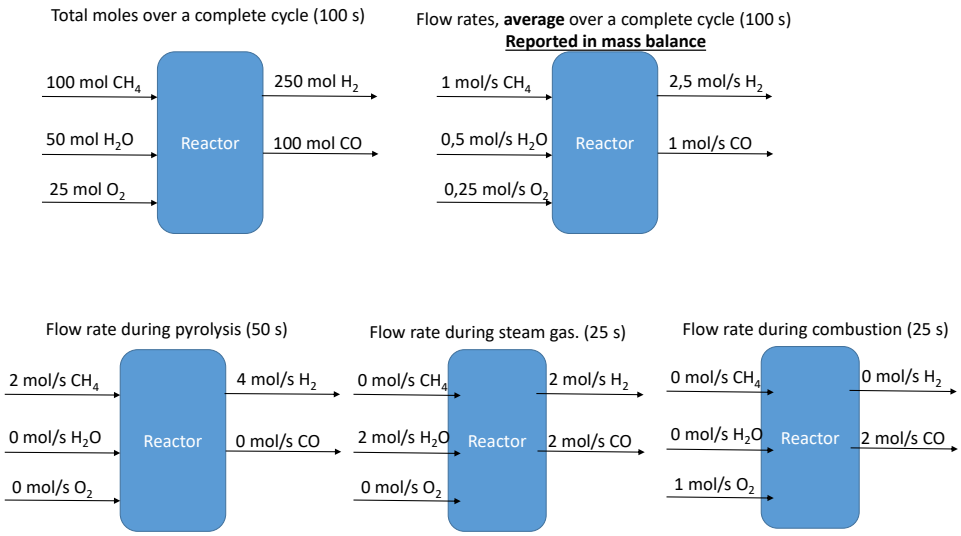

Figure A.1: Overview of reported values in mass balance for cyclic processes

Appendix C: How unsteady state processes are reported

For the cyclic processes, mass and energy balances have been made. Because of the cyclic nature, changes over time are present. To make a meaningful balance it is important to discuss how this unsteadyness is handled in the balances. Changes in flows over time are incorporated into a balance by averaging flows over the whole cycle, thereby also ensuring the balance can be closed. This means that a 100 $mol \cdot s^{-1}$ for that has a duty cycle of 50% is shown as a 50 $mol \cdot s^{-1}$ flow in the mole balance, but the flow fed to the reactor is indeed 100 $mol \cdot s^{-1}$.

Next to this, to ensure steady state, no mass or energy may build up over time or over the cycles. Practically this is ensured by comparison of the temperature and carbon loading at the beginning and end of a cycle, these should be identical. This also ensures that the moles reported in the mass balance flow in and out during the same cycle. This is reached by the model solving one parameter.

7 Conclusion

This work is a first step towards the industrial application of methane pyrolysis. Two goals were defined at the beginning of this thesis. First, as a practical goal, it was aimed to demonstrate a fully continuous lab scale methane pyrolysis – carbon gasification setup, operating at 1 bar and temperatures ranging between 1000 and 1200 °C. Secondly, it was aimed to identify the parameters and aspects crucial for further development towards a full scale implementation of this process.

7.1 The pyrolysis of methane

In chapter 2 and chapter 4, the deposition of carbon was investigated. Two aspects were central in this study. The deposition of carbon and the conversion of methane itself. It was shown that these are initially, to some extent, two uncoupled processes. They are discussed separately.

The deposition of carbon was measured on a single particle. An induction period is observed for most substrate materials. Initially the carbon deposition rate is near zero. After a few minutes, the carbon deposition rate accelerates. The present of this induction period is temperature dependent. Additionally, this induction period it is not an effect of porosity, as it was observed for both porous as nonporous particles. For some materials, (γ-Al_2O_3 and SiC and C), the induction period was not observed. The presence of this phenomena is (at least) partially related to the substrate material, and pyrolysis temperature. It is speculated that the presence of high energy groups reduce the presence of this induction period. Mechanistically, the acceleration of carbon deposition is understood. An initial nucleus is formed relatively slowly. Afterwards, carbon can grow from this nucleus, increasing the deposition rate. This was previously reported in literature, in good agreement with our results.

At higher loading, an eventual stop in carbon deposition was observed, again for porous and nonporous particles. This phenomena is not fully understood. It is speculated this is a result of changes in the surface morphology. This is substantiated by measurements using a nonporous smooth particle (Ra surface roughness 12 nm). This particle did not gather any measurable amount of carbon, hence this surface was not available for deposition. For porous particles a second explanation is plausible. For small pores, the pore diameter might become too small for an intermediate to penetrate, hence effectively stopping the deposition mechanism.

The conversion of methane was also investigated. It was found that methane conversion does not have an induction period. This means that although methane is converted, it is not deposited as carbon. Hence, it must end up in the gas phase, this was confirmed using GC measurements. Interestingly, at the point of a stop in carbon deposition, methane conversion also ceases. Moreover, when no area is present in the reactor, methane conversion also ceases. Hence, it is concluded that the present surface plays a role in the initial steps of the conversion, too.

7.2 The gasification of carbon

The gasification of carbon was investigated using steam, CO_2 and air as oxidant. It was found that air gasification is mass transfer limited in practically all systems. The gasification using steam and CO_2 exhibit a strong dependence on the pyrolysis conditions under which the carbon was deposited.

Carbon deposited at lower temperature and shorter solids residence time is significantly more reactive in the gasification phase. This is explained by the degree of graphitization of the material.

It was shown that the gasification rate is largely, but not completely, dependent on the H/C ratio of the material. Hence, no kinetics can be based on this material characteristic.

Information on the pyrolysis conditions is required to accurately describe the gasification rate. Measured gasification rates were used to formulate a rate equation. This parameterized equation was then used to successfully predict carbon gasification in a fixed bed system.

7.3 High temperature systems & measurement of these kinetics

The starting point of this work was to gather information on the reactions present. For this, a measurement method was developed. A high temperature gas-solid reactor was designed and used to measure carbon deposition and gasification kinetics.

It was found that in all cases of setup malfunction, a used material has been pushed beyond its operational temperature limit. The high temperatures in this system ensure that any point of weakness in the design will at some point fail. Hence, it is concluded that by far the most important aspect for the design of these system is robustness and simplicity. Especially during the design phase, the researcher should keep in mind this goal of simplicity. It is proposed that, should a completely new setup be designed, a researcher will reach significantly more with a robust, simple system than with a versatile more complicated system.

7.4 Operating a continuous pyrolysis – gasification process

In chapter 5, a continuous methane pyrolysis – gasification process was demonstrated, meeting the goal defined at the beginning of this project. This setup was designed towards maximum flexibility, allowing evaluation of a large amount of process parameters whilst being able to operate at a steady state.

The existence of this steady state was demonstrated experimentally, and was reached in this case withing a couple of cycles. At incomplete methane conversion, productivity of the system is eventually dictated by the amount of carbon that can be gasified. Hence, it is important to ensure sufficient carbon is gasified. This has been experimentally shown to occur even at points where the solid is not completely filled with carbon.

Separately measured pyrolysis and gasification kinetics are able to accurately describe a fully integrated continuous system. It was shown that these kinetics can be measured using relatively simple experiments.

No mass transfer limitations exist, either internally or externally. This was shown using modelling, as well as experimentally by opening up porous particles with various carbon loadings. Heat transfer is described accurately enough using an effective thermal conductivity, in good agreement with literature.

7.5 The industrial application of methane pyrolysis

The industrial application of methane pyrolysis has been investigated. It is concluded that externally heated systems do not yield efficient systems. Even with internal radiative energy transport, the systems operate at a severe limitation. It was found that heating using combustion of the deposited carbon is favourable for industrial application. The resulting systems are productive, well controllable and scale favorably. The combination of steam gasification and carbon combustion

yielded the most attractive configuration in terms of energy and carbon efficiency. Moreover, this configuration is technologically among the most simple to realize.

It was found that operating at industrial pressure allows significantly more efficient use of the present solids, operating at maximum conversion with a much lower solid to gas ratio. However, the pressure increase reduces energetic efficiency, due to the lower CH_4 conversion. It is concluded that the methane pyrolysis process at elevated pressure is less energy efficient than the current industrial standard. It is noted that this is largely due to the lower thermodynamic equilibrium and therefore difficult to circumvent.

Methane pyrolysis was also compared to a future industrial standard, assumed to be an electrically heated steam reformer (eSMR). The biggest differences between eSMR and the pyrolysis process lie in the constructional complexity and the potential for carbon efficient production. The eSMR system has the potential to be more carbon efficient, as more hydrogen is produced, per carbon.

The constructional complexity of the eSMR process is high. The most favourable pyrolysis process evaluated in the industrial study is significantly less complex, which is the major advantage for methane pyrolysis, at this point. It is noted that both technologies are in their infancy, hence much uncertainty is present at this point.

7.6 The sustainability aspects of a methane pyrolysis process

Some notes are presented on the sustainability of the methane pyrolysis process. Should the complete avoidance of scope 3 emissions[1] be desired, the carbon deposited cannot be used. The pyrolysis-only configuration evaluated in chapter six offers the advantage that carbon is separated effectively from the produced hydrogen. This configuration is technically challenging, due to the required movement of solids.

Energy and carbon efficiency of various methane pyrolysis process were evaluated. It was found that the carbon efficiency is dictated almost completely by the process configuration, and is influenced marginally by other factors such as reactor design or operating temperature. It is concluded that the carbon efficiency is essentially a choice made when a process configuration is selected. It is noted that, when a biogas is used, these processes are very attractive, due to the high carbon efficiencies reached. This bio sourced carbon would then not count towards the scope 3 emissions.

The energy efficiency of these process configurations was also evaluated. Clear differences were observed, partially due to the process configuration, and partially due to operating conditions. The operating temperature has the largest effect. Processes running at a lower temperature have the clear advantage, due to the lower heat loss. This benefit is increased further by the decreased need for high temperature heat exchange. In this work, assumptions were made about HEX, based on literature. In reality, such high temperature heat exchange is not ready to be implemented on an industrial scale. Hence, lowering the temperature has a compounded benefit.

7.7 Final remarks

During the course of this thesis, the desired final product of the pyrolysis process has been changed more than once. The ongoing development of measures taken for future sustainability, both by

[1] Scope 3 emissions include all carbon emissions along the value chain, including the end use of the product.

legislative bodies as in the private sector, complicates (long term) research. It is noted that this work was generally reactive towards these changes.

More specific for this thesis, over time it became clear that scope 3 emissions are the most important aspect in terms of carbon efficiency. Effectively, this prohibits the use of several gasification options identified in chapter 6. Hence, focus could have been shifted towards options more in line with reduced or zero scope 3 emissions.

7.8 Outlook

In this work, numerous questions were answered. However, this thesis still is only a first step towards an industrial methane pyrolysis process. Various parameters and aspects were identified to be important for further development of these processes. Before any scale up can occur, several more fundamental aspects should be investigated. First, the high pressure kinetics. Our equipment was kept at 1 bar, due to the technical complexity of working with high temperature. Now that significant experience has been obtained working with these systems, the next step for the lab scale study is the expansion towards higher pressures.

The second uncertainty comes from the mixing state of the solids in a continuous process. All work performed in this thesis was done on a fixed bed. The continuous setup can, with slight adaptions, operate as a fluidized bed. This allows experimental evaluation of various critical assumptions made during the course of this work.

Next to the challenges that can be evaluated in the lab, other uncertainties were identified. Most notably, high temperature heat exchange. This topic was addressed as a literature study. Since it is an important parameter it is worth addressing this in more detail.

Should scope 3 emissions indeed become limited to 0, one could conclude that process configurations where deposited carbon is gasified cannot be used. However, the gasification using CO_2 yields a process where overall, it is still possible to operate without net carbon emissions, or with carbon negative emissions. Depending on future regulations, energy and CO_2 emission prices these configurations might be worth exploring. It was observed that CO_2 gasification was strongly comparable to steam gasification in terms of observed phenomena. Hence, it is expected this will be possible in the same systems.

Appendix A: Numerical models used in this work

Table A.1: Symbols used in the appendices

Symbol	Description	Unit
ϵ	Void fraction	$m^3 \cdot m^{-3}$
C	Concentration	$mol \cdot m^{-3}$
C	Loading	$g \cdot m^{-2}$
t	Time	s
F	Flux	$mol \cdot m^{-2} \cdot s^{-1}$
z	Length	m
Λ	Conductivity	$J \cdot m^{-1} \cdot K^{-1} \cdot s^{-1}$
T	Temperature	K, °C
R	Gas constant	$J \cdot mol^{-1} \cdot K^{-1}$
D	Diameter	m
A	Area	m^2
τ	Residence time	s
ΔH_r	Reaction enthalpy	$J \cdot mol^{-1}$
r	Radius	m
u	Superficial velocity	$m^3 \cdot m^{-2} \cdot s^{-1}$
L	Length	m
E	Energy	kJ
V	Volume	m^3
M	Mass	kg
N	Amount	mol
ϕ	Flow	$m^3 \cdot s^{-1}$, $g \cdot h^{-1}$
n	Number	
η	Effectiveness factor	
F	View factor	
σ	Stefan-Boltzmann constant	$J \cdot m^{-2} \cdot K^{-4}$
W	Working capacity	$g \cdot m^{-2}$
P	Pressure, Productivity	bar, $mol \cdot m^{-2} \cdot s^{-1}$
S	Sensitivity	

Table A.2: Subscripts used in the appendices

Subscript	Description
H	Hydrogen
M	Methane
N	Nitrogen
0	Initial
dec	Decomposition, Pyrolysis
mod	Model
exp	Experimental
int	Internal
gas	Gas
tot	Total
eff	Effective
fix	Fixed bed
fl	Fluidized bed
b	Bulk
ox	Oxidant
∞	Infinite (time)
r	Reactor
C	Carbon
d	Dense (phase)

This appendix contains a selection of the numerical models used throughout this work.

A.1 Fixed bed model

In this appendix the fixed bed model is discussed in detail. This model has two goals. First, the prediction of methane conversion over time. From the kinetics in chapter 2 it was known that the decomposition reaction is dependent on the amount of deposited carbon present on the surface. The second goal is the prediction of the deposited carbon. This requires some additional discussion.

Within the reactor a temperature profile is present, as heat is lost via conduction to the outer walls. This temperature profile is presented in figure 2.13. As a direct result of this temperature profile decomposition rates vary with axial location along the bed, and form a distict carbon profile. An example of a carbon profile is presented in figure 2.5. Moreover, as previously stated the decomposition rate is also a function of carbon loading at that location, implicating a carbon deposition that is both a function of axial location and time. Therefore, the process is by definition a non-steady state process.

This was incorporated into a numerical model. The model uses the method of lines and models the gas phase fluxes of CH_4 , H_2 and N_2 as well as the solid phase carbon loading ($g \cdot m^{-2}$). The model domain is the fixed bed. , ranging from 0 to L. It was divided into n cylindrical elements so that $dz = L/n$. n was chosen so that the solution became independent of n. The model was solved in MATLAB using the ode15s solver.

The kinetics obtained using the single particle reactor were used without modification. The model inputs are process parameters such CH_4 and N_2 flow, runtime and particle type. The following flux balances are solved:

1. the CH_4 concentration C_M at z, t;

$$\epsilon_g \frac{dC_M}{dt} = \frac{dF_M}{dz} - R_{dec} \tag{A.1}$$

in which C_M is the local methane concentration, given by

$$C_M = \frac{F_M}{F_M + F_H + F_N} \frac{P}{RT} \tag{A.2}$$

and F_M the methane flux, given by:

$$F_M = \frac{u_g C_M}{A_r} \tag{A.3}$$

2. the H_2 concentration C_H at z, t;

$$\epsilon_g \frac{dC_H}{dt} = \frac{dF_H}{dz} + 2R_{dec} \tag{A.4}$$

3. the carbon mass at M_{ex} at z, t;

$$\frac{dM_{C,ex}}{dt} = R_{dec} M_C \tag{A.5}$$

With boundary conditions:

Table A.3: Boundary conditions of reactor model used at and $z = 0$

Variable	Value
F_M	$F_{M,in}$
F_H	0
F_N	$F_{N,in}$
$M_{C,ex}$	0

For the setup used in chapter 2 and 3, it is assumed that no radial temperature and concentration gradients are present, due to the small ID of the reactor (10 mm). Hence, this version of the model did not contain an energy balance. The continuous setup described in chapter 5 is described completely in appendix B. The fixed bed model used in chapter 6 uses the energy balance described in section A.3.

A.2 Fluidized bed model

The fluidized bed model is used only for the industrial case study. In this study a parameter sweep is desired. This means a large amount of model evaluations is required. Hence, a relatively simple model with short calculation time is preferred.

A simple fluidized system is the fast fluidized bed[8]. This is a fluidized bed with a very high linear gas velocity. It has excellent gas/solid contacting, and short gas residence times. These characteristics are strongly desired. The gas mixing state may be considered plug flow[4, 8], however some backmixing through the dense phase cannot be avoided.

The gas mass balance is a flux based PFR:

$$\frac{dF_g}{dz} = \frac{d\left(u_g C_x\right)}{dz} = R_x A_d \tag{A.6}$$

in which the subscript x denotes a reaction (pyrolysis, steam gasification or oxygen gasification). The solids can be considered perfectly mixed. Hence, the carbon loading is equal throughout the reactor. The total mass and energy balances of the solid phases are then:

$$\frac{dN_{c,d}}{dt} = \phi_d C_{c,d,in} - \phi_d C_{c,d,out} \pm \sum_1^n R_x A_d \epsilon A_r dz \tag{A.7}$$

$$\rho_d C_{p,d} V_d \frac{dT_{c,d}}{dt} = \phi_d \rho_d C_{p,d} T_{in} - \phi_d \rho_d C_{p,d} T_{out} \pm \sum_1^n R_x A_d \epsilon \Delta H_x A_r dz \tag{A.8}$$

in which the summation over n elements denote the rate at each of the n axial discretization points. All these equations are solved simultaneously, as the carbon loading and solids temperature are present in the reaction rate. For the energy balance, the initial energy, corresponding to the initial temperature, is defined to be 0. The resulting temperatures are then calculated via the change in energy. Initial conditions for C_g, C_d and E have to be specified.

From the energy balance, the temperature over time is calculated. More detail on this method is presented in section 6.4.1. From the heat transfer study presented in section A.3, it is known that no internal gradients are presented in the mixed solids phase, this is further substantiated in the industrial analysis (fig. 6.8).

A.3 Heat transfer study

In the particle following routine presented in section B.1.3 it is concluded that the pyrolysis temperature is a key parameter in the process. This temperature needs to be controllable. To investigate the heat transfer, and by extension the temperature in the reactor, a heat transfer analysis is presented here. Initially, a fixed bed is evaluated. This is later compared to a fluidized bed.

It is known from literature that heat transfer in high temperature (T>650 °C) is an interplay of conduction through the solid and solid contact areas, conduction and convection through the gas phase and radiative heat transport between the solid surfaces[1–3, 6, 7]. For a packed bed at 800 °C and up the majority of heat transport occurs via radiation[1, 3].

From table B.8 it is known that the operating temperatures of the decomposition reactor are in the range of 1120 °C. The gasification temperatures should be as high as possible, estimated in the range of 1200 °C. Because the foreseen temperatures are much higher than the temperature where radiation becomes dominant, this initial analysis only takes into account radiation.

Breitbach et. al. [1] published experimental data on effective conductivity (containing components of the material and radiation) at high temperature packed beds is available. The methane pyrolysis case is a very interesting one, as the bed (Al_2O_3) is coated with graphite over time. Even a miniature layer has a major effect on the radiative characteristics of the bed. The emissivity of Al_2O_3 is approximately 0.4, whilst the emissivity of graphite is 0.8[1]. This results in a assumed effective thermal conductivity that is significantly higher for graphtie coated Al_2O_3 .

Goal, assumptions made & model equation

Because a constraint on the pyrolysis temperature is present, a limit exists for the external heater temperature that can be used in this step. The goal of this study is to investigate what approximate heater temperature is suitable for the pyrolysis reactor. There are two parameters of interest for this. First, the fraction of carbon that is made at the desired temperature (T_{dec}< 1120 °C). Secondly the productivity [$mol_c \cdot m_r^{-3} \cdot s^{-1}$] of the decomposition reactor. Whilst a higher temperature increases productivity during pyrolysis, (too) high temperature carbon is detrimental to the gasification productivity. The effect of heater temperature on this trade off will be studied in this analysis.

Additionally, because heat transport is not infinitely fast, a temperature gradient will occur in the reactor. The reactor diameter will therefore also be an important parameter in this study. It is aimed to find out which approximate diameters are suitable.

These two parameters are coupled, as will be shown later on in this section. Since no reactor design has been made at this point, two analyses will be made. One for a fixed and one for a fluidized system.

Since this is still an exploratory study, several simplifications are made through assumptions:

- Mass transfer is not taken into account. Pyrolysis rates are calculated as if under pure CH_4 .
- No calculations on the carbon loading of the bed are performed. Because deposition is a nonlinear process in loading, for detailed modelling the carbon loading is required. The loading is set to $\pm$ 11 $g \cdot m_{p,ex}^{-2}$, which corresponds to the maximum deposition rate. This, coupled with the previous assumption, makes this the maximum obtainable rate. This can be considered a worst case for heat transport.
- The reactor is a tubular reactor irradiated on the complete outer surface by a heater at certain temperature T_h.
- The solved domain is the reactor tube only. It is not considered if the external heater can deliver the amount of power required.
- It is assumed that the gas phase is entering the reactor near reactor temperature. Hence, it does not require significant heating. In all experimental designs, it was ensured the gas was near reactor temperature, for example via preheaters.
- As stated, heat transport is dominated by radiation[1, 3]. Values for λ_{eff} are taken from experimental data[1].

- For all the beds, a porous carrier is assumed.

Three cases are incorporated, one for Al_2O_3 ($\lambda_{\text{eff}} = 4\ \text{W}\cdot\text{m}^{-1}\cdot\text{K}^{-1}$) and one for graphite ($\lambda_{\text{eff}}$ =16 $\text{W}\cdot\text{m}^{-1}\cdot\text{K}^{-1}$) and one for SiC carriers ($\lambda_{\text{eff}} = 100\ \text{W}\cdot\text{m}^{-1}\cdot\text{K}^{-1}$).

The relevant equation is a simple heat balance:

$$0 = \rho_b C_{p,b} \frac{dT}{dt} = \frac{1}{r}\frac{d}{dr}\left(r\lambda_{eff}\frac{d^2T}{dr^2}\right) - R_x \Delta H_r A_{tot}\eta \tag{A.9}$$

The solved domain is the reactor radius. The boundary condition at the center of the tube is given symmetry. The outer boundary condition is a continuous flux:

$$\lambda_{eff}\frac{dT_{r=R}}{dr} = \lambda_{wall}\frac{T_{w,ex} - T_{r=R}}{L_w} = \sigma\epsilon F_{1,2}\left(T_h^4 - T_{w,ex}^4\right) \tag{A.10}$$

where T_b is the bed temperature at the wall and T_h the set/measured heater temperature. $T_{w,ex}$ is the external wall temperature, and is a solved parameter that is dependent on the wall thickness, λ_{eff} and T_h. Note that the wall is assumed to be flat, rather than curved for this balance to hold true. Since the wall is relatively thin compared to the reactor radius (1 mm compared to 70 mm), this assumption is valid for most archetypes except for the multitubular archetypes.

Results

In figure A.1 the calculated temperature profile is presented for a fixed bed of 0.05 m radius. The heater temperature is set to 1300 °C. An internal temperature profile is clearly visible. Furthermore, it is noted that the external heater temperature is significantly higher than the internal temperature. Both these observations indicate that this pyrolysis reactor is limited to some extent by internal and external heat transfer. The used pyrolysis rate represent the fastest possible rates, making this a worst case in terms of heat consumption. Therefore, the actual temperature will be higher than this prediction and the heat transfer limitation less severe.

Because of this temperature gradient, not all carbon is deposited at an equal temperature. The share of carbon deposited at or below the desired temperature (1120 °C) is of interest. Hence, the fraction desired carbon is defined to be the number of moles C deposited at or below 1130 °C over the total number of moles deposited:

$$\text{Fraction desired carbon} = \frac{N_c(T < 1130°\text{C})}{N_{c,tot}} \tag{A.11}$$

In figure A.2 the fraction of desired carbon (fig. A.2a) and the productivity (fig. A.2b) of a clean Al_2O_3 fixed bed are presented. The heater temperature and reactor radius are varied.

Between the two subfigures one can see the predicted tradeoff between fraction of desired carbon and productivity. It is observed that a higher reactor radius is detrimental to the productivity of the system. The increase temperature gradient cannot be countered with an increased heater temperature. Therefore, it is concluded that the reactor tube diameter cannot be too large (max. order of 10 cm). Note that the productivity for the larger diameters is still fast, compared to the average industrial process[5].

When graphite is deposited on the surface of the material, the effective thermal conductivity changes[1]. This case is presented in figures A.1 and A.3. For equal conditions, the productivity of the system as well as the fraction of desired carbon increases. One can therefore conclude that higher internal heat transport is very favourable for this system. This is because of two reasons. First, the increased heat transport results in a smaller spatial temperature gradient in the reactor, and carbon is deposited at a more uniform temperature. This increases the share of desired carbon and allows operation at higher temperature without production of excess temperature carbon. Because the heat transport in the reactor is increased, the external (incoming) heat transfer also increases, via cooling of the outer wall.

In reality, the bed will start as clean Al_2O_3 due to assumption 1. Over time the bed will be coated with carbon. The actual effective thermal conductivity over time will therefore change from the situation in figure A.2 to A.3. The prediction of temperature gradient will lay in between the two cases.

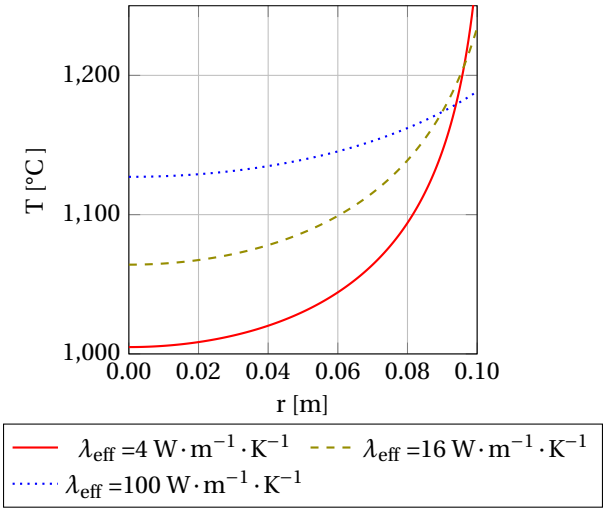

Figure A.1: Calculated temperature in the pyrolysis reactor, fixed bed, Al_2O_3 . Heater temperature 1300 °C , various effective conductivities

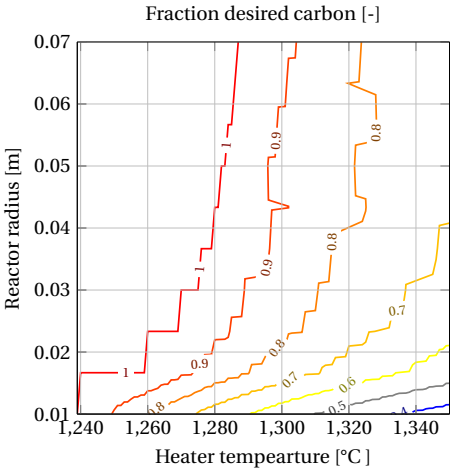

(a) Fraction of carbon produced at or below desired temperature of 1120 °C as function of reactor diameter and wall setpoint temperature. Uneven or rough shape of data was caused by a relatively large solver step size. This was chosen so to save computational time.

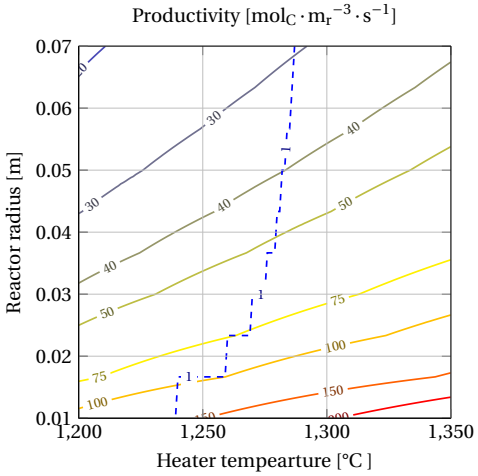

(b) Continious lines: productivity as function of reactor diameter and wall setpoint temperature. Dashed line: operating line for 100% desired carbon

Figure A.2: Heat transfer analysis result for fixed bed of noncoated Al_2O_3 . λ_{eff} = 4 $W \cdot m^{-1} \cdot K^{-1}$, lower end estimation. Uneven or rough shape of data was caused by a relatively large solver step size. This was chosen so to save computational time. Note that the reactor radius refers to the outer reactor radius of distinct reactors.

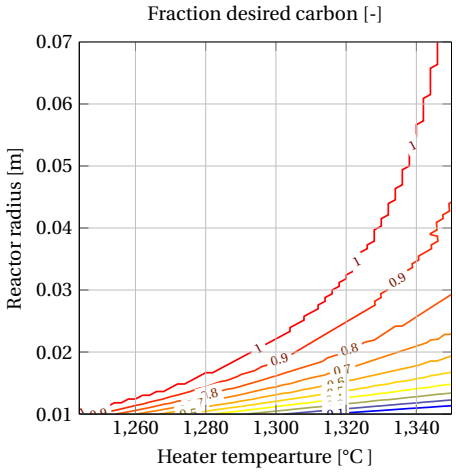

(a) Fraction of carbon produced at or below desired temperature of 1120 °C as function of reactor diameter and wall temperature. Uneven or rough shape of data was caused by a relatively large solver step size. This was chosen so to save computational time.

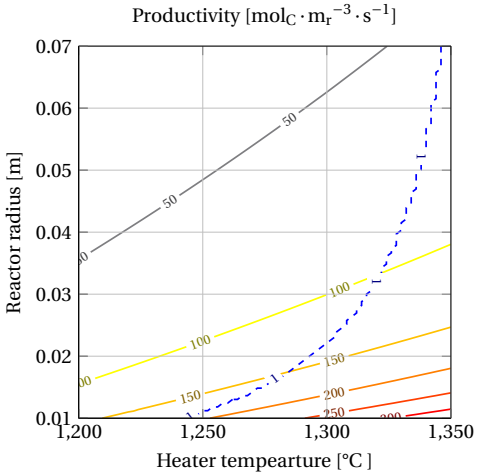

(b) Productivity as function of reactor diameter and wall temperature

Figure A.3: Heat transfer analysis result for fixed bed of coated Al_2O_3 . λ_{eff} = 16 W · m^{-1} · K^{-1}, higher end estimation

Conclusion

From the heat transfer study it is concluded that a relatively thin tube, in the range of 1-10 cm is suitable for the pyrolysis reactor. It is noted that high internal heat transfer is very beneficial for

this step of the process. These cases were for a fixed bed. A fluidized bed will have internal heat transport enhanced via solids mixing. Therefore, it can be concluded that a fluidized bed will have significantly more favourable heat transfer characteristics for this step of the process.

Bibliography

[1] G. Breitbach and H. Barthels. Radiant Heat Transfer in the High Temperature Reactor Core After Failure of the Afterheat Removal Systems. *Nuclear Technology*, 49(3):392–399, 1980. ISSN 00295450. doi: 10.13182/NT80-A17687.

[2] G. J. Cheng and A. B. Yu. Particle scale evaluation of the effective thermal conductivity from the structure of a packed bed: Radiation heat transfer. *Industrial and Engineering Chemistry Research*, 52(34):12202–12211, 2013. ISSN 08885885. doi: 10.1021/ie3033137.

[3] M. De Beer, P. G. Rousseau, and C. G. Du Toit. A review of methods to predict the effective thermal conductivity of packed pebble beds, with emphasis on the near-wall region. *Nuclear Engineering and Design*, 331(March):248–262, 2018. ISSN 00295493. doi: 10.1016/j.nucengdes.2018.02.029. URL `https://doi.org/10.1016/j.nucengdes.2018.02.029`.

[4] P. Gayán, L. F. De Diego, and J. Adánez. Radial gas mixing in a fast fluidized bed. *Powder Technology*, 94(2):163–171, 1997. ISSN 00325910. doi: 10.1016/S0032-5910(97)03322-6.

[5] Jacob A Moulijn, Michiel Makkee, and Annelies E Van Diepen. *Chemical process technology*, volume 51. John Wiley & Sons, 2013. doi: 10.5860/choice.51-2107.

[6] Prabal Talukdar, Miguel A.A. Mendes, Ritesh Kumar Parida, Dimosthenis Trimis, and Subhashis Ray. Modelling of conduction-radiation in a porous medium with blocked-off region approach. *International Journal of Thermal Sciences*, 72:102–114, 2013. ISSN 12900729. doi: 10.1016/j.ijthermalsci.2013.04.027. URL `http://dx.doi.org/10.1016/j.ijthermalsci.2013.04.027`.

[7] Gregor D. Wehinger. Radiation Matters in Fixed-Bed CFD Simulations. *Chemie-Ingenieur-Technik*, 91(5):583–591, 2019. ISSN 15222640. doi: 10.1002/cite.201800179.

[8] J. Yerushalmi, A. E. McIver, and A. M. Squires. Fast Fluidized Bed. 15(1):47–53, 1974.

Appendix B: The design of a continuous lab scale pyrolysis setup

This appendix documents our efforts made in order to reach the design of the continuous lab scale pyrolysis setup. In the chapters of this thesis, various references are made to the parts of this appendix. For the design of the lab scale system, the parts may be read chronologically, but can also be read individually. For this readability, selected data is presented twice in this appendix.

The appendix consists of three parts. First, a kinetic analysis is presented. In this, a particle is followed through a pyrolysis-gasification cycle. The goal of this exercise is to investigate the required conditions for these process steps, in order to yield the most desired system. This is measured via productivity. No assumptions on a reactor design or particle characteristics have been made, hence this analysis is valid for any reactor system.

Part two consists of a reactor selection procedure. For the continuous setup, goals are defined. Via an exclusion method, the most suitable reactor is selected. In part three, a detailed model of this reactor is constructed and evaluated.

B.1 Particle following routine

B.1.1 Introduction, goal & methodology

In this section, the kinetics of chapters 1-3 are used to investigate the process conditions in an industrial process. The used method follows an single particle as it passes through a series of reaction steps of the pyrolysis-gasification process, schematically shown in figure B.4. First, carbon is deposited on the surface in a pyrolysis step. Subsequently, the carbon is gasified in one or two gasification steps.

This study aims to investigate the operating window (in terms of process parameter values) of the pyrolysis-gasification cycle. No reactor design is made in this phase, nor are mass or energy transfer limitations taken into account. Hence, the findings of this study represent the kinetically limited process. The goal is to find out what combination of process parameters yields the highest productivity unit: $[g_C \cdot m_p{}^{-2} \cdot s^{-1}]$. The relevant process parameters and the definition of the ideal process are discussed further on in this section.

In reality, mass and energy transfer limitations as well as possible solids mixing will be present, possibly affecting the outcome of this study. This depends on characteristics of the designed reactor. The data obtained here is used as a starting point, or initial guess, for a reactor design.

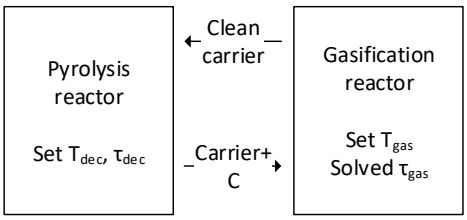

Figure B.4: Schematic of used system in particle following routine

As stated, this study will focus on a pyrolysis step followed by subsequent gasification. The following process configurations have been identified:

Table B.4: Overview of possible process steps

Pyrolysis	Gasification
CH_4	Steam
CH_4	CO_2
CH_4	Air

B.1.2 Included parameters and calculation method

For each of the process steps, a temperature and solids residence time is required. However, the gasification solids residence time cannot be chosen freely. This is due to assumption 1; the residence time of the solid in the gasification step is chosen so that the final carbon loading is 0. The relevant parameters are listed in table B.5.

The following assumptions are made:

1. After the final gasification step of a pyrolysis-gasification cycle, all the carbon is removed from the particle. This was done to simplify this analysis. Preliminary testing with nonzero carbon loading indicated that these options are less productive, due to the decreased pyrolysis rate. However, it cannot be concluded that a zero carbon loading is always more productive.
2. The process operates at 1 bara total pressure at all times.
3. The highest realizable temperature is 1300 °C for gasification.
4. The highest realizable temperature is 1200 °C for pyrolysis.

Table B.5: Overview of input parameters and solved process variables

Parameter	Input	
T_{dec}	Yes	Pyrolysis temperature
τ_{dec}	Yes	Pyrolysis solids residence time
T_{gas}	Yes	Gasification temperature
τ_{gas}	No	Gasification solids residence time, solved to ensure final loading is 0

For simplicity, this analysis now looks at the productivity P of a system. For this, the following parameters are defined:

Table B.6: Overview of output parameters

Output parameter	Description	Unit
W	Working capacity	$g_C \cdot m_p{}^{-2}$
P	Productivity	$g_C \cdot m_p{}^{-2} \cdot s^{-1}$

The parameters are calculated as follows. For the working capacity:

$$W = C_{dec} - C_{gas} - C_{dec} \tag{B.12}$$

where C_{dec} and C_{gas} denote the loading after the pyrolysis step and after the gasification step. Note that C_{gas} has a value of 0 due to assumption 1.

$$P = \frac{W}{\tau_{tot}} \tag{B.13}$$

where τ_{tot} [s] is the total cycle time given by

$$\tau_{tot} = \tau_{dec} + \tau_{gas} \tag{B.14}$$

B.1.3 Results

A parameter sweep was performed for all input parameters. The results are presented in figure B.5 for gasification using steam, CO_2 and air. The presented data denotes the cases for highest productivity of the system. This means that all other parameters are varied. $T_{gas}$was chosen as the presented parameter because it shows the observed trends the best.

For all cases, it is observed that the total cycle time τ_{tot}, presented in figure B.5c are in the order of minutes. The cycle time is dictated by two phenomena. First, the pyrolysis step is nonlinear in time, accelerating and decelerating with pyrolysis time. Hence, an optimal deposition time exists, resulting in the highest average deposition rate. Secondly, mainly for steam and CO_2 , the gasification rate is a strong function of pyrolysis conditions. At lower τ_{dec}, the gasification rate is significantly faster. These two phenomena dictate the gasification time, together with assumption 1.

For steam and CO_2 , it is observed that the decomposition temperature required for highest productivity is similar. Moreover, $T_{dec}$is not a strong function of the used gasification temperature. This is explained via the dependence of the gasification rate on the pyrolysis conditions. It was experimentally observed that a (too) high pyrolysis temperature yields a carbon that cannot be gasified using CO_2 or steam.

For air gasification this phenomena was not observed. This is also reflected in the optimal productivity, as the pyrolysis temperature is constant at the upper limit of 1200 °C. The increased pyrolysis temperature, combined with the much faster air gasification, results in a very high productivity (figure B.5a). It is noted that the productivity of this process can be improved by increasing T_{dec}.

To compare air gasification to steam and CO_2 at comparable pyrolysis temperature, a second air gasification case was incorporated, limiting the pyrolysis temperature to 1120 °C. This case shows that air gasification is able to keep up with deposition even at relatively low gasification temperatures. For steam and CO_2 , it is observed that the productivity is very low for low T_{gas}. The gasification step for these two cases needs a high temperature to keep up with the pyrolysis reaction.

This is also reflected in figure B.5d, here the share of gasification time in the total process time is presented. Should gasification be slow, this will be a high share, and gasification will be the limiting step in the process. One can see that for all cases, the share of gasification step reduces with

increasing T_{gas}. Furthermore, using low T_{dec}air gasification one can see that the decomposition step is limiting at all times. Concluding, using air gasification, for a high productivity, it is beneficial to increase the pyrolysis temperature to the highest realizable temperature. For steam and CO_2 the productivity can be increased most effectively via the gasification temperature.

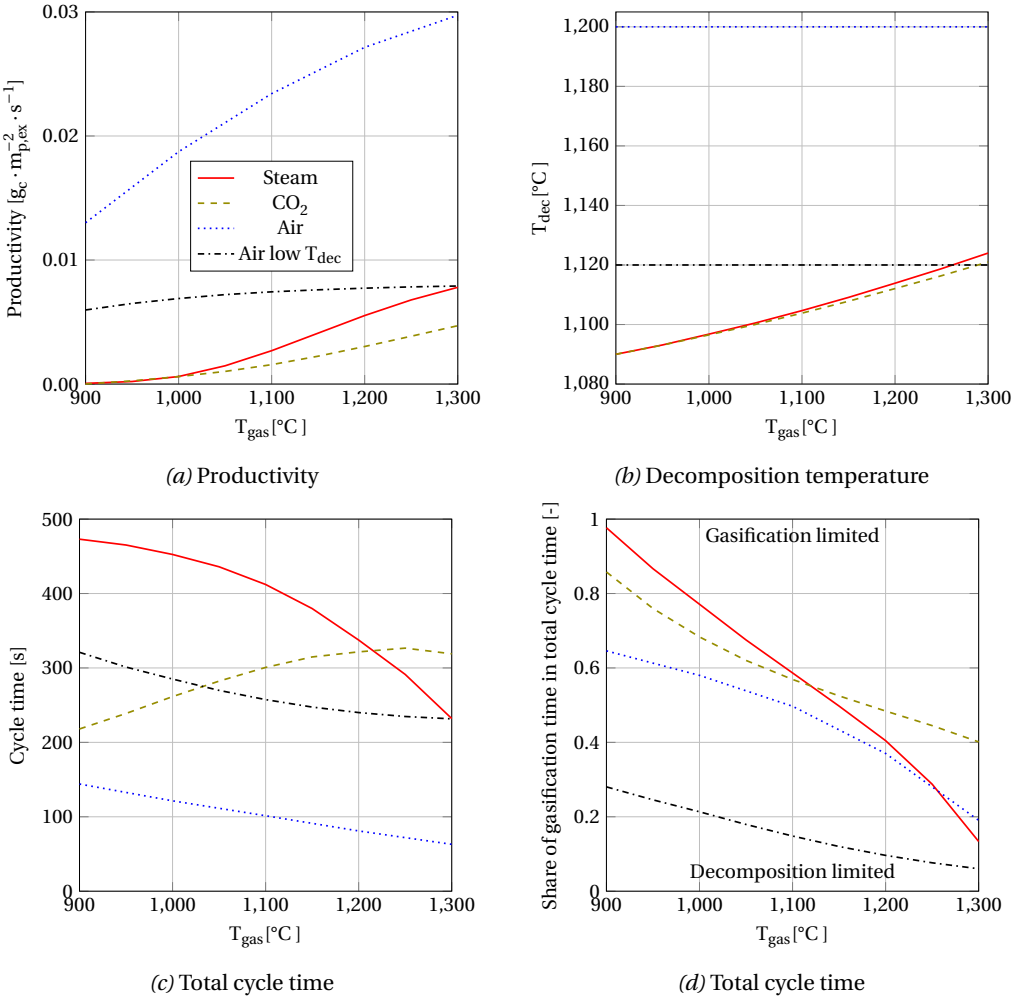

(a) Productivity

(b) Decomposition temperature

(c) Total cycle time

(d) Total cycle time

Figure B.5: Results of particle following routine for Steam, CO_2 and air gasification. All cases denote the highest obtainable productivity, all other parameters are variable within this dataset.

To put into perspective which of the process parameters are crucial to control, a sensitivity analysis was performed. The following relation was used to measure the effect of an input variable change (dI) in on the desired output variable, being productivity. The sensitivity is measured from the most optimal point, being the data presented in figure B.5. A relative change in in- and output variables is used, to allow direct comparison between several input variables.

$$S_I = \frac{\frac{\partial P}{P}}{\left|\frac{\partial I}{I}\right|} \tag{B.15}$$

The result of this analysis is presented in table B.7 for the three gasification options. Six input parameters were tested. The results are shown for both an increase and a decrease in input parameter. It is observed that the majority of changes result in a process with a lower productivity. This is expected as the investigated dataset represented the optimal conditions, which could not be improved further. Exceptions to this are the gasification temperature, which was the open parameter and the decomposition temperature for air gasification, as this was limited by assumption 3. The absolute sensitivity values of all calculated values did vary slightly with the used gasification temperature. This was relatively small however. The overall trends did not change significantly.

For steam and CO_2 gasification, the most sensitive parameter is the decomposition temperature. An increase causes the formation of inert carbon that cannot be gasified, thereby strongly decreasing the productivity of the system. A decrease lowers the amount of carbon deposited via the induction period observed for the carbon deposition rate.

Because of this high sensitivity for temperature, this result indicates that correct prediction of heat transport in the reactor in of great importance for modelling this process. Furthermore, for steam and CO_2 gasification, both an increase and a decrease of T_{dec}negatively affects productivity. This means that the pyrolysis temperature needs to be accurately controllable. For air gasification this is not the case, $T_{dec}$and T_{gas}only need to be sufficiently high. Note that for steam and CO_2 gasification, an increased gasification temperature does lead to a more productive system. This is because the gasification step is limiting, and the temperature temperature is limited by choice to 1300 °C.

Table B.7: Results of sensitivity analysis for various gasification options. Sensitivity calculated from the productivity output parameter. Input parameters are shown in the column headers, (+) denotes an increase, (-) denotes a decrease of this parameter.

Gasification	T_{dec}-	T_{dec}+	τ_{dec}-	τ_{dec}+	T_{gas}-	T_{gas}+
Steam	-13	-35	-2.5	-2.4	-8.6	6.1
CO_2	-9.2	-12	-2.4	-2.4	-7.3	5.4
Air	-26	22	-6.3	-3.6	-0.8	0.4

The findings of the particle following study are presented in table B.8 below. It can be concluded that operating this process using air gasification is significantly less complicated than using either CO_2 or steam as oxidant. The latter two have a more narrow operating regime, especially for the pyrolysis temperature. The findings of this study will be used as input for a reactor selection procedure.

To briefly add to this, this data represents a nonporous particle, used in chapters 2 and 3. The same process was repeated for various porous particles. The observed trends were visible during

the porous study. Moreover, the found temperature for $T_{dec}$was also comparable. Only the found productivity was significantly higher. This is expected as the deposition and gasification kinetics are strongly comparable between porous and nonporous particles. Hence, these results are presented only for the nonporous particles and are assumed to be valid for all particles evaluated in this work.

Table B.8: Summary of particle following routine for single gasification process configurations.

Gasification	T_{dec}[°C]	τ_{dec}	T_{gas}[°C]	τ_{gas}	Critical design parameter
Steam	1130	minutes	max.	minutes	T_{dec} controlled accurately
CO_2	1130	minutes	max.	minutes	T_{dec} controlled accurately
Air	max.	minutes	max.	seconds	T_{dec} sufficiently high

B.2 Reactor selection for the lab scale setup

B.2.1 Introduction & goal of the to be constructed setup

In sections B.1 and A.3 approximate process parameters and critical design aspects of a to be designed pyrolysis-gasification process have been determined. These will now be used as input for a reactor selection procedure, which is presented in this section. First, the to be designed setup is discussed, and demands are placed upon this setup. Using these demands unsuitable reactor archetypes are removed. In the second part of this document, (section B.3) the remaining possible reactor archetypes are modelled in detail and compared

The aim is to design a continuous lab scale process producing 100 $g_C \cdot h^{-1}$ of carbon via methane pyrolysis. Since this is a lab scale setup meant for research purposes, the most important demand placed on this setup is one of flexibility: that as many process parameters as possible can be varied, to be able to gather as much knowledge as possible. The desired products for this process are hydrogen and CO. Because the identified process configurations (table B.4) yield a different H_2:CO ratio some variation in the final product composition can occur. For this analysis, no desired ratio is defined, hence this is not taken into account for the final conclusions.

B.2.2 Demands placed on setup

Demands placed on the setup are discussed in this section. These demands are mainly incorporated to ensure the designed setup will operate properly. For each demand it is presented where this is based on. The demands are not placed in any particular order of importance.

Demands regarding operatability of the process

1. From section B.1 it is known that operating a methane pyrolysis process using steam or CO_2 as oxidant is more complicated than using oxygen or air as oxidant. For maximum flexibility of the to be designed setup, this setup should be able to operate using any of these oxidants. This means that the setup will be designed to operate using steam. Both steam and air/oxygen will be used in the actual experiments.
2. The production of gaseous carbon containing species other than CO should be avoided. Naturally a high selectivity towards the desired products is desired, however this is a op-

eratability demand. It is known from fixed bed experiments that the net production of intermediates causes blocking of tubing[1]. These intermediates condense and form a wax on the tubing, causing blockage. From experimental data it is known that the net production of these intermediates is avoided via a high methane conversion. Therefore, a demand is placed on CH_4 conversion, this should be as high a possible. Thermodynamically, near 100% conversion is possible[1], hence no limitations exist from this.

3. From section B.1 it is known that the solids residence time in contact with methane should be limited to ± 100-150 s to prevent deactivation of the deposited carbon. This also implies the solids residence time should be well defined, and should not have a residence time distribution.

4. Assuming the lab scale setup is heated via an external radiation element, from section A.3 it is known that the process requires a small (0.1 m scale) hydraulic diameter to provide sufficient energy. For a fluidized bed this length is larger, due to enhanced internal heat transfer.

5. From section B.1 it is known that a methane decomposition temperature of approximately 1120 °C is required.

6. From section B.1 it is known that the gasification temperatures should be as high as possible, preferably in excess of 1200 °C.

7. The preferred particle has a lot of area per volume, evident from measurements on porous and nonporous media[1].

Technical & practical demands

9. The reactor will be constructed from Aluminium oxide as it is inert and can be worked with much better than comparable inert ceramic materials. During previous work, experience was obtained working with this material. It has excellent thermal and chemical stability, and more importantly, can be fabricated in-house, yielding a short response time to repair parts.

10. The heating will be done by electrical Superkanthal A1 heating wires, again because significant experience has been gathered for this method.

11. Experts at Ceratec technical ceramics did not see an solution for a mechanical valve operating above 1000 °C in reductive or oxidative atmospheres in combination with solids. It is therefore not seen as a possible option to use such valves in the setup. Hence, a demand is placed on the design, that no such valves are used.

12. The maximum temperature obtainable is 1400 °C . This is the experimentally observed operating limit of the heating wire.

13. The preferred maximum continuous operating temperature is 1350 °C because of stability of the heating wire.

14. The maximum temperature change rate of the heaters in the order of 5-10 $K \cdot min^{-1}$. This is to prevent damage to the heating elements.

B.2.3 Selection steps

The reactor selection procedure is based on a rejection method. Hence, we start with a list of (nearly) all gas-solid reactor archetypes. The publication of van Swaaij [3], documents a wide range of possible reactors and reports on the characteristics of each type. In total 45 types (22 fixed bed (figure B.7 and 23 fluid beds (figure B.6) reactors are discussed by van Swaaij. These will not all be taken into account. Some of these are minor modifications of the original reactor type (e.g. Short bed with cooling compared to adiabatic with interstage cooling), or obviously not desired in this process (e.g. a microreactor). 17 reactor archetypes remain after this selection.

A first analysis is presented, on three demands. These were chosen first as they are the most critical, and/or can be evaluated without the need for complex calculations.

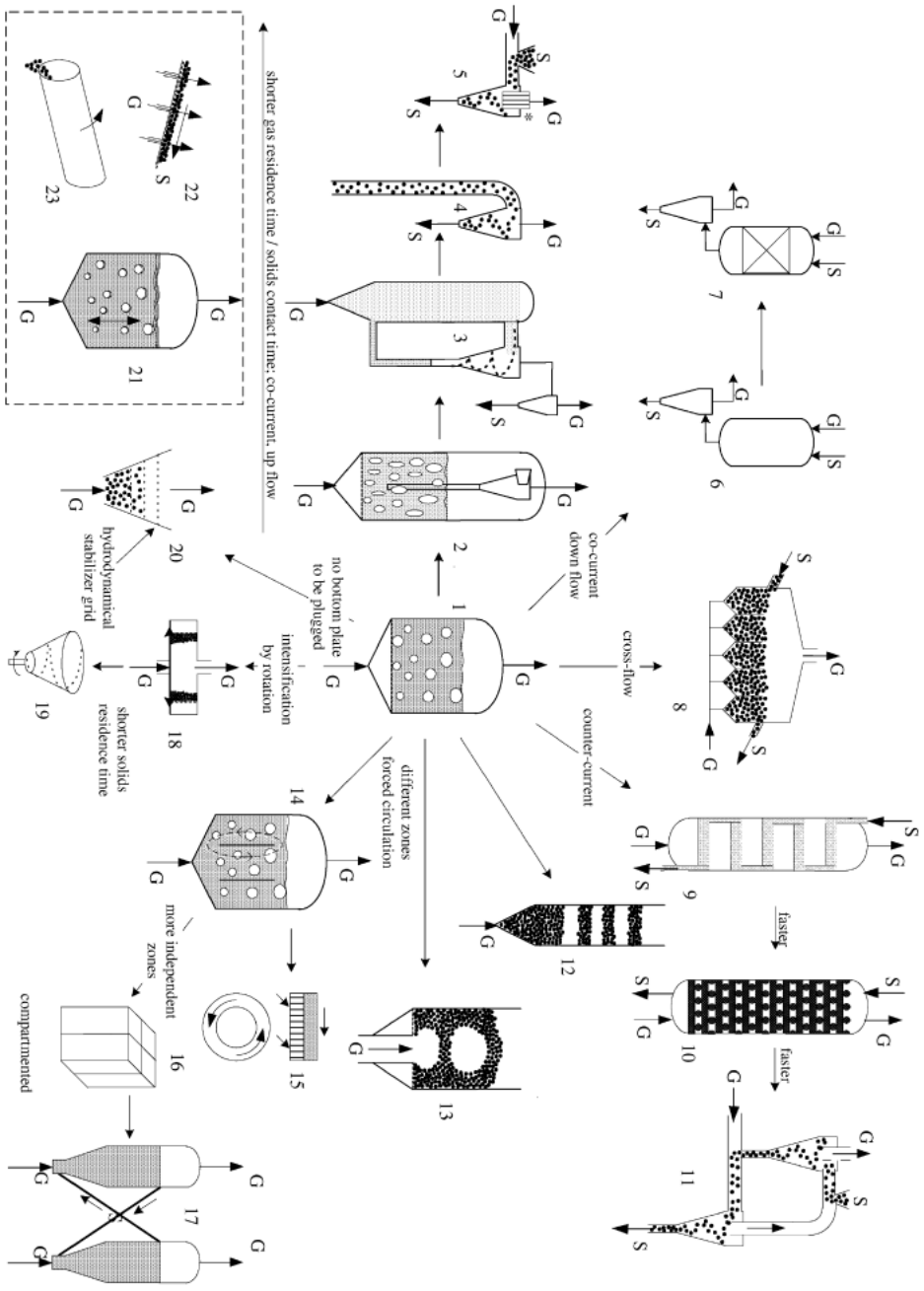

Figure B.6: Fluid bed archetypes, taken from van Swaaij et. al. [3]. 1, bubbling fluid bed 2, turbulent fluid bed 3, fast fluidized bed, 4 pneumatic conveying, 5 cyclone, 6 co-current downflow, 7 co-current trickle down flow, 8 cross-current bed, 9 counter-current multistage, 10 counter-current trickle flow, 11 counter current cyclones, 12 slugging fluidized bed, 13 spouted bed, 14 draft tube, 15 torbed, 16 compartment bed, 17 external circulating fluidized bed, 18 rotating fluidized bed, 19 rotating cone, 20 conical floating G-S fluidized bed, 21 vibrating fluidized bed, 22 inclined fluidized bed, 23 rotary kiln

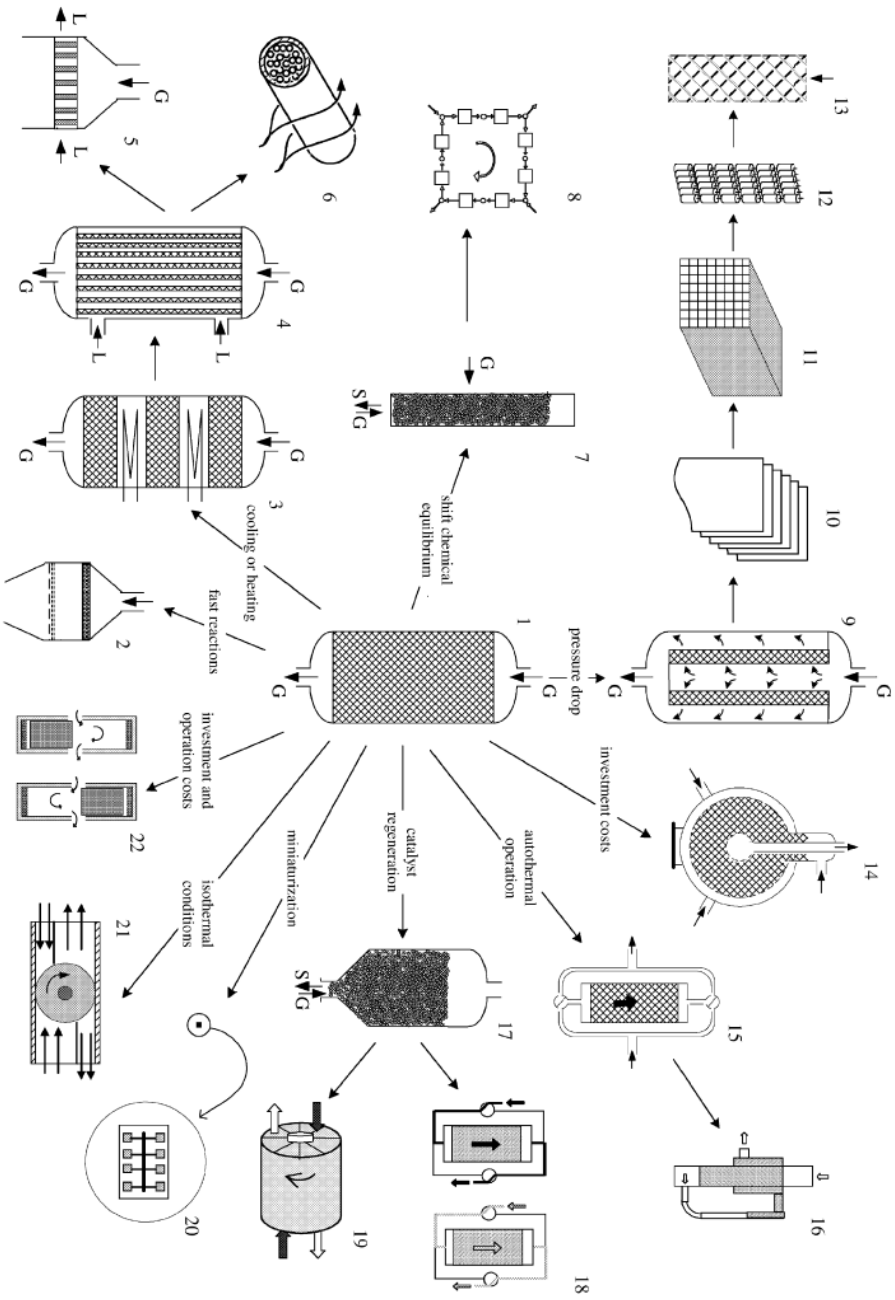

Figure B.7: Fixed bed archetypes, taken from van Swaaij et. al. [3]. 1, adiabatic bed2, gauze layers 3, adiabatic with intermediate cooling, 4 multitubular, 5 short bed with cooling, 6 annular bed, 7 continuous chromatographic, 8 simulated moving bed, 9 radial flow, 10 parallel passage, 11 monolith, 12 bead string, 13 polyith, 14 spherical, 15 reverse flow, 16 circulation loop, 17 moving bed, 18 coupling of end- and exothermic reactions, 17 simulated moving bed, 19 rotating fixed bed, 20 microreactor, 21 rotating disk, 22 pulsed compression

Control of solids residence time and temperature

A major point is the process conditions during pyrolysis. Mainly the solids residence time during pyrolysis (demand 3) and the narrow range of suitable pyrolysis temperatures (demand 5). Both of these demands exist to prevent the deposited carbon from becoming inert in the gasification phase.

Adding to this, it is known that the gasification temperature should be significantly higher than the decomposition temperature (demands 5 and 6). This, combined with the residence time demand yields two demands on the reactor archetype:

1. Controlled and sufficiently fast (order of seconds) removal of solids from a pyrolysis reactor volume, *or*
2. Controlled and sufficiently fast (order of seconds) switching of gasses from the pyrolysis reactor volume, combined with a sufficiently fast temperature change in pyrolysis reactor volume.

The majority of conventional fixed bed reactors are unable to switch gasses and temperature significantly quick. Hence, they are rejected. Most of the fluid bed family are able to remove solids from the reactor in a fast and controlled way. The basic fluidized bed and the draft tube lack this options and are discarded. Note that the fluidized bed options where solids leave the bed volume are included under various other categories. An overview of the types excluded is presented in table B.9.

Range of solids residence time

The residence time of the solids during decomposition needs to be controlled at around 100 s (demand 3). Not all reactors are able to do this. For example, a riser would need to be extremely long, or a cyclone impractically big. A rotating fixed bed reactor has the clear advantage that, as the solids are fixed in the moving bed, the residence time can be controlled to an almost perfect extent. For the fluid bed family options, a residence time distribution (RTD) will complicate control of solids residence time.

Complexity

The construction and operation of this setup is challenging because of the high temperature involved (demands 12 and 13). Therefore, technically more simple reactors are prioritized. The movement of solids from system to system at high temperature is seen as complicated, hence a yes/no statement is presented in the evaluation. A more simple option, where solids are transported between sections/units is presented in the next section.

The multistage fluidized bed might be able to control solids flow better than an externally circulating fluidized bed, as it can approach a PFR, however this is seen as overly complex. The type is therefore discarded.

These decisions were made after consulting with an experienced technician and experts of Ceratec Technical Ceramics. Especially the complex shapes of the reactor were seen as problematic, as they are more susceptible to thermal stress failures. Furthermore, they cannot be constructed in-house, not meeting demand 10. Another point that was seen as problematic was the controlled movement of solids at high temperature (demand 12).

Table B.9: Overview of selection steps 1-3

Reactor archetype	1: Solids residence time control, and fast temperature change	2: Range of solids residence time	3: Reactor design complexity
Fixed bed family			
Adiabatic bed	no		
Gauze layers	no		
Adiabatic with interstage cooling	no		
Multitubular fixed bed	no		
Continuous chromatographic	no		
Radial flow reactor	no		
Moving bed reactor	no		
Rotating fixed bed reactor	yes	yes	yes
Fluid bed family			
Fluidized bed	no		
Pneumatic conveying/Cyclone	yes	no	
Downflow reactor	yes	no	
Draft tube	yes	no	
Multistage fluidized bed	yes	yes	no
External circulating fluidized bed	yes	yes	yes/no
Rotating fluidized bed	yes	yes	yes
Rotary kiln	yes	yes	yes/no

B.2.4 Detailed analysis of possible reactor types

The number of possible reactors has been reduced to four types, possible meeting all three expectations in table B.9. In this section the applicability of the four types for a continuous methane pyrolysis process will be discussed. A more detailed analysis over the demands discussed in section B.2.2 will be performed. The reactors will be compared to each other. Since it is difficult to quantitatively make this comparison, a positive quality marked with a '+' sign and a negative quality with '-'.

First, a comparison regarding solids residence time control (demand 3) is made:

Table B.10: Detailed analysis of degree of solids residence time control

Reactor type	Rating	Comment
Rotating fixed bed	+++	Excellent control of solids residence time as the solids are fixed. No RTD.
Rotating fluidized bed	-	Better control than an externally circulated fluidized bed, however axial mixing will still cause an RTD to occur. A way to prevent this is the inclusion of compartments to prevent axial mixing. This will greatly reduce axial mixing and thereby the residence time distribution. **(Option added)**
Ext. circ. fluidized bed	- -	Control is possible via solids flow, however control is not as good/easy as with the rotating variants. Adding to this, RTD is present in these reactors.
Rotary kiln	++	Solids residence time can be controlled, little RTD expected as solids flow relatively uniform from top to bottom
Rotating compartmentalized fluidized bed	++	RTD partially removed via the inclusion of baffles in the bed

Demands 4,5,6,11,14,15 and 16 involve heat transfer. Since the decomposition reaction and CO_2 and steam gasification are endothermic, energy needs to be supplied into the reactor. From heat transfer analysis (section A.3), it was concluded that transferring adequate heat for the decomposition at 1130 °C might be problematic for externally heated reactors of larger (> 0.1 m) diameters. Since it is desired to use external heating elements for this lab scale setup, the internal heat transfer characteristics are compared:

Table B.11: Detailed analysis of internal heat transport characteristics

Reactor type	Rating	Comment
Rotating fixed bed	-	As the solids do not mix, internal heat transfer is conduction and radiation only. This is relatively slow, thereby reducing the possible sizes of the reactor that can be used effectively
Rotating fluidized bed	+	Relatively good solids mixing, this enhances the internal heat transfer.
Externally circulating fluidized bed	+	Relatively good solids mixing, this enhances the internal heat transfer.
Rotary kiln	+	Relatively good solids mixing, this enhances the internal heat transfer.
Rotating compartmentalized fluidized bed reactor	+	Relatively good solids mixing, this enhances the internal heat transfer.

Points 3,12 and 13 involve the construction of the setup, in particular the handling of solids movement. The (pneumatic) transport of solids without using mechanical valves is challenging but not impossible. An analysis is made on the technological challenge the transport and control of solids movement.

Table B.12: Detailed analysis of challenge in solids movement

Reactor type	Rating	Comment
Rotating fixed bed	+++	No solids movement, little challenge
Rotating fluidized bed	++	No net solids movement, little challenge
Ext. circ. fluidized bed	- - -	Solids movement between reactors, buffer vessels and J or U junctions. Very challenging
Rotary kiln	–	Solids movement from reactor to reactor, possibly less challenging than fluidized bed because the solids flow in the reactor occurs naturally. Still more challenging than rotating bed reactors
Rotating compartmentalized fluidized bed	++	No net solids movement, little challenge

Comparing detailed points

All the reactor design related points have been compared in three criteria, the results are summarized in table B.13. From the detailed analysis it is concluded that the rotating fixed or fluidized beds are the most simple systems. It is speculated this can be done in a single unit, thereby obtaining a system capable of operating in fixed and fluidized mode. This is very much desired, from the goal of designing the most flexible setup. In the next section, the rotating reactor is modelled. The major driver for this decision was the absence of moving solids between units in the rotating systems, whilst keeping the ability to quickly switch the reaction phase.

Table B.13: Overview of detailed analysis

Reactor type	Level of solids control, Presence of RTD	Internal heat transfer	Solids movement difficulty
Rotating fixed bed reactor	+++	-	+++
Rotating fluidized bed reactor	+	++	++
Externally circulating fluidized bed	-	+	- - -
Rotary kiln	++	+	-
Rotating compartmentalized fluidized bed reactor	++	+	++

B.3 Detailed reactor model for rotating reactor

B.3.1 Design methodology

In this section, a detailed reactor model is developed for the rotating reactor. It is developed to gather more insight into the behaviour of the proposed reactor. It is aimed to predict how this reactor may be operated. In particular the possible variation in process parameters that can be used is of interest. Hence, the aim of this part of the study is to identify the operating area; the range of process parameter variations available for stable operation.

The point of evaluation is the steady state cyclic operation, which occurs after a large (estimated 10-100) amount of cycles. This is defined to be operation where cycle *n* is identical to cycle *n-1*. Comparing under these conditions mitigates startup effects.

From section B.1 it is known that several process configurations are possible (table B.4). Furthermore, it is shown that operation using air (in any configuration) is easier than operating with only steam or CO_2 . Therefore, in order to be operate with steam as only oxidant, the designs will be based on this process configuration.

The design will be made for the set production of 100 $g_C \cdot h^{-1}$ whilst taking into account the demands presented in section B.2.2. It was stated before that the main demand on this system is to be able to change a large amount of process parameters. This demand will be investigated using the developed models.

Because no productivity [$g_C \cdot m_r^{-3} \cdot s^{-1}$] demands exist for this lab scale research setup, the amount of variable process parameters is the main interest for now. However, a comparison will indirectly be made on productivity. The reactor volume required to produce 100 $g_C \cdot h^{-1}$ is of interest for the design. A smaller volume is strongly favoured for construction complexity reasons. This is also the reason the reactor is not sized to CO_2 gasification.

A large amount of experimentally obtained kinetics are available from our previous work. It has been confirmed that these kinetics are able to predict methane conversion, carbon deposition and carbon gasification[1, 2] in a fixed bed reactor. Hence, it is assumed these kinetics are also able to make an accurate estimation of the workings of the reactors modelled in this section.

Reactor principle of operation

From the reactor selection, a favourable reactor is a rotating fixed bed. This fixed bed rotates along its axial center line. This design is presented conceptually in figure B.8a. Because of this rotation, solids are moved throughout the system. If the gasses fed to this rotating volume do not rotate and are fed at a stationary point, the solids can be transported from a decomposition to a gasification area, and so on. This allows quick switching of gasses, which was a requirement uncovered in section B.1. To prevent mixing of gasses in the bed, the reactor must be divided into a number of partitions. Additionally, if the outer heaters are stationary, the solid temperature will also be varied with location.

An alternative design may also be viable. In this case, presented in figure B.8b, the reactor itself is stationary. The bed is divided into a number of partitions, each with an own gas inlet. Using valves, the gasses are switched over the partitions over time, mimicking the transport of solids from area to area. The heater then needs to be divided in partitions and rotate, to still be able to facilitate the temperature change over time. The difference between this case and a conventional cyclically operating fixed bed is two fold. First, still the parts of the reactor volume have a different function at the same time, eg. decomposition or gasification. Secondly, the heater temperature over time can be constant over time. The movement of the heater results in the desired temperature change of the reactor over time. This is a major advantage, as a heater cannot change its temperature sufficiently fast.

Table B.14: Overview of RFBr design options

Option	Bed	Heater	Gas inlets
1	Rotating	Stationary	Stationary, no switching
2	Stationary	Rotating	Stationary, switching of gasses over time

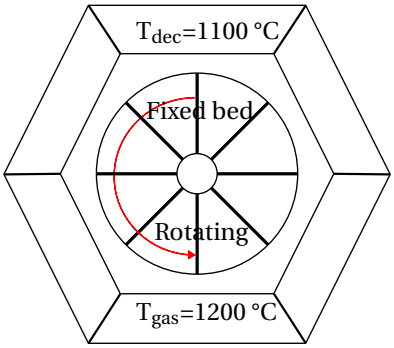

(a) Option 1: Rotating reactor with stationary heater. Gasses are fed at stationary points in space and are not switched over time. Heater temperature is constant over time.

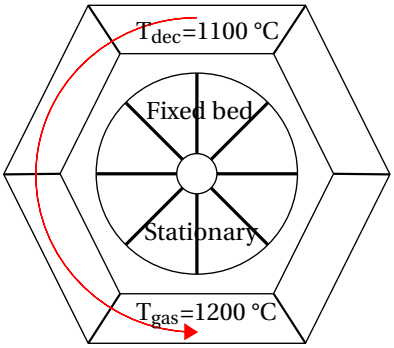

(b) Option 2: Rotating heater with stationary reactor. Gasses are fed at stationary points in space and are switched over time, corresponding to the local heater temperature. Heater temperature is constant over time.

Figure B.8: Two options for rotating fixed bed design. Fixed bed has 8 partitions. Temperatures are crude estimations of actual used heater temperatures.

Both options are presented in figure B.8 and summarized in table B.14. Note that the design points discussed in section B.2.2 are equally valid for both design options. A difference in construction complexity does exist however. After consulting with our experienced technicians, it was decided that option two is more favourable to construct, as the high temperature reactor is now completely stationary.

B.3.2 Model equations

In this section the workings of the model are presented. Since this is a continuous process, the rotating fixed bed will need to reach some kind of (quasi) steady state. What is meant with this is that even though the carbon loading and temperature of a particle within the bed will vary over time, the variation will be some repeating pattern, that is if this quasi steady state is reached.

The reactor geometry is transferred to MATLAB's solvepde solver. Normal fixed bed equations can be used, depending on the partition in which the relevant mesh element exists the equations change between decomposition and gasification.

The energy balance (equation B.16) heat transport through the solids as well as the reaction enthalpy, it has unit $\mathrm{J}\cdot\mathrm{m_r}^{-3}\cdot\mathrm{s}^{-1}$. The term R_x denotes either pyrolysis, gasification or air oxidation, and has a corresponding η and ΔH.

$$\epsilon\rho C_p\frac{dT}{dt} = \lambda\frac{d^2T}{dr^2} + \lambda\frac{d^2T}{d\theta^2} \pm \eta R_x \Delta H_{r,x} A_{ex} \tag{B.16}$$

Note that the gas phase is not taken into account for this equation. The energy required to heat up the gas phase from room temperature to reactor temperature cannot be ignored. However, the setup is designed in such a way that the gas temperature approaches the reactor solids temperature before it enters the bed. Hence, the energy required to heat the gas phase coming from the reactor is relatively small and can be ignored. This was verified further by a model calculation. Furthermore, the axial conductivity can also be ignored, as the temperature radial gradients (and therefore the amount of heat transported) are significantly larger than the axial gradients.

The boundary condition is given by the following continuous flux relation. The heater temperature T_h will vary over time, according to the set points and heater rotation speed.

$$\lambda_{eff}\frac{dT_{w,int}}{dr} = \lambda_{wall}\frac{T_{w,ex}-T_{w,int}}{L_w} = \sigma\epsilon F_{1,2}\left(T_h^4 - T_{w,ex}^4\right) \tag{B.17}$$

The ODE describing loading on the particle during gasification and decomposition, R_x being the gasification or decomposition rate, R_x=0 for the flush partitions, it has the unit $\mathrm{mol}\cdot\mathrm{m}^{-3}\cdot\mathrm{s}^{-1}$:

$$\frac{dC}{dt} = \pm\eta R_x A_{ex} \tag{B.18}$$

The gas phase is modelled as a PFR. At the high linear gas speeds, little backmixing is expected.

$$\frac{d(C_x u_g)}{dz} = \pm\eta R_x A_{ex} \tag{B.19}$$

Since the amount of moles in the gas phase due to the reactions in the partitions, a flux balance was used for all partitions. The model divides the length of the reactor in n elements of length dz. For each element or disk, the heat and mass balances are solved by matlabs solvepde routine.

B.3.3 Results

The included process parameters and their boundaries are presented in table B.15. All these boundaries were based on previous work. The model was used to determine the possible operating window within these established boundaries. No optimization solvers were used in this part of the work. Since the model is solved relatively fast, all combinations of these process parameters could be evaluated in a short amount of time. Because of the large number of varied parameters, the final dataset contains a lot of dimension, it is visualize this data. Therefore, the influence of these parameters is discussed step-wise. In table B.16 the parameters that will not be varied are presented. These are mostly set by the demands presented in section B.2.2.

Table B.15: Overview of parameters and boundary values used in RDR optimization

Parameter	Lower boundary	Upper boundary	Unit	Comment
T_{dec}	1100	1200	°C	From heat transfer section A.3
T_{gas}	1100	1300	°C	From heat transfer section A.3
r_r	0,03	0,08	m	From heat transfer section A.3
L_r	0,1	0,3	m	Based on experiments[1]
τ_{dec}	30	420	s	From particle follow section B.1
N_{dec}	2	5		From particle follow section B.1
N_{gas}	1	4		From particle follow section B.1

Table B.16: Overview of parameters constant throughout RDR optimization, [1] measured as amount of carbon gasified.

Parameter	Value	Unit	Comment
C[1] production	100	$g_C \cdot h^{-1}$	
Gas conversion	>99%	-	Stability reason
A_p	600000	${m_p}^2 \cdot {m_r}^{-3}$	Particle characteristic
ϕ_m	100	$g_C \cdot h^{-1}$	
ϕ_{ox}	165	g/h	10% molar excess
N_{tot}	6	-	Number of partitions, set for construction complexity

To clarify the results presented in this section, first the effects of varying T_{dec} and T_{gas} heater set point are presented for a single reactor size. ($r_{ex} = 0.06m, L = 0.3m$ N_{dec}:N_{gas}=4:2). In figure B.9 the obtained results are presented as contour plots. In the left figure, the fraction of carbon produced at or below the desired temperature is presented. Ideally this fraction is 1, so that the carbon is reactive during the gasification step. A lower value means that part of the carbon is produced above 1120 °C, thereby being less reactive during gasification. The right figure shows the overall amount of carbon produced, as measured in grams per hour gasified, corresponding to the same temperature set points. The contours show the important characteristics of the system, as function of the decomposition and gasification temperature set points. Operating at a desired steady state outside these arced surfaces is not possible, as a net carbon buildup over time exists in the system, eventually completely filling the reactor with carbon, significantly decreasing productivity.

In figure B.9 the trade-off between higher T_{dec} and T_{gas} heater set point temperatures, a higher CH_4 conversion and a lower fraction of desired carbon is visible. Note that the majority of these points do not meet the demand of near 100% CH_4 conversion and are therefore not suitable designs. To meet this required conversion, high temperature set points are required, yielding a carbon that cannot be gasified efficiently. That being said, if sufficiently high set points are used, this design can meet the demand of 100% CH_4 conversion.

Because this randomly chosen design can only operate at high heater set point temperatures, it is likely not the most optimal for our case. Therefore, the entire design area presented in table B.15 was modelled.

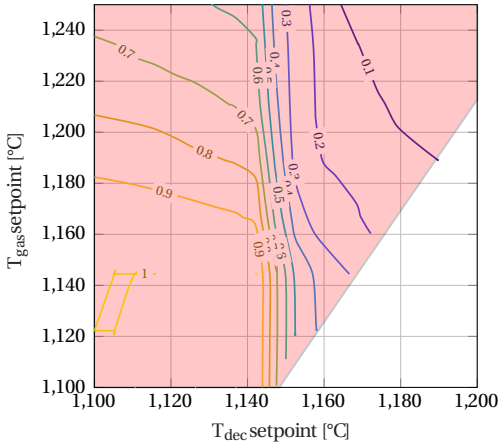

(a) Fraction of desired carbon as function of T_{dec} and T_{gas} setpoints.

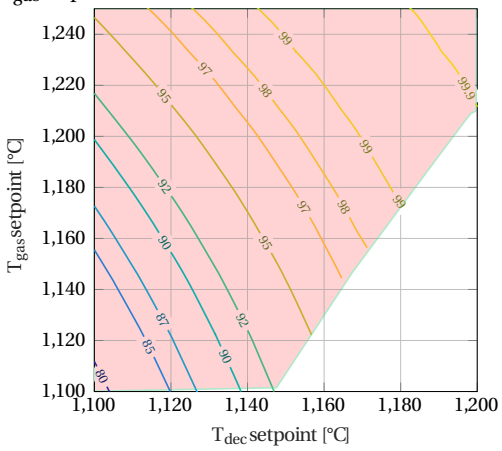

(b) Total production of carbon as function of T_{dec} and T_{gas} setpoints

Figure B.9: Modelled fraction of desired carbon and total C production for the RDR

In figure B.10 the model results are summarized. The data points in this figure denote a configuration, where steady state operating is possible. Varied parameters are the partition ratio (N_{dec}:N_{gas}, changing marker), τ_{dec} (marker size), reactor diameter (figure a-c), T_{dec} (indirectly from the y axis, explained in the paragraph) and T_{gas} (x axis). These area spanned by these points, together with marker size reflect the amount of possible combinations. It is therefore desired to span a large area, combined with a large amount of small and larger markers.

It was found that the most relevant unit to compare is the average carbon deposition temperature of the system. The decomposition temperature heater set point was highly correlated to the gasification temperature heater set point. At optimal conditions, these cannot be chosen completely freely. When carbon is deposited at higher temperature, a higher gasification temperature is

required to gasifiy this.

More diameters than the presented values were modelled, however it was found that smaller diameters only met production at extremely high temperature, which was undesired due to stability reasons. Furthermore, larger diameters were found to be inefficient in the heat transfer analysis.

From the figure, it can be seen that a larger reactor is operating at slightly lower temperature to convert all the incoming methane completely. The particle following study indicates that the optimal carbon deposition temperature for steam gasification is approximately 1140 °C. When approaching this temperature, another benefit is added. Ideally, the reactor is able to operate above, and below this temperature. Hence a radius of 0.07-0.08 m is seen as ideal.

An important find is that more than 1 order of magnitude in range of pyrolysis residence times are suitable for steady state operation, provided that the partition ratio is changed accordingly. Since this residence time and partition ratio is changed easily in this design, this is a powerful argument in favour of the rotating bed reactor.

Furthermore, with slight changes in temperature the solids residence time may be changed, at equal partition distribution. This means that the influence τ_{dec}may be evaluated (almost) independently.

Further findings in this study are summarized:

- A reactor length below 0.3 m greatly reduces the operating window, a large amount of lower temperature points disappear. Since 0.3 m is the approximate maximum heatable length for this lab scale setup, it was decided not to increase this value.
- The smaller diameters, next to not meeting CH_4 conversion, also do not perform the desired temperature swing. For smaller diameters, the total heater set point temperature difference across the reactor diameter results in a too severe temperature gradient, reducing the temperature difference between the gasification and decomposition partition.
- At larger diameters (>0.08 m), the temperature swing is more pronounced near the reactor wall. However, however the bed center temperature is too low to participate significantly in the reaction. All sizes are able to meet the 100% conversion demand, even at lower reactor lengths, due to the lower gas velocities present. Moreover, a construction perspective, the larger diameter is undesired.

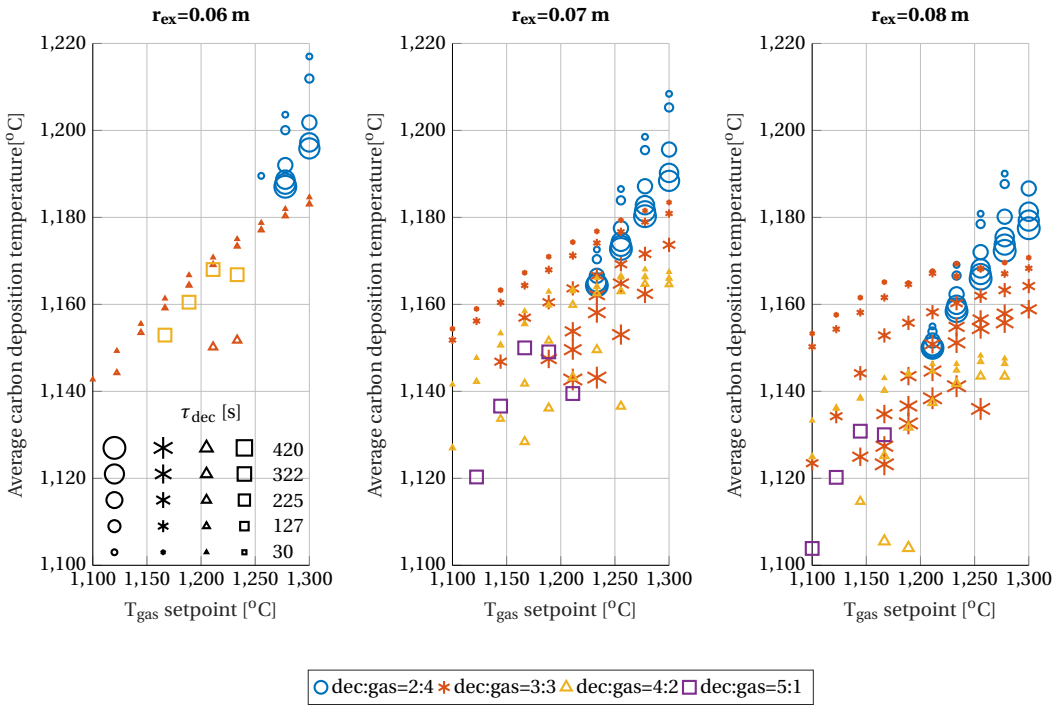

Figure B.10: Operating window for the RDR. Various τ_{dec} and T_{dec} and partition ratios as function of T_{gas}. For all data L_r=0.3 m, steam gasification only. Further data is presented in table B.16

B.3.4 Conclusion on RFBr

Detailed modelling indicates that a lab scale rotating fixed bed reactor (RFBr) divided into 6 partitions is able to facilitate a continuous methane pyrolysis-gasification process. After evaluating numerous combinations of process parameters, an ideal reactor radius has been estimated in the range of 0.07-0.08 m. This allows operating in a large range of parameters, whilst keeping the reactor volume in acceptable range.

From a research perspective, the ability to vary a large amount of process parameters is valuable. Therefore, the rotating bed reactor is seen as a suitable candidate for this stage of the project.

B.4 Conclusion

In this section, reactor design parameters were established for a lab scale setup. It was aimed to develop a setup, capable of varying as many controllable parameters as possible. Moreover, the operating window should be as big as possible. Before this information could be obtained, several studies were performed. First, a kinetic analysis was performed. For an arbitrary reactor the approximate operating window was established. Furthermore, the most ideal pyrolysis and gasification conditions were established. From this information, demands on the lab scale setup were formulated.

A reactor selection procedure yielded a rotating fixed or fluidized bed as the most ideal reactor archetype. The excellent solids residence time control, coupled with fast temperature change and relatively low technical complexity were the biggest arguments in favour of this type.

A simulation was constructed. The design parameters were investigated. It was found that a radius if 0.07-0.08 m and a length of 0.3 m yielded the most versatile system, hence this was the constructed size. The range in heater set point temperature was found to match with the specifications of the heaters used in previous work, hence this technology was selected. Required gas flows were used to size the rest of the equipment.

Bibliography

[1] T. Kreuger, W. P.M. van Swaaij, A. N.R. Bos, and S. R.A. Kersten. Methane decomposition kinetics on unfunctionalized alumina surfaces. *Chemical Engineering Journal*, 427(June 2021): 130412, 2022. ISSN 13858947. doi: 10.1016/j.cej.2021.130412. URL `https://doi.org/10.1016/j.cej.2021.130412`.

[2] Tomas Kreuger, Kersten, S.R.A, and A.N.R. Bos. Predicting gasification rates of pyrolytic graphite deposited from methane. *Chemical Engineering Journal*, 2022.

[3] W. P.M. Van Swaaij, A. G.J. Van der Ham, and A. E. Kronberg. Evolution patterns and family relations in G-S reactors. *Chemical Engineering Journal*, 90(1-2):25–45, 2002. ISSN 13858947. doi: 10.1016/S1385-8947(02)00066-9.

Dankwoord

Dit werk had zonder alle geweldige collega's niet tot stand kunnen komen. De afgelopen 4 jaar bij SPT hebben nooit echt als werk aangevoeld, hier zullen bepaalde mensen om lachen. Je weet wie ik bedoel. Voor mijn mooie tijd aan de Universiteit wil ik jullie allen bedanken.

Sascha, bedankt voor de kans te PhD'en. Op mijn "sollicitatiegesprek" was het ons beiden eigenlijk meteen duidelijk welk project ik zou gaan kiezen. Jouw heldere vragen en uitleg waren voor een beginnend wetenschapper erg waardevol. Tijdens mijn PhD heb je me veel geleerd over industriële en maatschappelijke thema's, en dat op tijd zijn absoluut geen vereiste is om binnen de UT carrière te maken. Ik heb onze gesprekken altijd als prettig ervaren, ook als ik een wat mindere eerste versie van een paper inleverde. Dank hiervoor.

Wim, jouw gevraagd en ongevraagd advies hebben dit project naar een ander niveau getild. Jouw luisterend oor en immense ervaring waren onmisbaar. Daarnaast kon ik altijd terecht voor een korte discussie. Vooral het design van de conusreactor en de interpretatie van de kinetiek waren zonder jou een stuk lastiger geworden.

Rene, Jan, Robert, Ronald and Baira. I have always appreciated the involvement from Shell's side during the course of this project. I thank all of you for the insightful discussions. It was interesting to see your generally different perspective on cases at hand. I have learned a lot from these. Without your help there are several parts of this thesis that would have looked very different! The LECO was essential, and indeed, the ordering of catalyst carrier is significantly easier using @shell.com rather than @utwente.nl. I thank you for offering this opportunity, and maybe we will meet again during a (now industrial) endeavour!

Yvonne, het was vanaf dag één duidelijk dat zonder jou de vakgroep binnen een week ontspoort. Zonder jouw navigatie in de trog die Hora-Finita heet had ik het niet gered. Bedankt voor alle hulp bij het inplannen van meetings met Sascha, en de communicatie met Amsterdam.

Louis, hoewel we inhoudelijk tijdens deze PhD weinig samengewerkt hebben, was je altijd geïnteresseerd in hoe het ging. De vele praatjes op de gang waren altijd gezellig. Project CT was altijd erg leuk om samen te doen. Wim, jij bent voor een groot deel de reden dat ik ben na gaan denken over een PhD. Ik heb het tijdens ons afstudeerproject dusdanig naar mijn zin gehad dat ik dan de knoop toch doorgehakt heb. Hier heb ik geen moment spijt van gehad. Dank hiervoor! Erna, dank voor alle hulp bij de verschillende analyses en veiligheidsdiscussies. De elemental analyzer had wat problemen met mijn samples, maar alle andere analyses gingen, vaak door jouw hulp, gelukkig wel goed! Pilar, thanks for the insightful discussions on carbon formation and your warm contribution to the group. Jean-Paul, dank voor alle kritische vragen. Na elke groepspresentatie kon ik ervan uitgaan dat ik hier wat ging leren! Henk, jouw interesse en kennis hielpen mij om het geheel in een groter perspectief te zien. Roel, dank voor alle interessante discussies over de meest uiteenlopende thema's.

Deze PhD, en mijn gehele tijd bij SPT, had compleet anders geweest zonder de technici van het HDL. Ik heb van jullie minstens net zoveel geleerd als dan van menig professor (sorry Sascha). Naast jullie enorme ervaring heb ik altijd bewonderd hoe behulpzaam en aanspreekbaar jullie naar alle studenten zijn.

Karst, ik zal jouw vrolijke lach, behulpzaamheid en geweldige muziek nooit vergeten. Panter radio staat nogsteeds vaak aan.

Ronald, jouw skills met de electrique van de setup zijn voor mij nog steeds magie. Door jou begrijp ik dit een stuk beter, wat me thuis al meermaals verder geholpen heeft. Zonder jou hadden we de oven denk ik met de hand moeten draaien. Dat klinkt als werk, en we weten beiden hoe ik daarover denk. Jij hebt me geleerd dat pauze heilig is en de zwaartekracht meestal oké is. Je bent een aanwinst voor de groep en ik hoop dat jij nog vele jaren de pauzes vult met lekkere frikandellen en ongepaste grappen.

Johan, jouw fantastische opmerkingen tijdens de pauze zullen me voor altijd bijblijven. Al jouw skills in de werkplaats waren voor dit project absoluut goud waard. Dank voor alle hulp, en de wijze lessen bij de frees. Ik verbaas me er elke keer weer over dat jouw werkbank er eigenlijk altijd hetzelfde uitziet, maar er toch een gigantische hoop gebeurt.

Benno, zonder jouw enorme ervaring hadden we experimenteel een stuk minder op de rit gekregen. De constructie van de oven was eigenlijk meteen goed, en heeft zich ondertussen als robuust bewezen. De keramische reactor was op het laatst misschien toch een stap te ver, maar hiervan hebben we denk ik toch een hoop geleerd. De stalen versie was verassend robuust, vooral toen hier de niet-pisbakken-staal-lasdraad in zat. Daarnaast heb jij bij mij de interesse in de werkplaats enorm aangewakkerd. Van jouw lessen aan de draaibank en frees heb ik voorlopig nog veel profijt. Dank voor alles. Ik hoop dat je je schuur ooit nog eens opgeruimd krijgt.

Daarnaast heb ik veel geluk gehad met de rest van de collega's binnen SPT. Vincent, jouw interessante verhalen over de meest uiteenlopende thema's waren altijd een goede toevoeging. Ik zal nooit vergeten dat je geen hout kunt zagen met een metaalzaag. (En dat jij Sascha's rozen verziekt hebt ook niet) Martin, dank voor de introductie binnen SPT, mijn afstuderen was een mooie tijd. Pushkar, I always enjoyed our talks. Zoë is always in for another meeting. Surika, tijdens de pauzes in het HDL was het met jou altijd gezellig. Op de group trip heb jij bewezen dat je zonder kaarttalent toch mee kunt spelen en de group trip had nóg beter geweest als jij de champangetour wel geregeld had. Rick, ik heb onze gesprekken in het HDL altijd gewaardeerd, en jouw precisie bij alles wat je doet erg bewonderd. Lisette, dank voor al jouw inzet voor de sociale events binnen de groep. Jouw baksels waren altijd erg lekker. Thomas, ik begrijp niks van jouw PhD project. Gelukkig hebben we altijd veel andere thema's gehad om over te praten. Dion, jouw aanwezigheid in het kantoor en bij de borrels waren genoeg voor veel onvergetelijke verhalen.

Yordi, mijn methaan-broeder. Ik ben nog steeds blij dat ze het moeilijke project aan jou gegeven hebben. Onze discussies over kinetiek en cross-correlatie hebben mij veel geleerd. Daarnaast vond ik het altijd fijn samen te werken voor MRT. Shabibi, sorry for using your real name. Your enthousiasm for your project and mercedes is unmatched. I loved our talks during our many borrels. Lets drink a deperados again? Tim, jouw skills met de computer zijn goud waard. Door jou begrijp ik beter wat er 'onder de motorkap' gebeurt. Jasper, man man man. Eline, jouw aanwezigheid binnen de groep doet iedereen goed. Het bureau in de meander is in goede handen. Tess, ik genoot altijd van onze gesprekken. Sas en Ronnie denk ik ook? Nicole, dank voor de vele koffiesessies. Het was altijd erg ontspannend samen een bakkie te drinken. Varsha, Chiel, Eshan, Anne, An, Vahideh, Masha, Lionel, Kai, Kasper, Tim, thanks for all the great moments and making my time at SPT great!

Dan zijn er nog drie andere kompanen. Juraj. Onze tijd in Enschede was vanaf dag 1 eigenlijk niks. Sindsdien is het alleen maar bergafwaarts gegaan. Jouw sociale skills zijn ongeëvenaard, je bent een absolute aanwinst voor onze groep. Jouw brouwsels zijn verschrikkelijk, maar toch elke keer weer lekker. Ik hoop dat we nog veel vaker rond een kampvuur sauerkrautsuppe koken, een tour op een mammoet maken, of een goed gesprek hebben. Tot slot mijn paranimfen. Jullie hebben

beiden al een dankwoord geschreven. Het is lastig deze te overtreffen. Ik heb erover nagedacht jullie helemaal niet te noemen, maar ik doe het toch: Martein, we kennen elkaar al meer dan 15 jaar. Tijdens deze tijd heb jij denk ik een net-positive bijdrage aan mijn leven geleverd. Ik heb jouw scherpe analyses van verschillende fenomenen of problemen altijd bewonderd. We wonen nu gelukkig ver uit elkaar. Dit weerhoudt ons er niet van om toch samen onverstandige dingen te doen. Ik ga ervan uit dat er nog vele ellendige weekenden zullen volgen. Ik wens jou en Alyssa het allerbeste. Thimo. Ik heb enorm veel bewondering hoe jij in het leven staat. Ik heb hier veel van kunnen leren. Daarnaast hebben we in en onder het huis het een en ander ondernomen. Jouw hands on approach was altijd erg mooi om te zien, het eindresultaat denk ik ook! Dank voor alle mooie weekenden, voetbalavondjes, discussies en soortgelijke ellende.

Ook wil ik mijn familie bedankten. Pa, ma, jullie hebben mij van jongs af aan uitgedaagd. Dit heeft natuurlijk veel geholpen tijdens mijn tijd aan de uni. Gelukkig ben ik bij de biologie weggebleven en ben ik meer richting staal gegaan. Anneke, je hebt de keuze gemaakt iets heel anders te gaan doen. Deze keuze bewonder ik enorm, ik weet niet of ik het ook had gedurfd.

An die Deutsche Truppe. Danke fürs herzliche Willkommen in eurem Land, und das Interesse an meiner Doktorarbeit.

Tot slot wil ik Julia bedanken. De laatste 9 jaar waren zeker niet altijd makkelijk, maar wij kunnen samen alles aan. Jij was er altijd voor mij. Jij bent voor mij in Enschede gebleven, iets waar ik de afgelopen 4 jaar enorm dankbaar voor ben geweest. Nu hebben wij samen met Zoë en Mika (en Voldemort, Bean, Benjamin Franklin en Betsie) in Duitsland iets moois opgebouwd. Ik kijk enorm uit naar de komende jaren die wij samen door gaan brengen.

- Tomas.

About the author

Tomas Kreuger was born April 4th in Hoorn, the Netherlands. After completing high school he moved to Enschede for a study in Chemical Engineering at the University of Twente. He completed his bachelor thesis on the subject of photocatalytic water splitting. He obtained his master degree in Chemical and Process Engineering on the subject of carbon capture in a fixed bed. During this time, he got offered the chance to complete a PhD at the same research group. In his free time he likes to spend time with family and friends, the dogs, and do various jobs in and around the house. Currently he is employed by Evonik Industries AG.